Signals for transversity and transverse-momentum-dependent quark distribution functions studied at the HERMES experiment

Der Naturwissenschaftlichen Fakultät der
Friedrich-Alexander-Universität Erlangen-Nürnberg
zur
Erlangung des Doktorgrades

vorgelegt von
Markus Diefenthaler
aus Augsburg

Als Dissertation genehmigt von der Naturwissenschaftlichen Fakultät der Universität Erlangen-Nürnberg.

When finishing an interminable work, the past and the future collide:
Thus, this thesis is dedicated to the memory of my godfather and
the path of life I have walked with Frau M..

Contents

Contents

1. The spin structure of the nucleon

Our knowledge of the inner structure of the nucleon is to a large extent based on the measurement of high-energy scattering processes, which are interpreted within quantum chromodynamics (QCD). This work contributes to the experimental effort in the investigation of the nucleon's spin structure.

The nucleon is composed of relativistic quarks that exchange gluons. Both types of elementary particles share the nucleon momentum in almost equal parts. The origin of the nucleon spin of $\frac{1}{2}\hbar$ has been extensively studied during the last 25 years in various polarised deep-inelastic scattering experiments. From these experiments it is now known that the spin of the quarks (spin-$\frac{1}{2}$ fermions) accounts only for about one third of the nucleon spin. Recent measurements also indicate that the contribution from the spin of the gluons (spin-1 bosons) is small, suggesting a rather significant role of the orbital angular momentum in the spin structure of the nucleon.

There are several arguments in favour of large orbital angular motion with in the nucleon: A relativistic quark confined in a small region of space must have orbital angular momentum, and the non-zero anomalous magnetic moment of the nucleon has been shown to be related to non-vanishing quark orbital angular momentum. This justifies the tremendous interest of the high-energy spin physics community in the study of orbital motion of the quarks and gluons. One active field concerns the global analysis of transverse-momentum-dependent parton distribution functions, which characterise in transverse momentum space the number densities of quarks or gluons in a certain state. These distribution functions are related to spin-orbit correlations in the nucleon and thereby also associated with single-spin asymmetries.

In this work information about transverse-momentum-dependent parton distribution functions for quarks only are provided in a Fourier analysis of single-spin asymmetries studied in semi-inclusive measurements of deep-inelastic scattering off a transversely polarised proton target at the HERMES experiment. Preliminary results of parts of this work allowed for the first extraction of the transverse-momentum-dependent quark distribution functions transversity and Sivers, which describe the distribution of transversely polarised and unpolarised quarks in a transversely polarised nucleon, respectively. The results presented in chapter 6 of this work will not only extend the knowledge about the transversity and Sivers distributions but also about three other transverse-momentum-dependent quark distribution functions.

This work is divided into five parts. In chapter 2 the concept of parton distribution functions is reviewed and transverse-momentum-dependent quark distribution functions are introduced, with emphasis given on their interpretation. It is shown that these quark distributions are related to single-spin azimuthal asymmetries of hadrons produced in deep-inelastic scattering. The contribution of each of the quark distributions of interest to the single-spin asymmetries can be identified by the distinct azimuthal dependence in the distribution of the hadrons observed.

In chapter 3 the setup of the HERMES experiment at the HERA beam facility is described, which is well-suited for the measurement of single-spin asymmetries. The polarised gas target permitted highly polarised target samples without dilution from unpolarised target material and allowed for a substantial reduction of time-dependent systematic uncertainties by the rapid reversal of the target spin orientation. The particle identification system enabled a very clean lepton-hadron separation and a clean identification of pion and charged kaon tracks, which is essential for studying the dependence of the transverse-momentum-dependent quark distributions on the quark flavours.
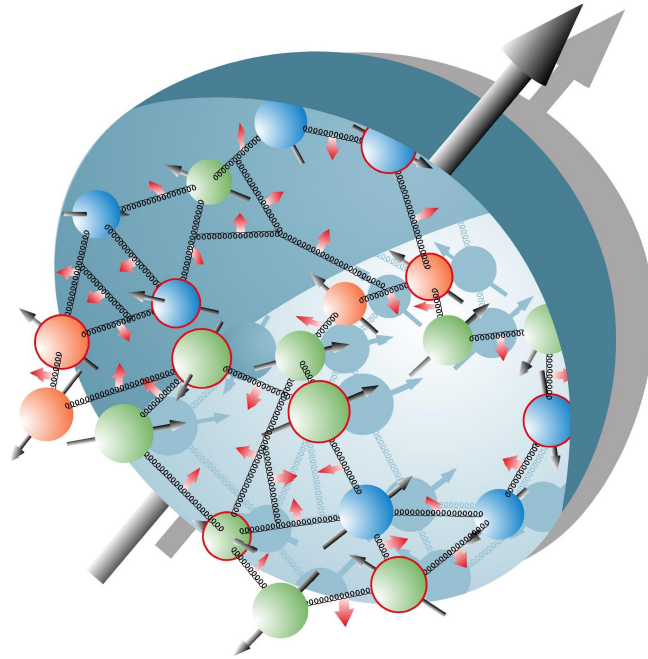
Figure 1.1.: Illustration of the inner structure of the nucleon (showing the quarks as spheres and the gluons as springs). The quark (gluon) spins are indicated as grey (red) arrows.

In chapter 4 the reconstruction of single-spin asymmetries from the selected events and the decomposition of the single-spin asymmetries in terms of Fourier components is explained. As this work constitutes a first decomposition based on the likelihood formalism, a detailed description is given.

The focus of chapter 5 is put on the study of systematic influences on the extracted Fourier components. The estimate of the consequential systematic uncertainties of the Fourier analysis is based on a fully differential model for the single-spin asymmetries constrained from data. This model is implemented in the PYTHIA Monte Carlo generator and allows for a model-independent study of systematic influences.

In chapter 6 the Fourier components are decomposed in terms of transverse-momentum dependent functions. The new results represent the most precise signals for the transversity and Sivers distribution and provide also sensitivity for the worm-gear distributions.

The results presented in this work play not only an important role in the understanding of lepton-nucleon scattering but also in other high-energy scattering processes as, e.g., the hadron-hadron collisions studied at the Relativistic Heavy Ion Collider (at BNL) or even the Large Hadron Collider (at CERN). They will help to test fundamental concepts of QCD such as factorisation or universality.

2. Spin-orbit correlations in the nucleon

An investigation of the orbital angular momentum of quarks and gluons within the nucleon requires measurements correlating the position of partons with their momenta. The most generic phase-space distribution describing this conjugate variable pair is the Wigner distribution [Ji03]. In the analysis of orbital motion in the nucleon, two projections of the Wigner distribution are an active field of research:

❏ In a fast moving nucleon, generalised parton distributions relate information about the parton's momentum in forward direction (one dimension in momentum space) to its localisation transverse to this direction (two dimensions in coordinate space) [Bur00, RP02, Die02, BJY04].

❏ Transverse-momentum-dependent parton distribution functions are sensitive to the parton's momentum both in forward and transverse direction of the fast moving nucleon and thus combine three dimensions in momentum space (section 2.2).

Both projections allow for a characterisation of the inner structure of the nucleon. Here, transverse-momentum-dependent parton distribution functions are discussed for quarks only with emphasis given to their interpretation and their observables (section 2.2 and 2.3).

Before presenting the description of the nucleon's inner structure in terms of transverse-momentum dependent quark distribution functions, i.e. quark distribution functions including the transverse momentum of quarks in the parametrisation, the concept of parton distribution functions is introduced by reviewing the parton model and its implementation in QCD (section 2.1).

Transverse-momentum dependent quark distribution functions cause distinctive signatures in the azimuthal dependence in the distribution of unpolarised hadrons produced in the deep-inelastic scattering process. This dependence is manifested in single-spin asymmetries, i.e. left-right asymmetries in the momentum distribution of these hadrons with respect to the transverse spin direction of the quarks. Signals for transverse-momentum dependent quark distribution functions can be studied in a Fourier analysis of these single-spin asymmetries (section 2.3).

2.1. Partonic images of the nucleon

2.1.1. Probing the quark-gluon structure of the nucleon

Deep-inelastic scattering measurements have revealed the inner structure of the nucleon consisting of valence quarks, sea quarks and gluons and established quantum chromodynamics (QCD) as the theory of the strong interactions. The deep-inelastic scattering process is illustrated in figure 2.1: a lepton (l) with high energy scatters off a nucleon (N) exciting the nucleon to a final state (X) with much higher mass. The reaction is described by the electroweak theory and for charged leptons (at typical energies of polarised scattering experiments) dominated by electromagnetism. In good approximation the interaction is mediated by the exchange of a single photon.

Scattering elementary particles like leptons off a confined state like the nucleon has the advantage that the leptonic part of the scattering process is well-known and the kinematics can be calculated, e.g. in the laboratory frame (lab), without further assumptions. In inclusive measurements, $lN \rightarrow l'X$,

only the scattered lepton (l') is detected with an energy of E' under a scattering angle θ. The lepton kinematics in the initial and final state define three Lorentz-invariant quantities:

❑ The squared centre-of-mass energy s of the deep-inelastic scattering process is determined by the four-momenta of the beam lepton ($k = (E, \mathbf{k})$) and the target nucleon P:

$$s = (k + P)^2 \stackrel{\text{lab}}{\approx} 2ME + M^2. \tag{2.1}$$

Here and henceforth, the mass of the leptons is neglected given the much larger lepton energies involved and an experiment with a fixed target ($P \stackrel{\text{lab}}{=} (M, \mathbf{0})$) is discussed.

❑ The squared four-momentum q^2 transferred from the beam lepton to the target nucleon is calculated from the four-momenta of the incident (k) and scattered lepton ($k' = (E', \mathbf{k}')$):

$$q^2 = (k - k')^2 \stackrel{\text{lab}}{\approx} -4EE' \sin^2\left(\frac{\theta}{2}\right) < 0. \tag{2.2}$$

The virtuality $Q^2 \equiv -q^2$ characterises the amount by which the virtual photon is off its mass shell. The zeroth component of the virtual photon's four-momentum, $q^0 \stackrel{\text{lab}}{=} E - E'$, commonly denoted as ν, states in the laboratory frame the energy transferred.

The spatial resolution of the deep-inelastic scattering process is limited by the reduced wave-length $\lambda/2\pi$ of the virtual photon, which is related to Q^2 and depends on the reference frame:

$$\frac{\lambda}{2\pi} \stackrel{\text{lab}}{=} \frac{1}{|\mathbf{q}|} = \frac{1}{\sqrt{\nu^2 + Q^2}}. \tag{2.3}$$

❑ The squared invariant mass of the virtual-photon nucleon system is obtained from the four-momenta of the target nucleon and the virtual photon:

$$W^2 = (P + q)^2 \stackrel{\text{lab}}{=} M^2 + 2M\nu - Q^2. \tag{2.4}$$

The deep-inelastic scattering process is also described by two dimensionless scaling variables measuring the inelasticy of the scattering process:

$$x = \frac{Q^2}{2P \cdot q} \stackrel{\text{lab}}{=} \frac{Q^2}{2M\nu}, \quad x \in [0; 1], \tag{2.5}$$

and the fractional energy transferred in the laboratory frame from the beam lepton to the nucleon:

$$y = \frac{P \cdot q}{P \cdot k} \stackrel{\text{lab}}{=} \frac{\nu}{E}, \quad y \in [0; 1]. \tag{2.6}$$

As the invariant mass of the hadronic final state is larger than the mass of the target nucleon:

$$W^2 > M^2 \Leftrightarrow \left(\frac{1 - x}{x}\right) Q^2 > 0, \tag{2.7}$$

the Bjorken scaling variable x is in the range of $[0; 1]$. In an elastic scattering process, $lN \to l'N$, the target nucleon remains intact, $W^2 = M^2$, and consequently the scaling variables are fixed to $x = 1$ and $y = Q^2/(2ME)$.
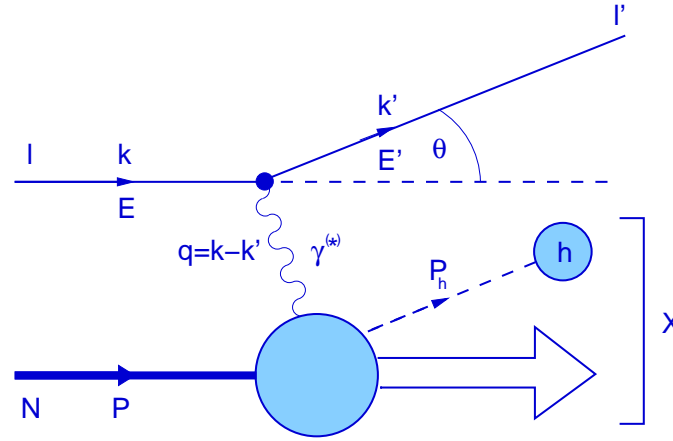
Figure 2.1.: Illustration of the deep-inelastic scattering process in the one-photon approximation.

The set of kinematic variables is overdetermined as $Q^2 = xys$. Inclusive measurements are commonly defined by x and Q^2 at a given centre-of-mass energy $\sqrt{s}$. In semi-inclusive measurements, $lN \to l'h_1 \dots h_n X$, where the hadrons, $h_1 \dots h_n$, formed in the final state are detected in coincidence with the scattered lepton, further kinematic variables are required. For single-hadron production ($n = 1$), one possible choice is the combination of the dimensionless scaling variable z:

$$z = \frac{P \cdot P_h}{P \cdot q} \stackrel{\text{lab}}{=} \frac{E_h}{\nu}, \quad z \in [0;1], \tag{2.8}$$

which measures in the laboratory frame the fraction of the transferred energy ν carried by the detected hadron, and the transverse momentum $\mathbf{P}_{h\perp}$ of the hadron in the final state:

$$|\mathbf{P}_{h\perp}| = \frac{|\mathbf{q} \times \mathbf{P_h}|}{|\mathbf{q}|}. \tag{2.9}$$

The cross section of deep-inelastic scattering can be decomposed in a model-independent way in terms of structure functions. Inclusive measurements off longitudinally or transversely polarised targets are, e.g., characterised by four structure functions: The spin-independent structure functions $F_1(x,Q^2)$ and $F_2(x,Q^2)$, investigated in cross-section measurements, and the spin-dependent structure functions $g_1(x,Q^2)$ and $g_2(x,Q^2)$, studied in measurements of the cross-section difference in parallel or anti-parallel polarisation of beam leptons and target nucleons. The analysis of structure functions has extended the knowledge about the nucleon's inner structure extensively. The evidence that the electrically charged constituents of the nucleon are spin-$\frac{1}{2}$ particles [CG69] or the determination of the quark spin contribution to the nucleon spin of about $1/3$ [HERMES07, COMPASS07] are two of many important results obtained. In section 2.3, the decomposition of the deep-inelastic scattering cross section in terms of structure functions is presented for the semi-inclusive measurement off a transversely polarised nucleon.

Below, the main focus is put on parton distribution functions (PDF) which describe intrinsic properties of the nucleon's constituents and are thus universal. Contrary to structure functions, parton distribution functions are not process-dependent and can be applied in various scattering processes due to their universality. The analysis of parton distribution functions enables a flavour-dependent investigation of the nucleon's structure, whereas structure functions can only be separated according to electromagnetic charge.

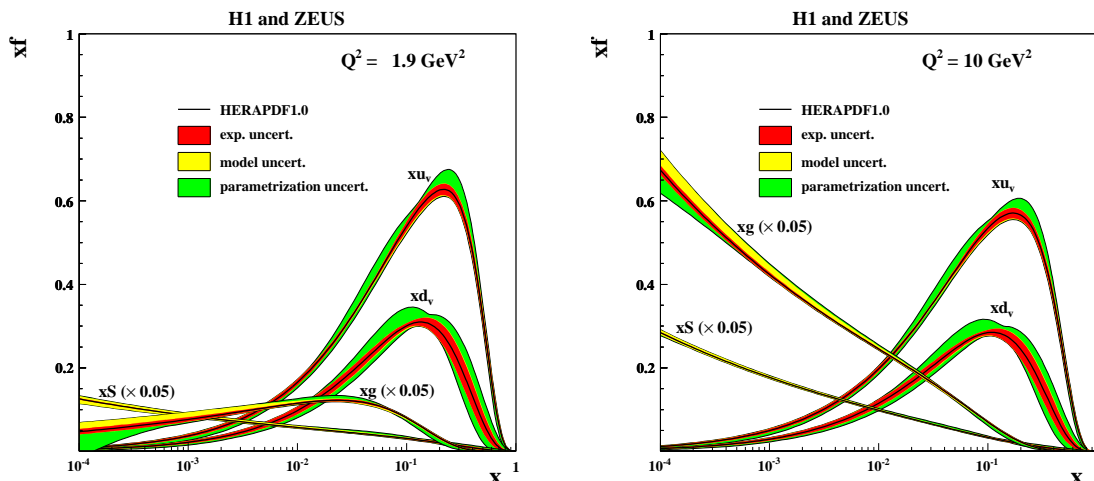Figure 2.2.: Parton distribution functions are obtained in a combined analysis of deep-inelastic scattering measurements by the H1 and ZEUS collaboration [HZ09]. The probability to measure valence quarks (xu_V, xd_v), sea quarks ($xS = 2x(\bar{u} + \bar{d})$) and gluons ($xg$) within momentum fraction $[x; x + dx]$ is presented at $Q^2 = 1.9\,\mathrm{GeV}^2$ (left panel) and $Q^2 = 10\,\mathrm{GeV}^2$ (right panel). The sea quark and gluon distributions are scaled by a factor of $1/20$.

2.1.2. Modelling the nucleon structure

The results of the first deep-inelastic scattering measurements were explained by the parton model. In the model by Bjorken [BP69] and Feynman [Fey72] the nucleon is made up of pointlike scattering centres, called partons. Each parton carries a fraction ξ of the nucleon's momentum P. The parton distribution function $f_1(\xi)$ describes the probability $f_1(\xi)d\xi$ to find a parton within momentum range $[\xi P; (\xi + d\xi)P]$.

The parton model can be illustrated in a dynamic view of the nucleon's constituents: In the rest frame, the interaction among partons by momentum exchange and creation or annihilation is assumed to occur at finite energies and in finite time. When the momentum of the nucleon increases, the times of interactions are dilated by the Lorentz transformation. In the infinite momentum frame, where the nucleon moves with infinite momentum, the partons appear to be not interacting at all and can be regarded as quasi-free and static. Only a single parton but not the other partons within the nucleon are involved in a scattering process.

Deep-inelastic scattering is interpreted as the incoherent sum of elastic scattering of virtual photons off quasi-free and static partons. In the scaling limit, $\xi^2 P^2 \ll Q^2$, the momentum fraction ξ is identical to the Bjorken scaling variable x. Charged partons can be identified as quarks. In the quark-parton model the parton distribution functions $f_1^q(x)$ describes the momentum distribution of quarks of flavour q within a fast moving nucleon. No scale dependence is considered as a scattering process off pointlike quarks is independent from the virtual photon's resolution.

However, there is a scale dependence observed (figure 2.2) which reflects the quantum fluctuations predicted by QCD and occurring at unknown energies and in unknown time. Due to Heisenberg uncertainty principle a sea of virtual gluons arises in the nucleon preferential at low momentum fraction. These gluons radiate off other gluons or pairs of quarks and anti-quarks.

The scale dependence of deep-inelastic scattering measurements can be explained by QCD. For low momentum transfer and for high momentum fraction only the three valence quarks within the nucleon can be probed. The valence quarks are embedded in a sea of virtual quarks and gluons
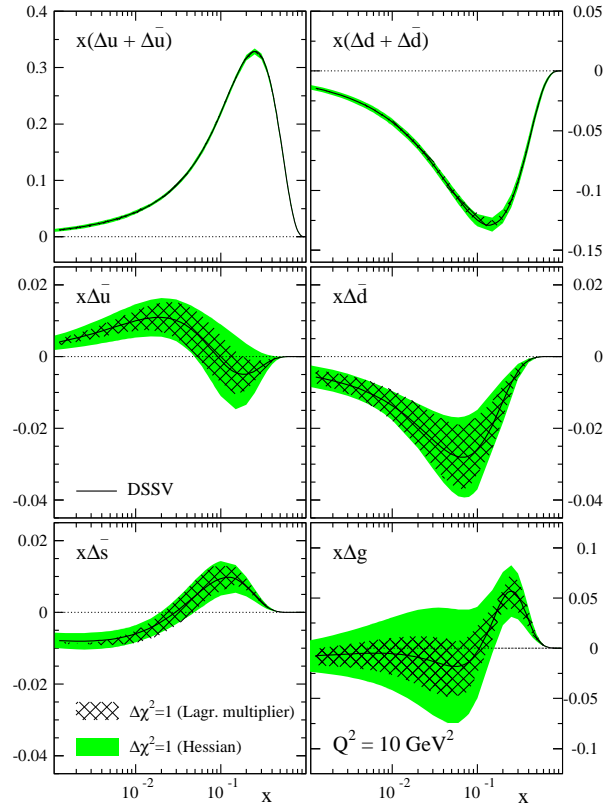
Figure 2.3.: Spin-dependent parton distribution functions are obtained in a QCD analysis of polarised deep-inelastic lepton-nucleon and proton-proton scattering measurements [dFSSV09]. Helicity distributions, here denoted as $\Delta q(x)$ and multiplied by x, are presented for quarks, anti-quarks and gluons at $Q^2 = 10\,\text{GeV}^2$. The green and dashed bands represent the uncertainty in the global fit evaluated in two complementary methods.

whose field accounts for a large portion of the nucleon's mass. With increasing momentum transfer, the resolution increases and more and more sea quarks are seen separated from the valence quarks. The sea quark distribution functions rise strongly towards lower values of x and proportional to the gluon distribution function (figure 2.2).

Factorisation theorems [CS81, JMY04, JMY05] interrelate deep-inelastic scattering cross sections and hence structure functions to parton distribution functions and enable their indirect measurement. In this implementation of the parton model's concept in QCD, structure functions as e.g.:

$$F_1(x, Q^2) = \sum_q e_q^2 \left(f_1^q(x, Q^2) + f_1^{\bar{q}}(x, Q^2) \right). \tag{2.10}$$

are obtained from the electric charge-weighted sum of quark distribution functions over quark (and anti-quark) flavours.

2.1.3. Leading-twist representation of quark spin and momentum

The contributions to deep-inelastic scattering are commonly classified by twist, a quantum number t, denoting the order in M/Q at which an effect arises [Jaf97]. Dominant contributions are labelled as twist-two, $t = 2$, higher twist contributions, $t > 2$, are suppressed by $(M/Q)^{t-2}$.

At leading twist (twist-two) three parton distribution functions characterise momentum and spin of the quarks within the nucleon [Jaf97]. In addition to the momentum distribution $f_1^q(x)$ [1], introduced in the discussion of the parton model (section 2.1.2), two spin-dependent functions appear: the helicity distribution $g_1^q(x)$ and the transversity distribution $h_1^q(x)$ [RS79, AM90, JJ91]. Spin-dependent parton distribution functions can measured in polarised deep-inelastic scattering processes:

Longitudinally polarised nucleons   The helicity distribution can be probed in deep-inelastic scattering of spin-polarised leptons off nucleons spin-polarised in directions longitudinal to the incoming leptons. The virtual photon, inheriting the lepton polarisation to a degree given by the lepton kinematics, can only interact with quarks polarised in opposite direction. This is a consequence of helicity conservation in the absorption of a spin-1 virtual photon by a spin-$\frac{1}{2}$ quark ($\gamma^* q \to q$). As the virtual photon selects only quarks of one polarisation, measurements of the cross section for anti-parallel ($\rightleftarrows$) or parallel polarisations ($\rightrightarrows$) of lepton ($\to$) and target nucleons ($\Rightarrow$) are sensitive to number densities q of quarks polarised along or against the nucleon polarisation. In the infinite momentum frame, these number densities are related to the helicity distribution $g_1^q(x)$, defined as the difference of the probability to find a quark polarised along or against the nucleon in a helicity eigenstate:

$$g_1^q(x) = q^{\rightrightarrows}(x) - q^{\rightleftarrows}(x). \tag{2.11}$$

The momentum distribution measuring the spin average is given by the sum of these probabilities:

$$f_1^q(x) = q^{\rightrightarrows}(x) + q^{\rightleftarrows}(x). \tag{2.12}$$

Transversely polarised nucleons   In the basis of transverse spin eigenstates ($\uparrow\Downarrow$ and $\uparrow\Uparrow$), the transversity distribution $h_1^q(x)$ measures the difference of the number densities of transversely polarised quarks aligned along or against the polarisation of the nucleon:

$$h_1^q(x) = q^{\uparrow\Uparrow}(x) - q^{\uparrow\Downarrow}(x). \tag{2.13}$$

The probabilistic interpretation of these parton distribution functions is illustrated in table 2.1.

Differences between the helicity and transversity distributions are a consequence of the relativistic motion of the quarks within the nucleon. Euclidean rotations and Lorentz boosts do not commute and thus longitudinally polarised nucleons cannot be converted in transversely polarised nucleons at infinite momentum. Only in case of non-relativistic quarks both distributions would be identical.

Another difference emerges from an analysis of helicity amplitudes. Forward quark-nucleon scattering amplitudes $\mathscr{A}_{\Lambda\lambda\Lambda'\lambda'}$, labelled by the helicities of quarks ($\lambda^{(\prime)} = \pm\frac{1}{2} \equiv \pm$) and nucleons ($\Lambda^{(\prime)} = \pm\frac{1}{2} \equiv \pm$), represent the absorption of a quark (λ) from a nucleon (Λ) and the subsequent emission of the quark (λ') by the nucleon (Λ'). Due to conservation of helicity, $\Lambda + \lambda = \Lambda' + \lambda'$, parity, $\mathscr{A}_{\Lambda\lambda\Lambda'\lambda'} = \mathscr{A}_{-\Lambda-\lambda-\Lambda'-\lambda'}$ and time reversal there are exactly three independent amplitudes:

$$\mathscr{A}_{++,++}, \quad \mathscr{A}_{+-,+-} \quad \mathscr{A}_{+-,-+}. \tag{2.14}$$

The optical theorem relates the forward quark-nucleon scattering amplitudes to the cross section of deep-inelastic scattering. Parton distribution functions can be considered as imaginary part of these amplitudes [Jaf97]: The momentum and helicity distributions correspond to amplitudes that conserve quark helicity:

$$f_1^q(x) \sim \Im[\mathscr{A}_{++,++} + \mathscr{A}_{+-,+-}], \tag{2.15}$$

$$g_1^q(x) \sim \Im[\mathscr{A}_{++,++} - \mathscr{A}_{+-,+-}], \tag{2.16}$$

---

[1] Here and henceforth, the weak scale dependence of the parton distribution functions is omitted.
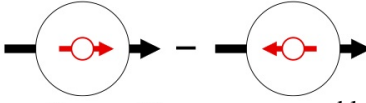
Table 2.1.: Pictorial representation and chiral properties of the leading-twist PDF: The notation of the quark distribution functions uses the letters f, g, h specifying the quark polarisation and a subscript indicating leading-twist (digit 1) or subleading-twist distributions (digit 2). Unpolarised quarks are denoted as f, longitudinally (transversely) polarised quarks as g (h). The dependence of the PDF on the quark flavour is included as superscript q.

whereas the amplitude that defines the transversity distribution involves a helicity flip:

$$h_1^q(x) \sim \Im[\mathscr{A}_{+-,-+}]. \tag{2.17}$$

The momentum distribution (figure 2.2) and the helicity distribution (figure 2.3) have been measured accurately in a variety of experiments. The measurement of the transversity distribution is hampered by its chiral properties. In the infinite momentum frame, where quark masses can be neglected, helicity and chirality properties of quarks are identical. Thus, the transversity distribution is associated with both a helicity and chirality flip and known as a chiral-odd function. Chiral symmetry can be dynamically broken for quark distribution (or fragmentation) functions which are described by non-perturbative QCD. But chirality is conserved for all perturbative QCD and electroweak processes such as inclusive measurements of deep-inelastic scattering. Hence, the transversity distribution can only be studied in interactions involving another chiral-odd (distribution or fragmentation) function. One example is an analysis of the Collins mechanism which is sensitive to transversity in conjunction with a chiral-odd fragmentation function (section 2.3).

Another consequence of the chiral properties is the simple scale-dependence of the transversity distribution. A helicity flip of spin-1 gluons would require a change of the nucleons' helicities by $|\Lambda - \Lambda'| = 2$. Thus, there is no analogon of transversity for gluons in a nucleon. Contrary to the momentum and helicity distributions, transversity does not mix with gluons under Q^2-evolution, i.e. there is no sea-quark contribution and transversity decreases slowly towards zero with increasing Q^2.

2.2. The interpretation of TMD

Leading twist effects are associated with quark-quark correlations; quark-gluon correlations enter at subleading twist. In section 2.1.3, the leading twist parametrisation of the nucleon structure is discussed in terms of the momentum $f_1^q(x)$, helicity $g_1^q(x)$ and transversity $h_1^q(x)$ distributions. Omitting also here the weak scale dependence, the three parton distribution functions depend only on the Bjorken scaling variable x, representing in the infinite momentum frame the longitudinal momentum

fraction of the quark. When including also the transverse momentum $\mathbf{p}_T$ of the quarks (defined with respect to the nucleon direction) in the description of the nucleon structure, i.e. when not integrating over $\mathbf{p}_T$, eight transverse-momentum dependent quark distribution functions[2] (TMD) emerge in the Dirac decomposition of the quark-quark correlation function $\Phi(x, \mathbf{p}_T)$ [MT96, BM98, DH05]:
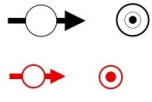
$$
\begin{aligned}
\frac{1}{2}\,\mathrm{Tr}\left[\left(\gamma^+ + \lambda\,\gamma^+\gamma_5\right)\Phi(x, \mathbf{p}_T)\right] &= \frac{1}{2}\left[f_1^q\left(x, \mathbf{p}_T^2\right) + S_T^i\,\varepsilon^{ij}p_T^j\,\frac{1}{M}\,f_{1T}^{\perp,q}\left(x, \mathbf{p}_T^2\right)\right. \\
&\qquad\left. + \lambda\Lambda\,g_1^q\left(x, \mathbf{p}_T^2\right) + \lambda S_T^i p_T^i\,\frac{1}{M}\,g_{1T}^{\perp,q}\left(x, \mathbf{p}_T^2\right)\right], \\
\frac{1}{2}\,\mathrm{Tr}\left[\left(\gamma^+ - s_T^j i\sigma^{+j}\gamma_5\right)\Phi(x, \mathbf{p}_T)\right] &= \frac{1}{2}\left[f_1^q\left(x, \mathbf{p}_T^2\right) + S_T^i\,\varepsilon^{ij}p_T^j\,\frac{1}{M}\,f_{1T}^{\perp,q}\left(x, \mathbf{p}_T^2\right)\right. \\
&\qquad + s_T^i\,\varepsilon^{ij}p_T^j\,\frac{1}{M}\,h_1^{\perp,q}\left(x, \mathbf{p}_T^2\right) + s_T^i S_T^i\,h_1^q\left(x, \mathbf{p}_T^2\right) \\
&\qquad + s_T^i\left(2p_T^i p_T^j - \mathbf{p}_T^2\delta^{ij}\right)S_T^j\,\frac{1}{2M^2}\,h_{1T}^{\perp,q}\left(x, \mathbf{p}_T^2\right) \\
&\qquad\left. + \Lambda s_T^i p_T^i\,\frac{1}{M}\,h_{1L}^{\perp,q}\left(x, \mathbf{p}_T^2\right)\right].
\end{aligned}
\tag{2.18}
$$

Here, leading-twist distributions are projected out for definite helicity, λ and Λ, and transverse spin, s_T and S_T, of quarks and the nucleon. Only three survive integration over transverse quark momenta:

$$
f_1^q(x) = \int d\mathbf{p}_T^2\,f_1^q\left(x, \mathbf{p}_T^2\right), \quad g_1^q(x) = \int d\mathbf{p}_T^2\,g_1^q\left(x, \mathbf{p}_T^2\right), \quad h_1^q(x) = \int d\mathbf{p}_T^2\,h_1^q\left(x, \mathbf{p}_T^2\right). \tag{2.19}
$$

Thereby, the leading-twist PDF $f_1^q(x)$, $g_1^q(x)$ and $h_1^q(x)$ are recovered. The five TMD, $f_{1T}^{\perp,q}\left(x, \mathbf{p}_T^2\right)$, $g_{1T}^{\perp,q}\left(x, \mathbf{p}_T^2\right)$ [3], $h_1^{\perp,q}\left(x, \mathbf{p}_T^2\right)$, $h_{1L}^{\perp,q}\left(x, \mathbf{p}_T^2\right)$ and $h_{1T}^{\perp,q}\left(x, \mathbf{p}_T^2\right)$, vanish when integrating over transverse quark momentum. Their probabilistic interpretation is illustrated in table 2.2.

2.2.1. The naive time reversal odd Sivers and Boer–Mulders functions

The scattering amplitudes that define quark distribution functions are constrained by Lorentz invariance, hermiticity, parity invariance and time-reversal invariance. In a time-reversal operation the final (initial) state is transformed into the initial (final) state and thereby spins and momenta are reversed. An observation related to a correlation, $\mathbf{S}\cdot(\mathbf{p}_1 \times \mathbf{p}_2)$, of some spin vector $\mathbf{S}$ and two non-collinear momenta, $\mathbf{p}_1$ and $\mathbf{p}_2$, implies either a violation of time-reversal invariance or the presence of interactions in the initial or final state.

From the spin-orbit correlations appearing in the Dirac decomposition of the quark-quark correlation function, the quantities $S_T^i\varepsilon^{ij}p_T^j$ and $s_T^i\varepsilon^{ij}p_T^j$, are of type $\mathbf{S}\cdot(\mathbf{p}_1 \times \mathbf{p}_2)$. The first spin-orbit correlation, e.g., corresponds to the mixed product, $\mathbf{S}_N\cdot(\mathbf{q} \times \mathbf{P}_h)$, of the nucleon's covariant spin vector $\mathbf{S}_N$, the momentum transfer $\mathbf{q}$ and the and the momentum $\mathbf{P}_h$ of the observed hadron.

The phenomenon of final-state interactions is well understood in decay processes, e.g. $\Lambda^0 \to p\pi^-$, and found in hadronisation, where the produced hadron can interact with the quark(s) involved in the fragmentation process. When not integrating over $\mathbf{p}_T$, also leading-twist quark distribution functions can be affected by initial- and final-state interactions. Non-vanishing signals for particular functions even require initial or final state interactions. These distributions are referred to as odd under naive time reversal[4] (naive-T-odd), defined as a time-reversal operation without interchange of initial and

---

[2] The transverse-momentum dependent PDF are also denoted as unintegrated PDF or transverse momentum distributions.

[3] For consistency the notation $g_{1T}^{\perp,q}$ is applied even though the chiral-even TMD is mostly denoted as g_{1T}^q in the literature.

[4] Contrary to time reversal, naive time reversal is not a symmetry of the QCD Lagrangian.

TMD	probabilistic interpretation	chiral properties	naive-T properties
$f_{1\mathrm{T}}^{\perp,q}\left(x,\mathbf{p}_T^2\right)$		chiral-even	naive-T-odd
$h_1^{\perp,q}\left(x,\mathbf{p}_T^2\right)$		chiral-odd	naive-T-odd
$h_{1\mathrm{T}}^{\perp,q}\left(x,\mathbf{p}_T^2\right)$		chiral-odd	naive-T-even
$h_{1\mathrm{L}}^{\perp,q}\left(x,\mathbf{p}_T^2\right)$		chiral-odd	naive-T-even
$g_{1\mathrm{T}}^{\perp,q}\left(x,\mathbf{p}_T^2\right)$		chiral-even	naive-T-even
legend	transverse and longitudinal nucleon polarisation		
	transverse and longitudinal quark polarisation		

Table 2.2.: Probabilistic interpretation and selected properties of leading-twist TMD: The notation of the PDF is used (see figure's 2.1 caption) and supplemented by a subscript referring to the longitudinal (*L*) or transverse (*T*) nucleon polarisation and a superscript $\perp$ to indicate the important role of transverse quark momenta (represented by blue arrows).

final states, i.e. reversal of spins and momenta only. Known examples are the Sivers and Boer–Mulders functions.

The chiral-even Sivers function $f_{1\mathrm{T}}^{\perp,q}\left(x,\mathbf{p}_T^2\right)$ [Siv90] entails the correlation, $S_T^i \varepsilon^{ij} p_T^j \frac{1}{M}$, between the transverse polarisation of the nucleon and the transverse momentum of the quarks and describes the probability to find an unpolarised quark in a transversely polarised nucleon. The probability to find a transversely polarised quark in an unpolarised nucleon is given by the chiral-odd Boer–Mulders function $h_1^{\perp,q}\left(x,\mathbf{p}_T^2\right)$ [BM98], related to the correlation, $s_T^i \varepsilon^{ij} p_T^j \frac{1}{M}$, between the transverse spin of the quarks and their own transverse momentum.

In semi-inclusive measurements of deep-inelastic scattering, these spin-orbit correlations can be interpreted as a final-state interaction of the struck quark in the colour field of target nucleon's remnant (section 2.3). Initial state interactions arise in the complementary Drell–Yan process, $pp \to l\bar{l}X$, where an incoming anti-quark (quark) annihilates with a target quark (anti-quark).

A detailed QCD analysis [BHS02, Col02, JY02, BJY03] revealed that the two naive-T-odd TMD are not constrained to zero as the corresponding Wilson lines, appearing in the quark-quark correlation functions, have paths that are not invariant under time reversal. These paths are attributed to gluon fields and describe the initial- and final-state interactions. It was also realised that the spin-orbit correlations associated with naive-T-odd functions involve quark orbital angular momenta and allow for the description of single-spin asymmetries observed in various scattering processes (section 2.3). As a consequence of the relevant Wilson lines, the single-spin asymmetries caused by the Sivers function in the Drell–Yan process has opposite sign compared to the one in deep-inelastic scattering [Col02], a fundamental QCD prediction that needs experimental verification.

2.2.2. The naive time reversal even pretzelosity function

Significant contributions from orbital angular momenta of quarks and gluons cause a non-spherical shape of the nucleon. The pretzelosity function $h_{1T}^{\perp;q}\left(x,\mathbf{p}_T^2\right)$ is sensitive to the shape of the nucleon [Mil07, Bur07]. It characterises the $\mathbf{p}_T$-dependence of the transverse quark polarisation in a transversely polarised nucleon and is related to a tensor structure, $s_T^i\left(2p_T^i p_T^j - \mathbf{p}_T^2 \delta^{ij}\right) S_T^j \frac{1}{2M^2}$, including non-collinear transverse quark momenta. In the helicity basis, the tensor structure corresponds to a flip of the quark and nucleon helicities in opposite directions, e.g., $\lambda = -\frac{1}{2} \to \lambda' = +\frac{1}{2}$ and $\Lambda = +\frac{1}{2} \to \Lambda' = -\frac{1}{2}$. Therefore, $h_{1T}^{\perp;q}\left(x,\mathbf{p}_T^2\right)$ is a chiral-odd TMD, which — due to the helicity mismatch by two units — must involve orbital angular momentum of the struck quark.

In general, independent unintegrated PDF are considered in QCD. However, in various model-dependent calculations, the pretzelosity function is related to the difference of the helicity and transversity distributions [AESY08]:

$$h_{1T}^{\perp;q}\left(x,\mathbf{p}_T^2\right) = g_1^q\left(x,\mathbf{p}_T^2\right) - h_1^q\left(x,\mathbf{p}_T^2\right), \tag{2.20}$$

and so measures the relativistic motion of the quarks within the nucleon (section 2.1.3).

2.2.3. The naive time reversal even worm-gear distributions

The chiral-even (chiral-odd) TMD $g_{1T}^{\perp;q}\left(x,\mathbf{p}_T^2\right)$ $\left(h_{1L}^{\perp;q}\left(x,\mathbf{p}_T^2\right)\right)$ describes the probability to find a longitudinally (transversely) polarised quark in a transversely (longitudinally) polarised nucleon. Its spin correlation, $\lambda S_T^i p_T^i \frac{1}{M}$ $\left(\Lambda s_T^i p_T^i \frac{1}{M}\right)$, involves a dot product of the nucleon's (quark's) transverse spin and the quark's transverse momentum. The worm-gear distribution $g_{1T}^{\perp;q}\left(x,\mathbf{p}_T^2\right)$ is the only TMD that is not affected by initial- or final-state interactions as it is neither chiral-odd nor naive-T-odd.

Common components are required for non-vanishing signals for the worm-gear distributions. In a nucleon that is, e.g., transversely polarised along the x-direction, a positive signal for the TMD $g_{1T}^{\perp;q}\left(x,\mathbf{p}_T^2\right)$ is found for quarks with positive helicity when moving along the x-direction and negative helicity when moving against the x-direction. At rest, a rotation around the transverse spin direction of the nucleon would not change the x-component of transverse quark momenta but would reverse the quark helicities and thereby the sign of $g_{1T}^{\perp;q}\left(x,\mathbf{p}_T^2\right)$. Due to rotational symmetry, the signal must vanish for a nucleon at rest and thus can only arise from relativistic boosts. Thus, the worm-gear distributions are also known as boost relations in some literature.

Approximate relations among unintegrated PDF are found [AEG$^+$08], correlating, e.g., the TMD $h_{1L}^{\perp;q}\left(x,\mathbf{p}_T^2\right)$ and $g_{1T}^{\perp;q}\left(x,\mathbf{p}_T^2\right)$) with the transversity and helicity distributions, respectively:

$$g_{1T}^{\perp;q}\left(x,\mathbf{p}_T^2\right) \approx x \int_x^1 \frac{1}{y} g_1^q\left(y,\mathbf{p}_T^2\right) dy, \tag{2.21}$$

$$h_{1L}^{\perp;q}\left(x,\mathbf{p}_T^2\right) \approx -x \int_x^1 \frac{1}{y} h_1^q\left(y,\mathbf{p}_T^2\right) dy \tag{2.22}$$

The applied approximations are not excluded by available experimental results. Thus, it might be possible to extract signals for the transversity (helicity) distribution from a longitudinally (transversely) polarised nucleon.
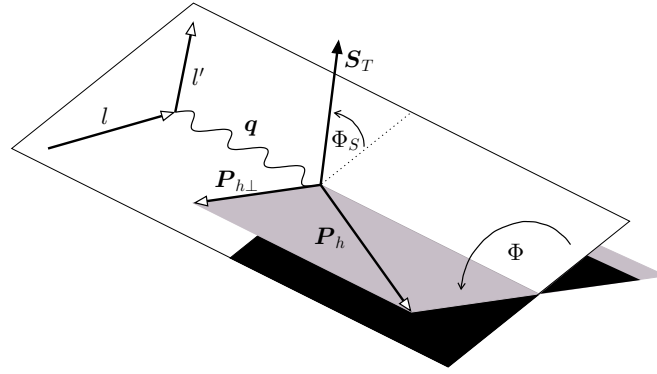
Figure 2.4.: In the semi-inclusive measurement of deep-inelastic scattering off a transversely po-
larised target, two planes are defined with respect to the virtual-photon direction **q**: the
lepton scattering plane, spanned by the directions of the incoming lepton, *l*, and **q**, and
the hadron production plane, spanned by the directions of **q** and the produced hadron,
P$_h$. The angle ϕ (ϕ_S) is defined as the azimuthal angle of the hadron production plane
(target spin axis **S**$_T$) relative to the lepton scattering plane.

2.3. Probing spin-orbit correlations in the nucleon

The TMD discussed in section 2.2 cause distinctive signatures in the azimuthal dependence in the
distribution of unpolarised hadrons produced in deep-inelastic scattering (figure 2.4). This depen-
dence is manifested in single-spin asymmetries (SSA). The analysis of single-spin asymmetries in
deep-inelastic scattering off transversely polarised nucleons gave first evidence for the chiral-odd
transversity distribution and the naive-T-odd Sivers function [HERMES05c]. This measurement
provides also signals for the worm-gear distribution $h_{1L}^{\perp;q}\left(x, \mathbf{p}_T^2\right)$ and the pretzelosity function. In
this section, the description of single-spin asymmetries within QCD, the decomposition of the deep-
inelastic scattering cross section in terms of extended structure functions and the interpretation of
these structure functions is presented.

2.3.1. Transverse single-spin asymmetries

Single-spin asymmetries are observed in various scattering processes over a wide range in the centre-
of-mass energy [DM08]. Prominent examples are the E704 effect seen in polarised pp scattering,
$p^{\Uparrow}p \to hX$, and the evidences found by the HERMES collaboration in deep-inelastic scattering.

❏ The E581/E704 collaborations (Fermilab) studied single-spin asymmetries in the inclusive
measurement of pions produced in the collision of transversely polarised (anti)protons with
an unpolarised hydrogen target. They reported large left-right asymmetries relative to the
direction of the incoming (anti)protons [E581 91, E704 91]. The results obtained at centre-
of-mass energies of about 20 GeV are confirmed by the STAR and BRAHMS collaboration
(RHIC) at centre-of-mass energies up to 200 GeV [STAR04, BRAHMS08].

❏ In the semi-inclusive measurement of deep-inelastic scattering off longitudinally and trans-
versely polarised targets, the HERMES collaboration observed single-spin asymmetries at a
centre-of-mass energy of about 7 GeV [HERMES00, HERMES01, HERMES05c].

13

Single-spin asymmetries are associated with spin-orbit correlations of the type $\mathbf{S} \cdot (\mathbf{p}_1 \times \mathbf{p}_2)$. In general, they are caused by the interference of scattering amplitudes with different complex phases coupling to the same final state [BHS02]. Transverse single-spin asymmetries, i.e. single-spin asymmetries involving transversely polarised hadrons, are related to the interference of scattering amplitudes with different hadron helicities. This interference is suppressed in hard scattering processes [KPR78], but can be caused by initial- or final-state interactions [BHS02]. The distribution and fragmentation function with the property to induce interactions in the initial or final state are known as naive-T-odd. At leading-twist, transverse single-spin asymmetries can only be related to two naive-T-odd function: the Sivers quark distribution or the Collins fragmentation function.

❏ Quarks with certain helicity can be selected in deep-inelastic scattering using longitudinally polarised leptons. In single-hadron production, transversely polarised quarks can be studied without requiring polarimetry in the final state via the Collins function $H_1^{\perp,q}\left(z, z^2\mathbf{k}_T^2\right)$ [Col93] only, which describes the hadronisation of a transversely polarised quark into an unpolarised hadron. Besides on z, this fragmentation function depends on the fragmenting quark's transverse momentum $\mathbf{k}_T$ defined with respect to the direction of the produced hadron.

The chiral-odd Collins function allows for the measurement of chiral-odd quark distribution functions: In conjunction with the chiral-odd transversity distribution, the naive-T-odd Collins function leads to a left-right asymmetry in the distribution of the produced hadron's momentum $\mathbf{P}_h$ with respect to the transverse spin $\mathbf{s}_q$ of the fragmenting quark and the direction of the virtual photon. This single-spin asymmetries is related to the mixed product $\mathbf{s}_q \cdot (\mathbf{p}_q \times \mathbf{P}_h)$ and manifests itself in a $\sin(\phi + \phi_S)$ modulation in the momentum distribution of the produced hadrons. The Collins function represents also the chiral-odd partner to access the chiral-odd pretzelosity function and the chiral-odd worm-gear distribution $h_{1L}^{\perp,q}\left(x, \mathbf{p}_T^2\right)$ in a semi-inclusive measurement of deep-inelastic scattering. The Collins mechanism in conjunction with the spin-orbit correlation of these TMD results in a $\sin(3\phi - \phi_S)$ and $\sin(2\phi)$ modulation in the cross section, respectively.

❏ The naive-T-odd Sivers function is related to the spin-orbit correlation, $\mathbf{S}_N \cdot (\mathbf{q} \times \mathbf{P}_h)$ (section 2.2.1), which can be interpreted as a left-right asymmetry of unpolarised quarks in a transversely polarised nucleon [Bur04b]. The spatial asymmetry of the TMD in directions transverse to the momentum of the virtual photon and the spin of the nucleon is transferred into a left-right asymmetry in the momentum distribution of the final-state hadron due to the final-state interaction. As a consequence, a $\sin(\phi - \phi_S)$ modulation is found in the cross section.

Final-state interactions are required for non-vanishing signals for the naive-T-odd Sivers function. The associated single-spin asymmetries is caused by the interference of scattering amplitudes involving a helicity flip of only the nucleon, which has to be compensated by orbital angular momentum of the unpolarised quarks [BHS02].

2.3.2. The azimuthal modulations in the cross section

The possible contributions to the cross section of deep-inelastic scattering in a semi-inclusive measurement arise from the various combinations in the scattering of unpolarised (U) or longitudinally polarised (L) leptons off unpolarised, longitudinally or transversely polarised (T) nucleons:

$$\sigma^h = \sigma_{\mathrm{UU}}^h + \lambda_l\,\sigma_{\mathrm{LU}}^h + S_L\,\sigma_{\mathrm{UL}}^h + \lambda_l S_L\,\sigma_{\mathrm{LL}}^h + S_T\,\sigma_{\mathrm{UT}}^h + \lambda_l S_T\,\sigma_{\mathrm{LT}}^h. \tag{2.23}$$

Here, λ_l states the helicity of the beam leptons. The degree of the longitudinal and transverse polarisation of the target nucleons is denoted as S_L and S_T.

The differential cross section of the process, $lN \rightarrow l'hX$, has been studied including the dependence on the azimuthal angles ϕ and ϕ_S [MT96, BM98, BJM00, BDG$^+$07]. In the one-photon exchange approximation, the general form of the cross section (equation 2.23) can be decomposed into extended structure functions F related to the various azimuthal modulations in the differential cross section:

$$\frac{d\sigma^h}{dx\,dy\,d\phi_S\,dz\,d\phi\,d\mathbf{P}_{h\perp}^2} = \frac{\alpha^2}{xyQ^2}\frac{y^2}{2(1-\varepsilon)}\left(1+\frac{\gamma^2}{2x}\right)$$

$$\Bigg\{ \Bigg[F_{\text{UU,T}} + \varepsilon F_{\text{UU,L}} \\ + \sqrt{2\varepsilon(1+\varepsilon)}\cos(\phi)F_{\text{UU}}^{\cos(\phi)} + \varepsilon\cos(2\phi)F_{\text{UU}}^{\cos(2\phi)} \Bigg]$$

$$+ \quad \lambda_l \quad \left[\sqrt{2\varepsilon(1-\varepsilon)}\sin(\phi)F_{\text{LU}}^{\sin(\phi)} \right]$$

$$+ \quad S_L \quad \left[\sqrt{2\varepsilon(1+\varepsilon)}\sin(\phi)F_{\text{UL}}^{\sin(\phi)} + \varepsilon\sin(2\phi)F_{\text{UL}}^{\sin(2\phi)} \right]$$

$$+ \quad S_L \quad \lambda_l \quad \left[\sqrt{1-\varepsilon^2}F_{\text{LL}} + \sqrt{2\varepsilon(1-\varepsilon)}\cos(\phi)F_{\text{LL}}^{\cos(\phi)} \right]$$

$$+ \quad S_T \quad \Bigg[\sin(\phi-\phi_S)\left(F_{\text{UT,T}}^{\sin(\phi-\phi_S)} + \varepsilon F_{\text{UT,L}}^{\sin(\phi-\phi_S)}\right) \\ + \varepsilon\sin(\phi+\phi_S)F_{\text{UT}}^{\sin(\phi+\phi_S)} + \varepsilon\sin(3\phi-\phi_S)F_{\text{UT}}^{\sin(3\phi-\phi_S)} \\ + \sqrt{2\varepsilon(1+\varepsilon)}\sin(\phi_S)F_{\text{UT}}^{\sin(\phi_S)} \\ + \sqrt{2\varepsilon(1+\varepsilon)}\sin(2\phi-\phi_S)F_{\text{UT}}^{\sin(2\phi-\phi_S)} \Bigg]$$

$$+ \quad S_T \quad \lambda_l \quad \Bigg[\sqrt{1-\varepsilon^2}\cos(\phi-\phi_S)F_{\text{LT}}^{\cos(\phi-\phi_S)} \\ + \sqrt{2\varepsilon(1-\varepsilon)}\cos(\phi_S)F_{\text{LT}}^{\cos(\phi_S)} \\ + \sqrt{2\varepsilon(1-\varepsilon)}\cos(2\phi-\phi_S)F_{\text{LT}}^{\cos(2\phi-\phi_S)} \Bigg]$$

$$\Bigg\} \quad .$$

(2.24)

The extended structure functions $F\left(x,Q^2,z,|\mathbf{P}_{h\perp}|\right)$ depend on the kinematic variables x, Q^2, z and $|\mathbf{P}_{h\perp}|$. Their azimuthal modulation is given as superscript. Besides the subscript for the lepton and nucleon polarisation, a third subscript indicates the polarisation of the virtual photon for the extended structure functions $F_{\text{UU,T}}$, $F_{\text{UU,L}}$, $F_{\text{UT,T}}^{\sin(\phi-\phi_S)}$ and $F_{\text{UT,L}}^{\sin(\phi-\phi_S)}$. The dependence of the longitudinal and transverse polarisation of the virtual photon is considered via the ratio ε of the longitudinal to the transverse photon flux:

$$\varepsilon = \frac{1-y-\frac{1}{4}\gamma^2y^2}{1-y+\frac{1}{2}y^2+\frac{1}{4}\gamma^2y^2}, \quad \gamma = \frac{2Mx}{Q^2}, \tag{2.25}$$

which is determined by the kinematics of the lepton.

For small transverse hadron momentum, $\mathbf{P}_{h\perp}^2 \ll Q^2$, the process-dependent structure functions can be interpreted in terms of a convolution over the intrinsic transverse momenta $\mathbf{p}_T$ and $\mathbf{k}_T$ of quark distribution and fragmentation functions [CS81, JMY04, JMY05]. Results complete at leading- and

subleading-twist accuracy and at leading order in α_s are obtained [BDG$^+$07]. Extended structure functions associated with leading-twist cross-section contributions are calculated as convolutions in transverse momentum space of one quark distribution and one fragmentation function. In the extended structure function $F_{\mathrm{UT}}^{\sin(\phi+\phi_S)}$ of the $\sin(\phi+\phi_S)$ modulation, e.g., the transversity distribution $h_1^h\left(x,\mathbf{p}_T^2\right)$ and the Collins fragmentation functions $H_1^{\perp,q}\left(z,z^2\mathbf{k}_T^2\right)$ appear. These functions are not factorised but appear as a convolution over intrinsic transverse momenta $\mathbf{p}_T$ and $\mathbf{k}_T$:

$$F_{\mathrm{UT}}^{\sin(\phi+\phi_S)} = x\sum_q e_q^2 \int d^2\mathbf{p}_T\, d^2\mathbf{k}_T\, \delta^2\left(\mathbf{p}_T - \mathbf{k}_T - \frac{\mathbf{P}_{h\perp}}{z}\right)\frac{-\mathbf{P}_{h\perp}\cdot\mathbf{p}_T}{|\mathbf{P}_{h\perp}|M_h}h_1^h\left(x,\mathbf{p}_T^2\right)H_1^{\perp,q}\left(z,z^2\mathbf{k}_T^2\right). \quad (2.26)$$

Henceforth, the notation is shortened by representing the convolution by the symbol $\mathscr{C}$, i.e.:

$$F_{\mathrm{UT}}^{\sin(\phi+\phi_S)} = \mathscr{C}\left[\frac{-\mathbf{P}_{h\perp}\cdot\mathbf{p}_T}{|\mathbf{P}_{h\perp}|M_h}h_1^h\left(x,\mathbf{p}_T^2\right)H_1^{\perp,q}\left(z,z^2\mathbf{k}_T^2\right)\right]. \quad (2.27)$$

The $\mathbf{p}_T$- and $\mathbf{k}_T$- dependence of the transversity distribution and Collins fragmentation function on the intrinsic quark momenta $\mathbf{p}_T$ and $\mathbf{k}_T$ is unknown, respectively, and thus the distribution and fragmentation functions cannot be extracted separately from the measured extended structure functions. The convolution can be solved assuming, e.g.[5], a Gaussian mode:

$$h_1^q\left(x,\mathbf{p}_T^2\right) = h_1^q(x)\frac{\exp\left(-\mathbf{p}_T^2/\left\langle\mathbf{p}_T^2\right\rangle\right)}{\pi\left\langle\mathbf{p}_T^2\right\rangle}, \quad H_1^{\perp,q}\left(z,z^2\mathbf{k}_T^2\right) = H_1^{\perp,q}(z)\frac{\exp\left(-\mathbf{k}_T^2/\left\langle z^2\mathbf{k}_T^2\right\rangle\right)}{\pi\left\langle z^2\mathbf{k}_T^2\right\rangle}, \quad (2.28)$$

where the Gaussian widths, $\left\langle\mathbf{p}_T^2\right\rangle$ and $\left\langle z^2\mathbf{k}_T^2\right\rangle$, characterise the $\mathbf{p}_T$- and $\mathbf{k}_T$-dependence. The Gaussian model has been studied extensively. According to most recent analysis [STM10], based on more and more precise experimental results than the studies from the years 2004–2006 [DM04, ABD$^+$05, CEG$^+$06], intrinsic transverse momenta in the deep-inelastic scattering and Drell–Yan processes are well-described in the Gaussian model. For the Gaussian widths a dependence on the centre-of mass energy but neither a flavour-dependence nor a x- or z-dependence has been found. These results are supported by recent Lattice QCD calculations [HMNS09]. In the Lattice QCD analysis, the Gaussian model is identified as regularisation prescription, i.e. the integral in equation 2.26 is finite without requiring explicit cutoff values.

In table 2.3, expressions for extended structure functions using the Gaussian model are listed. In view of the analysis of transverse single-spin asymmetries, presented in chapters 4 and 5, the focus is put on the extended structure functions of the cross-section contribution σ_{UT}^h as well as on those of the cross-section contributions σ_{UU}^h and σ_{UL}^h.

---

[5]An alternative, experimentally far more challenging, method is applying the $\mathbf{P}_{h\perp}$-weighted ansatz, where the convolution is solved by weighting the cross section with a factor proportional to the transverse momentum of the produced hadron.

spin-independent cross-section contribution

$$F_{\text{UU,T}} = \mathscr{C}\left[f_1 D_1\right]$$

$$F_{\text{UU,L}} = 0$$

$$F_{\text{UL}}^{\cos(\phi)} = \frac{2M}{Q}\mathscr{C}\left[\frac{\hat{\mathbf{h}}\cdot\mathbf{k}_T}{M_h}\left(xhH_1^\perp + \frac{M_h}{M}f_1\frac{\tilde{D}^\perp}{z}\right) - \frac{\hat{\mathbf{h}}\cdot\mathbf{p}_T}{M}\left(xf^\perp D_1 - \frac{M_h}{M}h_1^\perp\frac{\tilde{H}}{z}\right)\right]$$

$$F_{\text{UU}}^{\cos(2\phi)} = \mathscr{C}\left[-\frac{2\left(\hat{\mathbf{h}}\cdot\mathbf{k}_T\right)\left(\hat{\mathbf{h}}\cdot\mathbf{k}_T\right) - \mathbf{k}_T\cdot\mathbf{p}_T}{MM_h}h_1^\perp H_1^\perp\right]$$

longitudinal target spin-dependent cross-section

$$F_{\text{UL}}^{\sin(\phi)} = \frac{2M}{Q}\mathscr{C}\left[\frac{\hat{\mathbf{h}}\cdot\mathbf{k}_T}{M_h}\left(xh_L H_1^\perp + \frac{M_h}{M}g_{1\text{L}}\frac{\tilde{G}^\perp}{z}\right) + \frac{\hat{\mathbf{h}}\cdot\mathbf{p}_T}{M}\left(xf_L^\perp D_1 - \frac{M_h}{M}h_{1\text{L}}^\perp\frac{\tilde{H}}{z}\right)\right]$$

$$F_{\text{UL}}^{\sin(2\phi)} = \mathscr{C}\left[-\frac{2\left(\hat{\mathbf{h}}\cdot\mathbf{k}_T\right)\left(\hat{\mathbf{h}}\cdot\mathbf{k}_T\right) - \mathbf{k}_T\cdot\mathbf{p}_T}{MM_h}h_{1\text{L}}^\perp H_1^\perp\right]$$

transverse target spin-dependent cross-section

$$F_{\text{UT,T}}^{\sin(\phi-\phi_S)} = \mathscr{C}\left[-\frac{\hat{\mathbf{h}}\cdot\mathbf{p}_T}{M}f_{1\text{T}}^\perp D_1\right]$$

$$F_{\text{UT,L}}^{\sin(\phi-\phi_S)} = 0$$

$$F_{\text{UT}}^{\sin(\phi+\phi_S)} = \mathscr{C}\left[-\frac{\hat{\mathbf{h}}\cdot\mathbf{k}_T}{M_h}h_1 H_1^\perp\right]$$

$$F_{\text{UT}}^{\sin(3\phi-\phi_S)} = \mathscr{C}\left[\frac{2\left(\hat{\mathbf{h}}\cdot\mathbf{p}_T\right)\left(\mathbf{p}_T\cdot\mathbf{k}_T\right) + \mathbf{p}_T^2\left(\hat{\mathbf{h}}\cdot\mathbf{k}_T\right) - 4\left(\hat{\mathbf{h}}\cdot\mathbf{p}_T\right)^2\left(\hat{\mathbf{h}}\cdot\mathbf{k}_T\right)}{2M^2 M_h}h_{1\text{T}}^\perp H_1^\perp\right]$$

$$F_{\text{UT}}^{\sin(\phi_S)} = \frac{2M}{Q}\mathscr{C}\left\{\left(xf_T D_1 - \frac{M_h}{M}h_1\frac{\tilde{H}}{z}\right)\right.$$
$$\left.- \frac{\mathbf{p}_T\cdot\mathbf{k}_T}{2MM_h}\left[\left(xh_T H_1^\perp + \frac{M_h}{M}g_{1\text{T}}^\perp\frac{\tilde{G}^\perp}{z}\right) - \left(xh_T^\perp H_1^\perp - \frac{M_h}{M}f_{1\text{T}}^\perp\frac{\tilde{D}^\perp}{z}\right)\right]\right\}$$

$$F_{\text{UT}}^{\sin(2\phi-\phi_S)} = \frac{2M}{Q}\mathscr{C}\left\{\frac{2(\hat{\mathbf{h}}\cdot\mathbf{p}_T)^2 - \mathbf{p}_T^2}{2M^2}\left(xf_T^\perp D_1 - \frac{M_h}{M}h_{1\text{T}}^\perp\frac{\tilde{H}}{z}\right)\right.$$
$$- \frac{2(\hat{\mathbf{h}}\cdot\mathbf{k}_T)(\hat{\mathbf{h}}\cdot\mathbf{p}_T) - \mathbf{p}_T\cdot\mathbf{k}_T}{2MM_h}\left[\left(xh_T H_1^\perp + \frac{M_h}{M}g_{1\text{T}}^\perp\frac{\tilde{G}^\perp}{z}\right)\right.$$
$$\left.\left.+ \left(xh_T^\perp H_1^\perp - \frac{M_h}{M}f_{1\text{T}}^\perp\frac{\tilde{D}^{\perp,q}}{z}\right)\right]\right\}$$

Table 2.3.: Expressions for the extended structure functions $F\left(x, Q^2, z, \mathbf{P}_{h\perp}\right)$ of the cross-section contributions σ_{UU}^h, σ_{UL}^h and σ_{UT}^h are given in terms of convolutions over intrinsic quark momenta $\mathbf{p}_T$ and $\mathbf{k}_T$ of distribution functions and fragmentation functions. For the sake of clarity, the dependence of the distribution (fragmentation) functions on x (z) and $\mathbf{p}_T$ ($\mathbf{k}_T$) is omitted and the unit vector $\hat{\mathbf{h}} = \mathbf{P}_{h\perp}/|\mathbf{P}_{h\perp}|$ is introduced.

2. Spin-orbit correlations in the nucleon

3. The HERMES experiment

The HERMES experiment [HERMES 90] was designed for precise measurements of asymmetries in inclusive and semi-inclusive deep-inelastic scattering. The focus of the HERMES research program was and is on the investigation of the nucleon spin structure and thus the measurement of polarised deep-inelastic scattering processes. In general a polarised lepton beam and a polarised target are needed for such measurements; in the HERMES case two novel technological achievements were used for the experimental setup:

❑ longitudinal electron (and positron[1]) spin polarisation in a high-energy storage ring,

❑ usage of a nuclear-polarised gas target internal to the beam pipe.

The HERMES experiment was located at the DESY research centre in Hamburg, Germany. It used the longitudinally polarised electron beam of the HERA beam facility with an energy of $27.6\,\mathrm{GeV}$ and high currents up to $50\,\mathrm{mA}$. In the years 1995–2000 and 2002–2007 many million deep-inelastic scattering events were recorded at a centre-of-mass energy of about $7\,\mathrm{GeV}$ and several changes were applied to the experimental setup. The operation of the HERMES experiment can be divided into three main periods: data recorded using a longitudinally polarised target in the years 1995–2000, data recorded using a transversely polarised target in the years 2002–2005 and the data recorded with the the so-called Recoil Detector [HERMES02, Mus07] in the years 2006–2007. The following description of the HERMES experiment is restricted to the measurement of transverse single-spin asymmetries in semi-inclusive deep-inelastic scattering and thus to the experimental setup of the running period 2002–2005.

3.1. Longitudinal electron spin polarisation in HERA

The first deep-inelastic scattering experiments have been carried out at SLAC in the late sixties using a linear accelerator with a maximum beam energy of $25\,\mathrm{GeV}$. The results on the inner structure of the proton from the SLAC experiments provided the basis for the parton model by Bjorken [BP69] and Feynman [Fey72]. In order to improve the Q^2-resolution of these measurements higher centre-of-mass energies were needed and thus the idea of an electron-proton collider arose. This concept was realised with the HERA beam facility [Wii81] at DESY.

The HERA beam facility was based on two independent storage rings for electrons and protons with a circumference of $6.3\,\mathrm{km}$ each and allowed collisions of electron and proton bunches with a centre-of-mass energy up to $320\,\mathrm{GeV}$ and high luminosity. A sketch of the HERA beam facility and the location of the high-energy experiments is shown in figure 3.1. In the years 1992–2000 and 2002–2007 high-precision measurements of the proton structure and the strong forces within have been obtained by the H1 and ZEUS collaboration at HERA. For the HERMES fixed target experiment the achievement of longitudinal spin-polarisation of the electron beam was essential.

---

[1]Both electrons and positrons could be injected into the HERA storage ring. For the sake of convenience the term electron is henceforth used for both particle and anti-particle.
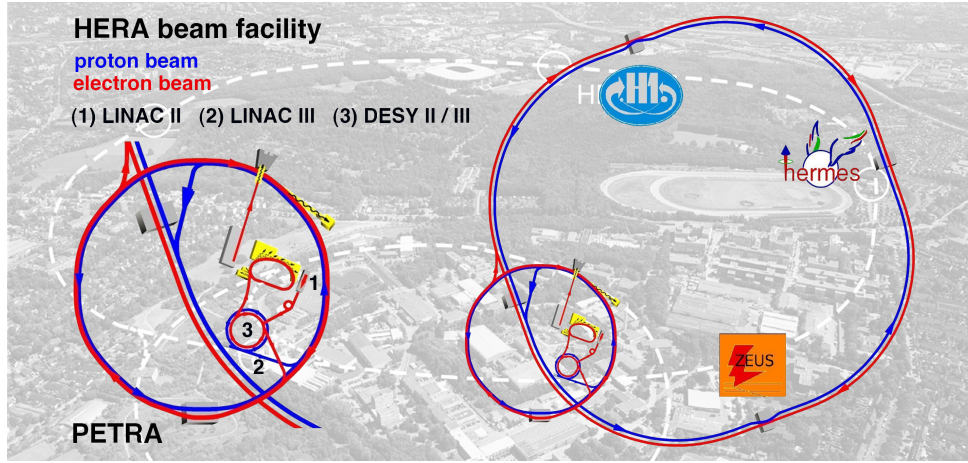
Figure 3.1.: Sketch of the preaccelerators and storage rings at DESY: Before the injection into the HERA storage ring, electrons (indicated red) and protons (indicated blue) passed a system of particle accelerators as illustrated in the detail on the left. Electrons (protons) were preaccelerated to $0.45\,\mathrm{GeV}$ ($0.05\,\mathrm{GeV}$) in the linear accelerator LINAC II (III) and accelerated further to $14\,\mathrm{GeV}$ ($40\,\mathrm{GeV}$) in the DESY II (III) and PETRA storage rings. In the HERA storage ring, the electrons (proton) bunches reached a final energy of $27.6\,\mathrm{GeV}$ ($920\,\mathrm{GeV}$). To the right the location of the high-energy experiments H1, ZEUS and HERMES is shown. Contrary to the electron-proton collider experiments H1 and ZEUS, only the electron beam is used for the HERMES experiment.

The HERA beam facility was designed with the aim of storing spin-polarised electrons [B+93, B+94]. The electron beam could become transversely polarised by the emission of synchrotron radiation in the curved sections of the storage ring. This effect was first predicted by Sokolov and Ternov [ST64] and was caused by a tiny spin-flip amplitude at the emission of synchrotron radiation. These rare spin-flip processes involved large asymmetries with respect to the spin-alignment and thus an enhanced spin-alignment anti-parallel to the vertical field of the bending magnets. For an ideal storage ring, i.e. when there are no horizontal magnetic fields on the closed orbit, the build-up of the polarisation P can be described as

$$P(t) = P_{\max}\left(1 - e^{-t/\tau}\right), \tag{3.1}$$

where the maximum of the achievable polarisation $P_{\max}$ is given by 92.4% and the polarisation build-up time τ is a strong function of the beam energy and the bending radius of the storage ring. In a real storage ring like HERA there were horizontal fields on the closed orbit and thus potentially strong depolarisation effects.

The emission of synchrotron radiation photons caused not only spin-flips but also excited energy oscillations which resulted in oscillations of the electron about the closed orbit. Horizontal magnetic fields on electrons off the closed orbit caused spin precession. Due to the stochastic nature of the photon emission, the precession resulted in spin diffusion and thus depolarisation. The depolarisation effects could be parametrised by the depolarisation time constant τ_D and resulted in a shorter build-up time and a reduced maximum beam polarisation P':

$$P \to P'_{\max} = P_{\max}\frac{\tau_D}{\tau + \tau_D}, \tag{3.2}$$

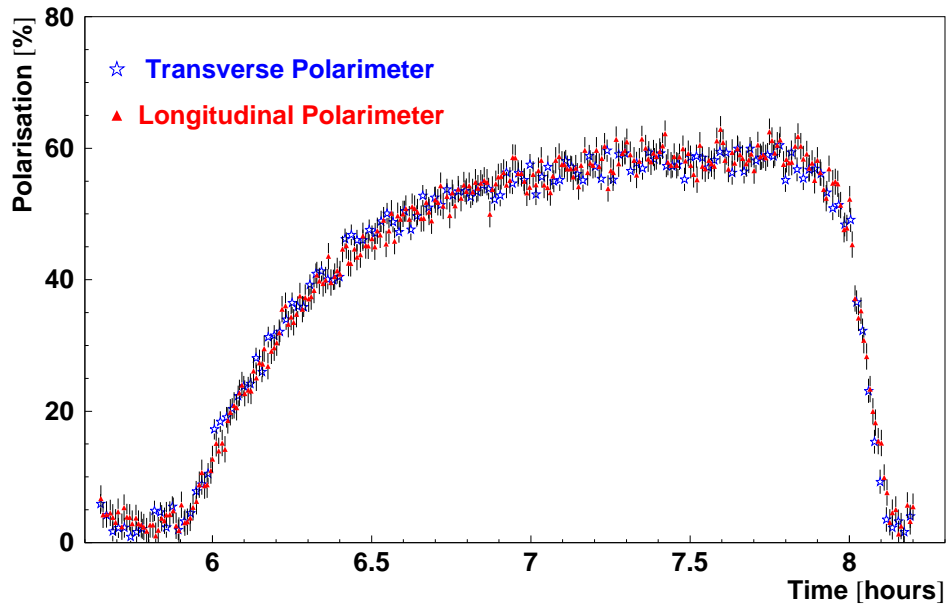$$\tau \to \tau' = \tau\frac{\tau_D}{\tau + \tau_D}. \tag{3.3}$$

Figure 3.2.: Rise time curve of the transverse and longitudinal beam polarisation as measured by the Transverse Polarimeter [B+93] in the west section of the ring and the Longitudinal Polarimeter [Bec00] installed downstream the HERMES experiment. Both polarimeters utilised the spin-dependent cross-section for Compton scattering of circularly polarised laser photons on the stored electrons.

Depolarisation effects could be limited by a precise alignment of the quadrupole magnets in the storage ring and spin-orbit corrections. In order to achieve high polarisation eight closed orbit correction coils, so-called harmonic bumps, were installed at strategic locations of the storage ring.

For a transversely polarised electron beam the spin-dependent variations of cross-sections are suppressed by the ratio of the electron mass and the electron beam energy. Spin orientation into the beam direction, i.e. longitudinal polarisation, is required for polarised scattering experiments. Longitudinal beam polarisation in the HERA storage ring [B+95] could be produced by the installation of an arrangement of interleaved horizontal and vertical bending magnets, so-called spin rotators. Upstream the HERMES interaction region the electron spin was turned from transverse to longitudinal orientation and turned back to transverse orientation downstream the HERMES interaction region. The longitudinal beam helicity was changed every few months. This allowed investigations of the dependence on the electron beam helicity and measurements with an unpolarised electron beam by balancing data for both helicity states. A typical rise time curve of the electron beam polarisation is shown in figure 3.2 for the running period 1995–2000, where longitudinal electron beam polarisation up to 70% was achieved. In 2001 extensive modifications of the HERA storage ring and the setup of the H1 and ZEUS experiments were carried out to upgrade the maximum luminosity at the interactions points of the collider experiments from $2 \cdot 10^{31} \frac{1}{\mathrm{cm}^2 \, \mathrm{s}}$ to $7.6 \cdot 10^{31} \frac{1}{\mathrm{cm}^2 \, \mathrm{s}}$ by decreasing the sizes of the proton and electron beam. Thereby quadrupole magnets were moved closer to the interactions points (and thus partially inside the detectors of the H1 and ZEUS experiments) and their magnetic fields were enhanced. The increase in luminosity involved an increase of depolarisation effects due to the Coulomb interaction of the colliding proton and electron bunches and thus limited the achievable electron polarisation in the years 2002–2005 to about 30%.
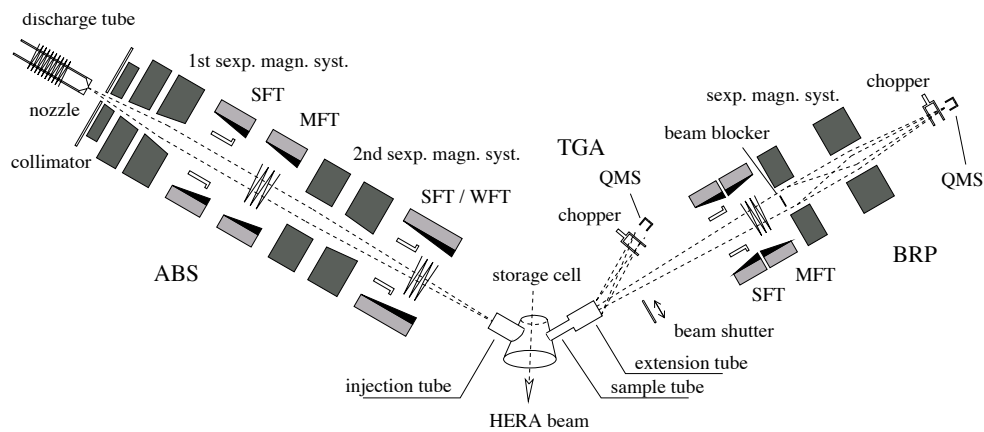
Figure 3.3.: Schematic representation of the HERMES polarised hydrogen target consisting of an atomic beam source (ABS), the storage cell, a Breit-Rabi polarimeter (BRP) and a target gas analyser (TGA): Molecular hydrogen was dissociated by the discharge tube and was formed into an intense atomic beam by adiabatic expansion through a cold nozzle and a set of collimators. The hyperfine states with magnetic electron spin quantum number $m = +\frac{1}{2}$ were focused by a system of sextupole magnets while those with $m = -\frac{1}{2}$ were deflected (Stern-Gerlach separation). High-frequency transitions allowed to attain nuclear polarisation by exchanging occupation numbers of hyperfine states. The nuclear spin orientation could be reversed rapidly. A small sample of target atoms was extracted from the sampling tube for target diagnostics by the BRP and the TGA.

3.2. The polarised hydrogen gas target

For the design of the HERMES experiment the use of polarised solid state targets was excluded. The areal density of solid state targets would have significantly reduced the lifetime of the HERA electron beam and thus interfered with the in parallel running of the H1, ZEUS and HERMES experiments. Instead a polarised gas target [HERMES05a] was installed internal to the HERA storage ring. Contrary to solid state targets pure gas targets permit highly polarised target samples without dilution from unpolarised target material and without any background arising from unwanted scattering at the target material container. Furthermore this technique allowed rapid reversals of the target spin and therefore provided a substantial reduction of time-dependent systematic uncertainties.

A schematic representation of the HERMES target region is given in figure 3.3: A beam of nuclear-polarised hydrogen atoms, formed in an atomic beam source, was injected into an open-ended storage cell, through which the circulating HERA electron beam was passed. Through the open ends of the storage cell, described in figure 3.4, the target atoms diffused into the storage ring and were removed by a high-speed differential pumping system. A small sample of the target atoms was extracted from the cell's sampling tube for the determination of the target polarisations. Synchrotron radiation emitted by the electron beam bunches could have heated the storage cell. Thus, the cell was shielded from synchrotron radiation by a systems of collimators in front of the target cell.

By injecting polarised atoms into a storage cell the target areal density could be enhanced by about two orders of magnitude compared to the free atomic beam of a typical polarised jet target. Due to many wall collisions the interaction probability with the electron beam was enhanced. In addition the storage cell was cooled to $100\,\mathrm{K}$ to decrease the thermal velocity of the target atoms. Thus an target areal density of $10^{14}\,\mathrm{H}$-atoms/cm^2 and a corresponding luminosity of about $10^{31}\,\mathrm{H}$-atoms/cm^2
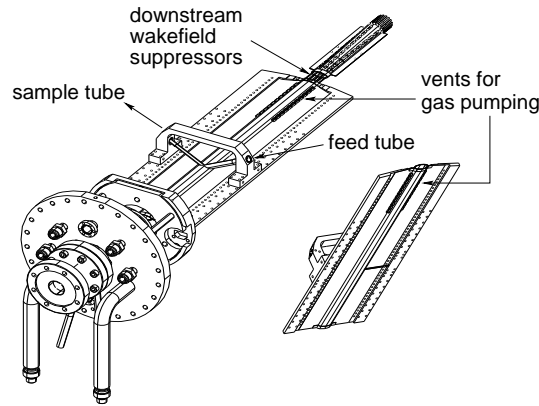
Figure 3.4.: Schematic view of the storage cell: The open-ended storage cell was made of two pure aluminium sheets and was constructed as thin as possible (0.075 mm) to minimise multiple scattering and bremsstrahlung for particles. It was 400 mm long and had an elliptical cross-sectioned shape of $21.0 \times 8.9\,\text{mm}^2$ determined by a HERA electron beam clearance of about 20σ. Polarised atoms were injected through a feed tube installed perpendicular to the beam axis and central in the centre of the cell. Wake-field suppressors up- and downstream of the storage cell provided a smooth transition between the storage cell and the beam pipe to avoid heating of the target cell by beam wake fields.

was reached. Recombination to hydrogen molecules and depolarisation of the target atoms caused by wall collisions could be minimised by coating the storage cell with Drifilm and by an additional thin layer of ice which was produced on the cell's wall during operation.

The storage cell was surrounded by a magnet generating a holding field transverse to the beam direction. The holding field in vertical direction provided the quantisation axis for the spin of the polarised hydrogen atoms in the storage cell and decoupled the spins of electrons and protons. The magnetic field was limited by the amount of synchrotron radiation generated by the Lorentz force induced deflection of the beam by the transverse target magnet. For the nominal magnetic field of 297 mT a homogeneity of $\Delta B \leqslant 0.15\,\text{mT}$ would be required to avoid possible beam-induced nuclear depolarisation resonances. Due to geometrical constraints a magnet field uniformity in horizontal direction was limited to $\Delta B_x \leqslant 0.60\,\text{mT}$, while in vertical direction and in beam direction an uniformity of $\Delta B_y \leqslant 0.15\,\text{mT}$ and $\Delta B_z \leqslant 0.05\,\text{mT}$ respectively could be achieved. In figure 3.5 a measurement of
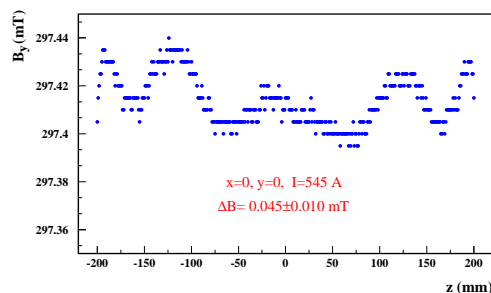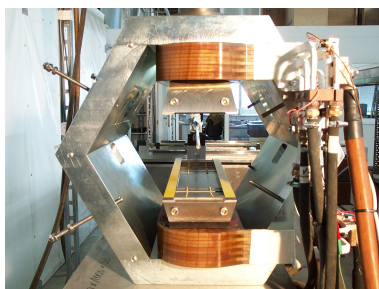

Figure 3.5.: The transverse target magnet: A picture of the magnet is shown in the left panel. In the right panel the transverse magnet field uniformity measured along the beam axis (z) is given for the nominal magnet field of $B = 297\,\text{mT}$.

the magnet field uniformity is given.

Due to many wall collisions the target atoms had a similar history. By analysing the composition and the polarisation of an extracted atomic beam sample the target polarisation could be evaluated with high precision. The target polarisation P had contributions from polarised hydrogen atoms and to a small extent from polarised hydrogen molecules due to recombination processes in the atomic beam source and the storage cell. The fraction of molecules and thus the degree of dissociation was measured in the target gas analyser. For the polarised hydrogen target it was about 0.97%. The relative occupation numbers of the different hyperfine states was obtained by a Breit-Rabi polarimeter. From a combined online-analysis of the TGA and BRP the target polarisation could be monitored during operation. For the running period 2002–2005 an average degree of polarisation of $P = 72.5 \pm 5.3\%$ could be achieved. The nuclear spin orientation was flipped at $1\text{--}3\,\text{m}$ time intervals to limit systematic influences to asymmetry measurements. According to the convention of the HERMES target group, target spin orientation "⇑" was defined as nuclear-polarisation parallel to the holding field of the transverse target magnet. In the HERMES coordinate system, the accordant target spin axis $\hat{\mathbf{S}}_\perp$ was given as $\hat{\mathbf{S}}_\perp = (0, -1, 0)$.

3.3. The HERMES spectrometer

The tracking and particle identification detectors of the the HERMES spectrometer [HERMES98] allowed the reconstruction of deep-inelastic scattering events. The spectrometer was designed as a forward magnetic spectrometer consisting of two identical halves, mounted above and below the electron and proton beam pipes of the HERA storage ring. A schematic representation of the forward magnetic spectrometer is given in figure 3.6. The beam pipes were shielded from the $1.5\,\text{Tm}$ dipole field of the spectrometer magnet by massive iron plates in horizontal direction. Scattering events were recorded according to fast trigger signals. The trigger was formed from a coincidence between the lead-glass electromagnetic calorimeter and certain scintillator hodoscopes and requiring an electron energy deposition of $1.4\,\text{GeV}$ in the calorimeter.

3.3.1. The track reconstruction

Momenta of charged particles and their trajectories were reconstructed by analysing the signals of various horizontal-drift chambers each consisting of six planes: In the front region of the spectrometer magnet the initial trajectory and in particular the polar and azimuthal scattering angles were measured by the front chambers (FC1/2). These information allowed the identification of the vertex within the target cell. The deflected trajectory behind the dipole magnet was measured by two pairs of drift chambers which were installed before (BC1/2) and behind (BC3/4) the ring imaging Čerenkov detector (RICH). From the deflection of the initial trajectory in the spectrometer magnet the particle momentum was determined. For the track reconstruction by the HERMES reconstruction program (HRC) a tree-search algorithm was applied for fast track finding and a look-up table was used for the momentum determination [Wan96]. In average angular and momentum resolutions of $\Delta\theta \leqslant 1.8\,\text{mrad}$ and $\Delta p/p < 2.6\%$ were achieved.

The magnetic holding field of the transversely polarised target affected the track reconstruction in the front region. The experienced deflection of the particles in the transverse target magnet due to the Lorentz force has to be accounted for when calculating the kinematics of the recorded deep-inelastic scattering events. Two different correction methods are provided by the transverse magnet correction (TMC) software [AMS$^+$07].
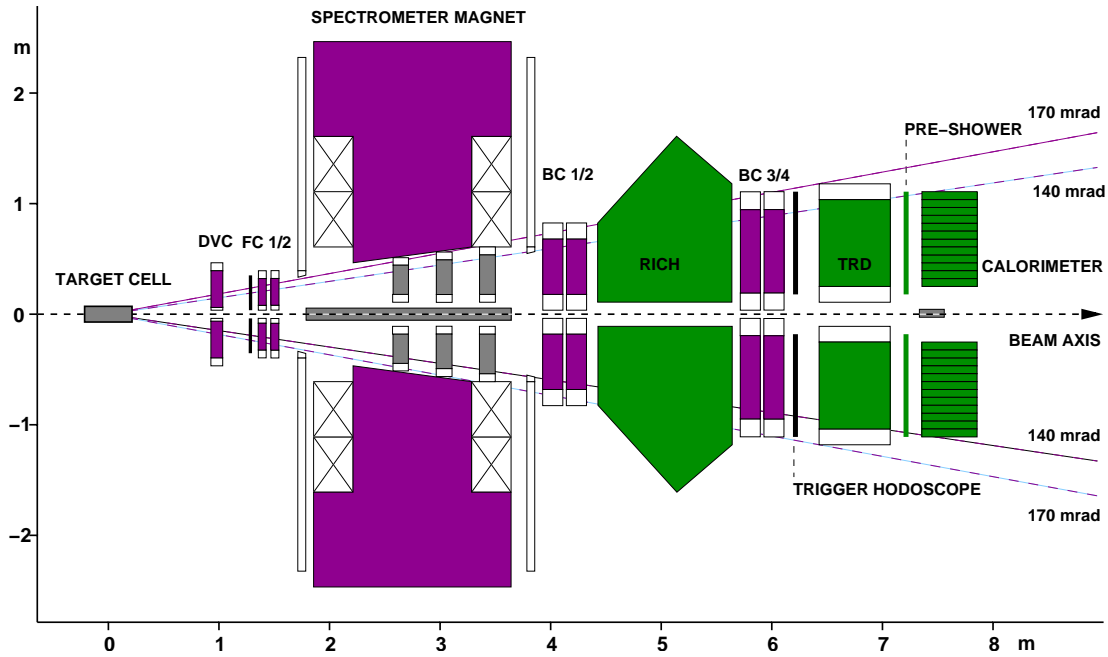
Figure 3.6.: Schematic side view of the HERMES spectrometer: Its acceptance spanned the ranges $40 < |\theta_{\text{vertical}}| < 140\,\text{mrad}$ and $|\theta_{\text{horizontal}}| < 170\,\text{mrad}$ in the scattering angle.

3.3.2. The particle identification system

A very clean separation of the scattered lepton tracks from the hadron tracks is essential for semi-inclusive measurements of the deep-inelastic scattering process. The particle identification (PID) system of the HERMES experiment consisted of a dual-radiator ring imaging Čerenkov detector, a transition radiation detector (TRD), a preshower scintillation counter and an electromagnetic calorimeter. The responses of the four different PID detectors (figure 3.7) were combined to suppress the large background of hadrons arising mainly from photo-production processes:

❑ In the TRD, the electromagnetic radiation emitted by charged particles that cross a boundary between two dielectric media was detected. The radiated energy is proportional to the Lorentz factor γ of the radiating particles. This allows for the separation of lepton and hadron tracks due to the much higher Lorentz factors of electrons compared to hadrons of the same energy. As only a small number of photons is radiated when a particle crosses a boundary, six modules were combined in order to be able to measure the transition radiation. Each module consisted of a proportional wire chamber and a preceding radiator with polyethylene fibres. Using solely the response of the six TRD modules and the truncated mean method, hadrons were rejected by a factor of more than 100 at an efficiency of about 90%.

❑ A preshower scintillation counter halve consisted of two radiation lengths of lead and a scintillator hodoscope. As leptons in the preshower scintillation counter induce electromagnetic showers with much higher probability than hadrons, hadrons were suppressed by a factor of 10 at an efficiency of about 95%.

❑ In the calorimeter, the energy of electromagnetic showers developing in the 42×10 lead-glass block array of a calorimeter halve was measured. Unlike hadrons, leptons deposited their whole energy in the lead-glass blocks of about 18 radiation lengths. A hadron-rejection factor of 100 was obtained.
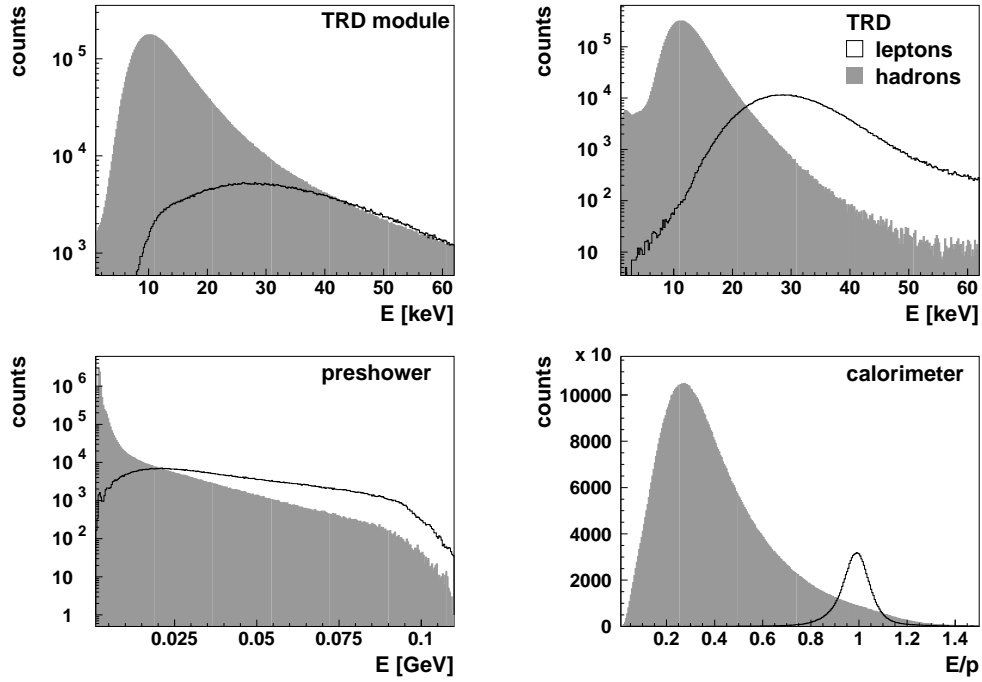
25

Figure 3.7.: Typical responses of the HERMES particle identification system: Hadron (filled areas) and lepton counts (unfilled areas) are given as a function of the energy deposited in a module of the TRD, the truncated mean of all six modules of a TRD halve, the preshower scintillation counter and the electromagnetic calorimeter.

The PID system provided a scattered lepton identification with an efficiency of 98% and a hadron contamination of less than 1%.

In the spectrometer acceptance about 95% of all hadron momenta were observed in the range 2.0 to 15.0 GeV. In this low momentum range the separation of charged pion, charged kaon and proton tracks was feasible by using a RICH detector with two radiators [A$^+$02] as shown in figure 3.9. The mass m of a reconstructed track can be measured by the properties of Čerenkov radiation. Charged particles with a momentum p exceeding a threshold momentum p_{thres}

$$p > p_{thres} = \frac{1}{\sqrt{n^2 - 1}} \tag{3.4}$$

in a radiator with refraction index n induce Čerenkov radiation. These particles traversed the radiator with a velocity v greater than the signal velocity in the radiator. The conical emission of the Čerenkov photons is related to the refraction index n of the radiator via the characteristic opening angle θ:

$$\theta = \arccos \frac{c}{vn} \tag{3.5}$$

The layout of the RICH detector is presented in figure 3.8: Particles passed first an entrance window of silica aerogel SiO_2 tiles with a refraction index n of 1.0304 and then a volume filled with the heavy fluorocarbon gas C_4F_{10} with a refraction index of 1.00137. The Čerenkov photons induced by charged particles were focused by a spherical mirror and detected by an array of photo-multiplier tubes (PMT), referred to as the PMT matrix.
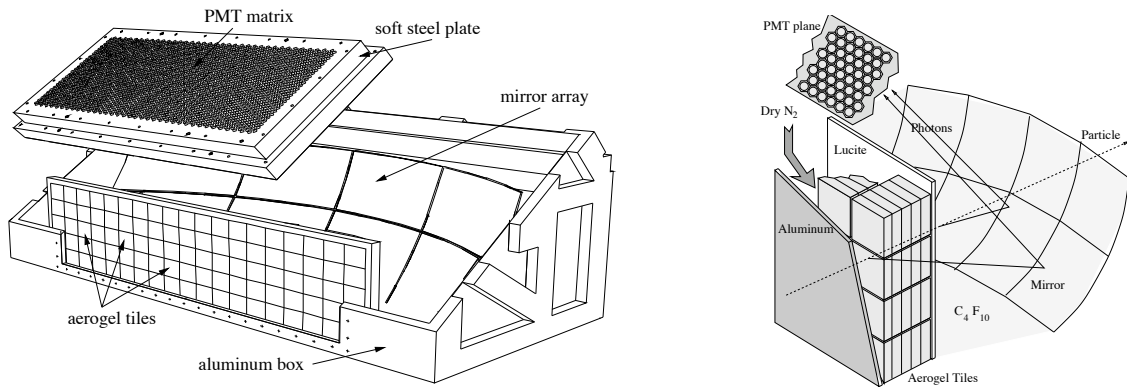
Figure 3.8.: The RICH detector: A cutaway schematic view of the upper RICH detector is shown in the left panel, whereas the basic configuration is presented in the right panel. A particle traversed first a wall of silica aerogel SiO_2 and then the detector interior filled with C_4F_{10}. The lightweight focusing mirror was made of resin-coated carbon-fibre surfaces of optical quality. The photon detector consisted of 1934 photo-multiplier tubes for each detector half, held in a soft-steel matrix to provide shielding against the residual field of the spectrometer magnet.
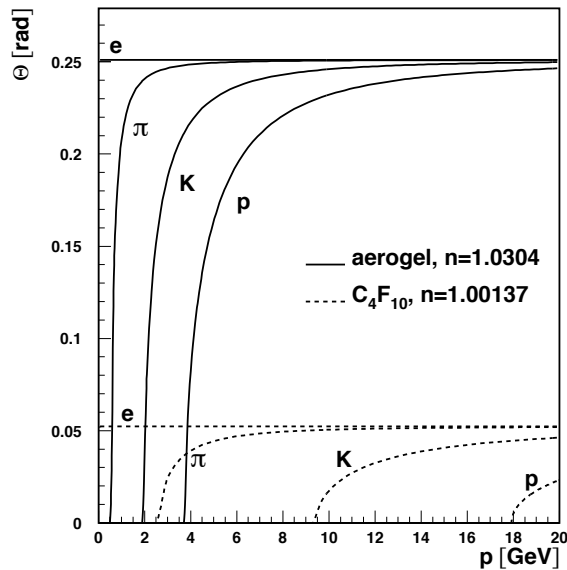

Figure 3.9.: Hadron identification using the RICH detector: For charged pions, charged kaons and protons the momentum dependence p of the Čerenkov cone angle θ is given. All pion momenta within the momentum acceptance of the spectrometer were above the pion threshold for SiO_2 of $0.6\,$GeV, 90% of the kaon and 78% of the proton momenta were above the kaon threshold of $2.0\,$GeV.

3. The HERMES *experiment*

The reconstruction of the Čerenkov angle was hampered by the non-linear optical properties of the spherical mirror array and the sparse statistics of hits in the PMT matrix. Due to the non-linearity of the spherical mirror array asymmetrically distorted ellipses instead of symmetric rings were detected by the PMT matrix. The average number of PMT hits was 10 (23) for an aerogel (C_4F_{10}) ellipse. Thus the reconstruction of the Čerenkov angle was sensitive to background processes, detector noise and acceptance effects and complex reconstruction methods were developed.

Inverse Ray Tracing (IRT)   For a given track and for each hit in the PMT matrix the corresponding Čerenkov angle was calculated from the optical geometry of the RICH detector by the Newton-Raphson method considering both radiator hypotheses. The evaluated angle was compared to the angles of the particle hypotheses pion, kaon and proton. The most probable particle type is determined from the conditional probabilities that the detected hits were generated by a hypothetical particle. The likelihoods for the two radiators were combined to an overall conditional probability.

Direct Ray Tracing (DRT)   In the DRT method [Cis97] the most probable particle type was obtained from the comparison of a simulated hit pattern in the PMT matrix to the detected hit pattern for each particle hypothesis. In the underlying Monte Carlo simulation a constant background and only one track per detector half was considered even if multiple tracks were detected in the particular detector half. The consideration of single track hypothesis only could lead to misidentification if the induced rings of a multiple track event overlap.

Event level reconstruction (EVT)   The EVT method [LH08] was developed as reconstruction method of Čerenkov angles for the PMT hit pattern originating from multiple track events in the top or bottom part of the spectrometer. EVT improved the hadron identification when more than one track was observed per detector half. The method is based on the simulated hit pattern by DRT and evaluates likelihoods for combined particle hypotheses, e.g. electron-kaon, pion-kaon, electron-kaon-proton etc.. In this process the simulated hit pattern of the relevant individual tracks were combined and the most probable combined particle hypothesis was obtained from the comparison of the combined simulated hit pattern to the observed hit pattern.

28

4. The measurement of transverse SSA

The observation of transverse single-spin asymmetries at the HERMES experiment provides signals for transverse-momentum dependent quark distribution and fragmentation functions such as the transversity and Sivers distributions and the Collins fragmentation function. In this chapter a Fourier analysis of transverse single-spin asymmetries for semi-inclusive electroproduction of π-mesons and charged K-mesons on a transversely nuclear-polarised hydrogen target is presented.

Transverse single-spin asymmetries $A^h_{\text{U}\perp}$ for some hadron type h and using an unpolarised lepton beam (U) are defined as the difference of the transverse-target ($\perp$) spin-dependent cross sections $\sigma^h_{\text{U}\Uparrow}$ and $\sigma^h_{\text{U}\Downarrow}$ for semi-inclusive electro-production of hadrons, normalised to the sum of these cross sections:

$$A^h_{\text{U}\perp} = \frac{\sigma^h_{\text{U}\Uparrow} - \sigma^h_{\text{U}\Downarrow}}{\sigma^h_{\text{U}\Uparrow} + \sigma^h_{\text{U}\Downarrow}}. \tag{4.1}$$

In an experiment, the transverse target spin orientation, denoted as "$\Uparrow$" and "$\Downarrow$", is aligned perpendicular to the lepton beam direction. Hence, the notation $A^h_{\text{U}\perp}$ is used for the measured transverse single-spin asymmetries in contrast to the notation A^h_{UT}, applied in theoretical works, where the transverse target spin orientation is aligned perpendicular to the direction of the virtual photon.

Transverse single-spin asymmetries depend on the azimuthal angle ϕ_S of the target spin axis and the azimuthal angle ϕ of the produced hadron (figure 2.4). A decomposition in terms of Fourier components in these azimuthal angles provides signals for the various contributions to the transverse target spin-dependent cross-section, e.g., for the $2\langle \sin(\phi + \phi_S)\rangle_{\text{U}\perp}$ Fourier component of the Collins mechanism and the $2\langle \sin(\phi - \phi_S)\rangle_{\text{U}\perp}$ Fourier component of the Sivers mechanism. The Fourier components, in the following denoted also as single-spin asymmetries amplitudes, are extracted using a maximum likelihood fit, alternately binned in the Bjorken scaling variable x, the fractional hadron energy z and the transverse hadron momentum $|\mathbf{P}_{h\perp}|$ but unbinned in the ϕ and ϕ_S.

The estimate of the systematic uncertainties and the interpretation of the extracted SSA amplitudes are presented in the subsequent chapters 5 and 6. In this chapter, the semi-inclusive measurement of the deep-inelastic scattering process on a transversely polarised proton target is described (section 4.1) and the Fourier analysis of the transverse single-spin asymmetries is explained (section 4.2).

4.1. The semi-inclusive measurement of the DIS process

Events from deep-inelastic scattering on a transversely nuclear-polarised hydrogen target were recorded with a positron beam in the running period 2002–2004 and with an electron beam in the year 2005. For the measurement of the transverse single-spin asymmetries $A^h_{\text{U}\perp}$ the data sets of the single years 2002, 2003, 2004 and 2005 are combined using well-understood data productions, labelled as `02c1`, `03c1`, `04c1` and `05c2` according to the HERMES convention. Studies of the compatibility of the recorded data are summarised in section 4.1.7.2. At first the selection of deep-inelastic scattering events according to data quality criteria (section 4.1.1), requirements on the track geometry (sections 4.1.2 and 4.1.3), the particle identification (sections 4.1.4 – 4.1.6) and the requirements on the event kinematics (section 4.1.7) are presented.

4.1.1. The data quality criteria

During data taking the running conditions of the HERA beam facility and the operation of the HER-MES target and spectrometer were continuously monitored. This information was read out roughly every $10\,\text{s}$. The recorded scattering events were grouped according to these $10\,\text{s}$ readout periods and quality criteria were elaborated by the HERMES data quality group for each group of scattering events based on the monitored information [Wen03]. For the measurement of transverse single-spin asymmetries data quality criteria have been chosen to ensure:

❑ a fully operational target system without high fluctuations of the target density,

❑ a properly working tracking and PID system,

❑ a reliably working data acquisition system with a trigger dead time not exceeding 50% and no faulty records (e.g. beam currents or luminosities beyond achievable values).

No polarised lepton beam is required for the measurement of the transverse single-spin asymmetries $A_{U\perp}^h$ and thus no quality criteria concerning the beam polarisation are applied.

Whereas the calorimeter was properly working during the HERMES running period 2003–2005, at least one non-responding calorimeter block was observed in 10% of the 2002 data due to ageing effects. The absence of trigger signals from these areas of the calorimeter had a negligible effect on the asymmetry measurement. However, the possible misidentification of leptons as hadrons resulted in a loss of semi-inclusive deep-inelastic scattering events [BESS03]. Even though relative and not absolute count-rates are required for an asymmetry measurement in general, a loss of semi-inclusive deep-inelastic scattering events in certain areas could influence the transverse single-spin asymmetries due to their dependence on the azimuthal angles ϕ and ϕ_S. In the case of an $A_{U\perp}^h$ measurement for charged particles no influence was found when requiring not more than one non-responding calorimeter block [BESS03]. This requirement reduced the amount of statistics by a negligible amount of only 0.6% instead of discarding 10% of the 2002 data. For the measurement of transverse single-spin asymmetries for neutral pions, periods with one or more non-responding lead-glass blocks were excluded from the analysis as the reconstruction of neutral pions relies solely on the calorimeter information.

In certain periods of the year 2004, the dark currents in the drift chambers were very high and thus the resolution in the reconstructed scattering angles and particle momenta was worse in particular for events with two or more tracks per detector half. It was shown that this effect cancels for an asymmetry measurement depending on the target-spin orientation due to the rapid target spin reversal [DE05] and thus no data were excluded from these periods.

4.1.2. The tracking correction

By limiting the geometrical acceptance of the spectrometer and checking the correct bending of the tracks no influence on the transverse single-spin asymmetries measurement due to the track reconstruction by HRC was found [BESS03]. However, the magnetic holding field of the transversely polarised target affected the track reconstruction in the front region of the spectrometer. The magnetic field in vertical direction had a large component perpendicular to the particle's momentum, leading to deflection due to the Lorentz force. As the front-track reconstruction determines the vertex and the scattering angle the experienced deflection has to be accounted for when calculating the kinematics of the recorded deep-inelastic scattering events.

The transverse magnet correction (TMC) software [AMS$^+$07] provides two different correction methods. Both methods rely on a field map of the target holding field. Whereas only a simulated

field map could be so far applied for the data recorded in the running period 2002–2003, detailed surveys of the field map were available for the data recorded in the running period 2003–2005. TMC correction methods 1 and 2 follow different ansätze:

❏ In the correction method 1 a base set of trajectories spanning the full spectrometer acceptance is calculated for a given magnet field map within the momentum range 0.5 GeV – 27.5 GeV. For each particle track the reference trajectory closest to the initial trajectory is chosen. The correction values for the vertex in beam direction and the polar and azimuthal scattering angle is obtained from the correction values to the kinematics of the reference track.

❏ In the correction method 2 the target region was regarded as an optical system. Applying the widely used MIT-RAYTRACE software for ion-optical systems, a set of reference tracks was tracked through the optical system to a reference plane where the magnetic field is negligible. Transfer coefficients from the initial to the final coordinates were obtained. In the correction procedure, observed tracks were transferred from the reference plane to the target region according to the transfer coefficients of adjacent reference tracks in an iterative procedure. Inside the target region, TMC method 2 attempted to find the closest approach of a helix to the beam line, while TMC method 1 looked up tracks that come a priori from the beam line.

Both TMC methods were carefully studied [AMS$^+$07, ESS03b, BESS03, CDPS07a, CDPS07b]: Even though no strong influence on the transverse single-spin asymmetries measurement was found, detailed Monte Carlo studies revealed that the distribution of the kinematic variables and the azimuthal angles ϕ and ϕ_S could only be correctly reconstructed when the TMC methods were applied. For both TMC methods consistent SSA amplitudes are obtained. As the position of the HERA electron beam changed during the running period 2002–2005 (section 4.1.7.2), TMC method 2 is preferred due to a more flexible consideration of the beam position. If TMC method 2 is not available for the reconstructed tracks, TMC method 1 is applied as alternative tracking correction.

4.1.3. The selection of tracks

Only tracks are regarded where an appropriate tracking correction by TMC is available. Particle tracks from the edges of the HERMES acceptance are discarded. Background processes are suppressed by ensuring that the selected tracks originated from within the target cell and did not pass
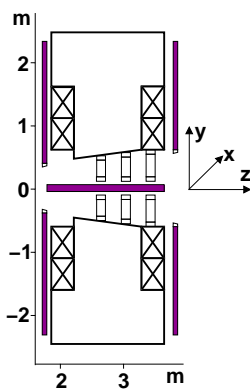
vertex:	$|z_{\text{vertex}}| \leqslant 0.18\,\text{m}$
front field clamp position:	$|x_{\text{ffc}}| < 0.31\,\text{m}$
rear field clamp position:	$|x_{\text{rfc}}| \leqslant 1.00\,\text{m}$
	$|y_{\text{rfc}}| \leqslant 0.54\,\text{m}$
iron plate position:	$0.07\,\text{m} < |y_{\text{ip}}|$
calorimeter positions:	$|x_{\text{c}}| < 1.75\,\text{m}$
	$0.3\,\text{m} < |y_{\text{c}}| < 1.08\,\text{m}$

Table 4.1.: Restrictions on the track geometry and a detail of the HERMES spectrometer where the field clamps around the spectrometer magnet and the iron plate around the beam pipes are shown (as filled areas in magenta).

through the field clamps around the spectrometer magnet or the massive iron plate which shielded the electron and proton beam pipes from the spectrometer magnet field. A requirement on the position in the calorimeter which ensures that the electro-magnetic shower is mostly contained within the calorimeter blocks is important for the separation of lepton and hadron tracks. For the determination of the electro-magnetic shower centre, the horizontal and vertical track positions as reconstructed in the centre of the spectrometer magnet are projected to the nominal position of the calorimeter front face of $z_c = 7.38\,\mathrm{m}$. The restrictions on the track geometry are listed in table 4.1.

4.1.4. The lepton-hadron separation

Lepton tracks are separated from hadron tracks by using calibrated signals from the RICH detector, the TRD, the preshower scintillation counter and the electro-magnetic calorimeter. Typical detector responses of the HERMES PID system are shown in figure 3.7. For the lepton-hadron separation the conditional probabilities $P_{E,p,\theta}\left(L(H)\right)$ of lepton tracks (hypothesis L) and hadron tracks (hypothesis H) were considered, given detector responses E by particle tracks of momenta p and polar angles θ. According to Bayes' theorem:

$$P_{E,p,\theta}\left(L(H)\right) = \frac{P_{p,\theta}\left(L(H)\right) P_{L(H),p}\left(E\right)}{P_{p,\theta}\left(L\right) P_{L,p}\left(E\right) + P_{p,\theta}\left(H\right) P_{H,p}\left(E\right)}, \tag{4.2}$$

these conditional probabilities are related to:

❑ the particle fluxes, i.e. the conditional probabilities $P_{p,\theta}\left(L(H)\right)$ of the hypothesis L (H) when a particle with momentum p and polar angle θ is observed,

❑ the marginal probabilities $P_{L(H),p}\left(E\right)$ to measure the detector response E for a lepton (hadron) track with momentum p.

The marginal probabilities describe the properties of the PID detectors and were extracted from the recorded scattering data to account for running conditions and changes of the PID system. From the ratio of the conditional probabilities for lepton and hadron identification the quantities $\mathrm{PID}_{\mathrm{detector}}$ were computed for each PID detector:

$$\log_{10}\frac{P_{E,p,\theta}\left(L\right)}{P_{p,E}\left(H\right)} = \log_{10}\frac{P_{L,p}\left(E\right)}{P_{H,p}\left(E\right)} + \log_{10}\frac{P_{p,\theta}\left(L\right)}{P_{p,\theta}\left(H\right)} = \mathrm{PID}_{\mathrm{detector}} + \log_{10}\Phi. \tag{4.3}$$

In doing so the particle flux factor $\log_{10}\Phi$ was obtained in an iterative procedure. In the left panel of figure 4.1 the $\mathrm{PID}_{\mathrm{detector}}$ quantity of the TRD (defined as PID3) is plotted against the summed $\mathrm{PID}_{\mathrm{detector}}$ quantities of the RICH detector, the preshower scintillation counter and the calorimeter (defined as PID5). The distribution of particle counts as a function of the total value of $\mathrm{PID3} + \mathrm{PID5} - \log_{10}\Phi$ is shown in the right panel of figure 4.1. By requiring limits on the total value, a lepton identification with an efficiency of 98% and a hadron contamination of less than 1% is achieved. The chosen limits of the lepton-hadron separation are listed in table 4.2:

leptons:	$\mathrm{PID3} + \mathrm{PID5} - \log_{10}\Phi > 2$
hadrons:	$\mathrm{PID3} + \mathrm{PID5} - \log_{10}\Phi < 0$

Table 4.2.: Lepton-hadron separation using the PID3 and PID5 quantities and the corresponding flux factor $\log_{10}\Phi$ which were evaluated from combined PID detector responses.

No strong dependence on the measured SSA amplitudes has been found by changing the limits on the total value to 1.5 (-0.5) or even 1 (-1) for leptons (hadrons) [CDPS07a].
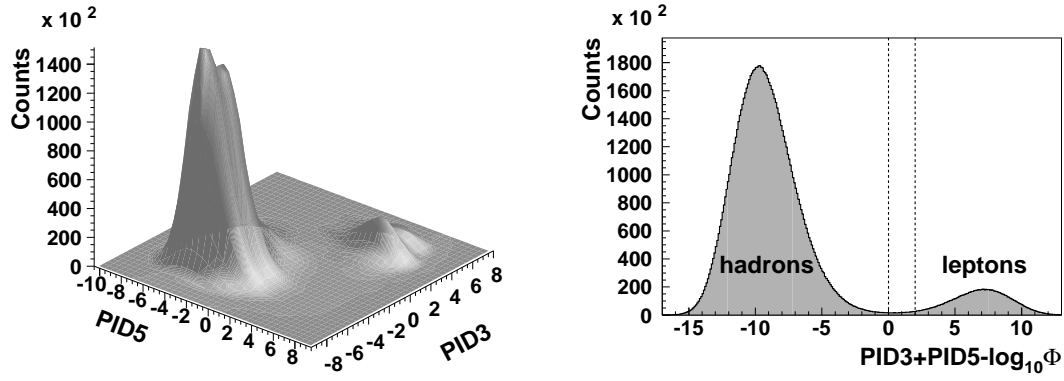
Figure 4.1.: Lepton-hadron separation: The information on the HERMES PID system is combined into the quantities PID3 and PID5 and the corresponding particle fluxes ($\log_{10}\Phi$). Lepton tracks are clearly separated from the large hadronic background according to the PID3 and PID5 quantities as shown in the left panel using the 2003 data as example. In the right panel the distribution of particle counts as a function of the total value of $\mathrm{PID3}+\mathrm{PID5}-\log_{10}\Phi$ is given. The dashed vertical lines indicate the chosen limits for the separation of lepton and hadron tracks.

4.1.5. The hadron identification

Based on the combined PID detector responses hadrons in coincidence with scattered leptons are identified with an efficiency of 99% and lepton contaminations smaller than 1%. Hadron tracks of pions, kaons and protons are separated using the RICH PID information (section 3.3.2). For each track within the momentum range 2–15 GeV the most probable hadron type and a corresponding quality parameter Q defined as

$$Q = \log_{10} \frac{P(\text{most probable hadron type})}{P(\text{second most probable hadron type})} \qquad (4.4)$$

was determined based on the *direct ray tracing* (DRT), the *event level* (EVT) and the *inverse ray tracing* (IRT) reconstruction method. By requiring a positive quality parameter Q semi-inclusive deep-inelastic scattering events from periods with a bad performance of the RICH detector or incorrect reconstructions of the Čerenkov angle were omitted.

The efficiency of the RICH detector and the contamination of the pion, kaon and proton identification were evaluated by Monte Carlo simulations of the RICH PID. Thereby the performance of the RICH detector was parameterised in terms of $\mathscr{P}$-matrices which related the identified hadron types to the true hadron types. The elements $P_h(h_{\mathrm{true}})$ of the $\mathscr{P}$-matrix denote the conditional probability that a hadron of true type h_{true} is identified as a particle of type h (or even unidentified as X):

$$\mathscr{P} = \begin{pmatrix} P_\pi(\pi) & P_\pi(K) & P_\pi(p) \\ P_K(\pi) & P_K(K) & P_K(p) \\ P_p(\pi) & P_p(K) & P_p(p) \\ P_X(\pi) & P_X(K) & P_X(p) \end{pmatrix}. \qquad (4.5)$$

The momentum dependence of these conditional probabilities for the different reconstruction methods is presented in figure 4.2. Whereas the charged pion identification has a large efficiency and the probability to misidentify a kaon or proton as a pion is small over almost the entire momentum range, for both kaons and protons a strong momentum dependence of the identification efficiencies is visible in figure 4.2.
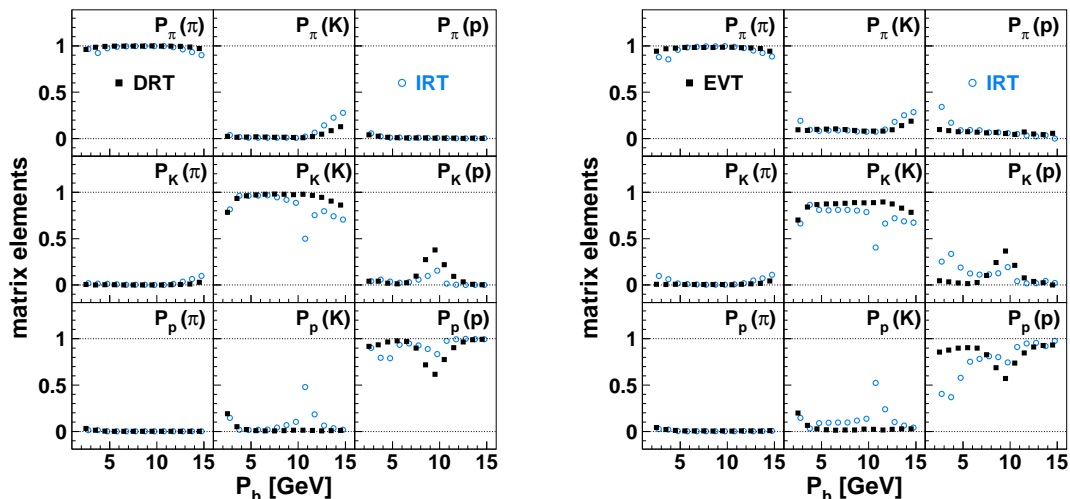
Figure 4.2.: The $\mathscr{P}$-matrices: The performance of the RICH detector was studied in Monte Carlo simulations in terms of the conditional probability $P_h(h_{\mathrm{true}})$ to identify hadrons of true type h_{true} as particles of type h. These conditional probabilities were composed into $\mathscr{P}$-matrices and evaluated as a function of the hadron momentum P_h and the event topology given by the number of tracks per detector half. In the left (right) panel, the elements of the $\mathscr{P}$-matrices obtained from the DRT (EVT) and IRT reconstruction methods are compared in the case of (more than) one track per detector half.

The elements of the inverse $\mathscr{P}$-matrix can be interpreted as event weights which relate the identified hadron types to the true hadron types. In the semi-inclusive measurement, pion weights, kaon weights and proton weights are assigned to each identified hadron track according to the inverse $\mathscr{P}$-matrix for a certain momentum bin and the event topology given by the number of tracks per detector half. Taking these event weights into account the extracted SSA amplitudes are corrected for a possible misidentification of hadrons [BDE+06]. While this correction barely affects SSA amplitudes of charged pions, there is an influence on SSA amplitudes of charged kaons which is related to the off-diagonal elements of the $\mathscr{P}$-matrices and thus to hadron misidentification.

In section 3.3.2 the reconstruction methods of the Čerenkov angle are described. While in previous analyses the IRT method was applied for all event topologies [HERMES05c, DE05, BDE+06, CDPS07a], the recently developed EVT method for multiple track events (42% of all identified hadrons) is chosen in combination with the DRT method for single-tracks (58% of all identified hadrons):

❑ Compared to DRT (in case of a single track topology) and EVT (in case of multiple track topologies) a lower hadron identification efficiency is found for the IRT reconstruction method as shown in figure 4.2. Lower particle identification efficiencies result in larger statistical uncertainties due to an enhancement of the off-diagonal elements of the $\mathscr{P}$-matrix.

❑ In case of multiple track topologies there are problems with the hadron identification by IRT when the signals of the induced Čerenkov radiation overlapped in the PMT matrix of the RICH detector. These overlaps are taken into account in the EVT method [LH08].

❑ Around the momentum threshold for kaons in the C_4F_{10} radiator of $10\,\mathrm{GeV}$ a large discrepancy is visible in figure 4.2. Whereas the conditional probability to misidentify a kaon as proton is
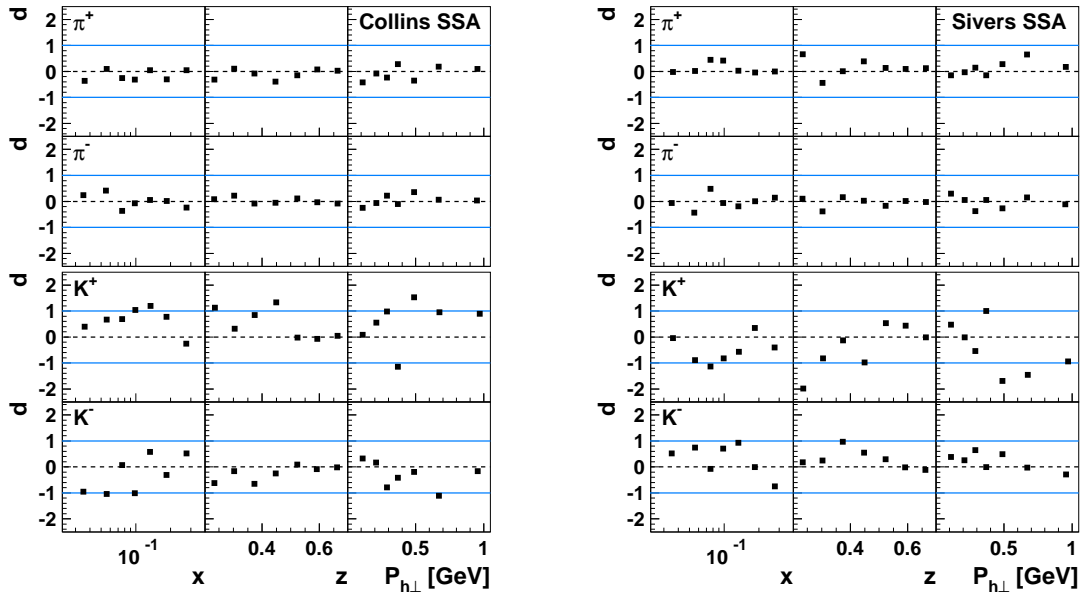
Figure 4.3.: Influence of the SSA amplitudes on the reconstruction method of the RICH PID: Collins (Sivers) amplitudes are extracted using either the IRT or DRT/EVT reconstruction method. In the left (right) panel the corresponding deviations are presented for charged pions and kaons as a function of x, z and $|\mathbf{P}_{h\perp}|$.

about 50% for the IRT reconstruction, no inefficiencies are found for both the DRT and EVT reconstruction method.

❑ For the IRT identification a dependence on the horizontal track position was found. In particular unphysical anti-proton yields were observed in the right side of the RICH detector [LH08].

Due to the EVT reconstruction method, the hadron identification for multiple tracks is improved and a possible misidentification of protons as kaons is corrected. The effect of the RICH PID reconstruction methods on the SSA amplitudes can be examined by evaluating in each kinematic bin i the deviation d of the SSA amplitudes extracted using either the DRT/EVT or IRT method:

$$d_i = \frac{2\langle\sin(\phi-\phi_S)\rangle_{\mathrm{U\perp}\,,i}^{\mathrm{DRT/EVT}} - 2\langle\sin(\phi-\phi_S)\rangle_{\mathrm{U\perp}\,,i}^{\mathrm{IRT}}}{\sqrt{\sigma^2_{2\langle\sin(\phi-\phi_S)\rangle_{\mathrm{U\perp}\,,i}^{\mathrm{DRT/EVT}}} + \sigma^2_{2\langle\sin(\phi-\phi_S)\rangle_{\mathrm{U\perp}\,,i}^{\mathrm{IRT}}}}. \tag{4.6}$$

According to equation 4.6 (given for Sivers amplitudes), deviations of $d = \pm 1$ correspond to a discrepancy of 1σ. In figure 4.3 the deviations of Collins and Sivers amplitudes are presented for charged pions and kaons. The SSA amplitudes extracted using either the DRT/EVT or IRT method are consistent for charged pions as the corresponding deviations fluctuate around zero. For deviations of charged kaons a systematic trend is visible which can be related to the possible misidentification of mainly protons as kaons in the IRT reconstruction method.

4.1.6. The neutral pion reconstruction

The branching ratio of the electromagnetic decay of the neutral pion π^0 into a photon-pair is about 98.8% [PDG08]. Other decay channels like $\pi^0 \to e^+e^-\gamma$ or $\pi^0 \to e^+e^-e^+e^-$ can be neglected due their small branching ratios and their limited acceptance in the HERMES spectrometer.

The energies and positions of the photons are reconstructed from their electro-magnetic shower profile in the lead-glass calorimeter: The calorimeter is calibrated according to the nominal value of $E/p = 1$ for the ratio of the electron energy E deposited in the calorimeter and the electron momentum p reconstructed in the HERMES spectrometer. Due to the different shower evolution of electrons and photons, the measured photon energies are corrected by a factor of 0.97 and the centre of the electro-magnetic shower of photons is shifted by $+9.5$ cm in longitudinal direction. For the neutral pion reconstruction a minimum energy deposit of $E_\gamma > 1$ GeV is required. The decay length of the neutral pion, $\tau = 25.1$ nm [PDG08], cannot be resolved in the HERMES spectrometer and hence the neutral-pion decay is considered to be instantaneous. Thereby the origin of the photon-pair is determined by the vertex of the deep-inelastic scattering process. Photons are not deflected by the spectrometer magnet. Therefore a tighter requirement on the calorimeter position as for charged particles is applied (table 4.3) as photons at larger calorimeter positions passed the spectrometer magnet material.

calorimeter positions:	$\|x_c\| \leqslant 1.25$ m
	0.3 m $\leqslant \|y_c\| \leqslant 1.05$ m

Table 4.3.: Requirements on the horizontal and vertical impact positions of the photons at the calorimeter front face. For the determination of the centre of the electro-magnetic shower of photons, a nominal position of the calorimeter front face of $z_c = 7.475$ m is considered.

For all selected photons in a scattering event the invariant mass of all possible photon-pair combinations $\gamma\gamma'$ is calculated:

$$M_{\gamma\gamma'} = \sqrt{2E_\gamma E_{\gamma'}\left(1 - \cos\theta\right)}, \tag{4.7}$$

where θ denotes the opening angle of the two photon system determined by the cluster positions in the calorimeter. The maximum number of photons per event is restricted to 6 in order to limit the background without reducing the number of reconstructed neutral pions by more than 0.5%. In figure 4.4 the invariant mass spectrum of the 2002–2005 data is presented. As shown in the right panel of figure 4.4 a reasonable description of the invariant mass spectrum within the range $M_{\gamma\gamma'} \in [0.04\,\text{GeV}; 0.23\,\text{GeV}]$ is obtained by a six-parameter fit to:

$$p_1 e^{-\left(M_{\gamma\gamma'} - p_2\right)^2 / \left(2p_3^2\right)} + p_4 \left(M_{\gamma\gamma'} - 0.0004\,\text{GeV}\right)^{p_5} e^{p_6 M_{\gamma\gamma'}}. \tag{4.8}$$

Whereas the signal contribution is fit by a Gaussian distribution, a Weibull distribution with a fixed starting point of 0.0004 GeV is used for the combinatorial background contribution. A neutral pion mass of $m_{\pi^0} = (134.34 \pm 0.04)$ MeV is found for the 2002–2005 data, which is in agreement with the value of $m_{\pi^0} = (134.9766 \pm 0.0006)$ MeV provided by the particle data group [PDG08].

4.1.7. The selection of deep-inelastic scattering events

For the semi-inclusive measurement all scattering events are selected where identified hadrons are detected in coincidence with at least one identified lepton. As described in section 4.1.5, the identification of hadrons is restricted to the momentum range:

$$2\,\text{GeV} < |\mathbf{P}_h| < 15\,\text{GeV}. \tag{4.9}$$

The scattered lepton of the deep-inelastic scattering process is identified as the electron or positron with the highest momentum of the scattering event (only in 0.5% of all events more than one lepton
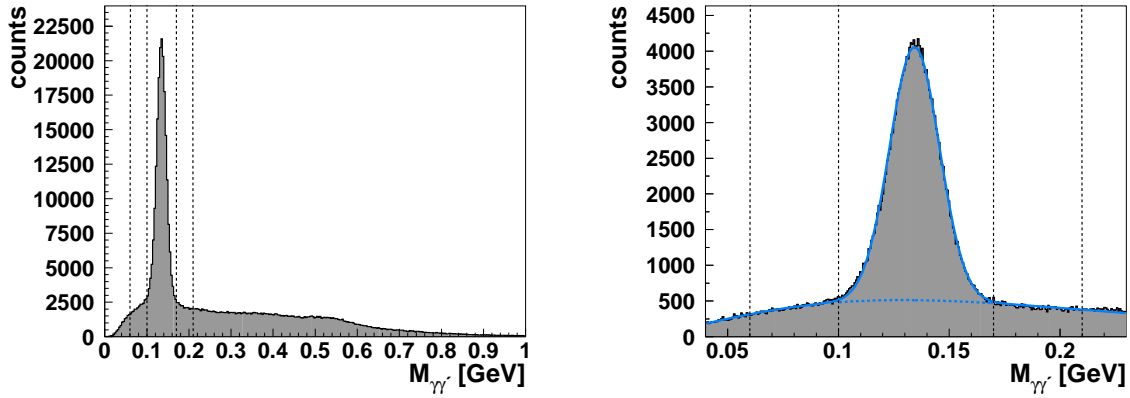
Figure 4.4.: The reconstruction of neutral pions: Neutral pions are reconstructed from the invariant mass $M_{\gamma\gamma'}$ of two photon systems. In the left panel the spectrum for all selected photon pairs is shown (in arbitrary units). The width of the peak of $0.1137 \pm 0.0004\,\mathrm{GeV}$ reflects the resolution of the calorimeter. A fit according to equation 4.8 is superimposed to the invariant mass spectrum in the right panel. The vertical lines indicate the signal range $M_{\gamma\gamma'} \in [0.10\,\mathrm{GeV}; 0.17\,\mathrm{GeV}]$ and the background ranges $M_{\gamma\gamma'} \in [0.06\,\mathrm{GeV}; 0.10\,\mathrm{GeV}] \cap M_{\gamma\gamma'} \in [0.17\,\mathrm{GeV}; 0.21\,\mathrm{GeV}]$ for the asymmetry determination (section 4.2.2.5).

is found). Even though scattered leptons originated from the incoming HERA electron (positron) beam, leptons with positive (negative) charge are not rejected in order to apply a correction for pair production processes (section 4.2.2.4). From the kinematics of the scattered lepton the kinematic variables Q^2, x, y and W^2 describing the deep-inelastic scattering process are determined.

Scattering events arising from the deep-inelastic scattering process are only selected according to kinematic criteria, no specific first level triggers are selected as trigger signals are formed according to various uncalibrated detector signals. Given the rapid change of the target spin orientation every 60–180 s, scattering events recorded according to various combinations of first level triggers are combined in the analysis. To ensure a clean sample of deep-inelastic scattering events, the following requirements are put on the four-momentum transfer Q^2 and the squared invariant mass W^2 of the virtual-photon nucleon system:

❑ In the deep-inelastic scattering domain the energy transferred from the virtual photon to the proton target is large compared to the four-momentum transfer:

$$\frac{\nu^2}{Q^2} = \frac{Q^2}{(2Mx)^2} \gg 1. \tag{4.10}$$

According to common practise the hard scattering scale of the deep-inelastic scattering process is fixed to:

$$Q^2 > 1\,\mathrm{GeV}^2. \tag{4.11}$$

As a consequence of the chosen scale and the limited angular acceptance of the spectrometer, the Bjorken scaling variable is bounded to the range:

$$0.023 < x < 0.4. \tag{4.12}$$

❑ Scattering events originating from the excitation of nucleon resonances and their subsequent strong decays are excluded by a requirement on W^2:
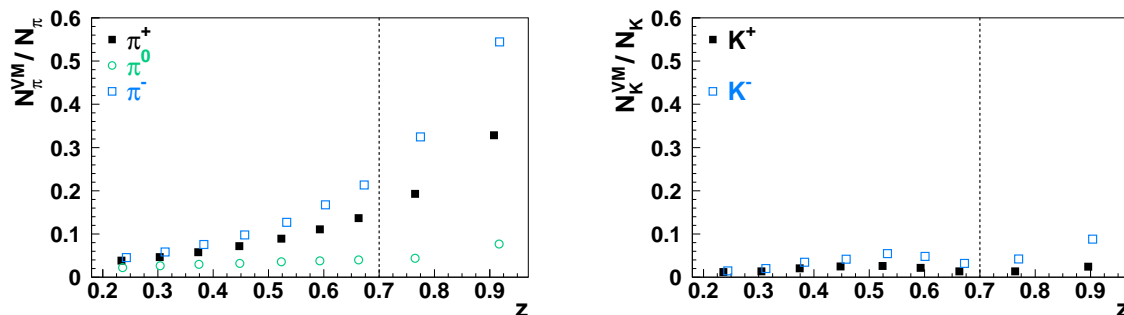
$$W^2 > 10\,\mathrm{GeV}^2, \tag{4.13}$$

37

Figure 4.5.: The simulated fraction of π-mesons (left panel) and K-mesons (right panel) originating from diffractive vector meson production and decay is shown as a function of the fractional hadron energy z (the open squares indicating π^- and K^- are slightly shifted in horizontal direction). The contributions from exclusive channels are simulated by a version of PYTHIA [S$^+$01] tuned for HERMES kinematics. By limiting z to 0.7, a kinematic region is probed where the vector meson contribution to the electroproduction of π-mesons and K-mesons is in particular for charged pions suppressed.

set above the highest mass of the nucleon resonances with very likely to certain existence, i.e. the $N(2600)$ resonance with a Breit–Wigner mass of about $2.6\,\mathrm{GeV}$ and a full Breit–Wigner width of about $0.65\,\mathrm{GeV}$ [PDG08].

To exclude kinematic regions where corrections on the reconstructed kinematics due to QED radiation effects would have to be applied, the fractional energy transfer y is in various HERMES analyses restricted to $y < 0.85$ corresponding to a minimum energy of the scattered lepton of about $4.1\,\mathrm{GeV}$. In deep-inelastic scattering events, where hadrons are observed in coincidence with the scattered lepton, QED radiation effects are suppressed. Thus, the upper limit was raised according to the calorimeter threshold of $1.4\,\mathrm{GeV}$ to:

$$y < 0.95, \qquad (4.14)$$

to slightly weaken the strong correlation of the scaling variables x and Q^2. As contributions from scattering on the collimators in front of the HERMES target cell increase strongly with y, it was ensured that also for the requirement of $y < 0.95$ the background from collimator scattering is suppressed given the semi-inclusive measurement and the chosen scale of $Q^2 > 1\,\mathrm{GeV}^2$ [Pap09]. In many analyses a lower limit of $y > 0.1$ is set for the fractional energy transfer to ensure a sufficient spectrometer resolution for scattered leptons with an energy up to $E' \approx 24.8\,\mathrm{GeV}$. As shown in figure 4.11 for π-mesons and in figure 4.12 for charged K-mesons a minimum value of about 0.18 is observed for the fractional energy transfer and thus no lower limit is set for the semi-inclusive measurement.

A possible interpretation of SSA amplitudes in terms of transverse-momentum distribution and fragmentation functions is based upon a factorisation theorem [JMY04, JMY05]. The adherence of factorisation is regarded in the semi-inclusive measurement:

❏ All identified hadrons are selected and not only the leading hadrons (i.e. the hadron with the highest momentum in the event). Given the averaged track multiplicity of roughly 1.5, only one identified hadron is observed in about 50% of all deep-inelastic scattering events. When comparing the extraction of SSA amplitudes for all selected hadrons and for leading hadrons only (roughly 75% of the selected data), no influence on the SSA amplitudes was found [ESS03a].
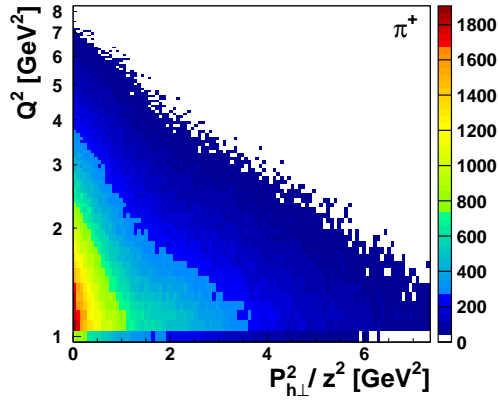
Figure 4.6.: Factorisation scales: The correlation of the hard scattering scale Q^2 and the partonic scale $|\mathbf{P}_{h\perp}|^2 / z^2$ is shown for the selected events including a positively charged pion.

❑ Hadrons originating from diffractive vector meson production and decay are only excluded in kinematic regions where exclusive channels dominate. As shown in figure 4.5 contributions due to exclusive channels (in particular for charged pions) could be suppressed by limiting z to

$$z < 0.7. \tag{4.15}$$

❑ In factorisation proofs soft quark momenta with respect to the hadron momenta are assumed. Therefore, the transverse hadron momenta $|\mathbf{P}_{h\perp}|^2$ and in particular the relevant partonic scale, $|\mathbf{P}_{h\perp}|^2 / z^2$, are required to be smaller than the hard scattering scale Q^2. As shown in figure 4.13 for pions and in figure 4.14 for kaons, the requirement $|\mathbf{P}_{h\perp}|^2 \ll Q^2$ is fulfilled for almost all deep-inelastic scattering events. According to studies of the correlation of the scales Q^2 and $|\mathbf{P}_{h\perp}|^2 / z^2$, a large fraction of the scattering events also support the requirement $(|\mathbf{P}_{h\perp}|^2 / z^2) \ll Q^2$ (figure 4.6). Thus, no cut on the transverse momentum of the observed hadrons is applied.

❑ The formation of hadrons is parametrised by quark fragmentation functions: In the quark fragmentation region hadrons are considered as fragments of the quark (or anti-quark) struck by the virtual photon in the deep-inelastic scattering process. These hadrons are observed in jets well separated from the spectator partons in the target (remnant). Kinematic criteria for the distinction of target fragmentation and quark fragmentation regions were addressed from phenomenological point of view [Ber87]. At HERMES kinematics where transverse mass effects cannot be neglected the criterion is based on a requirement on the fractional momentum of the struck quark by the formed hadron

$$z > 0.2, \tag{4.16}$$

and the squared invariant mass of the virtual-photon nucleon system

$$W^2 > 10 \, \text{GeV}^2. \tag{4.17}$$

The criterion was optimised between requiring a clean separation of the target fragmentation and retaining the amount of scattering events [Bec00].

In previous analyses [HERMES05c], the reconstructed transverse single-spin asymmetries were binned in the azimuthal angles ϕ and ϕ_S. A minimum opening angle $\theta_{\gamma^* h}$ between the momentum direction of the virtual photon (γ^*) and that of a produced hadron (h) of $\theta_{\gamma^* h} > 0.02 \, \text{mrad}$ was
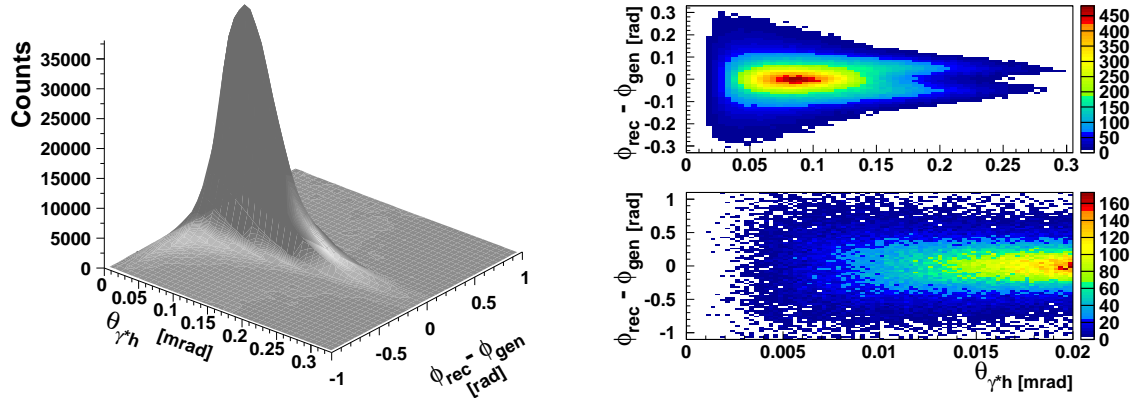
Figure 4.7.: Influence of the polar angle θ_{γ^*h}: In a Monte Carlo simulation of the HERMES experiment the difference between the azimuthal angle ϕ_{gen} as measured in an ideal detector and the azimuthal angle ϕ_{rec} as measured in the HERMES spectrometer is studied as a function of the opening angle θ_{γ^*h} between the virtual photon direction and that of the produced hadron (left panel). No indication for a flip of the hadron production plane due to smearing of ϕ to $\phi + \pi$ and also no indication for bin migration, i.e. smearing of ϕ to $\phi + 0.52$ (when considering 12 bins in ϕ), is found (right panel).

required to avoid bin migration due to QED radiation or detector smearing from, e.g., ϕ to $\phi + \pi$ for low opening angles. The minimum of $0.02\,\mathtt{mrad}$ was adjusted clearly above the resolution in θ_{γ^*h} and imposed a minimum on the detected transverse hadron momentum $|\mathbf{P}_{h\perp}|$ of about $0.04\,\mathtt{GeV}$. As shown in figure 4.7, no indication for significant smearing effects in the azimuthal angles ϕ and ϕ_S is found in a detailed Monte Carlo simulation of the HERMES experiment. This observation is supported by extracting consistent SSA amplitudes in the Monte Carlo simulation when using the azimuthal angles ϕ_{gen} and $\phi_{S,gen}$ as measured in an ideal detector and when using the azimuthal angles ϕ_{rec} and $\phi_{S,rec}$ as measured in the simulated HERMES spectrometer [Die08]. Furthermore, the requirement on the minimum opening angle barely improved the resolution in ϕ, ϕ_S and $|\mathbf{P}_{h\perp}|$ and is thus discarded. As a consequence, about 5.5% in statistics is gained and the analysis is extended to the low region in $|\mathbf{P}_{h\perp}|$.

The criteria for the selection of scattered leptons of the deep-inelastic scattering process and the hadrons detected in coincidence with the scattered lepton are summarised in table 4.4.

Scattered lepton:	$1\,\mathrm{GeV}^2 <$	Q^2	
	$10\,\mathrm{GeV}^2 <$	W^2	
	$0.023 <$	x	< 0.4
	$(0.1 \leqslant)$	y	< 0.95
Detected hadrons:	$2\,\mathrm{GeV} <$	$|\mathbf{P}_h|$	$< 15\,\mathrm{GeV}$
	$0.2 <$	z	< 0.7

Table 4.4.: The requirements on the kinematics of the scattered leptons and the hadrons detected in coincidence with the scattered leptons.
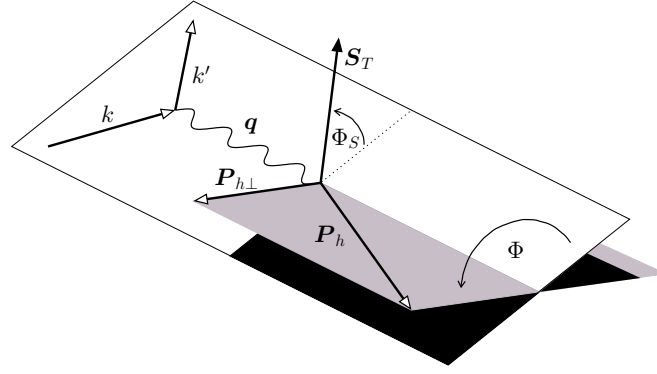
Figure 4.8.: Illustration of the azimuthal dependence of unpolarised hadrons produced in deep-inelastic scattering off a transversely polarised target. The lepton scattering plane (hadron production plane) is indicated in white (grey).

4.1.7.1. The calculation of the azimuthal angles ϕ and ϕ_S

For all selected deep-inelastic scattering events the azimuthal angles ϕ and ϕ_S are evaluated with respect to the lepton scattering plane spanned by the three-momenta of the incoming lepton $\mathbf{l}$ and the virtual photon $\mathbf{q}$ (figure 4.8). In accordance with the definition of the transverse single-spin asymmetries A_{UT}^h in theoretical works, the azimuthal angle ϕ_S of the target spin axis $\hat{\mathbf{S}}_\perp$ is determined for target spin orientation "$\Uparrow$"

$$\phi_S = \mathrm{sgn}\left(\mathbf{q}\times\mathbf{k}\cdot\hat{\mathbf{S}}_\perp\right)\arccos\left(\frac{\mathbf{q}\times\mathbf{k}\cdot\mathbf{q}\times\hat{\mathbf{S}}_\perp}{|\mathbf{q}\times\mathbf{k}|\cdot|\mathbf{q}\times\hat{\mathbf{S}}_\perp|}\right). \tag{4.18}$$

The azimuthal angle ϕ of the momentum direction $\mathbf{P}_h$ of a produced hadron is calculated as:

$$\phi = \mathrm{sgn}\left(\mathbf{q}\times\mathbf{k}\cdot\mathbf{P}_h\right)\arccos\left(\frac{\mathbf{q}\times\mathbf{k}\cdot\mathbf{q}\times\mathbf{P}_h}{|\mathbf{q}\times\mathbf{k}|\cdot|\mathbf{q}\times\mathbf{P}_h|}\right). \tag{4.19}$$

4.1.7.2. The compatibility of the selected sample

For the measurement of transverse single-spin asymmetries the data sets of the years 2002, 2003, 2004 and 2005 are combined using the well-understood data productions `02c1`, `03c1`, `04c1` and `05c2`. The relative amount of statistics per data production is listed in able 4.5. Within the running period 2002–2005, the experimental setup was essentially left unchanged apart from HERA running with electrons instead of positrons in the year 2005 and various maintenance work.

To analyse the compatibility of the data recorded in the single years 2002, 2003, 2004 and 2005, the distributions of the kinematic variables and the azimuthal angles as well as the extracted SSA amplitudes were compared in detail [CDPS07b, CDP$^+$09]. Between the data recorded in the years 2004 and 2005 systematic differences in the ϕ-distributions and the Collins amplitudes of charged pions were found. The systematic differences were traced back to an unexpected beam shift between the years 2004 and 2005.

Due to the holding field of the target transverse to the beam direction, changes of the beam slope were expected with different directions but similar size for an incoming positron and electron beam.

	fraction	beam charge	beam shifts		average target	neutral pion mass
			x-offset	y-offset	polarisation	
02c1	8.6%	e^+	$-0.1\,$mm	$+0.3\,$mm	78.3 ± 4.1%	$135.90 \pm 0.14\,$MeV
03c1	4.7%	e^+	$+0.0\,$mm	$+1.7\,$mm	79.5 ± 3.3%	$133.72 \pm 0.17\,$MeV
04c1	27.0%	e^+	$-0.4\,$mm	$+1.5\,$mm	73.8 ± 3.0%	$133.81 \pm 0.07\,$MeV
05c2	59.7%	e^-	$+2.8\,$mm	$+1.5\,$mm	70.6 ± 5.4%	$134.62 \pm 0.05\,$MeV

Table 4.5.: Selected year-dependent parameters and observables of the HERMES experiment for the data productions 02c1, 03c1, 04c1 and 05c2.

But the observed shift in horizontal direction (with respect to the alignment of the front chambers) of $0.7\,$mm in the year 2004 and $4.1\,$mm in the year 2005 indicated a misalignment of the HERMES spectrometer and/or the HERA beam. The observed beam shifts were accounted for in the applied tracking corrections according to TMC resulting in compatible data for the years 2004 and 2005 as, e.g., shown in figures 4.9 and 4.10 for the Collins and Sivers amplitudes.

In table 4.5 some year-dependent experimental quantities are summarised: In addition to the observed beam shifts (given with respect to the HERMES coordinate system), the average magnitude of the target polarisation and the reconstructed neutral pion mass are given.

The total number of particles selected from the full data recorded with a transversely nuclear-polarised hydrogen target is listed in table 4.6. The hadron counts are obtained from the sum of the RICH PID event weights for the given hadron type. In figures 4.11–4.14 the particle counts are shown as a function of Q^2, x, W^2, y, ϕ_S, $|\mathbf{P}_h|$, $|\mathbf{P}_{h\perp}|$, $|\mathbf{P}_{h\perp}|^2/Q^2$, z and ϕ.

	particle	N	$N_\Uparrow$	$N_\Downarrow$
inclusive measurement:	$e^\pm$	8764939.00	4378553.00	4386386.00
semi-inclusive measurement:	$e^\pm$	1716208.00	856874.00	859334.00
	π^+	730464.66	364878.67	365585.99
	π^0	213362.00	106715.00	106647.00
	π^-	524362.25	261219.58	263142.66
	K^+	130592.77	65205.91	65386.86
	K^-	53918.08	26902.00	27016.07

Table 4.6.: The total number of selected particles N and the accordant number $N_{\Uparrow(\Downarrow)}$ per target spin orientation is listed for the data recorded in the years 2002–2005.
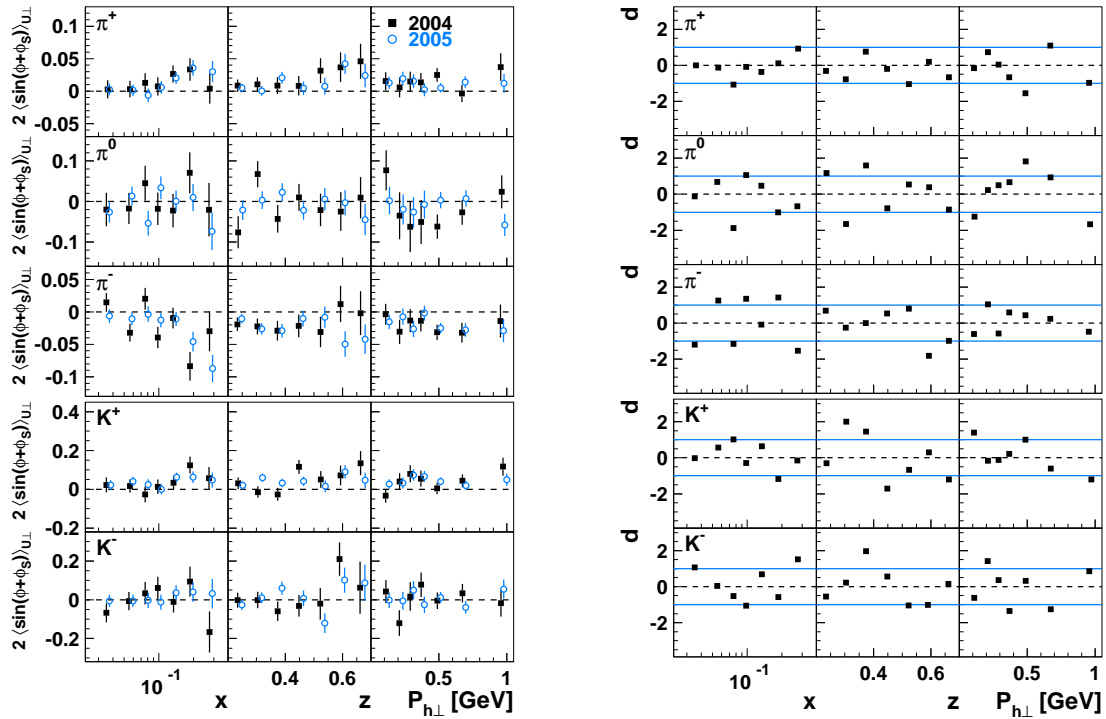
Figure 4.9.: Collins amplitudes extracted from 2004 (closed symbols) and 2005 data (open symbols) are compared (left panel) and the corresponding deviation d is given (right panel).
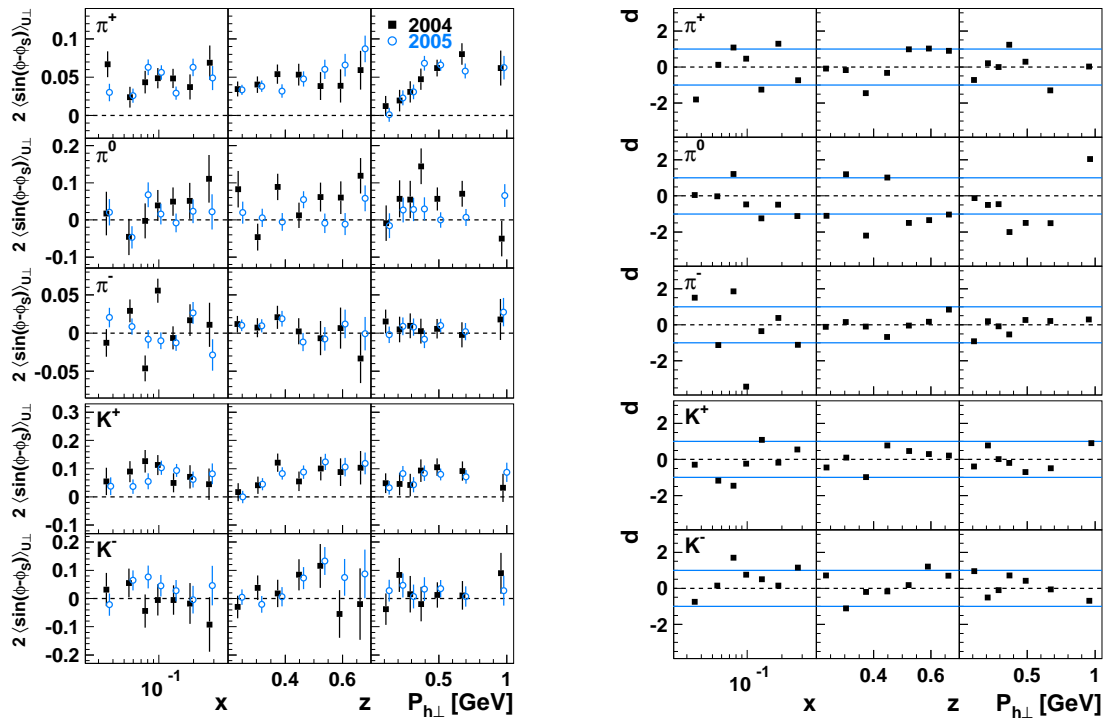

Figure 4.10.: Sivers amplitudes extracted from 2004 (closed symbols) and 2005 data (open symbols) are compared (left panel) and the corresponding deviation d is given (right panel).
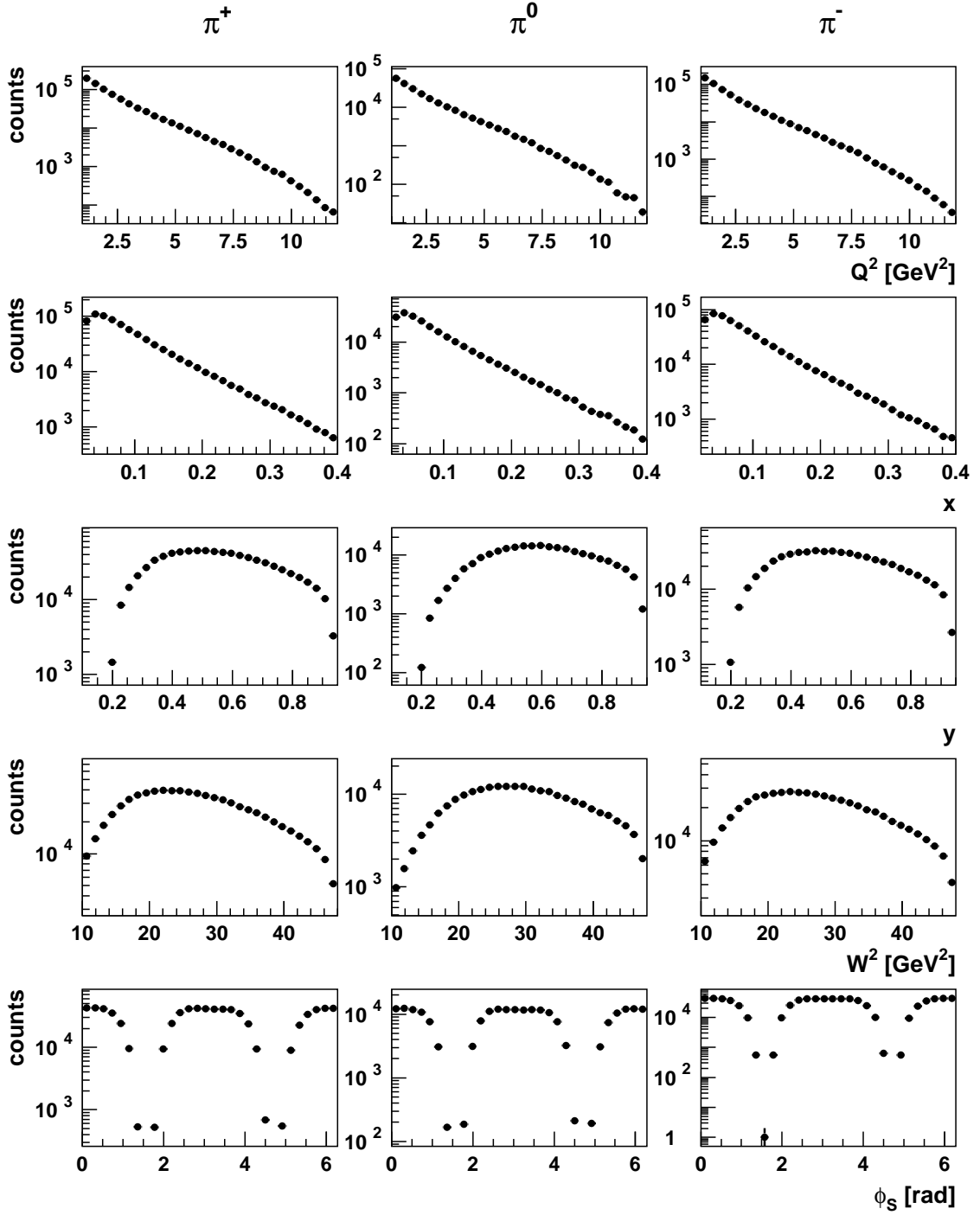
43

Figure 4.11.: Hadron counts as a function of the scaling variables Q^2, x, y and W^2 and the azimuthal angle ϕ_S for the semi-inclusive electro-production of π^+ (left panel), π^0 (central panel) and π^- (right panel) in deep-inelastic scattering of positrons and electrons off a transversely nuclear-polarised hydrogen target. The small gaps at $1.40\,\mathrm{rad} < \phi_S < 1.74\,\mathrm{rad}$ and $4.54\,\mathrm{rad} < \phi_S < 4.88\,\mathrm{rad}$ correspond to the limited acceptance of the HERMES spectrometer close the beam pipe.
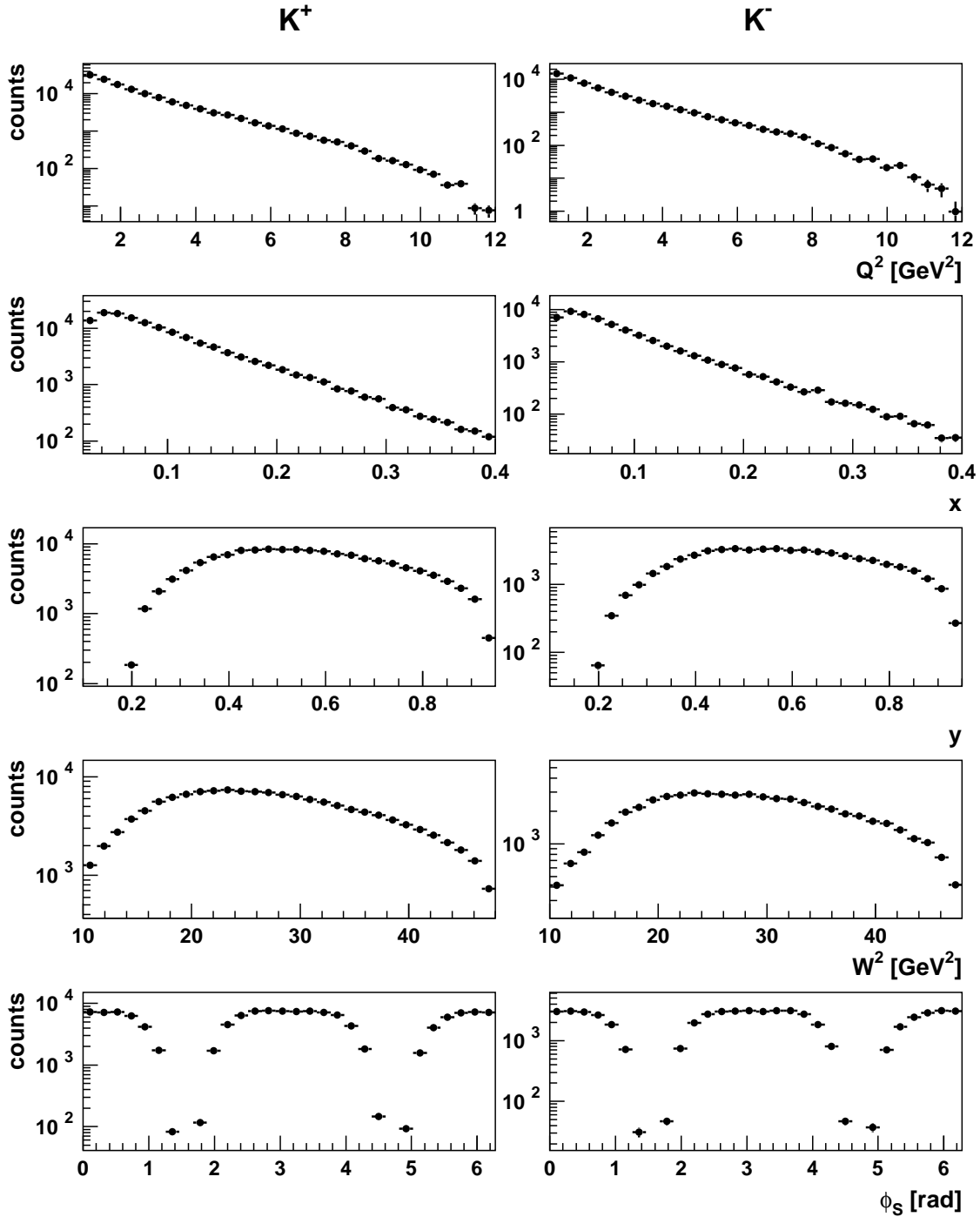
Figure 4.12.: Hadron counts as a function of the scaling variables Q^2, x, y and W^2 and the azimuthal angle ϕ_S for the semi-inclusive electro-production of K^+ (left panel) and K^- (right panel) in deep-inelastic scattering of positrons and electrons off a transversely nuclear-polarised hydrogen target. The small gaps at $1.40\,\mathrm{rad} < \phi_S < 1.74\,\mathrm{rad}$ and $4.54\,\mathrm{rad} < \phi_S < 4.88\,\mathrm{rad}$ correspond to the limited acceptance of the HERMES spectrometer close the beam pipe.
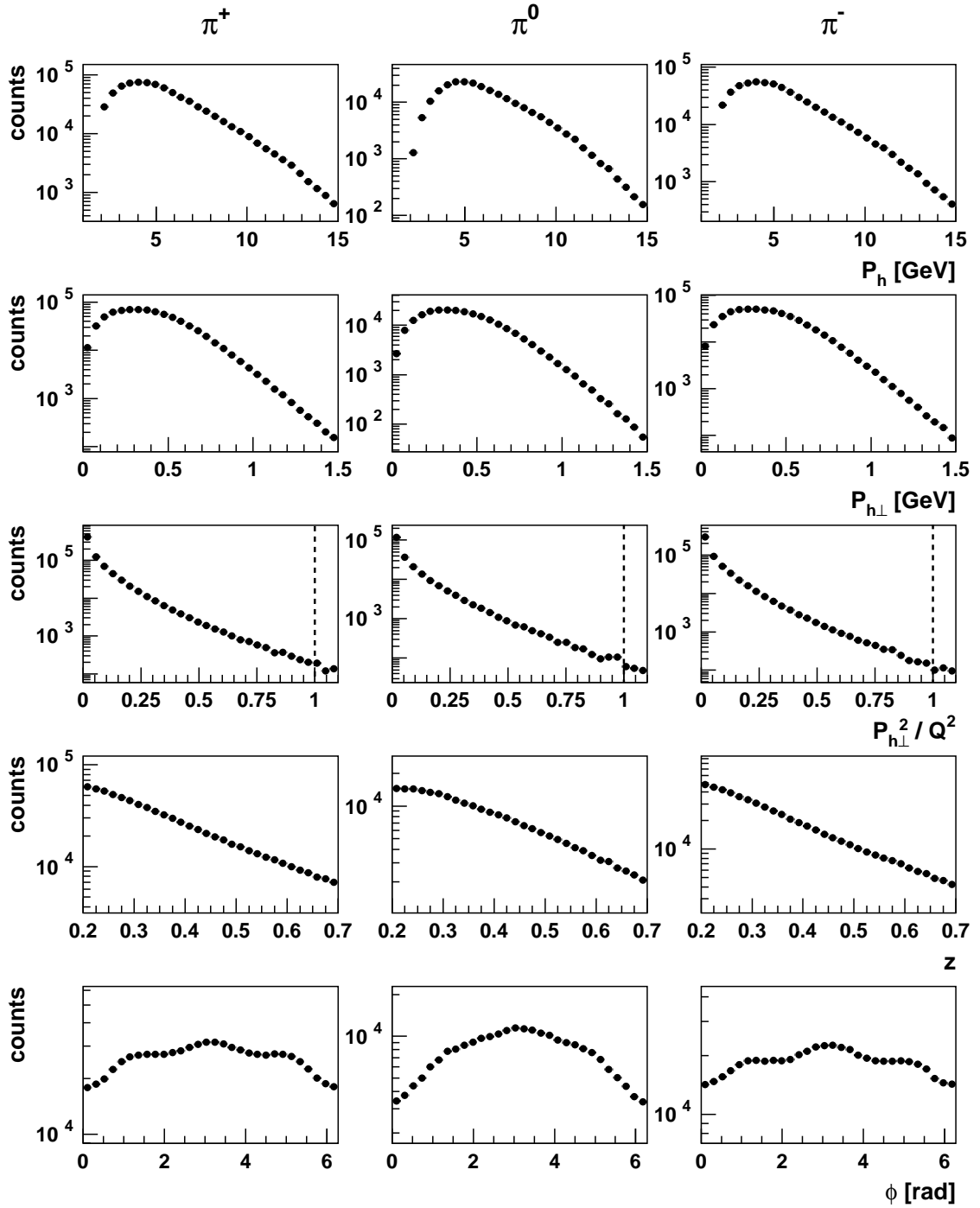
Figure 4.13.: Hadron counts as a function of the momentum $|\mathbf{P}_h|$, the transverse hadron momentum $|\mathbf{P}_{h\perp}|$, the ratio $|\mathbf{P}_{h\perp}|^2/Q^2$ and the fractional hadron energy z and the azimuthal angle ϕ for the semi-inclusive electro-production of π^+ (left panel), π^0 (central panel) and π^- (right panel) in deep-inelastic scattering of positrons and electrons off a transversely nuclear-polarised hydrogen target.
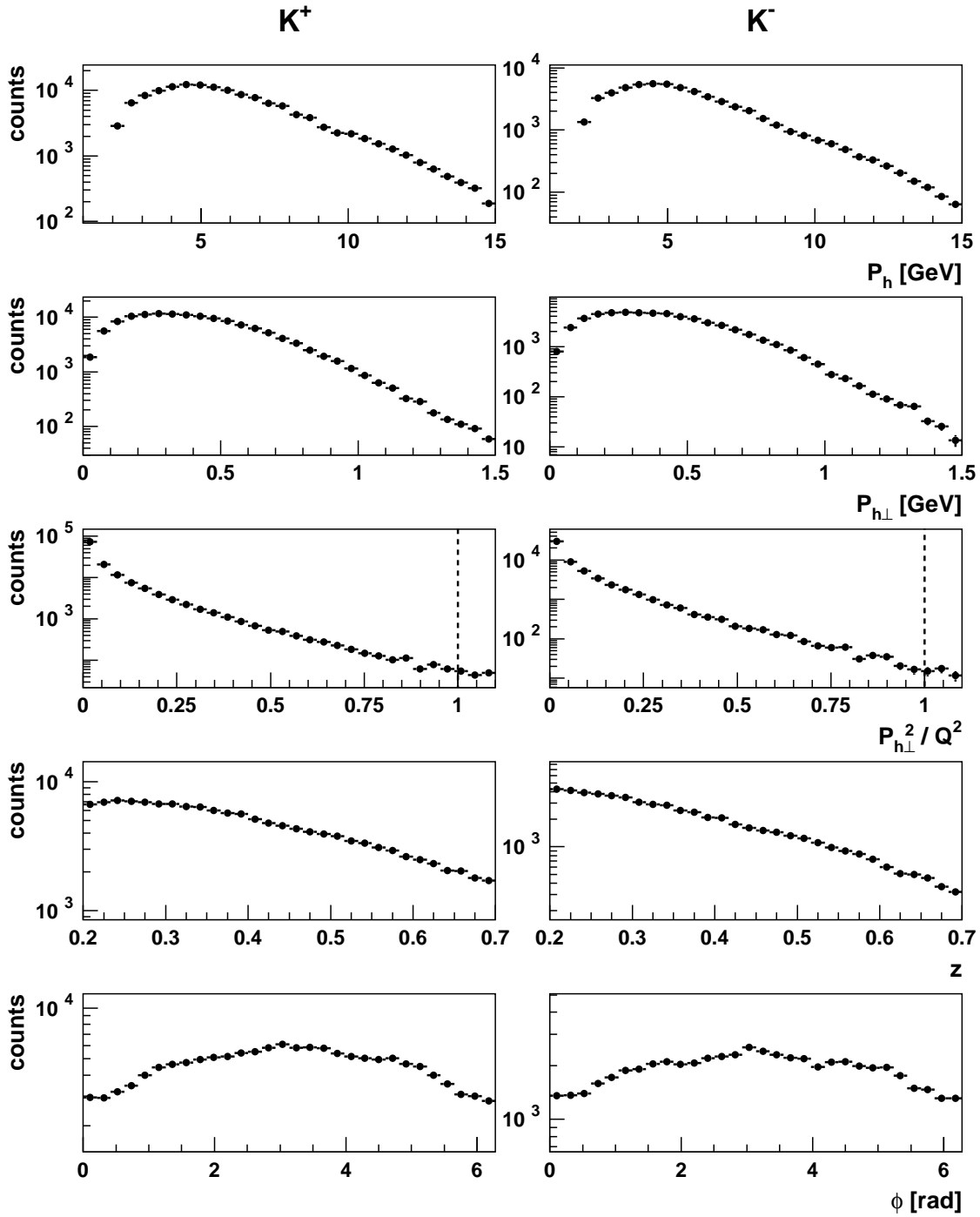
Figure 4.14.: Hadron counts as a function of the momentum $|\mathbf{P}_h|$, the transverse hadron momentum $|\mathbf{P}_{h\perp}|$, the ratio $|\mathbf{P}_{h\perp}|^2/Q^2$ and the fractional hadron energy z and the azimuthal angle ϕ for the semi-inclusive electro-production of K^+ (left panel) and K^- (right panel) in deep-inelastic scattering of positrons and electrons off a transversely nuclear-polarised hydrogen target.

Chapter 4

4.2. The extraction of SSA amplitudes

The semi-inclusive measurement of the deep-inelastic scattering process on a transversely polarised proton target is limited to the kinematic region where the cross section can be factorised in terms of transverse-momentum-dependent distribution and fragmentation functions. As the HERMES experiment was designed for measurements of asymmetries in contrast to absolute cross sections, transverse single-spin asymmetries are studied:

$$A_{\mathrm{U}\perp}^h = \frac{\sigma_{\mathrm{U}\Uparrow}^h - \sigma_{\mathrm{U}\Downarrow}^h}{\sigma_{\mathrm{U}\Uparrow}^h + \sigma_{\mathrm{U}\Downarrow}^h}. \tag{4.20}$$

The cross section $\sigma_{\mathrm{U}\Uparrow(\Downarrow)}^h$ is related to the spin-independent cross-section $\sigma_{\mathrm{UU}}^h = \frac{1}{2}(\sigma_{\mathrm{U}\Uparrow}^h + \sigma_{\mathrm{U}\Downarrow}^h)$ and the transverse single-spin asymmetries $A_{\mathrm{U}\perp}^h$ via:

$$\sigma_{\mathrm{U}\Uparrow}^h = \sigma_{\mathrm{UU}}^h (1 + A_{\mathrm{U}\perp}^h), \tag{4.21}$$
$$\sigma_{\mathrm{U}\Downarrow}^h = \sigma_{\mathrm{UU}}^h (1 - A_{\mathrm{U}\perp}^h). \tag{4.22}$$

Using the relation $\phi_S' = \phi_S + \pi$ between the azimuthal angle of the target spin axis defined for target spin orientation "$\Downarrow$" (ϕ_S') and target spin orientation "$\Uparrow$" (ϕ_S), the transverse single-spin asymmetries are given by the ratio of the spin-dependent and the spin-independent contribution to the cross section:

$$A_{\mathrm{U}\perp}^h = \frac{\sigma_{\mathrm{U}\perp}^h}{\sigma_{\mathrm{UU}}^h}. \tag{4.23}$$

Signals for the transverse-momentum-dependent distribution and fragmentation functions are extracted from the measured transverse single-spin asymmetries using a maximum likelihood fit to their distinctive signatures in the azimuthal angles ϕ and ϕ_S. The resulting SSA amplitudes, presented in the following figures 4.17 – 4.18, will be further examined in the subsequent chapters and in detail interpreted in chapter 6. In this chapter, the focus is put on the description of the measurement of the SSA amplitudes and particular in this section on the Fourier analysis.

4.2.1. The reconstruction of transverse single-spin asymmetries

The transverse single-spin asymmetries $A_{\mathrm{U}\perp}^h$ for some hadron type h are not reconstructed from a cross-section measurement but determined from the total numbers of hadrons $N_{\Uparrow(\Downarrow)}^h$ per target spin orientation. During data taking the hadron counts were detected in a certain kinematic region (ϕ, ϕ_S)[1]. The observed number of hadrons, as listed in table 4.6, is limited by the cross section $\sigma_{\mathrm{U}\Uparrow(\Downarrow)}^h$ and the luminosity $L_{\Uparrow(\Downarrow)}(t)$ of the measurement and affected by the spectrometer acceptance, represented by the acceptance function $\Omega(t, \phi, \phi_S)$, and the detection efficiency $\varepsilon(t, \phi, \phi_S)$ of the HERMES experiment. Expressing the cross section in terms of the spin-independent cross section $\sigma_{\mathrm{UU}}^h(\phi, \phi_S)$ and the transverse single-spin asymmetries $A_{\mathrm{U}\perp}^h(\phi, \phi_S)$, the total number of detected hadrons is given according to:

$$N_{\Uparrow}^h(\phi, \phi_S) = \int \sigma_{\mathrm{UU}}^h(\phi)\,\Omega(t, \phi, \phi_S)\,\varepsilon(t, \phi, \phi_S)\,L_{\Uparrow}(t)\left(1 + |S_\perp(t)|\,A_{\mathrm{U}\perp}^h(\phi, \phi_S)\right) dt, \tag{4.24}$$

$$N_{\Downarrow}^h(\phi, \phi_S) = \int \sigma_{\mathrm{UU}}^h(\phi)\,\Omega(t, \phi, \phi_S)\,\varepsilon(t, \phi, \phi_S)\,L_{\Downarrow}(t)\left(1 - |S_\perp(t)|\,A_{\mathrm{U}\perp}^h(\phi, \phi_S)\right) dt, \tag{4.25}$$

---

[1]Without loss of generality, only the dependence on the azimuthal angles ϕ and ϕ_S is explicitly stated instead of writing out the full kinematic dependence on the kinematic variables x, Q^2, z, $|\mathbf{P}_{h\perp}|$, ϕ and ϕ_S.

where $S_\perp(t)$ denotes the degree of the target polarisation. The detection efficiency $\varepsilon(t,\phi,\phi_S)$ is determined by the reconstruction efficiency $\varepsilon_r(t,\phi,\phi_S)$, which might vary over the spectrometer acceptance, and the efficiency of the data acquisition system $\varepsilon_D(t)$, which is independent of the kinematics of the scattering process. Whereas the efficiency of the data acquisition system could change on very short time scales, the reconstruction efficiency and the acceptance function are assumed to be time-independent as the setup of the HERMES experiment is left unchanged during various data taking periods and the detector performance was very stable:

$$N_\Uparrow^h(\phi,\phi_S) = \sigma_{UU}^h(\phi)\,\Omega(\phi,\phi_S)\,\varepsilon_r(\phi,\phi_S)\int \varepsilon_D(t)\,L_\Uparrow(t)\left(1+|S_\perp(t)|\,A_{U\perp}^h(\phi,\phi_S)\right)dt, \qquad (4.26)$$

$$N_\Downarrow^h(\phi,\phi_S) = \sigma_{UU}^h(\phi)\,\Omega(\phi,\phi_S)\,\varepsilon_r(\phi,\phi_S)\int \varepsilon_D(t)\,L_\Downarrow(t)\left(1-|S_\perp(t)|\,A_{U\perp}^h(\phi,\phi_S)\right)dt. \qquad (4.27)$$

When defining the dead-time corrected luminosities $L_{\Uparrow(\Downarrow)}$ as the sum over data taking periods where fluctuations in the degree of the target polarisation and the data acquisition system can be neglected:

$$L_{\Uparrow(\Downarrow)} = \sum_{t_i}\int_{t_i}^{t_{i+1}} \varepsilon_D(\tau)\,L_{\Uparrow(\Downarrow)}(\tau)\,d\tau, \qquad (4.28)$$

the total number of hadrons can be written as:

$$N_\Uparrow^h(\phi,\phi_S) = \sigma_{UU}^h(\phi)\,\Omega(\phi,\phi_S)\,\varepsilon_r(\phi,\phi_S)L_\Uparrow\left(1+|S_\perp|\,A_{U\perp}^h(\phi,\phi_S)\right), \qquad (4.29)$$

$$N_\Downarrow^h(\phi,\phi_S) = \sigma_{UU}^h(\phi)\,\Omega(\phi,\phi_S)\,\varepsilon_r(\phi,\phi_S)L_\Downarrow\left(1-|S_\perp|\,A_{U\perp}^h(\phi,\phi_S)\right). \qquad (4.30)$$

In the calculation of the transverse single-spin asymmetries with the average magnitude of the target polarisation degree $|S_\perp|$:

$$A_{U\perp}^h(\phi,\phi_S) = \frac{1}{|S_\perp|}\frac{L_\Downarrow N_\Uparrow^h(\phi,\phi_S) - L_\Uparrow N_\Downarrow^h(\phi,\phi_S)}{L_\Downarrow N_\Uparrow^h(\phi,\phi_S) + L_\Uparrow N_\Downarrow^h(\phi,\phi_S)}, \qquad (4.31)$$

the spin-independent cross-section $\sigma_{UU}^h(\phi,\phi_S)$, the acceptance function $\Omega(\phi,\phi_S)$ and the reconstruction efficiency $\varepsilon_r(\phi,\phi_S)$ drop out. The corresponding statistical uncertainty is obtained from the standard deviation $\delta N_{\Uparrow(\Downarrow)}^h = \sqrt{N_\Uparrow^h(\phi,\phi_S)}$ of the observed hadron counts via Gaussian error propagation:

$$\delta A_{U\perp}^h(\phi,\phi_S) = \frac{1}{|S_\perp|}\frac{2L_\Uparrow L_\Downarrow\sqrt{N_\Uparrow^h(\phi,\phi_S)N_\Downarrow^h(\phi,\phi_S)\left(N_\Uparrow^h(\phi,\phi_S)+N_\Downarrow^h(\phi,\phi_S)\right)}}{\left(L_\Downarrow N_\Uparrow^h(\phi,\phi_S)+L_\Uparrow N_\Downarrow^h(\phi,\phi_S)\right)^2}. \qquad (4.32)$$

In the first preliminary analyses of the Collins and Sivers mechanism [HERMES05c, DE05], the transverse single-spin asymmetries $A_{U\perp}^h$ were evaluated in a $\phi \times \phi_S$ binning as illustrated in the left panel of figure 4.15. The amplitudes for the Collins and Sivers mechanism were simultaneously extracted in a two-dimensional least-squares fit to the $A_{U\perp}^h(\phi,\phi_S)$ to avoid cross-contamination. For a better statistical description of the data and an improved estimate of the transverse single-spin asymmetries, the reconstruction method was changed to a maximum likelihood fit based Fourier decomposition unbinned in ϕ and ϕ_S.
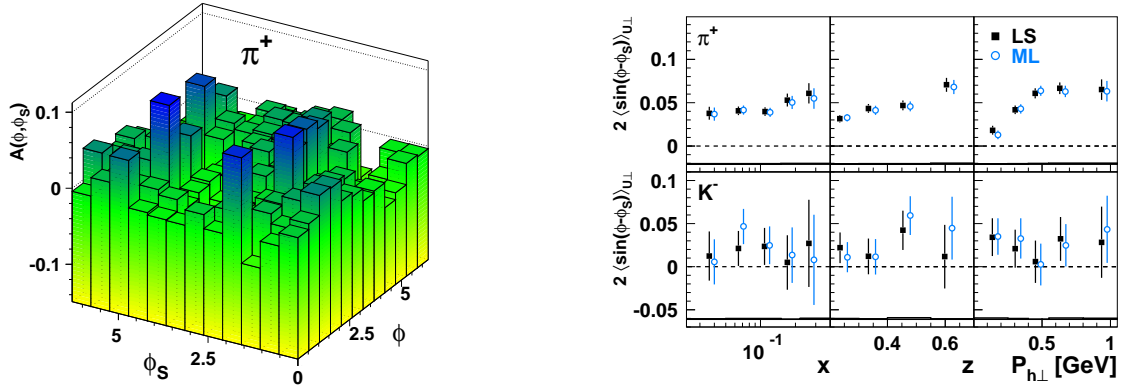
Figure 4.15.: The least-squares fit based Fourier decomposition: In the left panel the binning of the measured transverse single-spin asymmetries $A_{\mathrm{U}\perp}^{\pi^+}(\phi,\phi_S)$ in 12×12 equidistant $\phi\times\phi_S$ bins is illustrated for a sample of positively charged π-mesons selected in some kinematic bin. Using singular value decomposition [PTVF92] the SSA amplitudes are analytically determined in a two-dimensional least-squares fit of the 144 transverse single-spin asymmetries to the $\sin(\phi-\phi_S)$, $\sin(\phi+\phi_S)$, $\sin(3\phi-\phi_S)$, $\sin(\phi_S)$ and $\sin(2\phi-\phi_S)$ modulations in the cross section [BDE$^+$06]. In the right panel, the Sivers SSA amplitudes for positively charged π-mesons and negatively charged K-mesons are compared between the least-squares fit (black closed symbols) based extraction and the maximum likelihood fit based extraction (blue open symbols), where no binning in ϕ and ϕ_S has to be applied. The grey error band represents the systematic uncertainty arising due to the $\phi\times\phi_S$ binning in least-squares based extraction method [BDE$^+$06].

4.2.2. The maximum likelihood fit based Fourier decomposition

Whereas in the least squares fit based extraction method a binning of the data is required and thus information about every hadron event is lost, the full information about the hadron events can be regarded in the maximum likelihood fit based extraction method. When, e.g., not binning the observable(s) in ϕ and ϕ_S, acceptance effects in the azimuthal angles should cancel and the extracted Fourier components may only be affected by acceptance effects due to binning in other kinematic variables. In the extraction method on event level event weights due to, e.g., hadron identification or background corrections can easily be combined and periods with large fluctuations of the electron beam or target polarisation have not to be discarded in the event selection.

4.2.2.1. The likelihood formalism

In the likelihood formalism [Sol64, Bar04, PDG08], the distribution of each detected hadron event is described by a probability distribution P, which depends on a series of kinematic parameters, such as the full kinematic dependence of the scattering process x, Q^2, z, $\mathbf{P}_{h\perp}$, ϕ and ϕ_S, as well as on a series of to-be-extracted Fourier components, such as the SSA amplitude $2\langle\sin(\phi-\phi_S)\rangle_{\mathrm{U}\perp}^h$ of the Sivers mechanism. The joint probability distribution over all selected hadron events $N^h = N_\Uparrow^h + N_\Downarrow^h$ is defined as the likelihood:

$$\mathscr{L}(2\langle\sin(\phi-\phi_S)\rangle_{\mathrm{U}\perp}^h) = \prod_{n=1}^{N^h} P(x_n, Q_n^2, z_n, P_{h\perp,n}, \phi_n, \phi_{S,n}; 2\langle\sin(\phi-\phi_S)\rangle_{\mathrm{U}\perp}^h). \qquad (4.33)$$

The results of the maximum likelihood fit based Fourier decomposition are chosen by finding the SSA amplitudes that maximise the joint probability distribution or alternatively minimise its negative

logarithm. For the extraction of the most likely SSA amplitudes, the minimisation of the negative logarithm:

$$-\ln\left(\mathscr{L}(2\langle\sin(\phi-\phi_S)\rangle_{\mathrm{U}\perp}^h)\right)=\sum_{n=1}^{N^h}\ln\left(P(x_n,Q_n^2,z_n,P_{h\perp,n},\phi_n,\phi_{S,n};2\langle\sin(\phi-\phi_S)\rangle_{\mathrm{U}\perp}^h)\right), \quad (4.34)$$

is preferred due to the computational advantage of having a sum of small numbers instead of their product and the often analytically simple shape of the likelihood's negative logarithm at its minimum.

The approximately Gaussian distribution of the likelihood has typically a parabolic shape at the minimum of its negative logarithm. An absolute variation by 0.5 of the likelihood's negative logarithm around its minimum corresponds to a variation by 1σ. Thus, the statistical uncertainty of the SSA amplitudes can be evaluated from the series of fit parameters where the likelihood's logarithm falls by 0.5 to its minimum. The implementation of the maximum likelihood fit is based on the MIGRAD and HESSE methods of the MINUIT library [Jam94].

4.2.2.2. An example of the likelihood formalism

Without loss of generality, a measurement is considered here, where the asymmetry A^h are reconstructed from the total number of hadrons $N_{\Uparrow(\Downarrow)}^h$ as a function of the degree of the target polarisation $S_{\Uparrow(\Downarrow)}$ and the corresponding luminosity $L_{\Uparrow(\Downarrow)}$. In the simplified example, the degree of polarisation is $S_\Uparrow=+1$ for transverse target spin state "$\Uparrow$" and $S_\Downarrow=-1$ for transverse target spin state "$\Downarrow$". The unnormalised probability density function is chosen as:

$$P(S_\perp;A^h)=L_{\Uparrow(\Downarrow)}(1+S_{\Uparrow(\Downarrow)}A^h). \quad (4.35)$$

When evaluating the likelihood function:

$$\mathscr{L}(A^h)=\left(\frac{L_\Uparrow(1+A^h)}{\mathscr{N}(A^h)}\right)^{N_\Uparrow^h}\left(\frac{L_\Downarrow(1-A^h)}{\mathscr{N}(A^h)}\right)^{N_\Downarrow^h}, \quad (4.36)$$

it is required to account for the normalisation $\mathscr{N}(A^h)$ of the probability density function:

$$\mathscr{N}(A^h)=\sum_{S_\Uparrow,S_\Downarrow}L_{\Uparrow(\Downarrow)}(1+S_{\Uparrow(\Downarrow)}A^h)=L_\Uparrow(1+A^h)+L_\Downarrow(1-A^h), \quad (4.37)$$

which is determined by the normalisation factors of the not-to-be extracted parameters. The maximum of the likelihood occurs where:

$$-\frac{\partial\ln\mathscr{L}(A^h)}{\partial A^h}=-\frac{N_\Uparrow^h}{1+A^h}+\frac{N_\Downarrow^h}{1-A^h}+\frac{\left(N_\Uparrow^h+N_\Downarrow^h\right)\left(L_\Uparrow-L_\Downarrow\right)}{\left(L_\Uparrow(1+A^h)+L_\Downarrow(1-A^h)\right)}=0. \quad (4.38)$$

Assuming an approximately Gaussian likelihood about its global maximum, the variance of the transverse single-spin asymmetries can be expressed as:

$$-\frac{\partial^2\ln\mathscr{L}(A^h)}{\partial(A^h)^2}=\frac{N_\Uparrow^h}{(1+A^h)^2}+\frac{N_\Downarrow^h}{(1-A^h)^2}-\frac{\left(N_\Uparrow^h+N_\Downarrow^h\right)\left(L_\Uparrow-L_\Downarrow\right)^2}{\left(L_\Uparrow(1+A^h)+L_\Downarrow(1-A^h)\right)^2}=0. \quad (4.39)$$

The estimators for the asymmetry A^h, obtained from equation 4.38 and 4.39, are equivalent to the estimators for the transverse single-spin asymmetries $A_{\mathrm{U}\perp}^h$, given in equations 4.31 and 4.32. Thus, the transverse single-spin asymmetries, evaluated in the maximum likelihood based extraction method, are analogous to the transverse single-spin asymmetries, evaluated in the least squared based extraction method.

bin:	x-dependence:	z-dependence:	$|\mathbf{P}_{h\perp}|$-dependence:
1	]0.023; 0.045]	]0.20; 0.27]	]0.00 GeV; 0.17 GeV]
2	]0.045; 0.067]	]0.27; 0.34]	]0.17 GeV; 0.25 GeV]
3	]0.067; 0.086]	]0.34; 0.41]	]0.25 GeV; 0.33 GeV]
4	]0.086; 0.113]	]0.41; 0.49]	]0.33 GeV; 0.41 GeV]
5	]0.113; 0.160]	]0.49; 0.56]	]0.41 GeV; 0.58 GeV]
6	]0.160; 0.220]	]0.56; 0.63]	]0.58 GeV; 0.80 GeV]
7	]0.220; 0.400]	]0.63; 0.70]	]0.80 GeV; 2.00 GeV]

Table 4.7.: Definition of the binning: In the first column the number of each bin is listed; in the second, third and fourth column the corresponding limits in the kinematic variables x, z and $|\mathbf{P}_{h\perp}|$ are given. The binning was chosen to obtain approximately the same amount of statistics in every bin but slightly modified to improve the investigation of the kinematic regions $0.16 < x < 0.4$, $0.49 < z < 0.7$ and $0.41\,\text{GeV} < |\mathbf{P}_{h\perp}| < 2\,\text{GeV}$.

4.2.2.3. The choice of the probability density function

The SSA amplitudes are studied as an one-dimensional function of x, z and $|\mathbf{P}_{h\perp}|$. Thereby, the selected data is alternately binned in x, z and $|\mathbf{P}_{h\perp}|$ according to the kinematic limits given in table 4.7 but unbinned in the azimuthal angles ϕ and ϕ_S. The probability density function for the extraction of the SSA amplitudes is modelled according to the cross section for the semi-inclusive electroproduction of π-mesons and charged K-mesons on a transversely nuclear-polarised hydrogen target. From the various contributions to the differential cross section σ^h (section 2.3.2) only the transverse target spin-dependent contributions $\sigma^h_{U\perp}$ are regarded in the Fourier decomposition of $A^h_{U\perp}$. The possible influence of other cross-section contributions is studied in section 4.2.2.6.

There are five sine modulations of the cross section σ^h_{UT}, when the target is transversely polarised with respect to the virtual-photon direction: $\sin(\phi + \phi_S)$, $\sin(\phi - \phi_S)$, $\sin(3\phi - \phi_S)$, $\sin(\phi_S)$ and $\sin(2\phi - \phi_S)$. In the measurement presented the target was transversely polarised with respect to the lepton beam direction and thus an additional sixth modulation of $\sin(2\phi + \phi_S)$ arises [DS05]. All six sine modulations are included in the probability density function. Whereas statistical significant SSA amplitudes of the $\sin(\phi + \phi_S)$, $\sin(\phi - \phi_S)$ and $\sin(\phi_S)$ modulations are found (figures 4.16 and 4.17), the SSA amplitudes of the $\sin(3\phi - \phi_S)$, $\sin(2\phi - \phi_S)$ and $\sin(2\phi + \phi_S)$ modulations are consistent with zero (figures 4.17 and 4.18). A cross-contamination of the $2\langle\sin(\phi + \phi_S)\rangle^h_{U\perp}$, $2\langle\sin(\phi - \phi_S)\rangle^h_{U\perp}$ and $2\langle\sin(\phi_S)\rangle^h_{U\perp}$ amplitude is observed corroborating the simultaneous extraction to avoid cross-contamination of the the SSA amplitudes (figure 4.16).

When, e.g., investigating only the dependence on the Bjorken scaling variable x and thus integrating over the kinematic variables Q^2, z and $|\mathbf{P}_{h\perp}|$, the probability density function for the Fourier decomposition of the cross-section is defined as:

$$
\begin{aligned}
P\Big(x_n, \phi_n, &\phi_{S,n}; 2\langle\sin(\phi - \phi_S)\rangle^h_{U\perp}, 2\langle\sin(\phi + \phi_S)\rangle^h_{U\perp}, 2\langle\sin(3\phi - \phi_S)\rangle^h_{U\perp}, \\
& 2\langle\sin(\phi_S)\rangle^h_{U\perp}, 2\langle\sin(2\phi - \phi_S)\rangle^h_{U\perp}, 2\langle\sin(2\phi + \phi_S)\rangle^h_{U\perp}\Big) \\
= 1 + S_\perp\Big(&\sin(\phi - \phi_S)2\langle\sin(\phi - \phi_S)\rangle^h_{U\perp} + \sin(\phi + \phi_S)2\langle\sin(\phi + \phi_S)\rangle^h_{U\perp} + \\
& \sin(3\phi - \phi_S)2\langle\sin(3\phi - \phi_S)\rangle^h_{U\perp} + \sin(\phi_S)2\langle\sin(\phi_S)\rangle^h_{U\perp} + \\
& \sin(2\phi - \phi_S)2\langle\sin(2\phi - \phi_S)\rangle^h_{U\perp} + \sin(2\phi + \phi_S)2\langle\sin(2\phi + \phi_S)\rangle^h_{U\perp}\Big).
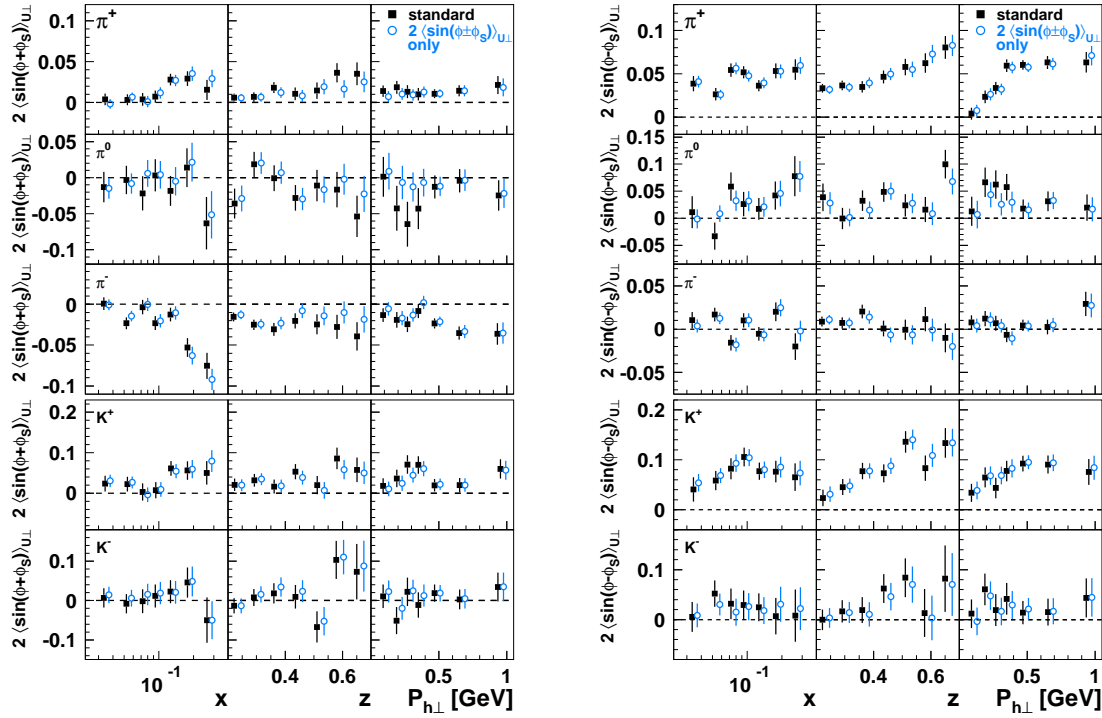\end{aligned}
\tag{4.40}
$$

Figure 4.16.: Results for the leading-twist Collins and Sivers amplitudes: Collins (left panel) and Sivers amplitudes (right panel) are extracted in a maximum likelihood fit based extraction method using a probability density function according to equation 4.40 (black closed symbols) and a modified probability density function where only the modulations of the Collins and Sivers mechanism are included (blue open symbols). A statistical correlation of the SSA amplitudes is observed; in particular the Collins and Sivers amplitudes for negatively charged pions and neutral pions are affected by the statistically significant contribution from the $2 \langle \sin(\phi_S) \rangle_{U\perp}^h$ SSA amplitude (figure 4.17).

The normalisation of the probability density function is not required [Mil06] as in the selected data the net target polarisation is found to be negligible. The normalisation integral is obtained from the joint probability density function over all selected hadron events averaged over the series of kinematic parameters and the target polarisation degree whose distribution is denoted as $\rho(S_\perp)$:

$$
\mathscr{N}\left(2\langle\sin(\phi-\phi_S)\rangle_{U\perp}^h, \ldots, 2\langle\sin(2\phi+\phi_S)\rangle_{U\perp}^h\right) =
$$
$$
\int dS_\perp dx \ldots d\phi_S\, \rho(S_\perp)\, \Omega(x,\ldots,\phi_S)\, \varepsilon(x,\ldots,\phi_S)\, \sigma_{UU}^h(x,\ldots,\mathbf{P}_{h\perp})\cdot \tag{4.41}
$$
$$
\left(1+S_\perp\left(\sin(\phi-\phi_S)2\langle\sin(\phi-\phi_S)\rangle_{U\perp}^h + \cdots + \sin(2\phi+\phi_S)2\langle\sin(2\phi+\phi_S)\rangle_{U\perp}^h\right)\right).
$$

In the probability density function the degree of target polarisation $S_\perp$ is included as a multiplicative factor. The integration over the target polarisation degree can be factorised:

$$
\mathscr{N}\left(2\langle\sin(\phi-\phi_S)\rangle_{U\perp}^h, \ldots, 2\langle\sin(2\phi+\phi_S)\rangle_{U\perp}^h\right) =
$$
$$
\int dS_\perp\, \rho(S_\perp) \int dx \ldots d\phi_S\, \Omega(x,\ldots,\phi_S)\, \varepsilon(x,\ldots,\phi_S)\, \sigma_{UU}^h(x,\ldots,\mathbf{P}_{h\perp})\cdot \tag{4.42}
$$
$$
\left(1+\frac{\int S_\perp \rho(S_\perp)\,dS_\perp}{\int \rho(S_\perp)\,dS_\perp}\left(\sin(\phi-\phi_S)2\langle\sin(\phi-\phi_S)\rangle_{U\perp}^h + \cdots\right)\right).
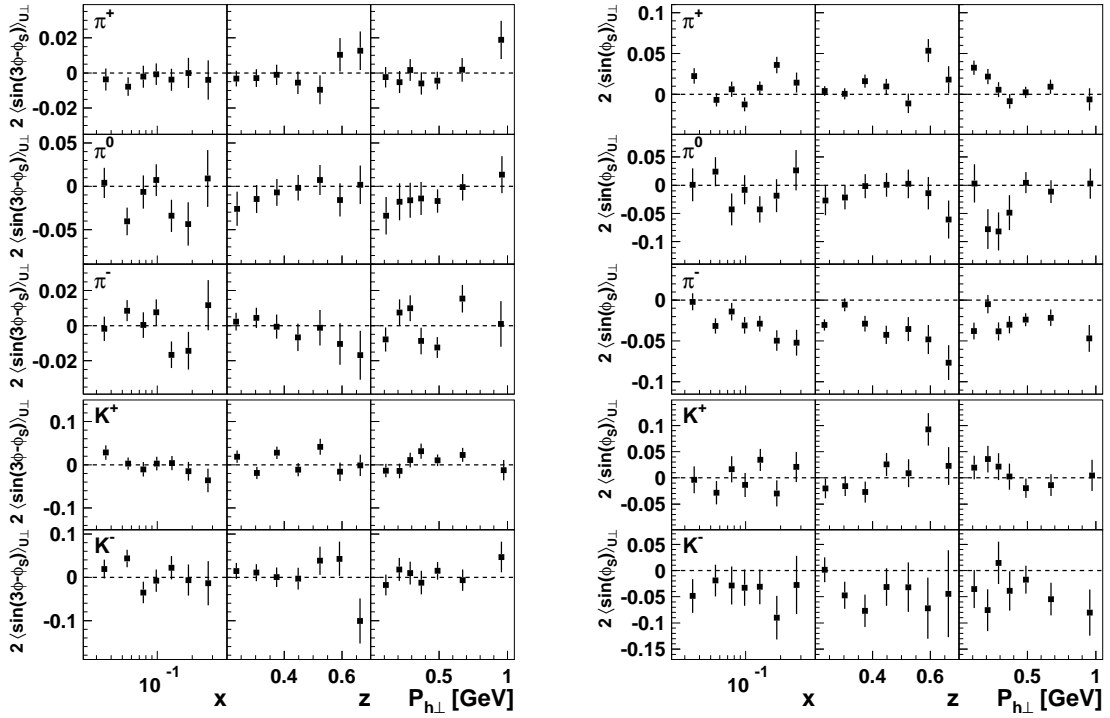$$

Figure 4.17.: Results for the leading-twist $2\langle\sin(3\phi-\phi_S)\rangle^h_{U\perp}$ amplitude (left panel) and the subleading-twist $2\langle\sin(\phi_S)\rangle^h_{U\perp}$ amplitude (right panel).

When the integrated target polarisation degree is zero, the normalisation integral is independent from the to-be-extracted SSA amplitudes and thus cannot influence the shape of the likelihood dependence on the SSA amplitudes. Therefore, in this case the normalisation of the probability density function can be neglected for the Fourier decomposition of the transverse single-spin asymmetries measurement.

4.2.2.4. The weighting of the probability density function

As described in section 4.1.5, pion weights, kaon weights and proton weights are assigned to each selected hadron track to account for the efficiency of the RICH detector and the contamination of the pion, kaon and proton identification. When the charge of the scattered lepton does not correspond to the charge of the incoming lepton beam, the weights are multiplied by -1 in order to subtract the background arising from the pair production process. In the likelihood formalism, each selected hadron event is counted according to the weight w_n:

$$-\ln\left(\mathscr{L}\left(2\langle\sin(\phi-\phi_S)\rangle^h_{U\perp},\ldots,2\langle\sin(2\phi+\phi_S)\rangle^h_{U\perp}\right)\right) =$$
$$\sum_{n=0}^{N^h} w_n \ln\left(P\left(x_n,\phi_n,\phi_{S,n};2\langle\sin(\phi-\phi_S)\rangle^h_{U\perp},\ldots,2\langle\sin(2\phi+\phi_S)\rangle^h_{U\perp}\right)\right). \tag{4.43}$$

As the sum over all weights $\sum_{n=0}^{N^h} w_n \neq N^h$ does not coincide with the number of detected hadrons N^h, the statistical uncertainties of the extracted SSA amplitudes have to be corrected for the weighting. According to the correction by Solmitz [Sol64], the covariance matrix C, obtained in the maximum
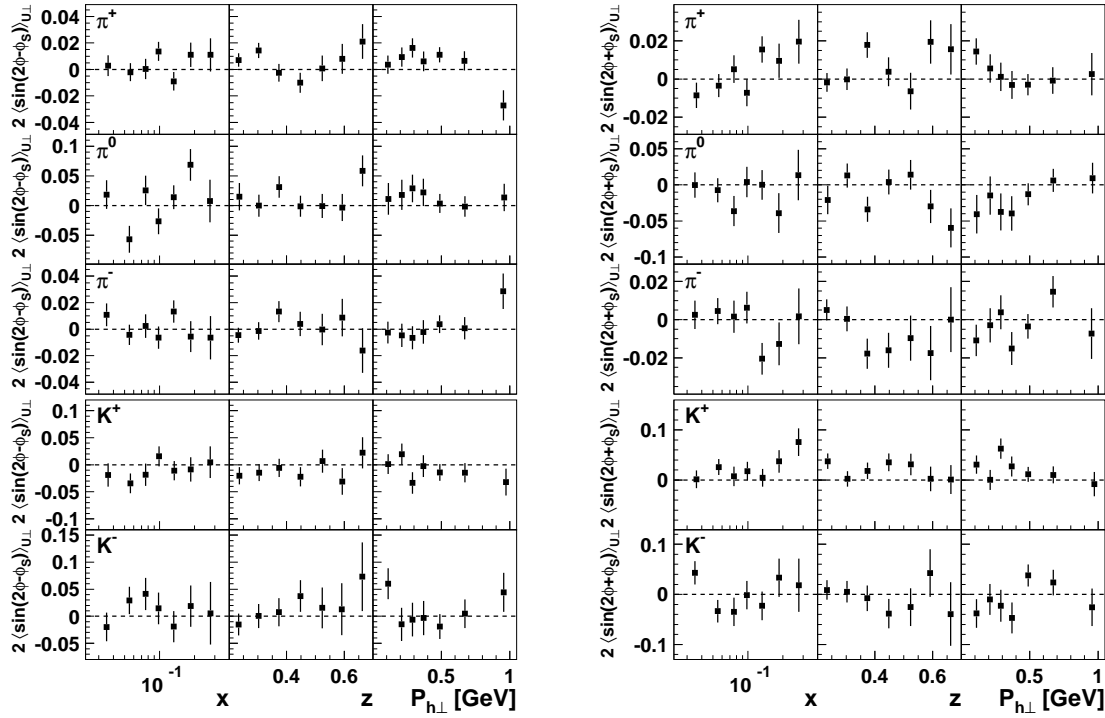
Figure 4.18.: Results for the subleading-twist $2\langle\sin(2\phi-\phi_S)\rangle^h_{U\perp}$ amplitude (left panel) and the subleading-twist $2\langle\sin(2\phi+\phi_S)\rangle^h_{U\perp}$ amplitude (right panel).

likelihood fit based extracted method, is corrected by the covariance matrix K

$$C' = CK^{-1}C, \tag{4.44}$$

which is obtained in a maximum likelihood fit based extraction method when weighting the events with w_n^2 instead of w_n. The statistical uncertainties are evaluated from the corrected covariance matrix C' defined in equation 4.44.

4.2.2.5. The transverse single-spin asymmetries for neutral pions

The invariant mass spectrum of photon pairs detected in the electro-magnetic calorimeter can be described by a Gaussian distribution for the neutral-pion peak and a Weibull distribution for the combinatorial background (section 4.1.6). Neutral-pion events are selected in the signal range of the invariant mass spectrum defined as:

$$M_{\gamma\gamma'} \in [0.10\,\text{GeV}; 0.17\,\text{GeV}], \tag{4.45}$$

corresponding to a deviation from the neutral pions mass by the tripled calorimeter resolution of $0.1137 \pm 0.0004\,\text{GeV}$.

Given the average ratio of neutral pion events and background events in the signal range of 2.977 ± 0.384, the measurement of transverse single-spin asymmetries of neutral pions has to be corrected for the combinatorial background contribution. Considering the dependence of the combinatorial background contribution on the Bjorken scaling variable x, the fractional hadron energy z and the transverse hadron momentum $\mathbf{P}_{h\perp}$ (figure 4.19), the combinatorial background contribution
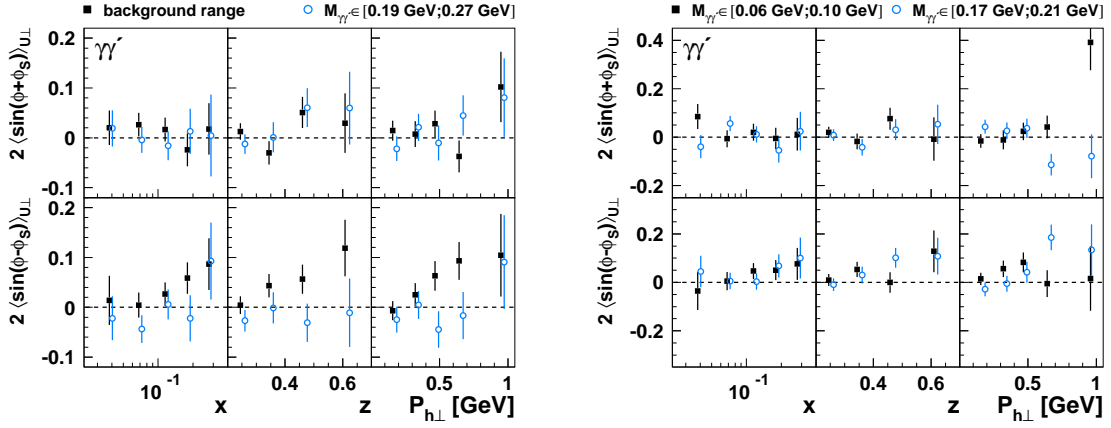
55

Figure 4.19.: The transverse single-spin asymmetries of the combinatorial background contribution: The influence of the invariant mass ranges is studied for the background range $M_{\gamma\gamma'} \in [0.06\,\text{GeV}; 0.10\,\text{GeV}] \cap M_{\gamma\gamma'} \in [0.17\,\text{GeV}; 0.21\,\text{GeV}]$ and the invariant mass range $M_{\gamma\gamma'} \in [0.19\,\text{GeV}; 0.27\,\text{GeV}]$. Whereas the Collins amplitudes (left, upper panel) of the photon pairs $\gamma\gamma'$ appear to be independent from the selected invariant ranges, a kinematic dependence is observed for the Sivers SSA amplitudes (left, lower panel). Consistent Collins (right, upper panel) and Sivers amplitudes (right, lower panel) are extracted from the transverse single-spin asymmetries $A_{U\perp}^{\gamma\gamma'}$ evaluated separately in the invariant mass ranges $M_{\gamma\gamma'} \in [0.06\,\text{GeV}; 0.10\,\text{GeV}]$ and $M_{\gamma\gamma'} \in [0.17\,\text{GeV}; 0.21\,\text{GeV}]$.

is estimated from ranges in the invariant mass close to the signal range:

$$M_{\gamma\gamma'} \in [0.06\,\text{GeV}; 0.10\,\text{GeV}] \cap M_{\gamma\gamma'} \in [0.17\,\text{GeV}; 0.21\,\text{GeV}]. \tag{4.46}$$

The width of the side bands are adjusted to have the same number of background events as in the signal range according to the description of the combinatorial background by the Weibull distribution. As the SSA amplitudes extracted from the side bands $M_{\gamma\gamma'} \in [0.06\,\text{GeV}; 0.10\,\text{GeV}]$ and $M_{\gamma\gamma'} \in [0.17\,\text{GeV}; 0.21\,\text{GeV}]$ are consistent (figure 4.19), the transverse single-spin asymmetries in the sidebands are assumed to reveal the transverse single-spin asymmetries of the combinatorial background. The transverse single-spin asymmetries $A_{U\perp}^{\pi^0}$ of neutral pions are simultaneously evaluated from photon pairs selected in the signal range and in the side bands. Thereby, the events selected in side bands gain an additional event weight of -1 to be subtracted as the combinatorial background contribution.

4.2.2.6. The influence of other cross-section contributions

In addition to $\sigma_{U\perp}^h$, there are other contributions to the differential cross section σ^h that could influence the extraction of the six amplitudes from the transverse single-spin asymmetries $A_{U\perp}^h$ due to a possible statistical correlation among the SSA amplitudes or the azimuthal modulations of the spin-independent cross-section contributions present in the denominator of the asymmetries:

❑ The spin-independent cross-section contribution σ_{UU}^h: The $2\langle\cos(\phi)\rangle_{UU}^h$ and $2\langle\cos(2\phi)\rangle_{UU}^h$ amplitudes arising from Cahn and Boer-Mulders effects or kinematic smearing effects can affect the maximum likelihood based extraction as they are related to an additive component of σ_{UU}^h, whereas $2\langle\cos(\phi)\rangle_{UU}^h$ and $2\langle\cos(2\phi)\rangle_{UU}^h$ amplitudes caused by acceptance effects can
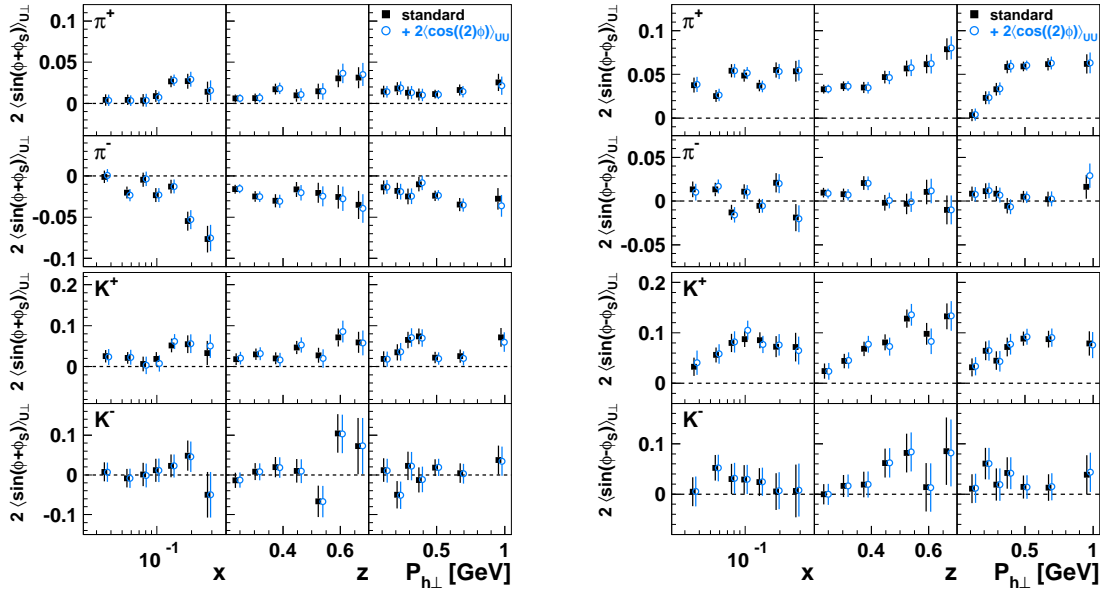
Figure 4.20.: Influence of $2\langle\cos(\phi)\rangle_{UU}^{h}$ and $2\langle\cos(2\phi)\rangle_{UU}^{h}$ amplitudes on the extraction: Collins (left panel) and Sivers amplitudes (right panel) are extracted from recorded hadron events including (blue open symbols) and not including (black closed symbols) parameterisations of the $\cos(\phi)$ and $\cos(2\phi)$ modulations in the probability density function.

be regarded as a multiplicative component and thus cannot affect the extraction. The possible influence of the additive component is investigated in two studies:

In the reconstruction of $A_{U\perp}^{h}$ from recorded data, the $\cos(\phi)$ and $\cos(2\phi)$ modulations are included in the probability density function. The $2\langle\cos(\phi)\rangle_{UU}^{h}$ and $2\langle\cos(2\phi)\rangle_{UU}^{h}$ amplitudes are not extracted but estimated for each hadron event using a parametrisation of preliminary HERMES results [GL09] corrected for acceptance and smearing effects. Except for the Collins amplitudes of charged pions in the last three z-bins (figure 4.20), no influence on the SSA amplitudes is found (a statistical anti-correlation is observed between the SSA amplitudes of K^{+}). However, the agreement between the estimated $2\langle\cos(\phi)\rangle_{UU}^{h}$ and $2\langle\cos(2\phi)\rangle_{UU}^{h}$ amplitudes and the amplitudes affected by smearing effects in the recorded data is unknown.

Thus, the parametrisation in addition to a model of the transverse single-spin asymmetries is used to simulate the azimuthal modulations of the cross-sections contributions σ_{UU}^{h} and σ_{UT}^{h}. In this Monte Carlo simulation, the $2\langle\cos(\phi)\rangle_{UU}^{h}$ and $2\langle\cos(2\phi)\rangle_{UU}^{h}$ amplitudes are known but this study is hampered by the good but not perfect description of the experiment. Nevertheless, the same influence is observed (figure 4.21) as in the study on recorded data (figure 4.20).

Given the negligible effects of the inclusion of the $\cos(\phi)$ and $\cos(2\phi)$ modulations in the probability density function, the azimuthal modulations of σ_{UU}^{h} are not regarded in the Fourier decomposition.

❑ The longitudinal target-spin-dependent contribution σ_{UL}^{h}: Due to the small target-spin component longitudinal to the virtual-photon direction, the extracted SSA amplitudes might be influenced by the longitudinal target spin-dependent contribution σ_{UL}^{h} to the cross section. This influence is regarded as contribution to the systematic uncertainty (section 5.1).

❑ The contributions σ_{LU}^{h}, σ_{LL}^{h} and σ_{LT}^{h}: During the data taking period 2002–2005, the beam
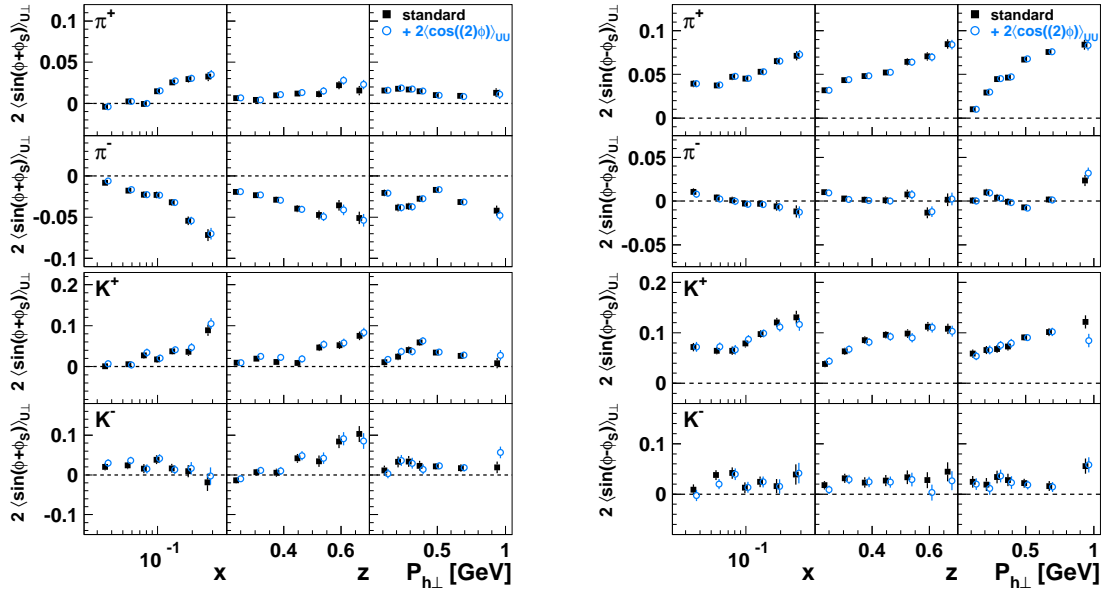
Figure 4.21.: Influence of $2\langle\cos(\phi)\rangle^h_{UU}$ and $2\langle\cos(2\phi)\rangle^h_{UU}$ amplitudes on the extraction: Collins (left panel) and Sivers amplitudes (right panel) are extracted from simulated hadron events including (blue open symbols) and not including (black closed symbols) parameterisations of the $\cos(\phi)$ and $\cos(2\phi)$ modulations in the probability density function.

helicity λ_e was flipped every few months, resulting in a net beam polarisation of $\langle\lambda_e\rangle = -0.020\pm0.001$. As a consequence, the electron beam can be considered as unpolarised. In addition, no influence on the azimuthal amplitudes of the cross-section contribution σ^h_{UT} is found, when including the double-spin asymmetry amplitudes $2\langle\cos(\phi-\phi_S)\rangle^h_{L\perp}$, $2\langle\cos(\phi_S)\rangle^h_{L\perp}$ and $2\langle\cos(2\phi-\phi_S)\rangle^h_{L\perp}$ depending not only on the target spin orientation but also on the beam helicity in the probability density function (figure 4.22). The extracted $2\langle\cos(\phi-\phi_S)\rangle^h_{L\perp}$, $2\langle\cos(\phi_S)\rangle^h_{L\perp}$ and $2\langle\cos(2\phi-\phi_S)\rangle^h_{L\perp}$ amplitudes of the double-spin asymmetries $A^h_{L\perp}$ are shown in figures 4.22 and 4.23.

Also when extracting SSA amplitudes solely for beam helicity eigen state $+1$ or -1, consistent SSA amplitudes are obtained [CDPS07a]. Thus, the contributions σ^h_{LU}, σ^h_{LL} and σ^h_{LT} were omitted in the probability density function.
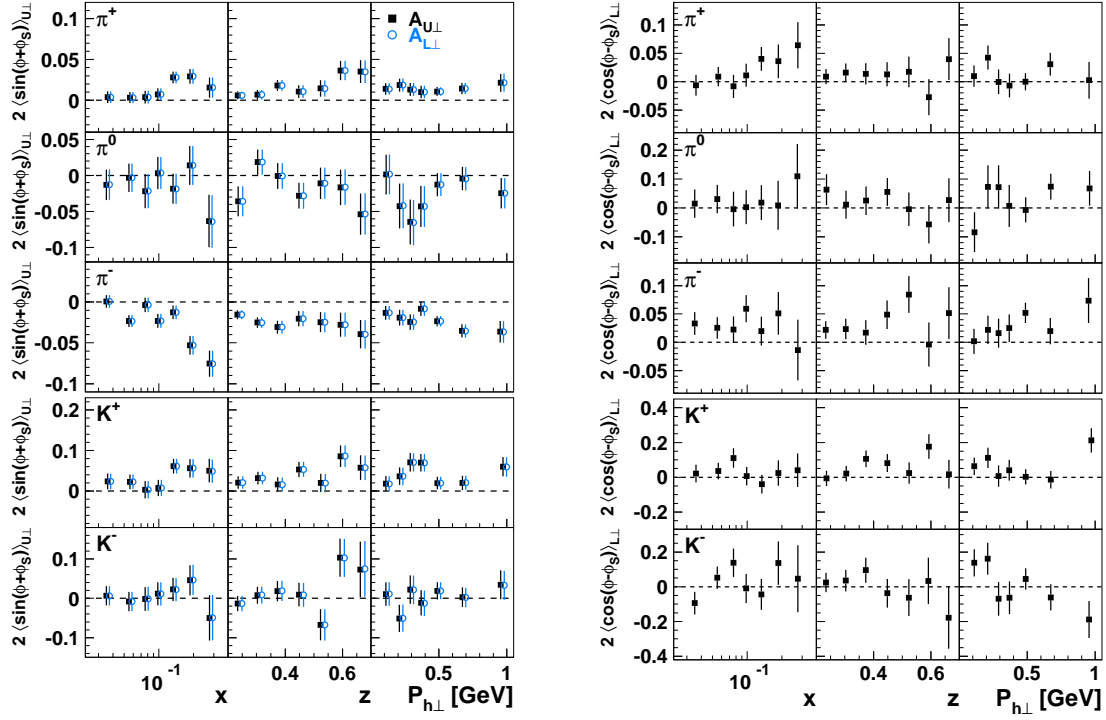
Figure 4.22.: Influence of the longitudinal beam polarisation: In the left panel, Collins amplitudes are extracted using the probability density function according to equation 4.40 (black, closed symbols) and a probability density function where in addition to the terms in equation 4.40 also the longitudinal beam-polarisation-dependent term $S_\perp \lambda_e \left(2 \left\langle \cos \left(\phi - \phi_S \right) \right\rangle_{L\perp}^h + 2 \left\langle \cos \left(\phi_S \right) \right\rangle_{L\perp}^h + 2 \left\langle \cos \left(2\phi - \phi_S \right) \right\rangle_{L\perp}^h \right)$ is included. In the right panel, the results for the leading-twist $2 \left\langle \cos \left(\phi - \phi_S \right) \right\rangle_{L\perp}^h$ double-spin asymmetry amplitudes are shown as a function of the kinematic variables x, z and $|\mathbf{P}_{h\perp}|$.
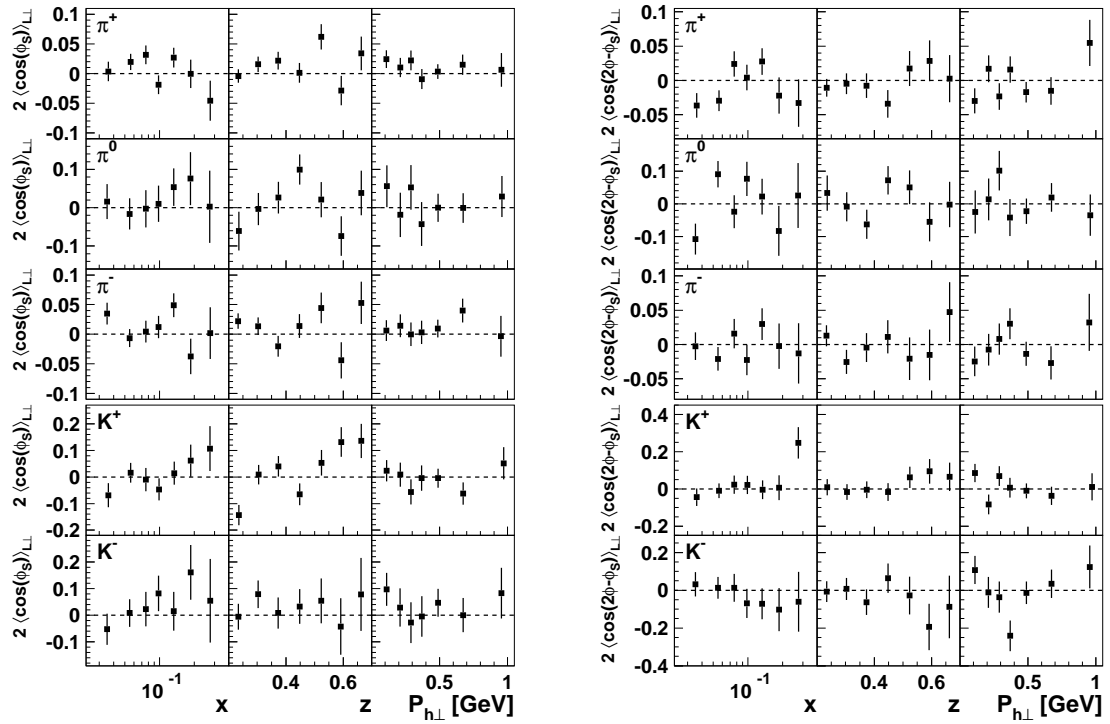
Figure 4.23.: Results for the subleading-twist $2\langle\cos(\phi_S)\rangle^h_{L\perp}$ and $2\langle\cos(2\phi-\phi_S)\rangle^h_{L\perp}$ double-spin asymmetry amplitudes as a function of the kinematic variables x, z and $|\mathbf{P}_{h\perp}|$.

5. The analysis of the measured SSA

In chapter 4 the measurement of the transverse single-spin asymmetries is described. Before interpreting the extracted SSA amplitudes in chapter 6, the analysis is supplemented by an estimate of the systematic uncertainties (section 5.1), an consistency check of the SSA amplitudes (section 5.2) and an investigation of possible higher twist contributions (section 5.3. In addition, the difference in the Collins and Sivers amplitudes for positively charged pions and kaons is examined (section 5.4).

5.1. The estimate of the systematic uncertainty

Systematic uncertainties on the SSA amplitudes represent the uncertainty in the estimate of systematic effects on the measurement of transverse single-spin asymmetries arising from:

❑ the accuracy of the target polarisation measurement,

❑ acceptance effects,

❑ kinematic smearing effects,

❑ the hadron identification using the RICH detector and

❑ the non-vanishing longitudinal target spin-dependent cross-section contribution σ_{UL}^h.

Whereas the accuracy of the target polarisation measurement is taken into account as a scale uncertainty on the extracted SSA amplitudes, the systematic uncertainties due to acceptance effects, kinematic smearing effects and the hadron identification are estimated simultaneously in a Monte Carlo simulation using an asymmetry model constrained from data. In addition, a systematic uncertainty due to the longitudinal target-spin component is assigned in the measurement of transverse single-spin asymmetries.

5.1.1. The contributions to the systematic uncertainty

Measurements (in particle physics) are hampered by acceptance effects caused by limitations in the geometric acceptance of the detector(s), complicated final states or kinematic requirements in the event selection. In the reconstruction of transverse single-spin asymmetries (section 4.2.1), effects due to the finite spectrometer acceptance Ω and the reconstruction efficiency ε_r, which might vary over the spectrometer acceptance, cancel only when not binning the selected hadron events. The SSA amplitudes extracted in a maximum likelihood fit reconstruction method unbinned only in the azimuthal angles ϕ and ϕ_S are affected by acceptance effects due to the binning in the kinematic variables x, z and $\mathbf{P}_{h\perp}$, i.e. integrating the numerator and denominator of the transverse single-spin asymmetries $A_{U\perp}^h$ over finite ranges in those kinematic variables (below abbreviated as ξ):

$$
\begin{aligned}
A_{U\perp}^h(\xi,\phi,\phi_S) &= \frac{\sigma_{UT}^h(\xi,\phi,\phi_S)\,\Omega(\xi,\phi,\phi_S)\,\varepsilon_r(\xi,\phi,\phi_S)}{\sigma_{UU}^h(\xi,\phi,\phi_S)\,\Omega(\xi,\phi,\phi_S)\,\varepsilon_r(\xi,\phi,\phi_S)} \\
&\neq \frac{\int d\xi\,\sigma_{UT}^h(\xi,\phi,\phi_S)\,\Omega(\xi,\phi,\phi_S)\,\varepsilon_r(\xi,\phi,\phi_S)}{\int d\xi\,\sigma_{UU}^h(\xi,\phi,\phi_S)\,\Omega(\xi,\phi,\phi_S)\,\varepsilon_r(\xi,\phi,\phi_S)} \neq A_{U\perp}^h(\phi,\phi_S).
\end{aligned}
\tag{5.1}
$$

The reconstruction of the kinematic variables and in particular the reconstruction of the azimuthal angles ϕ and ϕ_S is also influenced by higher order QED processes such as initial or final state Bremsstrahlung and kinematic smearing effects due to finite spectrometer resolution.

The SSA amplitudes extracted in a maximum likelihood fit reconstruction method as a function of x, z and $\mathbf{P}_{h\perp}$ are not corrected for acceptance and kinematic smearing effects: For the selected hadron events, an application of an unfolding algorithm as, e.g., applied in the HERMES determination of the spin structure function g_1 [HERMES07] is not feasible given the dependence on x, Q^2, z, $\mathbf{P}_{h\perp}$, ϕ and ϕ_S for the semi-inclusive measurement of the transverse single-spin asymmetries $A^h_{\mathrm{U}\perp}$ instead of the dependence on x and Q^2 for the inclusive measurement of the double-spin asymmetry $A_\parallel$. An alternative correction [Mil06] by evaluating the full kinematic dependence through a fully differential maximum likelihood fit of the selected hadron events and folding the result with the spin-independent cross section σ^h_{UU} is rejected due to an inadequate knowledge of the spin-independent cross section as a function of x, Q^2, z, $\mathbf{P}_{h\perp}$ and ϕ.

In the maximum likelihood fit based reconstruction method, weights as pion track, kaon track and proton track are assigned to each hadron track to account for the efficiency of the RICH detector and the contamination of the hadron identification (section 4.1.5). The weights are obtained from the inverse $\mathscr{P}$-matrix determined in Monte Carlo simulations of the hadron identification using the RICH detector. The evaluation of the $\mathscr{P}$-matrix is affected by the choice of the Monte Carlo generator and the estimate of the background on the PMT matrix of the RICH detector. Thus, $\mathscr{P}$-matrices are calculated for various background estimates using different Monte Carlo generators. The influence of the hadron identification using the RICH detector can be studied by comparing the SSA amplitudes extracted with weights according to the various $\mathscr{P}$-matrices [CDPS07a, CDPS08] or by comparing SSA amplitudes extracted for the generated hadron type and SSA amplitudes according to the reconstructed hadron types.

In the measurement, transverse single-spin asymmetries $A^h_{\mathrm{U}\perp}$ with a target spin orientation aligned perpendicular to the lepton beam direction are reconstructed. Due to the target spin component longitudinal to the virtual-photon direction, the measurement is influenced by the longitudinal target spin-dependent cross section contribution σ^h_{UL}. The contributions of σ^h_{UL} and σ^h_{UT} to the transverse single-spin asymmetries $A^h_{\mathrm{U}\perp}$ can be disentangled combining measurements on a longitudinally and transversely nuclear-polarised hydrogen target. As only longitudinal single-spin asymmetries for π-mesons have been measured by the HERMES collaboration [HERMES00, HERMES01], the influence of the longitudinal target component is estimated and included in the systematic uncertainty to present transverse single-spin asymmetries A^h_{UT} with respect to the virtual photon direction.

5.1.2. The choice of the simulation

A Monte Carlo simulation of transverse single-spin asymmetries at the HERMES experiment is needed to investigate the various systematic influences on the Fourier decomposition. In addition to a model of azimuthal single-spin asymmetries in the semi-inclusive electroproduction of π-mesons and charged K-mesons on a transversely polarised proton target, a detailed description of the reconstruction of deep-inelastic scattering events in the HERMES spectrometer is required. In the spectrometer simulation, the deflection of particles in the holding field of the target magnet transverse to the beam direction and a possible misalignment of the incoming HERA electron beam and the HERMES spectrometer have to be included.

From the various event generators used in the HERMES Monte Carlo, only GMC_TRANS [BEM$^+$04] provides a model for azimuthal single-spin asymmetries at a transversely polarised proton target. In GMC_TRANS hadron events are generated according to a cross-section expression of one-hadron production [MT96] using a skewed Gaussian Ansatz for all transverse-momentum dependent
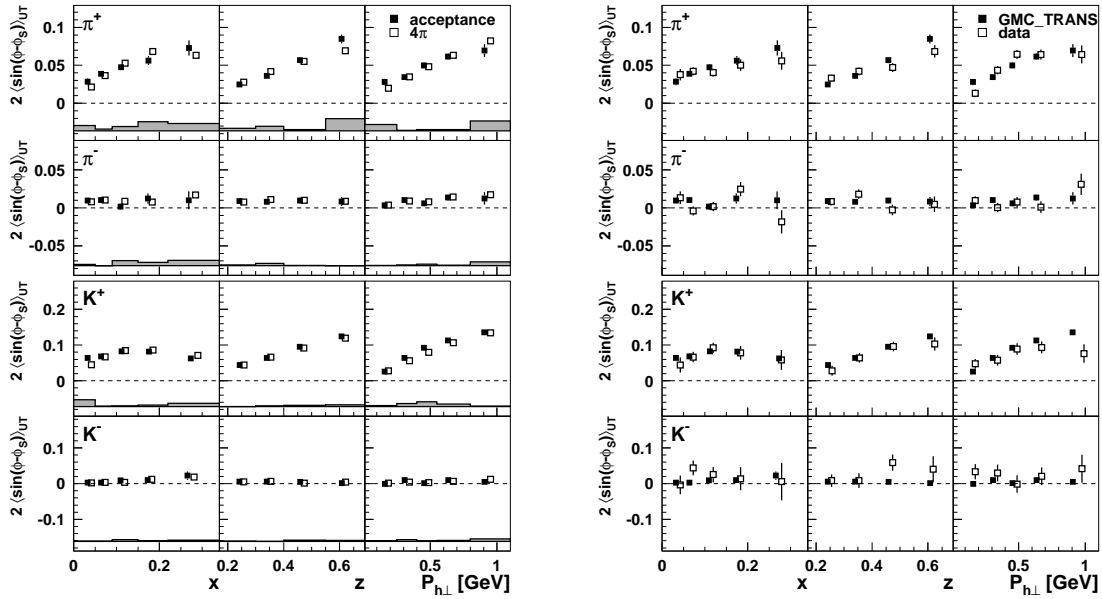
Figure 5.1.: Reminiscenceon the estimate of systematic uncertainties using the GMC_TRANS event generator: The grey error band in the left panel represents the systematic uncertainty due to acceptance and detector smearing effects evaluated from the difference of the Sivers amplitudes generated by GMC_TRANS (open symbols) and those reconstructed in the spectrometer acceptance (closed symbols). In the right panel, interim results for the extraction of Sivers amplitudes (open symbols) from recorded data are compared to GMC_TRANS simulated SSA amplitudes (closed symbols) using a parametrisation of the Sivers function [ABD$^+$09a] and a global fit of fragmentation functions [dFSS07].

distribution and fragmentation functions. The simulation of the $2 \langle \sin(\phi + \phi_S) \rangle_{\mathrm{UT}}^h$, $2 \langle \sin(\phi - \phi_S) \rangle_{\mathrm{UT}}^h$ and $2 \langle \sin(\phi_S) \rangle_{\mathrm{UT}}^h$ amplitudes allows the investigation of acceptance and detector smearing effects by a direct comparison of the generated SSA amplitudes and the SSA amplitudes reconstructed in the HERMES spectrometer (left panel of figure 5.1). Due to the missing implementation of higher order QED effects, only kinematic smearing effects arising from finite detector resolution can be studied. Even though a good agreement of simulated and measured SSA amplitudes is obtained for various model parameters as, e.g., shown in the right panel of figure 5.1, a strong dependence on the parameters of the GMC_TRANS event generator is found for the estimated systematic uncertainties [Die07b].

Thus, an empirical model for azimuthal single-spin asymmetries is constrained from recorded data. By applying a fully differential maximum likelihood fit, the model is unaffected by acceptance effects and can be incorporated in Monte Carlo data produced according to the spin-independent cross section.

In the PYTHIA event generator [S$^+$01], scattering events are generated according to the relative cross section of various processes such as deep-inelastic scattering, photon-gluon fusion, elastic vector meson production and decay. The version of PYTHIA used in the simulation is tuned for HERMES kinematics and extended with RADGEN [ABR98] to account for QED radiative effects. Detailed simulations are available where the particle deflection in the holding field of the target magnet is considered in the track reconstruction and the efficiency and cross-contamination of the hadron identification due to the RICH detector is taken into account. In these simulations also

approximations for the unknown beam or spectrometer misalignment are included.

Systematic uncertainties can be estimated from detailed simulation of the HERMES experiment by comparing the SSA amplitudes reconstructed in the the HERMES spectrometer and the SSA amplitudes evaluated from the model at the reconstructed kinematics.

5.1.3. The model for transverse single-spin asymmetries

In due consideration of the full kinematic dependence, a model for transverse single-spin asymmetries is constrained from recorded data using a fully differential maximum likelihood fit. As no binning in the kinematic variables x, Q^2, z, $|\mathbf{P}_{h\perp}|$ as well as in the azimuthal angles ϕ and ϕ_S is applied, the constrained model is not affected by acceptance effects.

The functional form of the model cannot be defined a priori and thus is based on an empirical model [Mil06] optimised for the description of a GMC_TRANS Monte Carlo simulation including only the Collins and Sivers mechanism. In the fully differential maximum likelihood fit a probability density function was considered:

$$
\begin{aligned}
P&\left(x,Q^2,z,|\mathbf{P}_{h\perp}|,\phi,\phi_S;\Xi_{22}^{\sin(\phi-\phi_S),h},\Xi_{22}^{\sin(\phi+\phi_S),h}\right)\\
&=1+S_\perp\left(\sin(\phi-\phi_S)\,\Xi_{22}^{\sin(\phi-\phi_S),h}+\sin(\phi+\phi_S)\,\Xi_{22}^{\sin(\phi+\phi_S),h}\right),
\end{aligned}
\tag{5.2}
$$

where the parametrisation of the Sivers $\Xi_{22}^{\sin(\phi-\phi_S),h}$ and the Collins mechanism $\Xi_{22}^{\sin(\phi+\phi_S),h}$ was taken from a Taylor expansion in $x'\equiv x-\langle x\rangle$, $Q^{2'}\equiv Q^2-\langle Q^2\rangle$, $z'\equiv z-\langle z\rangle$ and $|\mathbf{P}_{h\perp}|'\equiv|\mathbf{P}_{h\perp}|-\langle|\mathbf{P}_{h\perp}|\rangle$ (only statistically significant parameters are included):

$$
\begin{aligned}
\Xi_{22}^{\sin(\phi\pm\phi_S),h} &= \Xi_{22,1}^{\sin(\phi\pm\phi_S),h} &&+\quad \Xi_{22,2}^{\sin(\phi\pm\phi_S),h}\,x' &&+\\
&\quad\ \Xi_{22,3}^{\sin(\phi\pm\phi_S),h}\,Q^{2'} &&+\quad \Xi_{22,4}^{\sin(\phi\pm\phi_S),h}\,z' &&+\\
&\quad\ \Xi_{22,5}^{\sin(\phi\pm\phi_S),h}\,|\mathbf{P}_{h\perp}|' &&+\quad \Xi_{22,6}^{\sin(\phi\pm\phi_S),h}\,x'^2 &&+\\
&\quad\ \Xi_{22,7}^{\sin(\phi\pm\phi_S),h}\,z'^2 &&+\quad \Xi_{22,8}^{\sin(\phi\pm\phi_S),h}\,|\mathbf{P}_{h\perp}|'^2 &&+\\
&\quad\ \Xi_{22,9}^{\sin(\phi\pm\phi_S),h}\,x'z' &&+\quad \Xi_{22,10}^{\sin(\phi\pm\phi_S),h}\,x'\,|\mathbf{P}_{h\perp}|' &&+\\
&\quad\ \Xi_{22,11}^{\sin(\phi\pm\phi_S),h}\,z'\,|\mathbf{P}_{h\perp}|' &&+\quad \Xi_{22,12}^{\sin(\phi\pm\phi_S),h}\,x'^3 &&+\\
&\quad\ \Xi_{22,13}^{\sin(\phi\pm\phi_S),h}\,x'z'^2 &&+\quad \Xi_{22,14}^{\sin(\phi\pm\phi_S),h}\,x'^2z' &&+\\
&\quad\ \Xi_{22,15}^{\sin(\phi\pm\phi_S),h}\,x'^2\,|\mathbf{P}_{h\perp}|' &&+\quad \Xi_{22,16}^{\sin(\phi\pm\phi_S),h}\,x'\,|\mathbf{P}_{h\perp}|'^2 &&+\\
&\quad\ \Xi_{22,17}^{\sin(\phi\pm\phi_S),h}\,z'^2\,|\mathbf{P}_{h\perp}|' &&+\quad \Xi_{22,18}^{\sin(\phi\pm\phi_S),h}\,z'\,|\mathbf{P}_{h\perp}|'^2 &&+\\
&\quad\ \Xi_{22,19}^{\sin(\phi\pm\phi_S),h}\,x'^2|\mathbf{P}_{h\perp}|'^2 &&+\quad \Xi_{22,20}^{\sin(\phi\pm\phi_S),h}\,z'^2|\mathbf{P}_{h\perp}|'^2 &&+\\
&\quad\ \Xi_{22,21}^{\sin(\phi\pm\phi_S),h}\,x'z'\,|\mathbf{P}_{h\perp}|' &&+\quad \Xi_{22,22}^{\sin(\phi\pm\phi_S),h}\,x'^2z'\,|\mathbf{P}_{h\perp}|' &&.
\end{aligned}
\tag{5.3}
$$

The functional form of the empirical model has to be modified for the description of the measured transverse single-spin asymmetries:

❑ The number of model parameters is limited by the amount of statistics.

❑ The kinematic dependence of the measured transverse single-spin asymmetries different from the one simulated by GMC_TRANS might influence the significance of the various kinematic correlations and thus the functional form of the model.

❑ Also the $\sin(3\phi-\phi_S)$, $\sin(\phi_S)$, $\sin(2\phi-\phi_S)$ and $\sin(2\phi+\phi_S)$ modulations of the transverse target spin-dependent cross section have to be accounted for in the model for the measured transverse single-spin asymmetries.
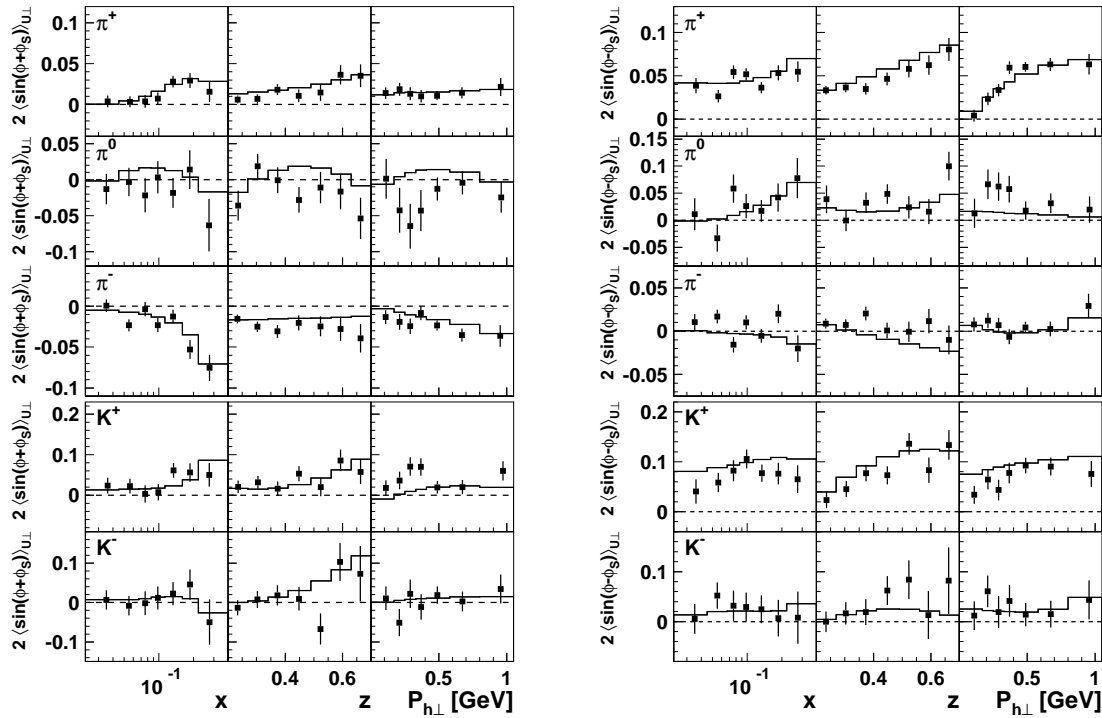
Figure 5.2.: Description of the Collins and Sivers amplitudes: In every bin of x, z and $|\mathbf{P}_{h\perp}|$, the fully differential model is evaluated at the mean kinematics of of the transverse single-spin asymmetries measurement. The result (solid black line) is compared to the extracted Collins (left panel) and Sivers amplitudes (right panel).

A Model with each 22 parameters for the description of the Sivers and Collins mechanism could be constrained from the GMC_TRANS Monte Carlo simulation generated with a large amount of statistics. To determine also statistically significant parameterisations for the SSA amplitudes extracted from recorded data, the number of parameters has to be reduced. Apart from problems in the convergence of the fully differential maximum likelihood fit for the recorded π^0 and K^- events, also unphysical systematic uncertainties were estimated when fitting small signals with too many parameters. When, e.g., using 16 parameters for the description of the Sivers mechanism of π^-, the systematic uncertainties of SSA amplitudes extracted with the additional requirement of $Q^2 > 4\,\mathrm{GeV}^2$ were significantly larger than the systematic uncertainties of SSA amplitudes extracted for the usual requirement $Q^2 > 1\,\mathrm{GeV}^2$ [CDPS08].

Choosing the number of model parameters and in particular selecting the kinematic correlations in the Taylor expansion in a quantitative way is not feasible given the missing measure of goodness of unbinned maximum likelihood fits. First attempts to follow a proposal [Raj05] for a measure of goodness by studying transformation properties of the likelihood ratio of the theoretically predicted probability density function to that of the data confirmed the empirical results [Pap08]: The model improves considerably with the inclusion of the $\sin(\phi_S)$ modulation and continually with the number of parameters whereas a saturation after 11 parameters for the description of each considered amplitude is found.

A model with each 11 parameter for the significant $2\langle\sin(\phi-\phi_S)\rangle_{\mathrm{UT}}^h$, $2\langle\sin(\phi+\phi_S)\rangle_{\mathrm{UT}}^h$ and
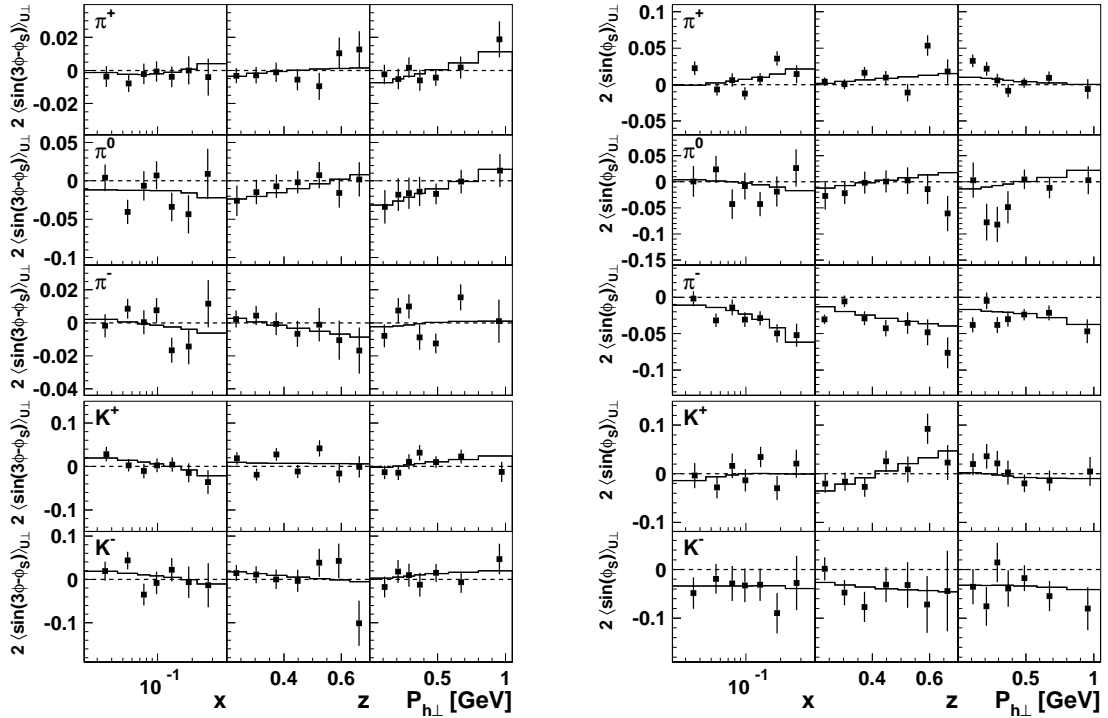
Figure 5.3.: Description of the $2\langle\sin(3\phi-\phi_S)\rangle^h_{UT}$ and $2\langle\sin(\phi_S)\rangle^h_{UT}$ amplitudes: In every bin in x, z and $|\mathbf{P}_{h\perp}|$, the fully differential model is evaluated at the mean kinematics of of the transverse single-spin asymmetries measurement. The result (solid black line) is compared to the extracted $2\langle\sin(3\phi-\phi_S)\rangle^h_{U\perp}$ (left panel) and $2\langle\sin(\phi_S)\rangle^h_{U\perp}$ amplitudes (right panel).

$2\langle\sin(\phi_S)\rangle^h_{UT}$ amplitudes is chosen:

$$
\begin{aligned}
\Xi^{\sin(\phi\pm\phi_S),h}_{11} = {} & \Xi^{\sin(\phi\pm\phi_S),h}_{11,1} && + && \Xi^{\sin(\phi\pm\phi_S),h}_{11,2}x' && + \\
& \Xi^{\sin(\phi\pm\phi_S),h}_{11,3}Q^{2\prime} && + && \Xi^{\sin(\phi\pm\phi_S),h}_{11,4}z' && + \\
& \Xi^{\sin(\phi\pm\phi_S),h}_{11,5}|\mathbf{P}_{h\perp}|' && + && \Xi^{\sin(\phi\pm\phi_S),h}_{11,6}x'^2 && + \\
& \Xi^{\sin(\phi\pm\phi_S),h}_{11,7}z'^2 && + && \Xi^{\sin(\phi\pm\phi_S),h}_{11,8}|\mathbf{P}_{h\perp}|'^2 && + \\
& \Xi^{\sin(\phi\pm\phi_S),h}_{11,9}x'z' && + && \Xi^{\sin(\phi\pm\phi_S),h}_{11,10}x'|\mathbf{P}_{h\perp}|' && + \\
& \Xi^{\sin(\phi\pm\phi_S),h}_{11,11}z'|\mathbf{P}_{h\perp}|' && \,.
\end{aligned}
\tag{5.4}
$$

For the description of the $2\langle\sin(3\phi-\phi_S)\rangle^h_{UT}$, $2\langle\sin(2\phi-\phi_S)\rangle^h_{UT}$ and $2\langle\sin(2\phi+\phi_S)\rangle^h_{UT}$ amplitudes, only a constant parameter and parameters linear in x, Q^2, z and $\mathbf{P}_{h\perp}$ are considered as the observed signals are consistent with zero but some kinematic dependence is required for an reasonable estimate of systematic uncertainties.

When estimating the systematic uncertainties of the Sivers and Collins amplitudes, the $\sin(\phi_S)$ modulation has to be included in the probability density function due to the statistical correlation of the $2\langle\sin(\phi-\phi_S)\rangle^h_{U\perp}$, $2\langle\sin(\phi+\phi_S)\rangle^h_{U\perp}$ and $2\langle\sin(\phi_S)\rangle^h_{U\perp}$ amplitudes. The $\sin(3\phi-\phi_S)$, $\sin(2\phi-\phi_S)$ and $\sin(2\phi+\phi_S)$ modulations whose SSA amplitudes are consistent with zero can be

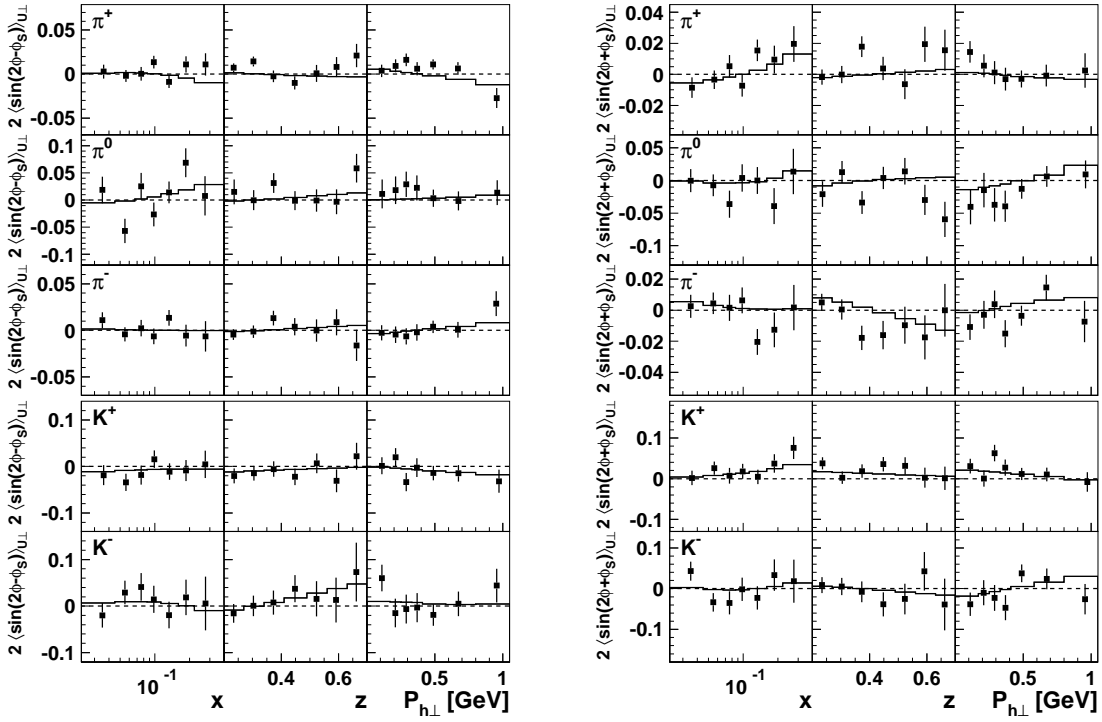Figure 5.4.: Description of the $2\langle\sin(2\phi-\phi_S)\rangle^h_{UT}$ and $2\langle\sin(2\phi+\phi_S)\rangle^h_{UT}$ amplitudes: In every bin in x, z and $|\mathbf{P}_{h\perp}|$, the fully differential model is evaluated at the mean kinematics of of the transverse single-spin asymmetries measurement. The result (solid black line) is compared to the extracted $2\langle\sin(2\phi-\phi_S)\rangle^h_{U\perp}$ (left panel) and $2\langle\sin(2\phi+\phi_S)\rangle^h_{U\perp}$ amplitudes (right panel).

neglected:

$$P\left(x,Q^2,z,|\mathbf{P}_{h\perp}|,\phi,\phi_S;\Xi_{11}^{\sin(\phi-\phi_S),h},\Xi_{11}^{\sin(\phi+\phi_S),h},\Xi_{11}^{\sin(\phi_S),h}\right)$$
$$=1+S_\perp\left(\sin(\phi-\phi_S)\,\Xi_{11}^{\sin(\phi-\phi_S),h}+\sin(\phi+\phi_S)\,\Xi_{11}^{\sin(\phi+\phi_S),h}+\sin(\phi_S)\,\Xi_{11}^{\sin(\phi_S),h}\right). \tag{5.5}$$

Only for the estimate of the systematic uncertainties of the $2\langle\sin(3\phi-\phi_S)\rangle^h_{U\perp}$, $2\langle\sin(2\phi-\phi_S)\rangle^h_{U\perp}$ and $2\langle\sin(2\phi+\phi_S)\rangle^h_{U\perp}$ amplitudes, the $\sin(3\phi-\phi_S)$, $\sin(2\phi-\phi_S)$ and $\sin(2\phi+\phi_S)$ modulations have to be regarded in the probability density function. To limit the number of model parameters, the description of the Sivers and Collins amplitudes are included in the probability density function as fixed parameters and the number of model parameters for the description of the $2\langle\sin(\phi_S)\rangle^h_{UT}$ amplitude is reduced to 5:

$$P\left(x,Q^2,z,|\mathbf{P}_{h\perp}|,\phi,\phi_S;\Xi_5^{\sin(3\phi-\phi_S),h},\Xi_5^{\sin(\phi_S),h},\Xi_5^{\sin(2\phi-\phi_S),h},\Xi_5^{\sin(2\phi+\phi_S),h}\right)=$$
$$1+S_\perp\left(\sin(\phi-\phi_S)\,\Xi_{11}^{\sin(\phi-\phi_S),h}+\sin(\phi+\phi_S)\,\Xi_{11}^{\sin(\phi+\phi_S),h}+\sin(3\phi-\phi_S)\,\Xi_5^{\sin(3\phi-\phi_S),h}+ \tag{5.6}$$
$$\sin(\phi_S)\,\Xi_5^{\sin(\phi_S),h}+\sin(2\phi-\phi_S)\,\Xi_5^{\sin(2\phi-\phi_S),h}+\sin(2\phi+\phi_S)\,\Xi_5^{\sin(2\phi+\phi_S),h}\right).$$

When evaluating the constrained model at the mean kinematics of the extracted SSA amplitudes, a good description of the SSA amplitudes is found (figures 5.2 – 5.4). However, the model for transverse single-spin asymmetries could be improved in future works by constraining the models of the

67

SSA amplitudes simultaneously instead of limiting first the models for the Collins and Sivers amplitudes and then restricting the models of the $2\langle\sin(3\phi-\phi_S)\rangle^h_{UT}$, $2\langle\sin(\phi_S)\rangle^h_{UT}$, $2\langle\sin(2\phi-\phi_S)\rangle^h_{UT}$ and $2\langle\sin(2\phi+\phi_S)\rangle^h_{UT}$ amplitudes as done in the current work.

5.1.4. Modelling the SSA amplitudes

In the PYTHIA event generator, scattering events are generated according to the cross section of spin-independent processes. Spin-orbit correlations like transverse single-spin asymmetries are incorporated in the chosen Monte Carlo simulation by assigning the target spin orientation of each generated event randomly according to the transverse target spin-dependent cross section contribution σ^h_{UT}. The cross section $\sigma^h_{U\Uparrow}$ of transverse target spin orientation "$\Uparrow$" is related to the transverse single-spin asymmetries A^h_{UT} by:

$$\sigma^h_{U\Uparrow} = \sigma^h_{UU}(1+A^h_{UT}). \tag{5.7}$$

Using the empirical model, the transverse single-spin asymmetries can be approximated:

$$A^h_{UT} \approx \sin(\phi-\phi_S)\,\Xi^{\sin(\phi-\phi_S),h}_{11} + \sin(\phi+\phi_S)\,\Xi^{\sin(\phi+\phi_S),h}_{11} + \sin(\phi_S)\,\Xi^{\sin(\phi_S),h}_{11}, \tag{5.8}$$

where without loss of generality the asymmetry model for the estimate of systematic uncertainties on the Collins and Sivers amplitudes is given. For each scattering event, the approximated cross section contribution is evaluated at the generated kinematics of the event corrected for higher order QED processes. If a number ρ randomly generated in the range $[0;1]$ does (not) fulfil the condition:

$$\rho < \frac{1}{2}(1+\sin(\phi-\phi_S)\,\Xi^{\sin(\phi-\phi_S),h}_{11} + \sin(\phi+\phi_S)\,\Xi^{\sin(\phi+\phi_S),h}_{11} + \sin(\phi_S)\,\Xi^{\sin(\phi_S),h}_{11}), \tag{5.9}$$

then target spin orientation "$\Uparrow$" ("$\Downarrow$") is assigned. The sequence of random numbers is fixed to repeat systematic studies using an identical distribution of transverse target spin states. Thereby, no influence on the estimate of the systematic uncertainties on the SSA amplitudes was found within the statistical accuracy of the simulated data[Die09].

Higher order QED processes such as Bremsstrahlung are not regarded by the PYTHIA event generator. So RADGEN is applied to decide whether or not a real photon is emitted in the initial or the final state of the process given the kinematics generated by PYTHIA. The information about the four-momentum of the radiated real photon k_γ but not the information about Bremsstrahlung in the initial or final state is provided by RADGEN. Whereas the correction of the scaling variables such as Q^2 is invariant under initial or final state Bremsstrahlung:

$$\text{radiation off incoming lepton } k: \quad Q^2_{cor} = ((k-k_\gamma)-k')^2 = (k-k'-k_\gamma)^2, \tag{5.10}$$

$$\text{radiation off scattered lepton } k': \quad Q^2_{cor} = (k-(k'+k_\gamma))^2 = (k-k'-k_\gamma)^2, \tag{5.11}$$

the azimuthal angles ϕ and ϕ_S are affected as the lepton scattering plane spanned by $\mathbf{k}\times(\mathbf{k}-\mathbf{k}')$ is not invariant under the correction for initial or final state Bremsstrahlung.

Studying the correlation of the polar angle θ_γ of the radiated photon and the opening angle $\theta_{l'\gamma}$ between the the momentum direction of the scattered lepton and that of the radiated photon, initial and final state Bremsstrahlung can be distinguished. As shown in figure 5.5 two regions are clearly separated when evaluating the polar angle θ_γ as a function of the opening angle $\theta_{l'\gamma}$:

❑ For very small values of the polar angle θ_γ, the Bremsstrahlung photon is collinear to the beam direction and thus was radiated off in the initial state.
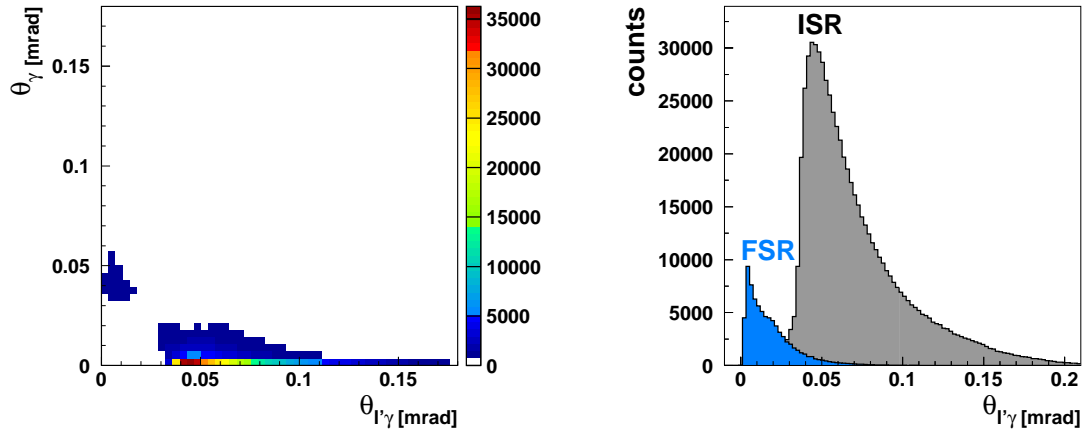
Figure 5.5.: Distinction of initial and final state Bremsstrahlung: In the left panel, the correlation of the radiated photon's polar angle θ_γ and the opening angle $\theta_{l'\gamma}$ between the momentum direction of the scattered lepton and that of the radiated photon is given. Real photons radiated off from the incoming lepton beam ($\theta_\gamma < \theta_{l'\gamma}$) and from the scattered lepton ($\theta_\gamma > \theta_{l'\gamma}$) are identified according to the requirements on the polar angles θ_γ and $\theta_{l'\gamma}$. In the right panel, hadron counts as a function of the opening angle θ_γ are shown for both initial (ISR) and final state Bremsstrahlung (FSR).

❑ For very small values of the opening angle $\theta_{l'\gamma}$, the Bremsstrahlung photon is collinear to the direction of the scattered lepton and thus was radiated off in the final state.

Identifying initial and final state Bremsstrahlung according to the requirement $\theta_\gamma < \theta_{l'\gamma}$ for initial state radiation and $\theta_\gamma > \theta_{l'\gamma}$ for final state radiation, the azimuthal angles ϕ and ϕ_S can be corrected for those higher order QED processes.

5.1.5. The resulting estimates

5.1.5.1. Scale uncertainty due to the target polarisation measurement accuracy

The measured transverse single-spin asymmetries scale according to the average degree of target polarisation. For the selected data, an average degree of $P = 72.5 \pm 5.3\%$ could be achieved. The accuracy of the target polarisation measurement affects both the central values and and the statistical uncertainties of the SSA amplitudes and is thus regarded as scale uncertainty of 7.3%.

5.1.5.2. Influence of acceptance, kinematic smearing and hadron misidentification

Effects on the measurement of transverse single-spin asymmetries due to acceptance, kinematic smearing and hadron misidentification can influence each other. Systematic uncertainties representing these effects are estimated simultaneously to account for possible correlations.

For each hadron generated by the chosen PYTHIA Monte Carlo simulation, the target spin orientation is randomly assigned according to the fully differential model. SSA amplitudes are extracted in the spectrometer acceptance applying the data selection criteria and reconstruction methods as described in chapter 4. The difference between SSA amplitudes reconstructed in the spectrometer acceptance and the model evaluated at the mean reconstructed kinematics is assigned as systematic uncertainty. In the measurement of transverse single-spin asymmetries, this difference reflects the
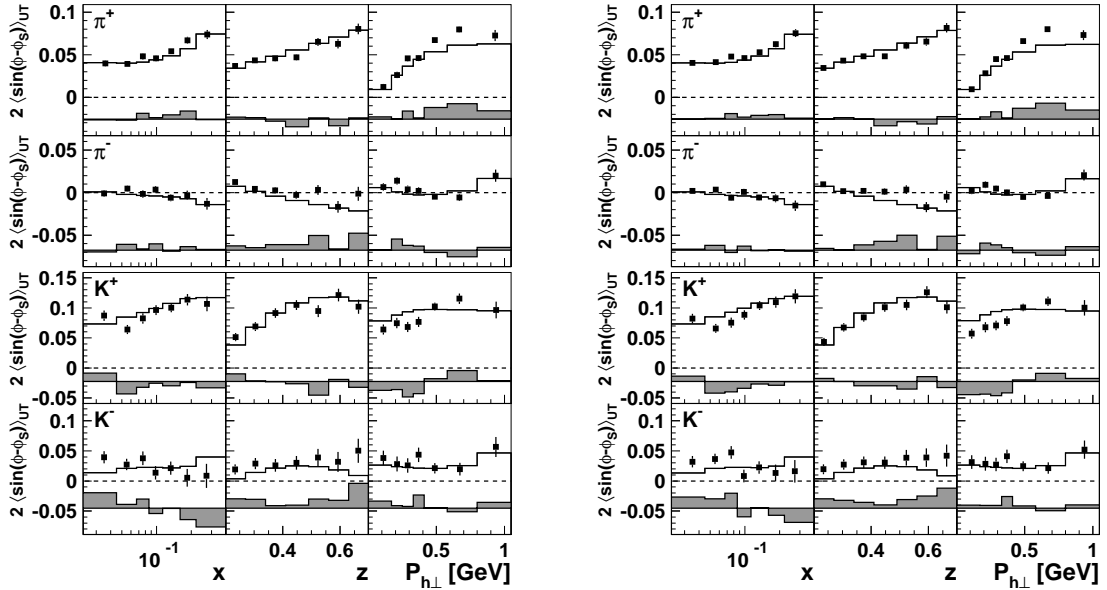
Figure 5.6.: Estimate of the systematic uncertainty on the Sivers amplitudes: From the reconstructed events of the PYTHIA Monte Carlo simulation Sivers amplitudes (black closed symbols) are extracted using perfect hadron identification (left panel) as well as RICH PID (right panel) and compared to the empirical model evaluated at the mean reconstructed kinematics (black solid line). The difference is assigned as systematic uncertainty represented by the grey error bars.

influence of acceptance, kinematic smearing and hadron misidentification on the comparison of the extracted SSA amplitudes to any theoretical model evaluated at the kinematics of the measurement.

Using the Sivers amplitudes as example, the estimate of the systematic uncertainties is illustrated in figure 5.6. In the right panel of figure 5.6 the Sivers amplitudes are extracted from identified hadron determined from the simulated RICH PID; in the left panel the generated hadron type was used. The small difference between both estimates suggests a small systematic contribution from hadron misidentification compatible with the difference in the comparison of SSA amplitudes extracted using various $\mathscr{P}$-matrices [CDPS07a, CDPS08].

The changes of sign visible in the error bands are an indication that the estimate is affected by statistical fluctuations. To reveal the underlying systematic effects the error bands are smoothed using a linear fit depending on either x, z or $|\mathbf{P}_{h\perp}|$. The resulting error bands are shown in the left panel of figure 5.7 using the Sivers amplitudes for π^+ as example. Within the accuracy of the linear
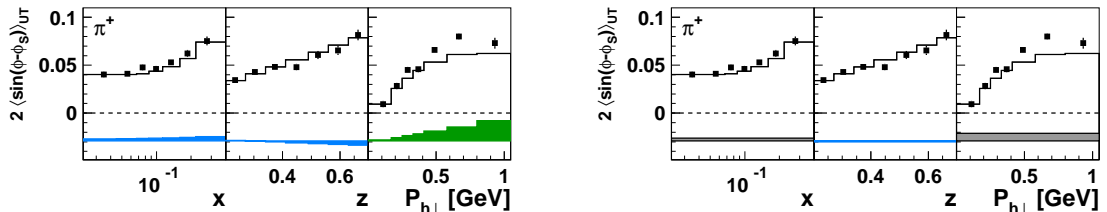

Figure 5.7.: Smoothing of the estimated systematic uncertainty on the Sivers amplitudes for π^+ using either a linear (left panel) or constant fit function (right panel).
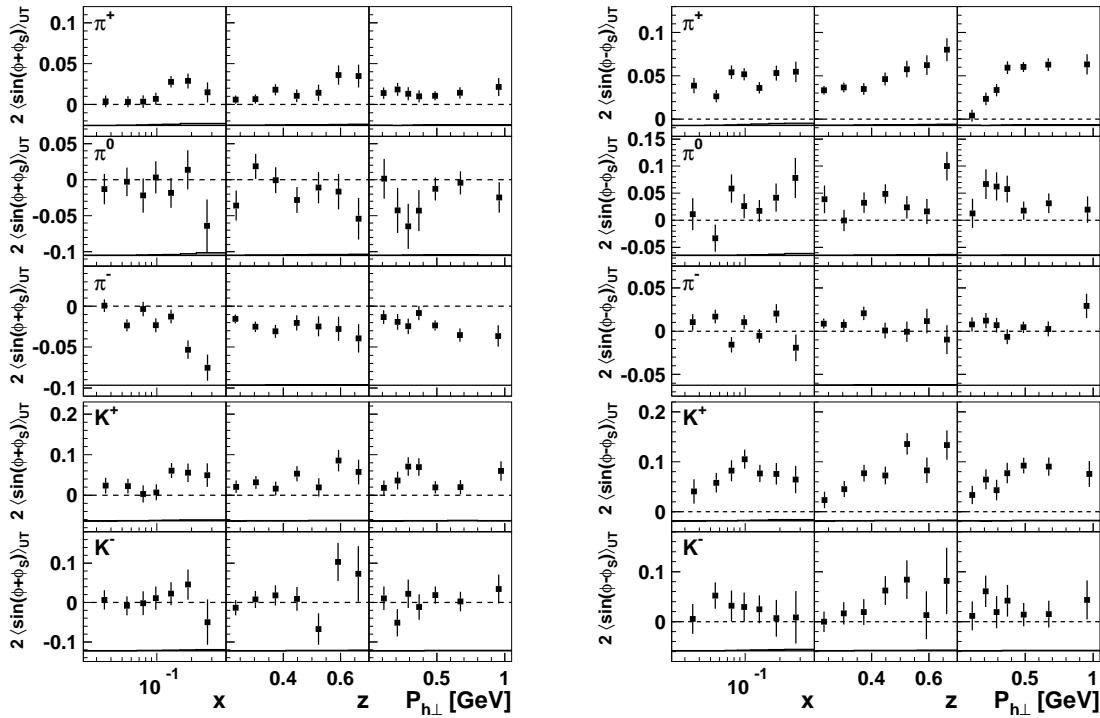
Figure 5.8.: Collins (left panel) and Sivers amplitudes (right panel) are extracted from a measurement of transverse single-spin asymmetries $A_{\mathrm{U}\perp}^{h}$ with respect to the lepton beam direction. The grey error band represents the small systematic uncertainty due to the influence of the longitudinal target component calculated for π-mesons and estimated for K-mesons. When taken this influence into account, the SSA amplitudes can be presented as amplitudes of transverse single-spin asymmetries $A_{\mathrm{U}\perp}^{h}$ with respect to the virtual photon direction.

fit, the slope of the error band as a function of x and z is significant but not the y-intercept (blue error bands). Otherwise the slope is not well-determined for the dependence on $|\mathbf{P}_{h\perp}|$ except for the y-intercept (green error band). When using a constant to smooth the systematic uncertainties (right panel of figure 5.7), significant error bands are obtained for the dependence on x and $|\mathbf{P}_{h\perp}|$ (grey error bands). Even though the slopes or y-intercepts are not well-constrained in some kinematic bins, the error bands are smoothed using a linear fit as the unsmoothed error bands provide indications for a kinematic dependence in most of the bins (and thus are not in agreement with constant error bands). For the final systematic uncertainties, absolute values are used for the error band.

5.1.5.3. Influence of the longitudinal target spin component

The SSA amplitudes are extracted from a semi-inclusive measurement of deep-inelastic scattering on a hydrogen target transversely polarised with respect to the lepton beam direction. With respect to the virtual photon direction, there is besides a dominant transverse component of the spin vector $\mathbf{S}_T \approx \cos\left(\theta_{l'\gamma^*}\right)\mathbf{S}_\perp$ also a small longitudinal component $\mathbf{S}_L \approx \sin\left(\theta_{l'\gamma^*}\right)\cos\left(\phi_S\right)\mathbf{S}_\perp$ [DS05]. The transverse and longitudinal components of the spin vector are related to the spin vector $\mathbf{S}_\perp$ of the measurement via the opening angle $\theta_{l'\gamma^*}$ between the momentum direction of the incoming lepton beam and that of the virtual photon. The Lorentz-invariant quantity $\theta_{l'\gamma^*}$ is calculated from the lepton

5. The analysis of the measured SSA

kinematics:

$$\sin\theta_{l'\gamma^*} = \gamma\sqrt{\frac{1-y-\frac{1}{4}\gamma^2 y^2}{1+\gamma^2}}, \quad \gamma = 2x\frac{M}{Q}. \tag{5.12}$$

In the analysis of SSA amplitudes values of $\sin\theta_{l'\gamma^*}$ up to 0.15 are obtained.

Using results on the $2\langle\sin(\phi)\rangle^h_{U\parallel}$ amplitudes of the longitudinal target spin-dependent cross section contribution σ^h_{UL}, amplitudes of transverse single-spin asymmetries $A^h_{U\perp}$ with respect to the lepton beam direction can be transformed into amplitudes of transverse single-spin asymmetries A^h_{UT} with respect to the virtual photon direction [DS05]:

$$\begin{pmatrix} 2\langle\sin(\phi)\rangle^h_{UL} \\ 2\langle\sin(\phi-\phi_S)\rangle^h_{UT} \\ 2\langle\sin(\phi+\phi_S)\rangle^h_{UT} \end{pmatrix} = \mathscr{T} \begin{pmatrix} 2\langle\sin(\phi)\rangle^h_{U\parallel} \\ 2\langle\sin(\phi-\phi_S)\rangle^h_{U\perp} \\ 2\langle\sin(\phi+\phi_S)\rangle^h_{U\perp} \end{pmatrix},$$

$$\mathscr{T} = \begin{pmatrix} \cos\theta_{l'\gamma^*} & \sin\theta_{l'\gamma^*} & \sin\theta_{l'\gamma^*} \\ -\frac{1}{2}\sin\theta_{l'\gamma^*} & \frac{2-\sin\theta_{l'\gamma^*}^2}{2\cos\theta_{l'\gamma^*}} & -\frac{1}{2}\sin\theta_{l'\gamma^*}\tan\theta_{l'\gamma^*} \\ -\frac{1}{2}\sin\theta_{l'\gamma^*} & -\frac{1}{2}\sin\theta_{l'\gamma^*}\tan\theta_{l'\gamma^*} & \frac{2-\sin\theta_{l'\gamma^*}^2}{2\cos\theta_{l'\gamma^*}} \end{pmatrix}. \tag{5.13}$$

For the sake of clarity, only Collins and Sivers amplitudes are considered in equation 5.13.

The influence of the longitudinal target component on transverse single-spin asymmetries A^h_{UT} with respect to the virtual photon direction is calculated for π-mesons and estimated for K-mesons using a parametrisation of $2\langle\sin(\phi)\rangle^h_{U\parallel}$ amplitudes measured by the HERMES collaboration for π-mesons [HERMES00, HERMES01]. Thereby, a small influence is found which is shown is figure 5.8 as as grey error band and included in the systematic uncertainties when presenting amplitudes of A^h_{UT} instead of $A^h_{U\perp}$.

5.2. The isospin relation

The isospin triplet of π-mesons is reflected in an isospin relation among their asymmetry amplitudes. This general relation for single-spin and also double-spin asymmetries $A^{\pi\text{-meson}}$:

$$A^{\pi^+} + CA^{\pi^-} - (1+C)A^{\pi^0} = 0, \quad C = \frac{\sigma_{UU}^{\pi^-}}{\sigma_{UU}^{\pi^+}}, \tag{5.14}$$

is valid for semi-inclusive deep-inelastic scattering measurements at leading and subleading-twist accuracy and at leading and next-to-leading order in α_S [Mak03, Die05b]. The relation is proved for any target provided that the isospin relations between fragmentation functions such as D_1 hold:

$$D_1^{q\to\pi^0} = \frac{1}{2}\left(D_1^{q\to\pi^+} + D_1^{q\to\pi^-}\right), \tag{5.15}$$

and a flavour structure is given where only a single quark or gluon fragments into a π-meson. The assumption on fragmentation functions in equation 5.15 implies that both the spin-independent and spin-dependent cross sections for electroproduced π^0 are the average of these cross sections for electroproduced π^+ and π^-.

The isospin relation is checked for the extracted SSA amplitudes. In the calculation only the statistical but not the systematic uncertainties are taken into account. For a check including the systematic uncertainties, their correlation would have to be studied. Also, differences in the kinematic mean values for π^+, π^0 and π^- (table 5.1) are not accounted for, even though this could affect the isopspin relation in case of distinct non-linear SSA amplitudes. For each kinematic bin, the cross-

π-meson	kinematic mean values				
	$\langle Q^2 \rangle$	$\langle x \rangle$	$\langle y \rangle$	$\langle z \rangle$	$\langle |\mathbf{P}_{h\perp}| \rangle$
π^+	$2.420\,\text{GeV}^2$	0.094	0.545	0.363	$0.394\,\text{GeV}$
π^0	$2.454\,\text{GeV}^2$	0.087	0.590	0.393	$0.441\,\text{GeV}$
π^-	$2.344\,\text{GeV}^2$	0.091	0.549	0.354	$0.393\,\text{GeV}$

Table 5.1.: Kinematic mean values for the selected π-mesons.

section ratio $C(x, z, |\mathbf{P}_{h\perp}|)$ is estimated from the charged pion yields $N^{\pi^{\pm}}(x, z, |\mathbf{P}_{h\perp}|)$ in the given bin. Acceptance effects almost cancel out in the ratio, $C(xz, |\mathbf{P}_{h\perp}|) = N^{\pi^-}(x, z, |\mathbf{P}_{h\perp}|)/N^{\pi^+}(x, z, |\mathbf{P}_{h\perp}|)$, thus only a negligible influence on the isospin relation's result arises from the approximation in C.

In table 5.2 results for the isospin relation, $I_R = A^{\pi^+} + CA^{\pi^-} - (1+C)A^{\pi^0}$, are compiled for SSA amplitudes integrated over the full kinematic range of the measurement: The isospin rela-

SSA amplitude	Isospin relation I_R
$2\langle\sin(\phi+\phi_S)\rangle_{U\perp}^h$	0.0223 ± 0.0141
$2\langle\sin(\phi-\phi_S)\rangle_{U\perp}^h$	-0.0076 ± 0.0147
$2\langle\sin(3\phi-\phi_S)\rangle_{U\perp}^h$	0.0154 ± 0.0120
$2\langle\sin(\phi_S)\rangle_{U\perp}^h$	0.0165 ± 0.0168
$2\langle\sin(2\phi-\phi_S)\rangle_{U\perp}^h$	-0.0141 ± 0.0140
$2\langle\sin(2\phi+\phi_S)\rangle_{U\perp}^h$	0.0205 ± 0.0136

Table 5.2.: Results of the isospin relation for the overall SSA amplitudes.

tion is fulfilled for the $2\langle\sin(\phi-\phi_S)\rangle_{U\perp}^h$, $2\langle\sin(\phi_S)\rangle_{U\perp}^h$ and $2\langle\sin(2\phi-\phi_S)\rangle_{U\perp}^h$ amplitudes within
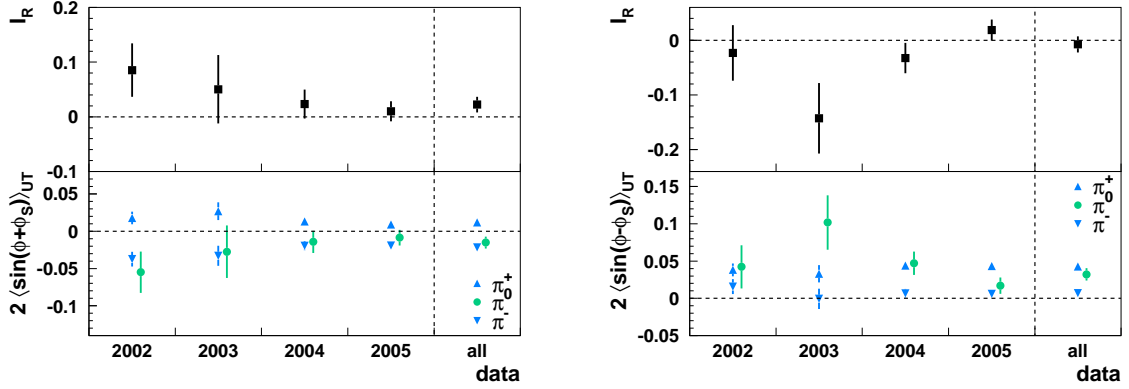
Figure 5.9.: Year dependence of the isospin relation: Collins (left lower panel) and Sivers amplitudes (right lower panel) for π-mesons and the isospin relation among them (upper panel) are presented for each year of data taking and the combined Data set.

the statistical accuracy of the measurement. For the $2\langle\sin(\phi+\phi_S)\rangle^h_{U\perp}$, $2\langle\sin(3\phi-\phi_S)\rangle^h_{U\perp}$ and $2\langle\sin(2\phi+\phi_S)\rangle^h_{U\perp}$ amplitudes, no significant violation is found.

Apart from systematic uncertainties, not regarded in the check, also statistical fluctuations among the SSA amplitudes can affect the isospin relation. In particular for the results of the single years 2002, 2003, 2004 and 2005, large fluctuations are observed in the SSA amplitudes for neutral pions (figure 5.9). In addition, a statistical correlation of the values on I_R is found, when studying the kinematic dependence of the isospin relation (figure 5.10).

But in conclusion, no statistically significant violation of the isospin relation can be reported. As a consequence, the SSA amplitudes extracted separately for π^+, π^0 and π^- reflect the isospin triplet of the π-mesons.
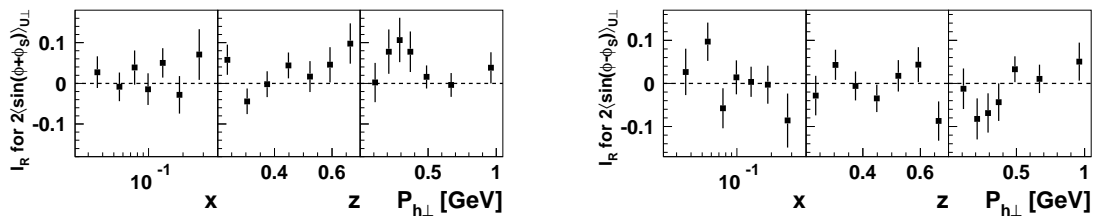

Figure 5.10.: Kinematic dependence of the isospin relation: Results for the isospin relation of Collins (left panel) and Sivers amplitudes (right panel) are shown as a function of x, z and $|\mathbf{P}_{h\perp}|$.
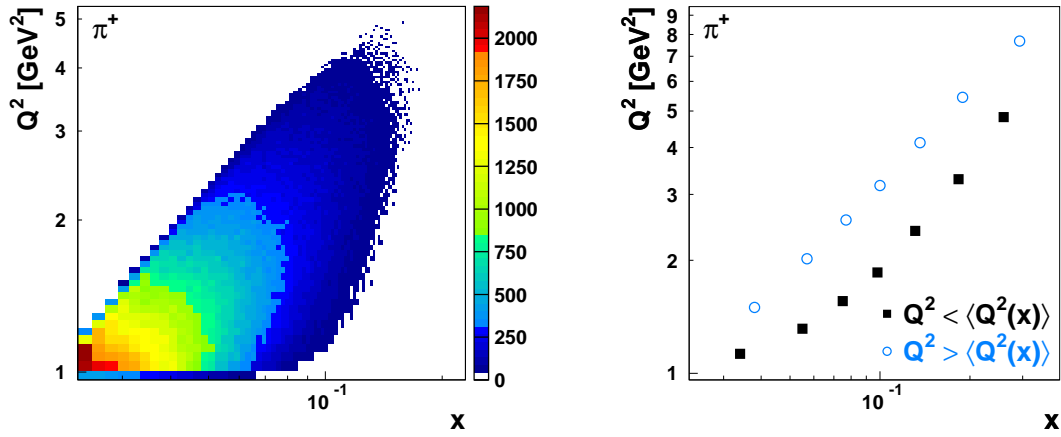
Figure 5.11.: Correlation of x and Q^2: In the left panel, the scale Q^2 of the selected π^+ is studied as a function of Bjorken-x. Due to the limited geometric acceptance of the HERMES spectrometer and the kinematic requirements in the event selection the correlation is enhanced. In the right panel, average Q^2 values are shown for every x-bin when splitting the events (as indicated) according to the mean value in $Q^2(x)$ of the bin.

5.3. The role of higher twist terms

In an analysis of single-spin asymmetries on a longitudinally polarised target, the size of subleading-twist and leading-twist effects was found to be similar [HERMES05d]. This observation indicates that higher twist terms cannot be neglected a priori in the interpretation of single-spin asymmetries. The various contributions to the transverse single-spin asymmetries are known at leading-twist (twist-two) and subleading-twist (twist-three) accuracy [BDG$^+$07]. There is no twist-three contribution to the twist-two Collins, Sivers and $\sin(3\phi - \phi_S)$-terms. The $\sin(\phi_S)$, $\sin(2\phi - \phi_S)$ and $\sin(2\phi + \phi_S)$ terms are related to twist-three contributions. The possible influence of twist-four (or even higher twist) effects on the significant Collins, Sivers and $2\langle\sin(\phi_S)\rangle_{U\perp}$ amplitudes is investigated by studying the Q^2-dependence of the SSA amplitudes and examining the contribution from decay products of exclusive vector-meson production.

5.3.1. The scale dependence of the SSA amplitudes

As a consequence of the strong correlation of the scaling variables x and Q^2 (figure 5.11), in particular for low values of x or Q^2, not only a scale dependence of the SSA amplitudes is observed (left panels of figures 5.12–5.14), but also the study of possible $\frac{1}{Q^2}$-suppressed contributions is hampered. When increasing the requirement on Q^2, the mean values in x change in addition to the scale of the measurement. For this reason, SSA amplitudes extracted in various ranges in Q^2, as e.g. shown in figures 5.12–5.14 for $Q^2 > 4\,\mathrm{GeV}^2$ and $Q^2 < 4\,\mathrm{GeV}^2$, are difficult to compare. The differences seen, e.g., for the Collins amplitudes of π^- are related to the strong x-dependence of these amplitudes.

To study SSA amplitudes at different scales but at fixed x, the hadron events in each bin are divided into two Q^2 ranges below and above the average Q^2 of the particular bin. As shown in figure 5.11 for π^+ events, the mean values in Q^2 differ by a factor of 1.7, while the mean values in x (as well as z and $|\mathbf{P}_{h\perp}|$) are in good agreement. When there is a strong x-dependence such as for the Collins amplitudes for charged pions, also a clear difference in the SSA amplitudes for $Q^2 > \langle Q^2(x,z,|\mathbf{P}_{h\perp}|)\rangle$ and $Q^2 < \langle Q^2(x,z,|\mathbf{P}_{h\perp}|)\rangle$ is found due to the correlation (figures 5.12–5.14).
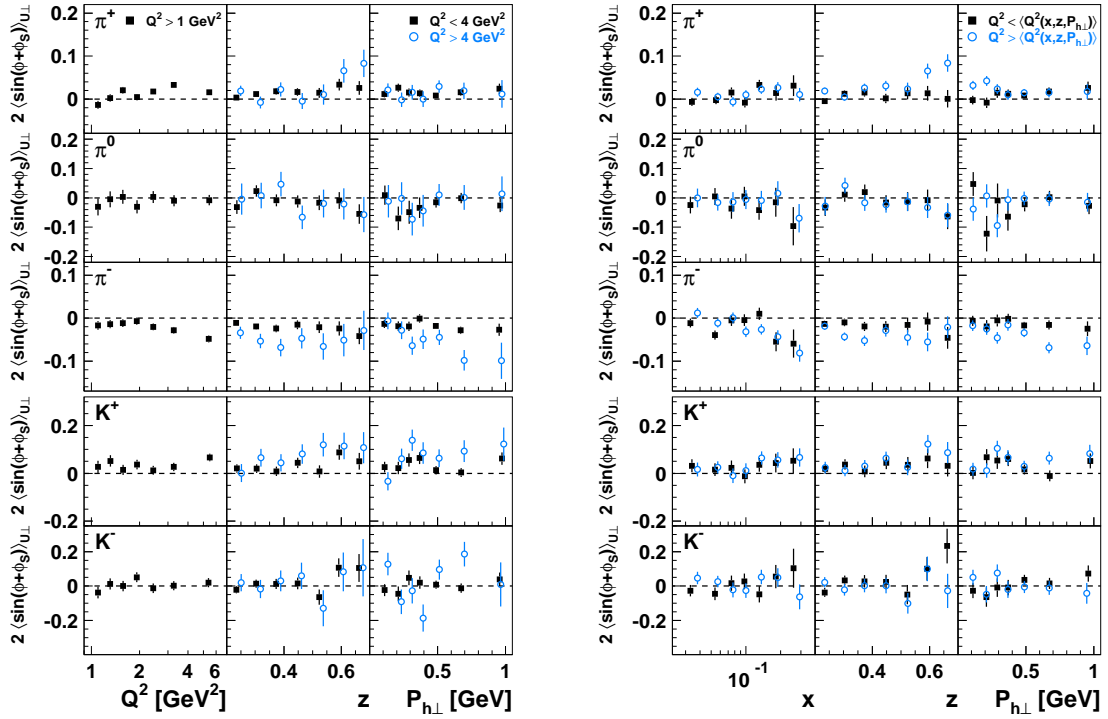
Figure 5.12.: Scale dependence of the Collins amplitudes: The dependence on Q^2 is shown in addition to the Collins amplitudes for $Q^2 \lessgtr 4\,\text{GeV}^2$ (including horizontal shifts for visibility) and $Q^2 \lessgtr \langle Q^2(x, z, |\mathbf{P}_{h\perp}|) \rangle$ (including no horizontal shifts).
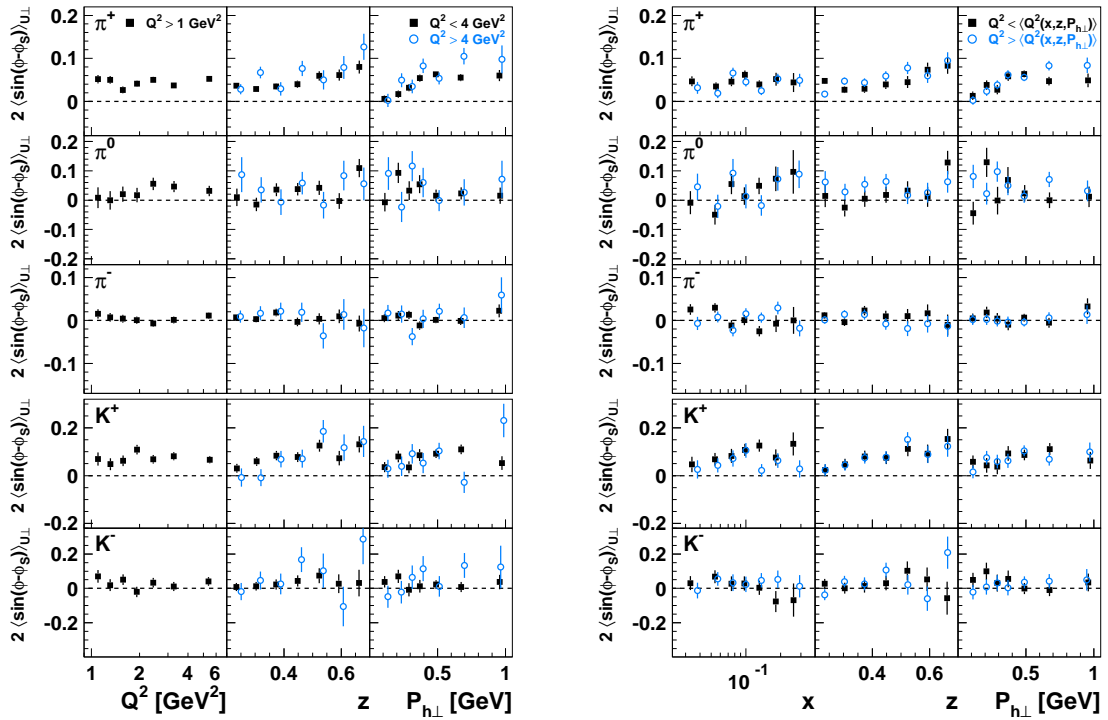

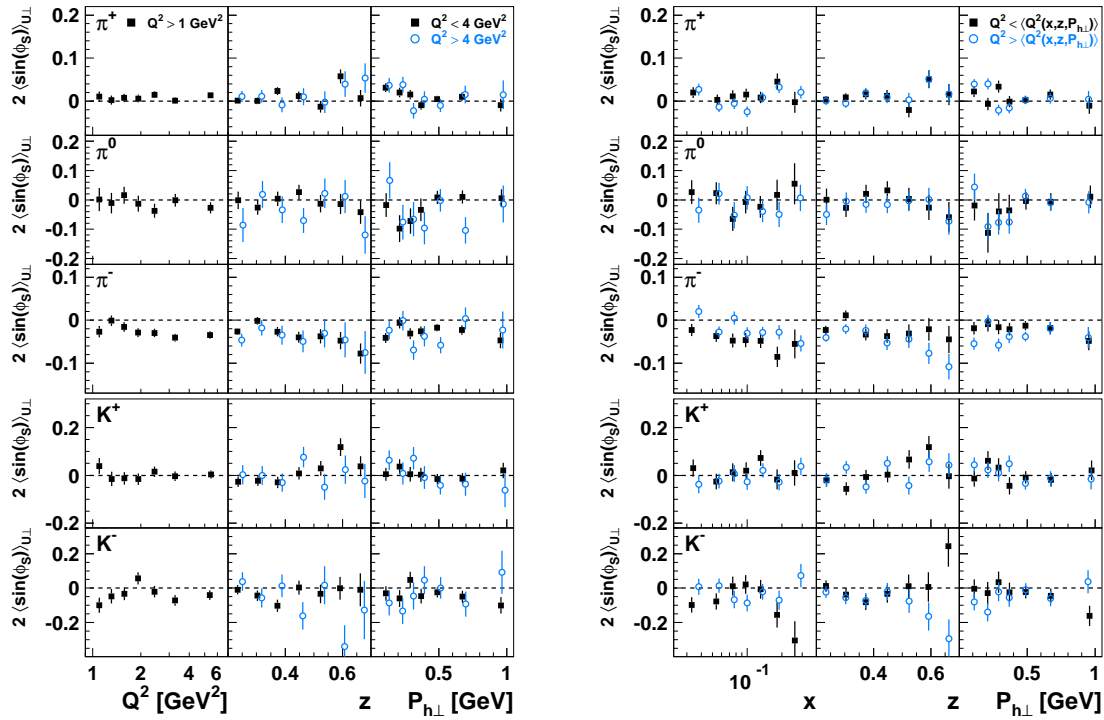Figure 5.13.: Scale dependence of the Sivers amplitudes (analogue to figure 5.12).

Figure 5.14.: Scale dependence of the $2\langle\sin(\phi_S)\rangle^h_{U\perp}$ amplitudes: The dependence on Q^2 is shown in addition to $2\langle\sin(\phi_S)\rangle^h_{U\perp}$ amplitudes for $Q^2 \lessgtr 4\,\mathrm{GeV}^2$ (including horizontal shifts for visibility) and $Q^2 \lessgtr \langle Q^2(x,z,|\mathbf{P}_{h\perp}|)\rangle$ (including no horizontal shifts).

Only the Sivers amplitudes are independent from the ratio ε of longitudinal and transverse photon flux (section 2.3.2). This ratio depends on the kinematics of the lepton beam and the scattered lepton. Thus, changes visible in the Collins and $2\langle\sin(\phi_S)\rangle_{U\perp}$ amplitudes might be related to the scale-dependence of the ratio ε.

Consistent Sivers amplitudes for π^+, π^- and K^- are extracted in the regions $Q^2 \lessgtr \langle Q^2(x,z,|\mathbf{P}_{h\perp}|)\rangle$. The Sivers amplitudes for K^+ are systematically smaller in the region $Q^2 > \langle Q^2(x,z,|\mathbf{P}_{h\perp}|)\rangle$ than those in the region $Q^2 < \langle Q^2(x,z,|\mathbf{P}_{h\perp}|)\rangle$.

Even though this might be an indication for a higher twist effect, no evidence for significant $\frac{1}{Q^2}$-suppressed contributions is found in the reported studies. But as the studies are hampered by the strong correlation of x and Q^2, higher twist effects cannot ruled out and a comparison with upcoming results from other experiments is required for further studies.

5.3.2. The influence of vector meson production and decay

In a semi-inclusive measurement of deep-inelastic scattering, decay products of exclusive vector meson production are a $\frac{1}{Q}$-suppressed contribution to the cross section. This contribution is accounted for in the factorisation proofs and limited in the measurement by the requirement of $z < 0.7$ on the fractional hadron energy. However, the possible influence of exclusive channels is subject of extensive discussions and thus studied in detail.

The fraction of π-mesons and K-mesons originating from exclusive production and decay of ρ^0, ω and ϕ mesons is estimated from a PYTHIA simulation tuned for HERMES kinematics. In every bin in x, z and $\mathbf{P}_{h\perp}$, the fraction of charged pions is significantly larger than the one of charged
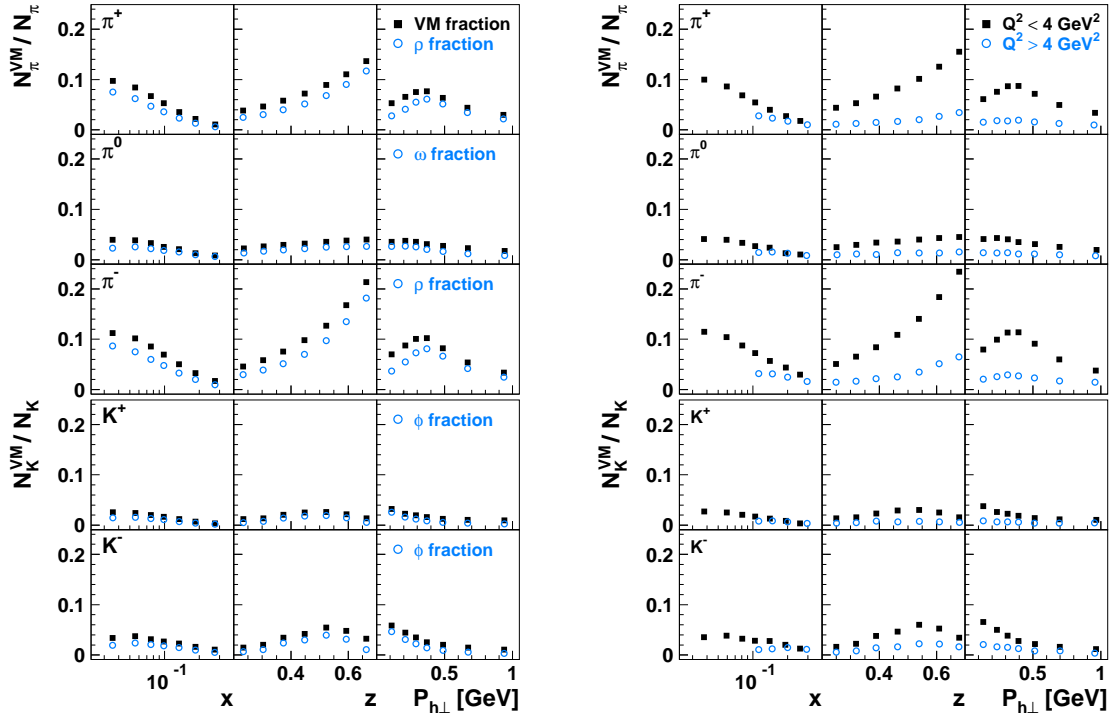
Figure 5.15.: Simulated fraction of decay products of exclusive vector meson production: In the left panel, the fraction (black closed symbols) is given for pions and charged kaons in addition to the fraction of the only dominant contribution (blue open symbols). The fraction for the ranges $Q^2 < 4\,\mathrm{GeV}^2$ (black closed symbols) and $Q^2 > 4\,\mathrm{GeV}^2$ (blue open symbols) is provided in the right panel.

kaons (figure 5.15). The overall fraction is about 6%–7% for charged pions and about 2%–3% for charged kaons. In particular for charged pions, a strong increase with z is observed. By raising the requirement on Q^2, the fraction of decay products can be suppressed (right panel of figure 5.15). Due to the correlation of the scaling variables x and Q^2, a decrease of the fraction with x is found.

Given the small fraction of K^+ stemming from exclusive vector meson production and decay, the significant SSA amplitudes for K^+ provide some indication that the measurement of transverse single-spin asymmetries is not dominated by exclusive channels. Also no influence from decay products is seen when comparing SSA amplitudes for the region $Q^2 < 4\,\mathrm{GeV}^2$ and the region $Q^2 > 4\,\mathrm{GeV}^2$, where the contribution from exclusive channels is suppressed.

The largest fraction of decay products is estimated for charged pions originating from exclusive ρ^0 production and the decay into $\pi^+\pi^-$ pairs. This contribution can be removed from the selected charged pion events by extracting pion-difference asymmetries:

$$A_{\mathrm{UT}}^{\pi^+ - \pi^-} = \frac{\left(\sigma_{\mathrm{U}\Uparrow}^{\pi^+} - \sigma_{\mathrm{U}\Uparrow}^{\pi^-}\right) - \left(\sigma_{\mathrm{U}\Downarrow}^{\pi^+} - \sigma_{\mathrm{U}\Downarrow}^{\pi^-}\right)}{\left(\sigma_{\mathrm{U}\Uparrow}^{\pi^+} - \sigma_{\mathrm{U}\Uparrow}^{\pi^-}\right) + \left(\sigma_{\mathrm{U}\Downarrow}^{\pi^+} - \sigma_{\mathrm{U}\Downarrow}^{\pi^-}\right)}, \tag{5.16}$$

i.e. the SSA in the difference in the cross section for the semi-inclusive measurement of π^+ and π^-. The pion-difference SSA can be reconstructed via two methods:

❑ Using the maximum likelihood based reconstruction method, the pion-difference SSA amplitudes are extracted from the charged pion events by assigning an extra weight of -1 for each π^- event.
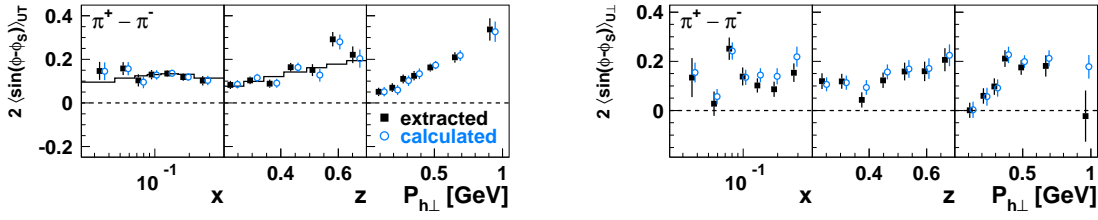
Figure 5.16.: Sivers amplitudes of the pion-difference asymmetry: The extraction (black closed symbols) and calculation (blue open symbols) of pion-difference SSA is compared. In the left panel, pion-difference Sivers amplitudes are reconstructed from a GMC_TRANS Monte Carlo simulation. For the dependence on x and z, also the implemented Sivers amplitudes are shown in addition to the reconstructed one. In the right panel, the pion-difference Sivers amplitudes of the recorded data is shown.

❑ Using the spin-independent cross-section ratio C for the electroproduction of π^+ and π^-, the transverse single-spin asymmetries of the pion-difference SSA can be calculated from the asymmetries for π^+ and π^-:

$$A_{U\perp}^{\pi^+-\pi^-} = \frac{1}{1-C} A_{U\perp}^{\pi^+} - \frac{C}{1-C} A_{U\perp}^{\pi^-}, \quad C = \frac{\sigma_{UU}^{\pi^-}}{\sigma_{UU}^{\pi^+}}. \tag{5.17}$$

When calculating the pion-difference SSA for simulated data, the cross section ratio C can be obtained. For reconstructed data, it can be determined in good approximation from the ratio $C \approx \frac{N^{\pi^-}}{N^{\pi^+}}$ of count rates for π^+ and π^-.

A good agreement of reconstruction methods is found for both simulated and recorded data (figures 5.16 and 5.17). The differences in extracting and calculated pion-difference SSA are attributed to the values of C not exactly known for both the simulated and recorded data. In the simulation, constant values have to be applied for all bins, whereas the C values can be approximated from the count N^{π^+} and N^{π^-} of charged pions in the measurement.

In addition to the large SSA amplitudes for K^+ and the observation of consistent SSA amplitudes in the ranges $Q^2 \lessgtr 4\,\text{GeV}^2$, the significant $2\langle\sin(\phi+\phi_S)\rangle_{U\perp}^h$, $2\langle\sin(\phi-\phi_S)\rangle_{U\perp}^h$ and $2\langle\sin(\phi_S)\rangle_{U\perp}^h$ amplitudes of the pion-difference asymmetries give further evidence for no influence of exclusive channels on the measurement of transverse single-spin asymmetries.
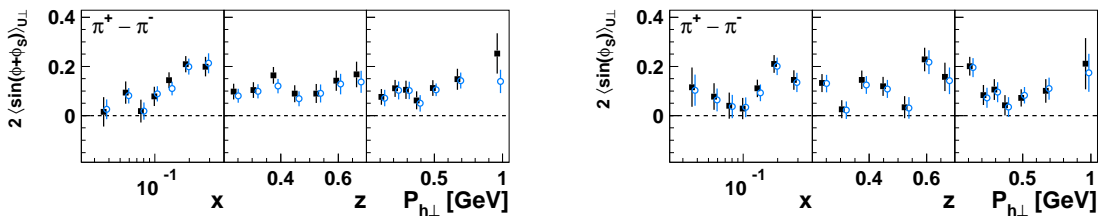

Figure 5.17.: Collins and $2\langle\sin(\phi_S)\rangle_{U\perp}^h$ amplitudes of the pion-difference asymmetry: The extraction (black closed symbols) and calculation (blue open symbols) of the Collins amplitudes (left panel) and $2\langle\sin(\phi_S)\rangle_{U\perp}^h$ amplitudes (right panel) of the pion-difference SSA is compared for recorded data.
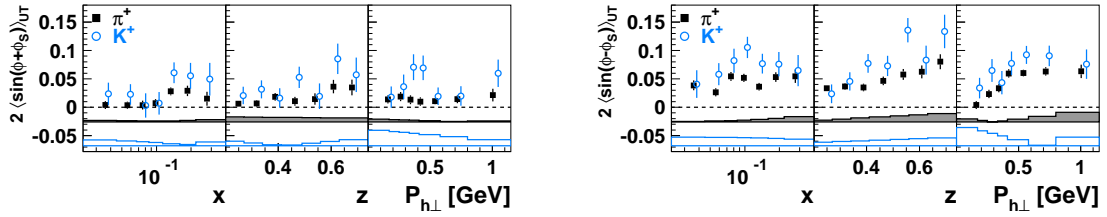
Figure 5.18.: The $K^+ - \pi^+$ difference: Collins (left panel) and Sivers amplitudes (right panel) for charged pions (black closed symbols) and kaons (blue open symbols) are compared.

5.4. The difference in the Collins and Sivers SSA for positively charged pions and kaons

In the interpretation of deep-inelastic scattering measurements on a proton target, the scattering off u quarks is commonly assumed to be the dominant contribution. This assumption is, e.g, supported by the HERMES measurement of the double-spin asymmetry A_1^h,

$$A_1^h(x,z) = \frac{\sum_q e_q^2 g_1^q(x) D_1^q(z)}{\sum_q e_q^2 f_1^q(x) D_1^q(z)}, \tag{5.18}$$

in the electroproduction of $\pi^+ = |u\bar{d}\rangle$ and $K^+ = |u\bar{s}\rangle$ [HERMES05b]. In the analysis of the double-spin asymmetries for $A_1^{\pi^+}$ and $A_1^{K^+}$ the contributions from u quarks is found as the dominant contribution due to their electric-charge factors, $e_u = 2/3$, and their large densities $f_1^u(x)$ in the proton ($p = |uud\rangle$). The double-spin asymmetries $A_1^{\pi^+}$ and $A_1^{K^+}$ are signals for mainly the u-quark polarisation, $g_1^u(x)/f_1^u(x)$. In the assumption of u-quark dominance, only this term is considered in the interpretation.

On the basis of u-quark dominance, similar SSA amplitudes are expected for positively charged pions and kaons. But the extracted Collins and Sivers amplitudes for K^+ are found to be larger than those for π^+ (figure 5.18). Also differences are seen in the Collins and Sivers amplitudes for π^+ and protons (figure 5.19) as well as K^+ and protons. In the interpretation of the SSA amplitudes for protons, the assumption of u-quark dominance is hampered by the poorly understood role of diquarks in the electroproduction of protons. Thus, the focus is put on positively charged pions and kaons only.

Before discussing in chapter 6 the implications of the observed difference, effects on the $K^+ - \pi^+$ difference due to the identification of hadrons or the possible influence of target remnant fragmentation are studied using the Sivers amplitudes as example.
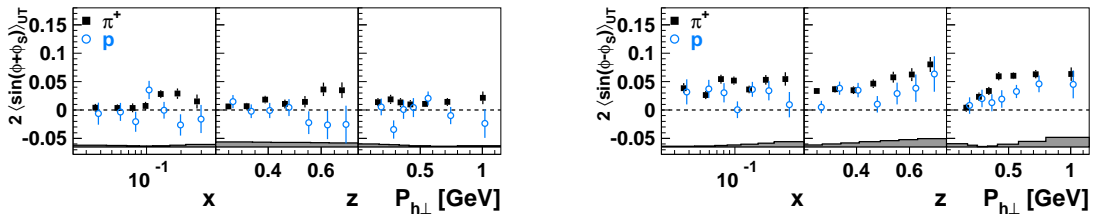

Figure 5.19.: The $p - \pi^+$ difference: Collins (left panel) and Sivers amplitudes (right panel) for charged pions (black closed symbols) and protons (blue open symbols) are compared.

Analogue to the discussion of higher twist contributions (section 5.3), the Sivers amplitudes for positively charged pions and kaons are compared for various ranges in Q^2:

❑ In the comparison at a lower scale, the x-dependence is presented for $Q^2 < \langle Q^2(x) \rangle$ and the additional requirement of $Q^2 < 4\,\mathrm{GeV}^2$ is imposed for the dependence on z and $|\mathbf{P}_{h\perp}|$.

❑ Correspondingly, the higher scale is defined as $Q^2 > \langle Q^2(x) \rangle$ and $Q^2 > 4\,\mathrm{GeV}^2$.

To analyse the difference in the π^+ and K^+ Sivers amplitudes, the hypothesis of their consistency is tested via the Student's t-test, in which contrary to χ^2-tests the sign of the deviation can be regarded. In a given bin i, the deviation d_i [1] is evaluated:

$$d_i = \frac{2\,\langle \sin(\phi - \phi_S) \rangle_{U\perp,i}^{K^+} - 2\,\langle \sin(\phi - \phi_S) \rangle_{U\perp,i}^{\pi^+}}{\sqrt{\sigma^2_{2\langle \sin(\phi - \phi_S) \rangle_{U\perp,i}^{K^+}} + \sigma^2_{2\langle \sin(\phi - \phi_S) \rangle_{U\perp,i}^{\pi^+}}}}. \tag{5.19}$$

From the deviation's mean value $\langle d \rangle$ in $n = 7$ bins in x, z or $|\mathbf{P}_{h\perp}|$ and the accordant standard deviation σ_d the Student's t is calculated:

$$t = \sqrt{n}\,\frac{\langle d \rangle - \mu(d)}{\sigma_d}, \tag{5.20}$$

by using the null hypothesis for the expectation $\mu(d)$. The null hypothesis, $\mu(d) = 0$, corresponds to an ideal consistency of the π^+ and K^+ Sivers amplitudes and can be rejected (accepted) when the calculated Student's t is greater (less) than the Student's t for a chosen confidence level as, e.g., listed in table 5.3.

confidence level	corresponding Student's t
85%	1.134
90%	1.440
95%	1.943
99%	3.143

Table 5.3.: Student's t-values for $n - 1 = 6$ degrees of freedom and selected confidence levels.

Changes of the mean deviation within the statistical accuracy of the measurement can be estimated using the Student's t-distribution. In the Student's t-test, the probable error $\delta \langle d \rangle$ of a mean is given according to the t-value for a chosen confidence level:

$$\delta \langle d \rangle = \frac{\sigma_d}{\sqrt{n}}\,t. \tag{5.21}$$

----

[1] The sum over the squared deviations of all bins in x, z or $|\mathbf{P}_{h\perp}|$ can be identified as a χ^2.
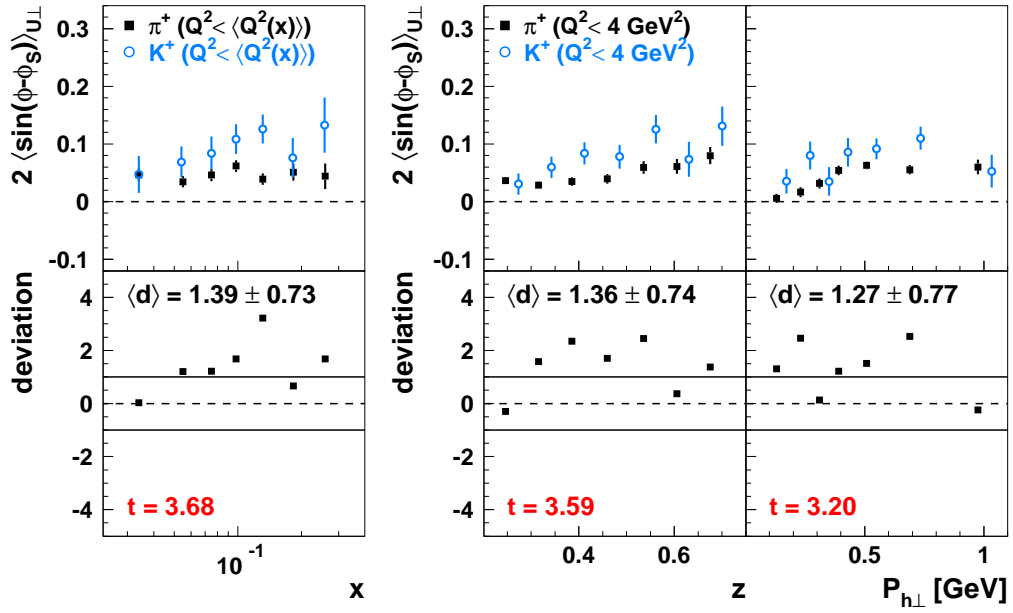
Figure 5.20.: Investigation of $K^+ - \pi^+$ difference at a lower scale: The Sivers amplitudes for positively charged pions (black closed symbols) and kaons (blue open symbols) are compared for $Q^2 < \langle Q^2(x) \rangle$ and $Q^2 < 4\,\mathrm{GeV}^2$ in the upper panel. In the lower panel the corresponding deviations are shown including estimates of their statistical significance.

In figures 5.20 and 5.21, the Sivers amplitudes for positively charged pions and kaons are compared at a lower scale (figure 5.20) and a higher scale (figure 5.21). The corresponding mean deviation is given in addition to results of the Student's t-test. The difference observed at a lower scale cannot be attributed to statistical fluctuations. At a confidence level of 95%, a non-zero mean deviation $\langle d \rangle$ is found for the x, z and $|\mathbf{P}_{h\perp}|$ dependence. Also the Student's t-values are greater than the value of $t = 1.943$ for 95% confidence level:

kinematic dependence:	mean deviation:	Student's t:
x	$\langle d \rangle = 1.39 \pm 0.73$	$t = 3.68$
z	$\langle d \rangle = 1.36 \pm 0.74$	$t = 3.59$
$|\mathbf{P}_{h\perp}|$	$\langle d \rangle = 1.27 \pm 0.77$	$t = 3.20$

Table 5.4.: Results of the Student's t-test at the lower scale.

The statistically significant difference vanishes at the higher scale where the mean deviation $\langle d \rangle$ is consistent with zero and the Student's t is less than 1.943:

kinematic dependence:	mean deviation:	Student's t:
x	$\langle d \rangle = 0.33 \pm 0.57$	$t = 1.11$
z	$\langle d \rangle = 0.21 \pm 1.07$	$t = 0.38$
$|\mathbf{P}_{h\perp}|$	$\langle d \rangle = 0.20 \pm 1.15$	$t = 0.34$

Table 5.5.: Results of the Student's t-test at the higher scale.

The kinematic distributions of π^+ and K^+ are in good agreement and the small differences in certain kinematic regions can neither explain the difference in the Sivers amplitudes at a lower scale
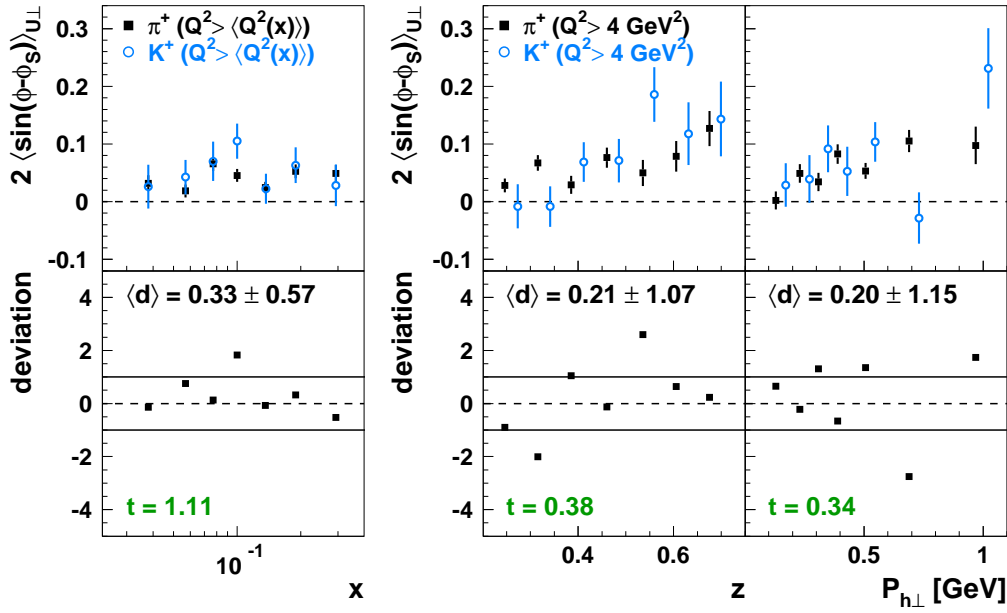
Figure 5.21.: Investigation of $K^+ - \pi^+$ difference at a higher scale: The Sivers amplitudes for positively charged pions (black closed symbols) and kaons (blue open symbols) are compared for $Q^2 > \langle Q^2(x) \rangle$ and $Q^2 > 4\, \mathrm{GeV}^2$ in the upper panel. In the lower panel the corresponding deviations are shown including estimates of their statistical significance.

nor the inconsistency between the lower and the higher scale. Thus, the $K^+ - \pi^+$ difference must be either related to unknown properties of the Sivers mechanism or caused by instrumental effects.

The hadron identification using the RICH detector can affect the (in)consistency of the Sivers amplitudes. Apart from a systematic misidentification of positively charged pion and kaon tracks also a dependence of the RICH PID on the scattering angle and thus an implicit dependence on Q^2 might influence the (in)consistency. These effects are studied by examining the impact of the reconstruction method and the event topology in the RICH detector on the $K^+ - \pi^+$ difference and investigating the dependence on the hadron energy for various scales:

❑ Hadrons are identified using the DRT/EVT reconstruction method (section 4.1.5). The event-level based method substituted the track-level based IRT method due to the improved hadron identification in case of multiple track topologies. The results obtained with the IRT and DRT/EVT reconstruction methods give similar results as a function of z and $|\mathbf{P}_{h\perp}|$: An inconsistency of the π^+ and K^+ Sivers amplitudes is found at a lower scale (figure 5.22) and a consistency is observed at a higher scale (figure 5.23). But there is an disagreement for the x-dependence where using IRT the inconsistency vanishes at a lower scale (figure 5.22) and appears at a higher scale (figure 5.23). However, the comparison of the reconstruction methods is hampered by the dependence of IRT on the horizontal track position (section 3.3.2).

❑ To study the possible influence of overlapping signals in the RICH detector, the event topology is determined only from the number of hadron tracks passing a detector half and not from the number of lepton and hadron tracks as done for the RICH unfolding (section 4.1.5). In 65.5% (66.5%) of the π^+ (K^+) events, the single track topology is observed where a single π^+ (K^+) is identified in one detector half. When more hadrons are found in a detector half (34.5% (33.5%) of the π^+ (K^+) events), the multiple track topology is given. For the single track
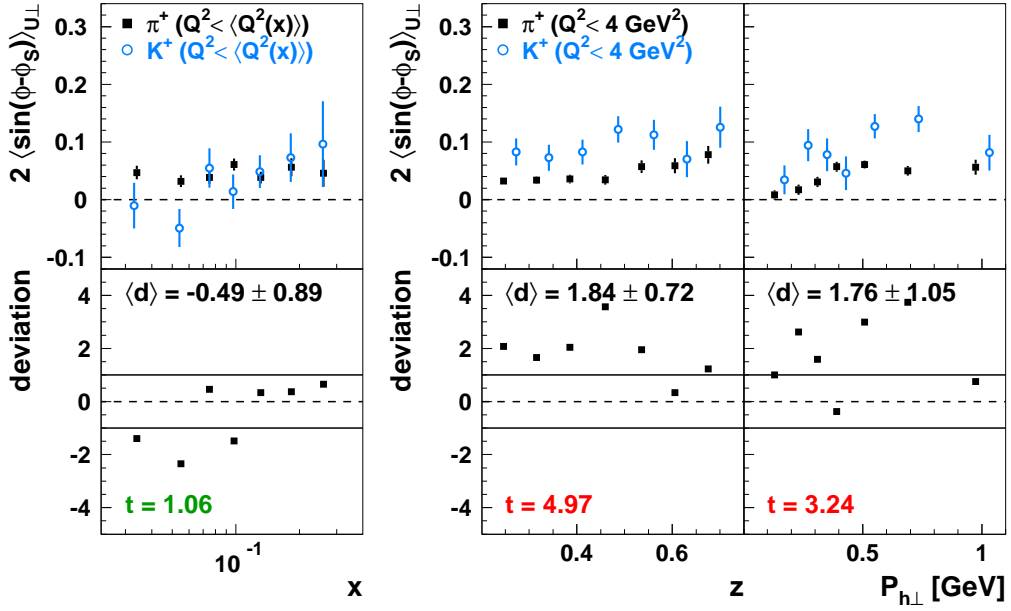
Figure 5.22.: Investigation of the $K^+ - \pi^+$ difference at a lower scale: The same comparison as in figure 5.20 is shown for an extraction of SSA amplitudes using the IRT instead of the DRT/EVT reconstruction method of the RICH PID.

topology rings of the induced photons cannot overlap and thus the efficiency of the hadron identification is larger than the one of the multiple track topology.

The $K^+ - \pi^+$ difference is investigated for solely the single track topology (figures 5.24 and 5.25) and the multiple track topology (figures 5.26 and 5.27). An agreement with the results without constraints on the event topology (figures 5.20 and 5.21) is obtained. Only for the single track topology at a lower scale a disagreement, i.e. a consistency instead of an inconsistency, is found for the Sivers amplitudes as a function of $|\mathbf{P}_{h\perp}|$. Also at a lower scale but for the multiple track topology an interesting facet is observed: The Sivers amplitudes for K^+ increase with x, whereas the Sivers amplitudes of π^+ are constant in the range $x \in\,]0.023; 0.113]$ and decrease with x in the range $x \in\,]0.113; 0.400]$.

❑ The energy of hadrons inducing Čerenkov radiation in the RICH detector is related to the detected pattern of Čerenkov photons. A dependence of the Sivers amplitudes on the unphysical variable hadron energy different for various scales would reveal an instrumental effect on the $K^+ - \pi^+$ difference. The Sivers amplitudes as a function of the hadron energy are in good agreement for $Q^2 > 1\,\mathrm{GeV}^2$ and $1 < Q^2 < 4\,\mathrm{GeV}^2$ and compatible with those for $Q^2 > 4\,\mathrm{GeV}^2$ (figure 5.30).

In those studies no evidence for an influence of the hadron identification on the $K^+ - \pi^+$ difference is provided. Also in a Monte Carlo simulation including the RICH PID no indication is found: A consistency of the π^+ and K^+ Sivers amplitudes is introduced by applying the model for the Sivers mechanism of π^+ not only for pion tracks but also for kaon and proton tracks. Sivers amplitudes are reconstructed in the HERMES acceptance using the generated hadron information and the simulated RICH PID. A consistency of the reconstructed Sivers amplitudes is expected and seen in the simulation with a perfect hadron identification and a hadron identification as in the measurement (figures 5.28 and 5.29). Neither at a lower scale nor at a higher scale a $K^+ - \pi^+$ difference appears.
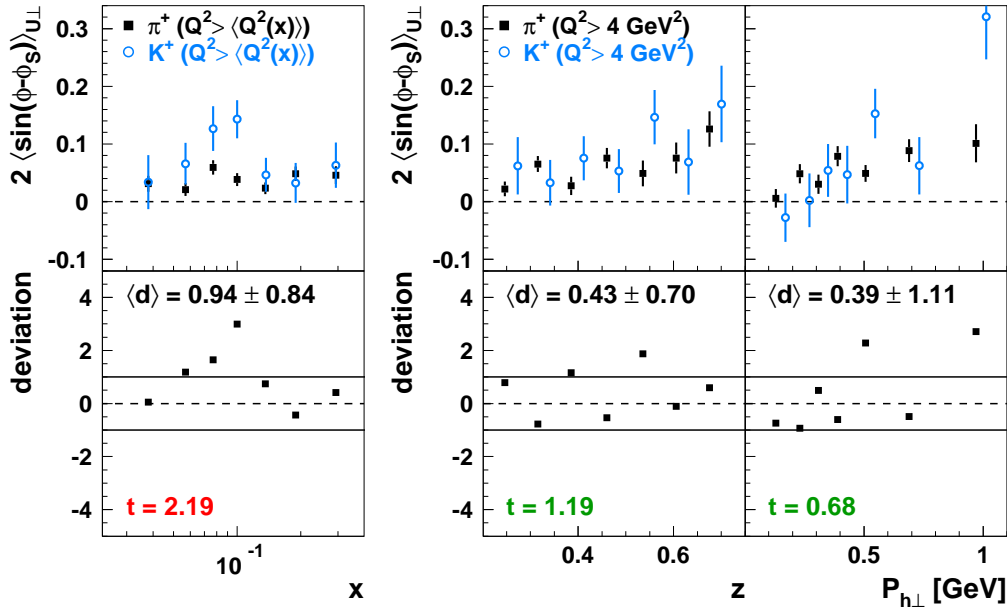
Figure 5.23.: Investigation of the $K^+ - \pi^+$ difference at a higher scale: The same comparison as in figure 5.21 is shown for an extraction of SSA amplitudes using the IRT instead of the DRT/EVT reconstruction method of the RICH PID.

In addition to the studies on the hadron identification also the effect of the target remnant is analysed. The criterion presented by Berger [Ber87] enables a separation between the target and current fragmentation regions when requiring that the squared invariant mass W^2 of the virtual-photon nucleon system and the fractional hadron energy z are above the values:

$$z > 0.2, \quad W^2 > 24 \, \text{GeV}^2. \tag{5.22}$$

In the presented analysis of transverse single-spin asymmetries the requirements (section 4.1.7):

$$z > 0.2, \quad W^2 > 10 \, \text{GeV}^2, \tag{5.23}$$

have been used. This distinction between the target fragmentation and current fragmentation regions can be enhanced by increasing the requirement on W^2. For the Sivers amplitudes no strong dependence on W^2 is found (figure 5.31). The Sivers amplitudes for $W^2 > 25 \, \text{GeV}^2$ are in agreement with the Sivers amplitudes for $W^2 < 25 \, \text{GeV}^2$ (figure 5.31). In the comparison of the Sivers amplitudes for these ranges in W^2 no indication for a target remnant effect is seen. But this comparison is hampered by the correlation of the scaling variables x, Q^2 and W^2. Thus, the results for $W^2 < 25 \, \text{GeV}^2$ and $W^2 > 25 \, \text{GeV}^2$ are not explicitly presented for a lower and higher scale.

Possible influences on the $K^+ - \pi^+$ difference due to the identification of hadrons or the target remnant are ruled out. Even though other instrumental effects might affect this interesting facet of the π^+ and K^+ Sivers and also Collins amplitudes, an indication for physical phenomena causing the $K^+ - \pi^+$ difference is found. Possible implications on the Collins and Sivers mechanism will be discussed in chapter 6.

Chapter 5

Figure 5.24.: Investigation of the $K^+ - \pi^+$ difference at a lower scale: The same comparison as in figure 5.20 is shown for an extraction of SSA amplitudes when requiring solely single track topology in a RICH detector's half.

Figure 5.25.: Investigation of the $K^+ - \pi^+$ difference at a higher scale: The same comparison as in figure 5.21 is shown for an extraction of SSA amplitudes when requiring solely single track topology in a RICH detector's half.
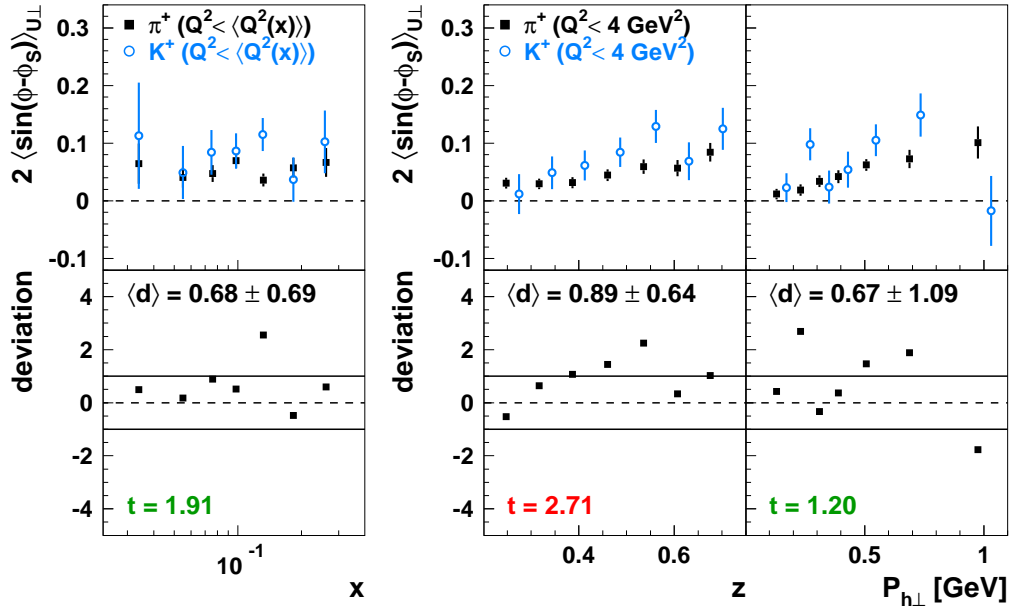
Figure 5.26.: Investigation of the $K^+ - \pi^+$ difference at a lower scale: The same comparison as in figure 5.20 is shown for an extraction of SSA amplitudes when requiring solely multiple track topology in a RICH detector's half.
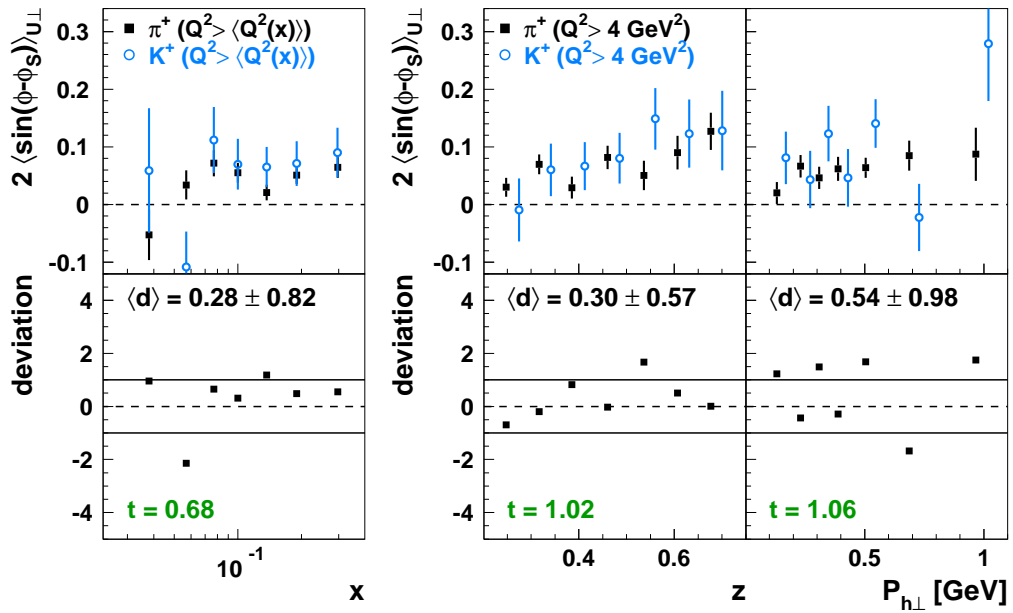

Figure 5.27.: Investigation of the $K^+ - \pi^+$ difference at a higher scale: The same comparison as in figure 5.21 is shown for an extraction of SSA amplitudes when requiring solely multiple track topology in a RICH detector's half.
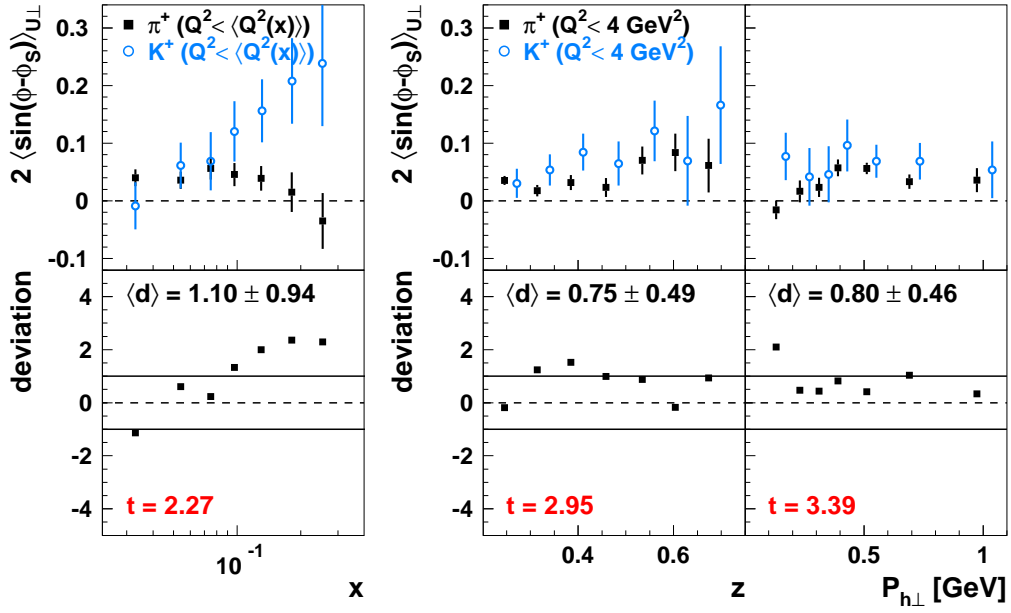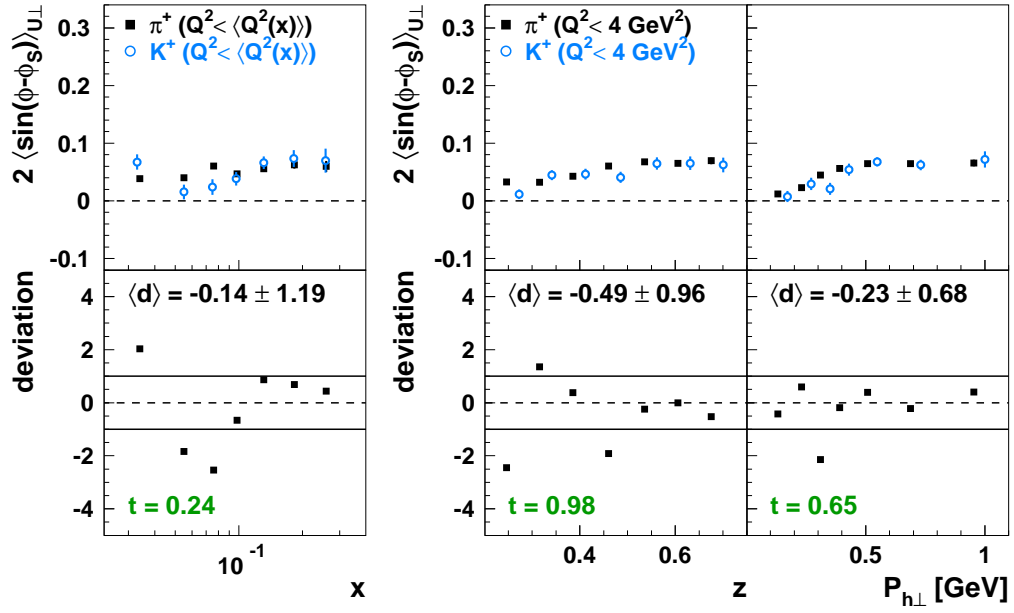
Figure 5.28.: Investigation of the $K^+ - \pi^+$ difference at a lower scale: The same comparison as in figure 5.20 is shown for an extraction of SSA amplitudes from a Monte Carlo simulation including the RICH PID.
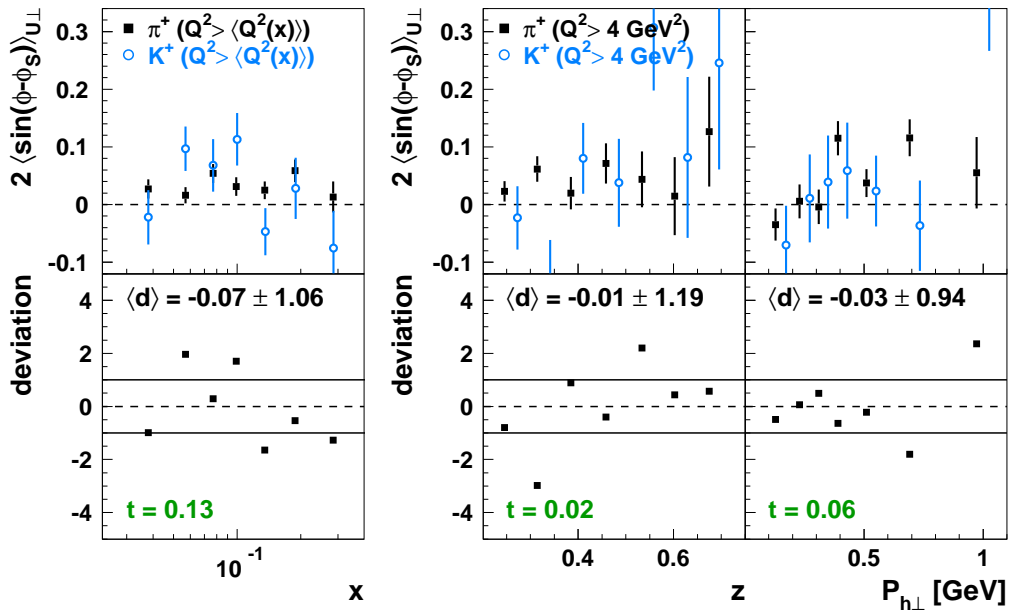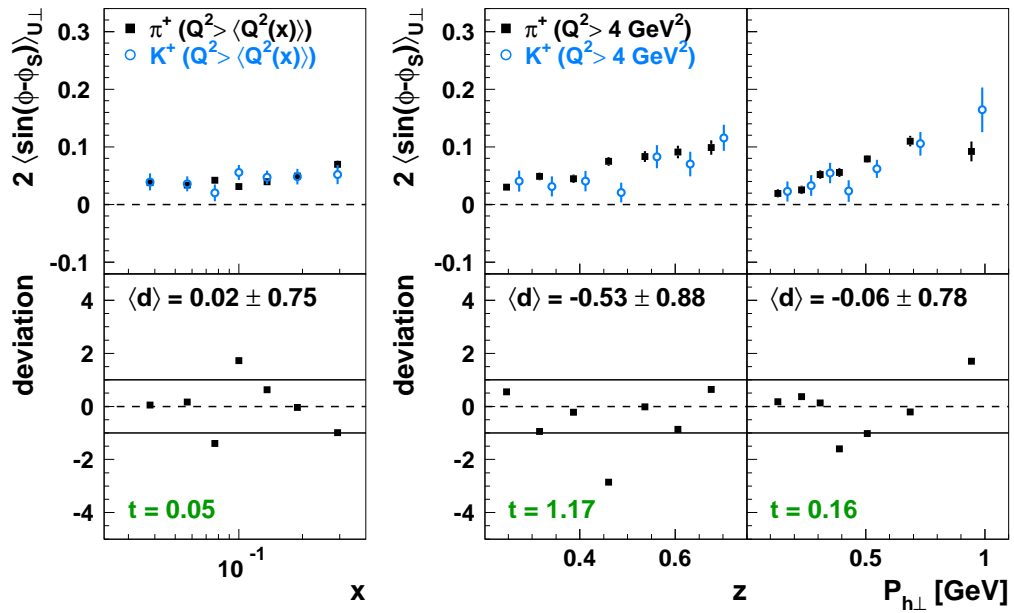

Figure 5.29.: Investigation of the $K^+ - \pi^+$ difference at a higher scale: The same comparison as in figure 5.21 is shown for an extraction of SSA amplitudes from a Monte Carlo simulation including the RICH PID.
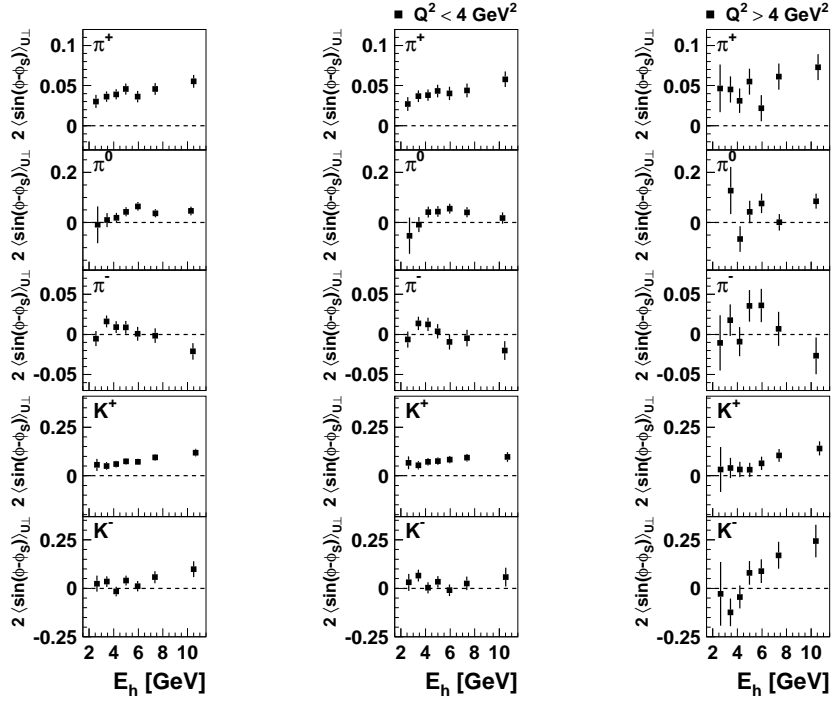
Figure 5.30.: In the left panel Sivers amplitudes for π-mesons and charged K-mesons are shown as a function of the hadron energy E_h. The same dependence of the Sivers amplitudes is presented in the centre panel for $Q^2 < 4\,\mathrm{GeV}^2$ and in the right panel for $Q^2 > 4\,\mathrm{GeV}^2$.
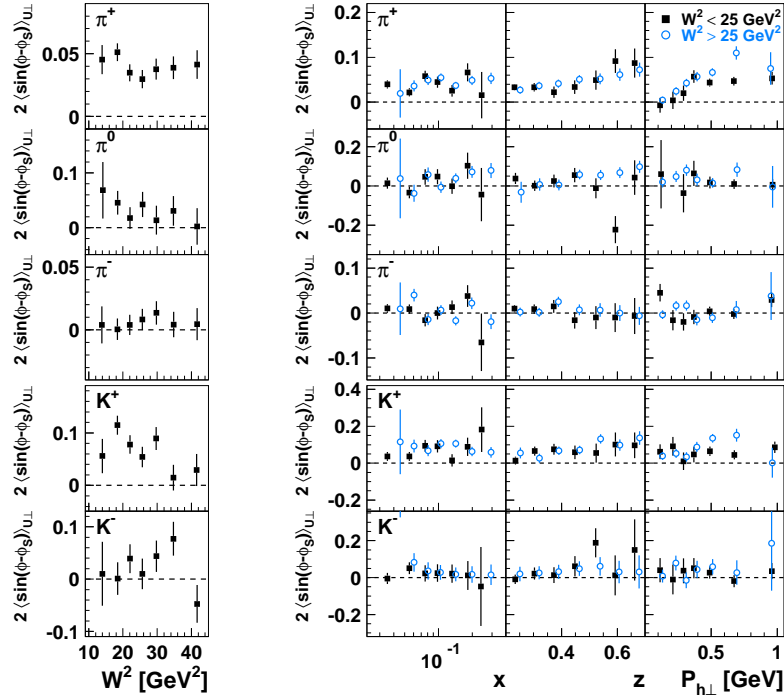
Figure 5.31.: Excluding target remnant effects: In the left panel the dependence of the Sivers amplitudes on W^2 is shown. In the right panel Sivers amplitudes are compared for $W^2 < 25\,\mathrm{GeV}^2$ and $W^2 > 25\,\mathrm{GeV}^2$.

5. The analysis of the measured SSA

6. The interpretation of the measured SSA

The analysis of transverse-momentum dependent quark distribution functions (TMD), which are related to spin-orbit correlations of the quarks within the nucleon, is an active field of research. On the experimental side, information about TMD is provided in semi-inclusive measurements of deep-inelastic scattering. In this process, transverse-momentum dependent effects cause distinctive signatures for TMD in the azimuthal distribution of the hadrons produced.

In chapters 4 and 5, a Fourier analysis of azimuthal single-spin asymmetries A_{UT}^h is presented. The single-spin asymmetries (SSA) are studied in a semi-inclusive measurement of deep-inelastic scattering of longitudinally polarised (L) positrons and electrons off a transversely polarised proton target (T). The lepton beam can be considered as unpolarised (U) as the data recorded is balanced with respect to the beam helicity states. The extracted Fourier components, denoted as SSA amplitudes, can be interpreted as convolution in transverse momentum space of transverse-momentum dependent distribution and fragmentation functions. In the Fourier decomposition, three SSA amplitudes provide leading-twist signals for the naive-T-odd Sivers functions (section 6.1) and the chiral-odd transversity (section 6.2) and pretzelosity distributions (section 6.3). Two other SSA amplitudes are related to subleading-twist contributions (section 6.4).

A subtlety in the analysis allows for the study of the worm-gear distributions (section 6.5). As the HERMES target was transversely polarised with respect to the beam direction, a small longitudinal target spin component arises with respect to the virtual-photon direction. The associated SSA amplitude provides sensitivity to $h_{1L}^{\perp,q}\left(x,\mathbf{p}_T^2\right)$. The other worm-gear distribution, $g_{1T}^{\perp,q}\left(x,\mathbf{p}_T^2\right)$, is studied in a Fourier analysis of double-spin asymmetries A_{LT}^h (section 6.5), which can be reconstructed when taken the longitudinal polarisation of the HERA lepton beam into account.

In the analysis, the deep-inelastic scattering process is characterised by variables calculated from the kinematics of the HERA lepton beam and the scattered leptons. Thus, SSA amplitudes of lepton-beam asymmetries are extracted, which contrary to the virtual-photon asymmetries used in theoretical calculations depend on the lepton kinematics. In particular, the polarisation of the virtual photon is given by the lepton kinematics. At present it is, however, impossible to obtain amplitudes of virtual-photon asymmetries from the extracted SSA amplitudes as they require a separation of their longitudinal and transverse components, which is only possible if semi-inclusive measurements of deep-inelastic scattering are performed at the same kinematics with various beam energies.

The SSA amplitudes for π-mesons and charged K-mesons are presented as functions of the Bjorken scaling variable x, the fractional meson energy z and the transverse meson momentum $|\mathbf{P}_{h\perp}|$ in the kinematic region:

$$0.023 < x < 0.4, \quad 0.2 < z < 0.7, \quad 0.0\,\mathrm{GeV} < |\mathbf{P}_{h\perp}| < 2.0\,\mathrm{GeV}. \tag{6.1}$$

The corresponding mean kinematic values are listed in table 6.1.

The error bars in the plots indicate the statistical uncertainties of the SSA amplitudes. The grey error bands represent the systematic uncertainties of the results arising from acceptance effects, finite detector resolution, higher order QED effects, a possible misidentification of hadrons and the non-vanishing cross-section contribution σ_{UL}^h (section 5.1). In addition, there is a scale uncertainty of 7.3% on the SSA amplitudes due to uncertainties in the measurement of the target polarisation.

meson	kinematic mean values				
	$\langle Q^2 \rangle$	$\langle x \rangle$	$\langle y \rangle$	$\langle z \rangle$	$\langle |\mathbf{P}_{h\perp}| \rangle$
π^+	$2.420\,\text{GeV}^2$	0.094	0.545	0.363	$0.394\,\text{GeV}$
π^0	$2.454\,\text{GeV}^2$	0.087	0.590	0.393	$0.441\,\text{GeV}$
π^-	$2.344\,\text{GeV}^2$	0.091	0.549	0.354	$0.393\,\text{GeV}$
K^+	$2.497\,\text{GeV}^2$	0.095	0.552	0.394	$0.419\,\text{GeV}$
K^-	$2.365\,\text{GeV}^2$	0.087	0.572	0.359	$0.414\,\text{GeV}$

Table 6.1.: Mean kinematic values for π-mesons and charged K-mesons.

6.1. Evidence for the naive-T-odd Sivers function

6.1.1. A semi-classical picture of the Sivers mechanism

The experimental study of the Sivers mechanism in various processes is of particular interest in order to analyse the Wilson line formalism and its consequences in factorisation proofs and the concept of universality. The naive-T-odd Sivers function describes the distribution of unpolarised quarks in a transversely polarised nucleon. It entails an asymmetry in transverse momentum space via a spin-orbit correlation, $S_T^i \varepsilon^{ij} p_T^j$, between the transverse polarisation of the nucleon and the transverse momentum of the quarks. An observation of non-vanishing Sivers amplitudes is related to orbital angular momentum of the quarks within the nucleon.

The Sivers mechanism can be illustrated in a model for quark distributions in impact parameter space [Bur02]. In this semi-classical model, the transverse-position dependence of quark distribution functions is studied instead of their transverse-momentum dependence. The position $\mathbf{b}_\perp = (b_x, b_y)$ of the quarks is defined with respect to the nucleon's transverse centre of momentum.

Unpolarised quarks within a transversely polarised nucleon are probed in a semi-inclusive measurement of deep-inelastic scattering at fixed values of x given by the lepton kinematics. In a frame, where the nucleon is at rest, the orbiting quarks move towards the virtual photon on one side of the nucleon and away on the other side. In the infinite momentum frame, the observed momentum fraction x has two components: one from the longitudinal motion of the quarks and the other from the orbital motion of the quarks. The quarks moving towards the virtual photon carry a smaller fraction of the nucleon's longitudinal momentum than those moving away. Quark distribution functions strongly depend on the Bjorken scaling variable x. Thus, the interaction probability with the virtual photon is enhanced on one side and reduced on the other side resulting in a spatial asymmetry in quark distributions. The transverse distortion due to quark orbital angular momentum is presented in figure 6.1. In the first (third) column, the distribution of unpolarised u (d) quarks in an unpolarised target is shown at fixed values of x. The grey scale of each panel is normalised to the central slice. The transverse position space is limited by the momentum fraction. In the second (fourth) column, the distributions of unpolarised u (d) quarks in a transversely polarised proton are shown. At larger values of x, the distribution are shifted perpendicular to the spin of the nucleon (pointing to the right) and its momentum (pointing into the page. The shift for u and d quarks is in opposite directions.

After the interaction with the virtual photon, the quark moves away and is thereby attracted towards the nucleon's centre of momentum (along the direction of the virtual photon) due to an interaction with the colour field of the remaining spectators (figure 6.2). As a result, the struck quark and thus also the quark jet is deflected towards the opposite side. Due to the final-state interaction, the spatial asymmetry of the quark distribution function is transferred into an azimuthal asymmetry of the produced hadrons with respect to the transverse polarisation of the nucleon. The SSA of the Sivers mechanism is manifested as $\sin(\phi - \phi_S)$ modulation in the cross section.
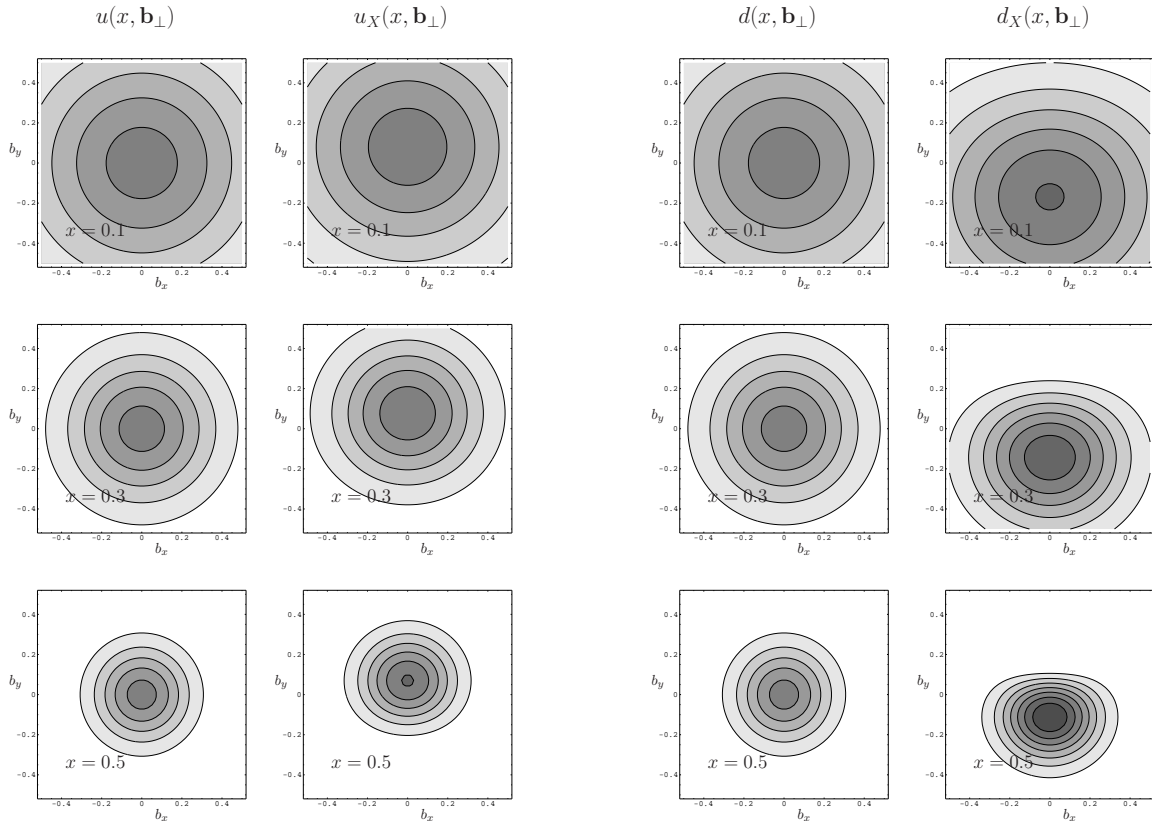
Figure 6.1.: Transverse distortion of impact-parameter dependent quark distributions in a transversely polarised nucleon [Bur02]: In the first (third) column the impact parameter dependence of the distribution of unpolarised *u* (*d*) quarks in a longitudinally nucleon is shown at fixed values of *x*. In the second (fourth) column the same dependence is given for the distribution of unpolarised *u* (*d*) quarks in a transversely polarised nucleon.
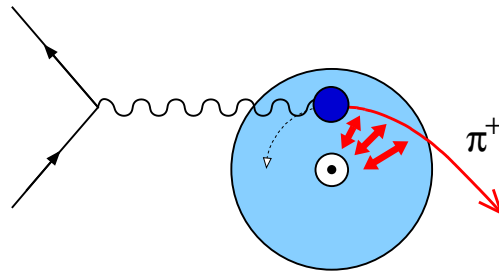
Figure 6.2.: Semi-classical picture of the Sivers mechanism: The scattering off a *u* quark is illustrated in a nucleon polarised perpendicular to the lepton scattering plane ($\phi_S = \pi/2$). The distortion of quark distributions in a transversely polarised nucleon and the chromodynamical lensing [Bur04a] due to an attractive interaction in the final state lead to a single-spin azimuthal asymmetry. The π^+-mesons produced in the final state, e.g., are observed on the right-hand side of the nucleon ($\phi = \pi$) resulting in a positive Sivers amplitude.

Chapter 6

6.1.2. The Sivers amplitude

In a semi-inclusive measurement of deep-inelastic scattering, the $\sin(\phi - \phi_S)$ modulation appears in the differential cross section (equation 2.24) as azimuthal modulation of the extended structure functions $F_{\mathrm{UT,T}}^{\sin(\phi-\phi_S)}$ and $F_{\mathrm{UT,L}}^{\sin(\phi-\phi_S)}$:

$$\frac{d\sigma^h}{dx\,dy\,d\phi_S\,dz\,d\phi\,d\mathbf{P}_{h\perp}^2} \propto \dots + S_T\left[\sin(\phi - \phi_S)\left(F_{\mathrm{UT,T}}^{\sin(\phi-\phi_S)} + \varepsilon F_{\mathrm{UT,L}}^{\sin(\phi-\phi_S)}\right) + \dots\right] + \dots \quad (6.2)$$

At leading- and subleading-twist accuracy and in the one-photon exchange approximation, the structure function $F_{\mathrm{UT,T}}^{\sin(\phi-\phi_S)}$ can be interpreted as convolution in transverse momentum space of the Sivers function, $f_{1\mathrm{T}}^{\perp,q}(x,\mathbf{p}_T^2)$, and the spin-independent fragmentation function, $D_1^q(z,z^2\mathbf{k}_T^2)$:

$$F_{\mathrm{UT,T}}^{\sin(\phi-\phi_S)} = \mathscr{C}\left[-\frac{\hat{\mathbf{h}}\cdot\mathbf{p}_T}{M}\,f_{1\mathrm{T}}^{\perp,q}(x,\mathbf{p}_T^2)\,D_1^q(z,z^2\mathbf{k}_T^2)\right]. \quad (6.3)$$

In the conditions given above, the extended structure function $F_{\mathrm{UT,L}}^{\sin(\phi-\phi_S)}$ is zero. It is at least $\mathbf{P}_{h\perp}^2/(z^2Q^2)$-suppressed compared to $F_{\mathrm{UT,T}}^{\sin(\phi-\phi_S)}$ and can be generated by α_s-corrections at high transverse momentum $\mathbf{P}_{h\perp}$. In the studies, presented in section 5.3, the possible influence of higher twist effects on the SSA amplitude is examined. No evidence for twist-four or even higher twist contributions is found. But also higher twist effects cannot be excluded given the strong correlation of the scaling variables x and Q^2.

The SSA amplitude of the $\sin(\phi - \phi_S)$ modulation is considered as signal for the extended structure function $F_{\mathrm{UT,T}}^{\sin(\phi-\phi_S)}$ only:

$$2\langle\sin(\phi - \phi_S)\rangle_{\mathrm{UT}}^h = -\frac{\mathscr{C}\left[\dfrac{\hat{\mathbf{h}}\cdot\mathbf{p}_T}{M}f_{1\mathrm{T}}^{\perp,q}(x,\mathbf{p}_T^2)\,D_1^q(z,z^2\mathbf{k}_T^2)\right]}{\mathscr{C}\left[f_1^q(x,\mathbf{p}_T^2)\,D_1^q(z,z^2\mathbf{k}_T^2)\right]}, \quad (6.4)$$

and thus provides a signal for the Sivers mechanism.

6.1.3. The results for the Sivers amplitude

The Sivers amplitudes for π-mesons and charged K-mesons are presented in figure 6.3. Significantly positive amplitudes are extracted for π^+, π^0, K^+ and K^-. The Sivers amplitudes for π^- are consistent with zero. In the naive picture of u-quark dominance (section 5.4), amplitudes of similar size would be expected for positively charged pions and kaons. But the Sivers amplitudes for K^+ are found to be larger than those for π^+.

As the amplitudes are sensitive to the convolution of the Sivers function and the spin-independent fragmentation function (equation 6.4), a dependence on both x and z is expected. The pronounced z-dependence of the non-vanishing Sivers amplitudes, compatible with a monotonically increasing function, underlines the role of hadronisation in the Sivers mechanism.

Transverse momentum $\mathbf{P}_{h\perp}$ of the mesons produced in the final state is required for non-vanishing Sivers amplitudes. In the results a decrease of the signal is observed, when the transverse meson momentum $\mathbf{P}_{h\perp}$ approaches to zero. For the Sivers amplitudes of π^+ and K^+ a linear decrease is found. The functional form of the weighting factor in the convolution, related to $(\hat{\mathbf{h}}\cdot\mathbf{p}_T)/M$, would imply an increase of the Sivers amplitudes with transverse meson momentum. But in the case of π^+ and K^+, the extracted amplitudes saturate in the range $|\mathbf{P}_{h\perp}| \in [0.4\,\mathrm{GeV}; 2.0\,\mathrm{GeV}]$.
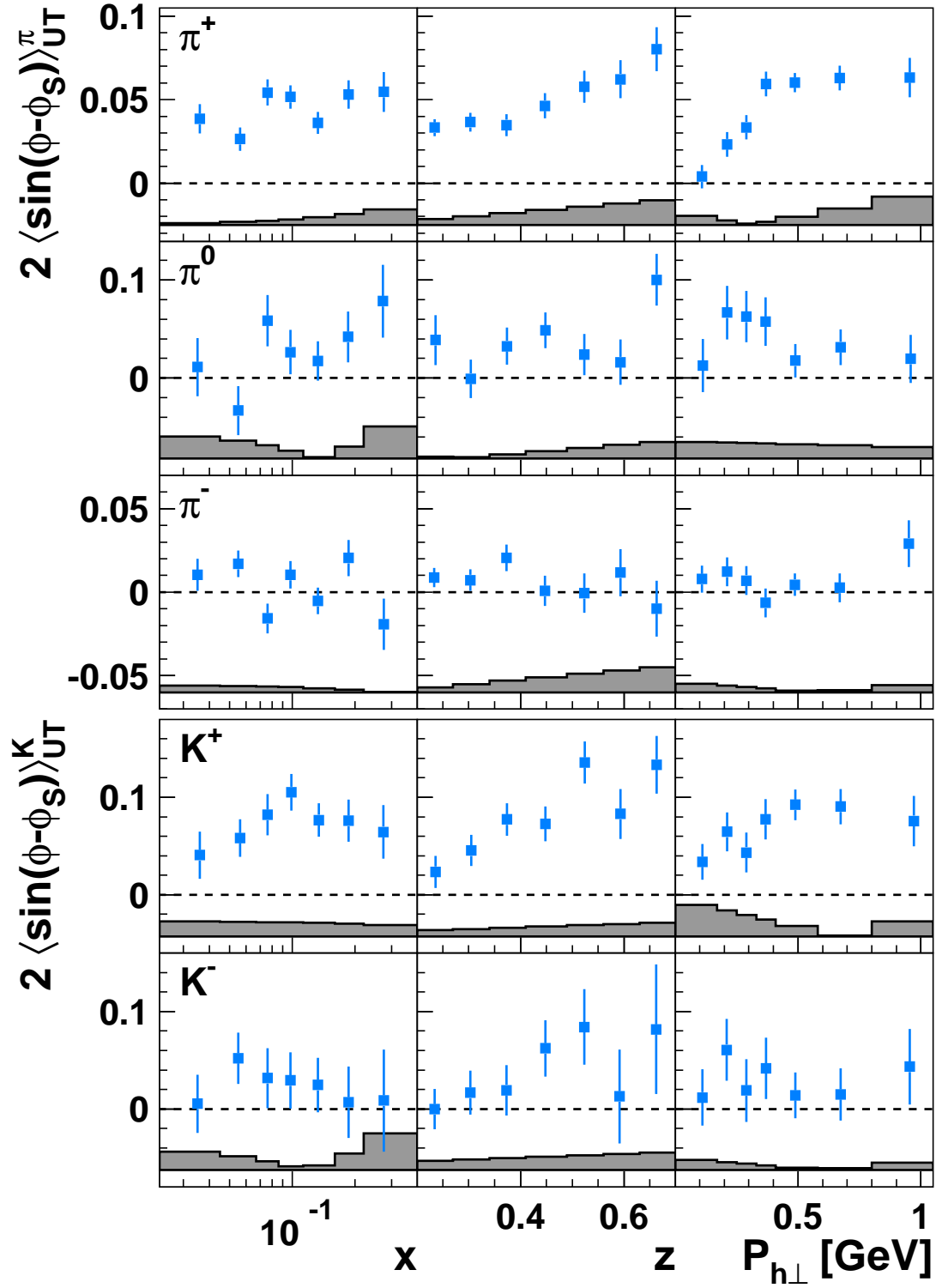
Figure 6.3.: The Sivers amplitudes for π-mesons and charged K-mesons are presented as a function of the Bjorken scaling variable x, the fractional meson energy z and the transverse momentum $|\mathbf{P}_{h\perp}|$ of the meson.
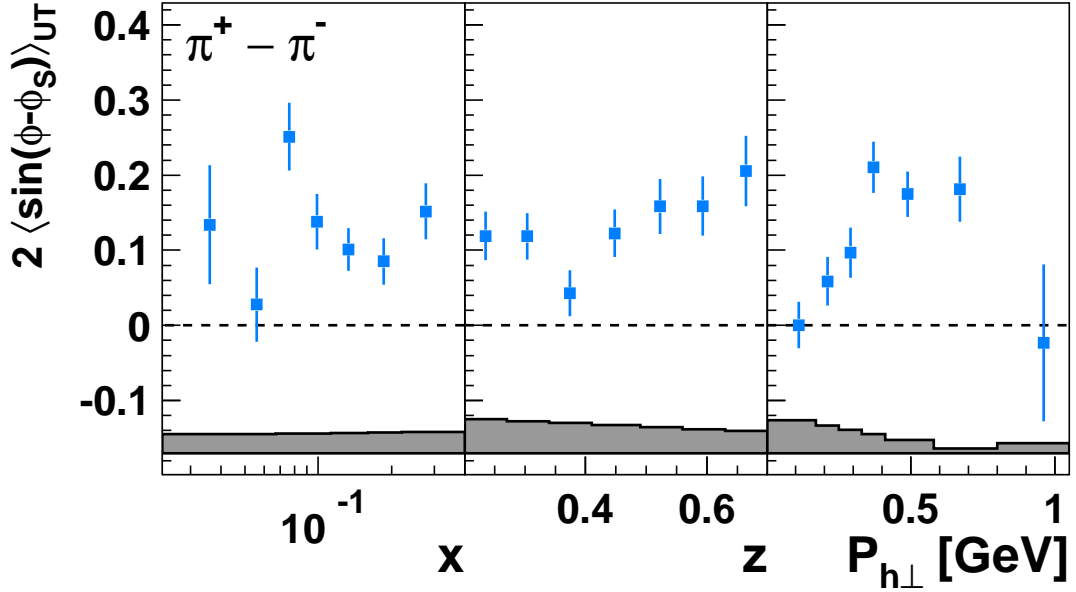
Figure 6.4.: The Sivers amplitudes for the pion-difference SSA are presented as a function of the Bjorken scaling variable x, the fractional meson energy z and the transverse momentum $|\mathbf{P}_{h\perp}|$ of the meson.

This saturation is also seen for the pion-difference Sivers amplitudes, shown in figure 6.4. Assuming charge conjugation and isospin symmetry among fragmentation functions, the pion-difference Sivers single-spin asymmetries can be interpreted in terms of valence-quark distributions solely:

$$2\left\langle\sin\left(\phi-\phi_S\right)\right\rangle_{\mathrm{UT}}^{\pi^+-\pi^-} = -\frac{4f_{1T}^{\perp,u_v}\left(x,\mathbf{p}_T^2\right)-f_{1T}^{\perp,d_v}\left(x,\mathbf{p}_T^2\right)}{4f_1^{u_v}\left(x,\mathbf{p}_T^2\right)-f_1^{d_v}\left(x,\mathbf{p}_T^2\right)}. \tag{6.5}$$

The momentum distributions $f_1^q\left(x,\mathbf{p}_T^2\right)$ are positive for both valence quarks and sea quarks and in the valence-quark region significantly larger for u quarks than for d quarks. Hence, the significantly positive pion-difference Sivers amplitudes provide evidence for large and negative Sivers function for u quarks. This is also suggested by the positive Sivers amplitudes for π^+ and K^+, where the u quarks might be the dominant contribution.

In the semi-classical picture of the Sivers mechanism, a negative Sivers functions implies a positive contribution from u quarks to the orbital angular momentum, but so far no quantitative relation between the Sivers mechanism and the contribution of quark orbital angular momenta to the total spin of the nucleon is known.

Except for negatively charged pions ($\pi^- = |d\bar{u}\rangle$) significantly positive Sivers amplitudes are observed. Cancellation effects are required for the vanishing Sivers amplitudes for π^-. A possibility would be a positive Sivers effect for d quarks. The COMPASS collaboration measured azimuthal single-spin asymmetries of electroproduced charged pions and charged and neutral kaons on a transversely polarised ^{6}LiD target and extracted Sivers amplitudes consistent with zero [COMPASS09]. This observation is interpreted as indication of u- and d-quark Sivers functions of similar size but of opposite sign given the suppressed contributions due to sea quarks on the isoscalar target. This interpretation is supported by phenomenological studies based on preliminary versions [Die05a, Die07a] of the Sivers amplitudes presented here and the COMPASS results [VY05, CEG$^+$06, ABD$^+$09a]. The Sivers function extracted from an analysis of the HERMES and COMPASS measurements is shown in figure 6.6 for all six quark flavours within the nucleon.
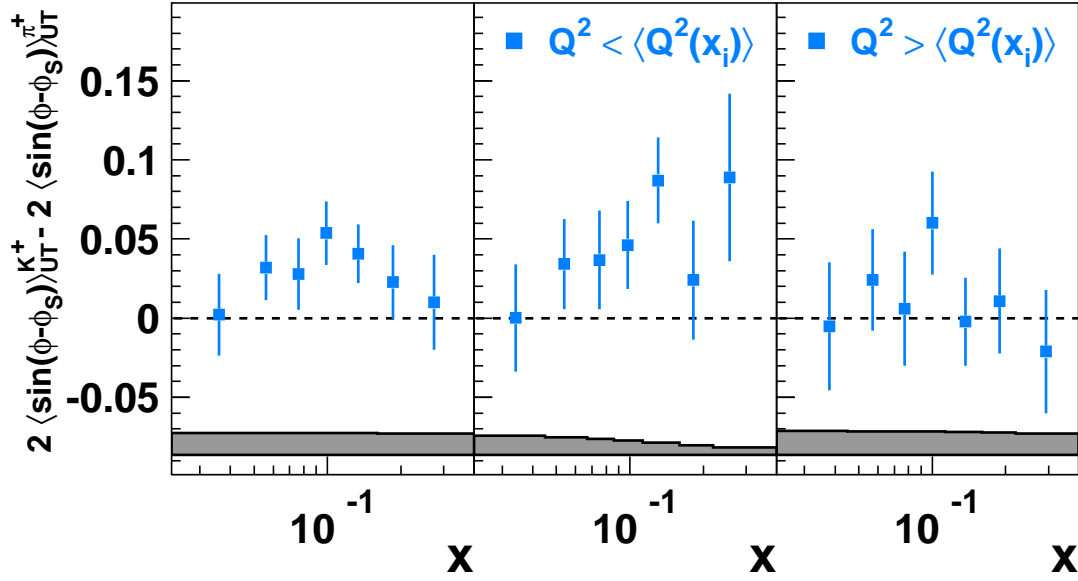
Figure 6.5.: The difference in the Sivers amplitudes for K^+ and π^+ is presented as a function of the Bjorken scaling variable x. In the right panels the difference in these amplitudes is also shown for a lower ($Q^2 < \langle Q^2(x) \rangle$) and a higher scale ($Q^2 > \langle Q^2(x) \rangle$).

The sea-quark Sivers functions might play a crucial role in the understanding of the difference in the Sivers amplitudes for π^+ and K^+. In figure 6.5 the x-dependence of the $2\langle \sin(\phi - \phi_S) \rangle_{UT}^{K^+} - 2\langle \sin(\phi - \phi_S) \rangle_{UT}^{\pi^+}$ difference is shown. The systematic uncertainties of these amplitudes are not estimated using the difference in the models for K^+ and π^+ but using a model for the difference to account for a possible correlation of the systematic uncertainties. At a confidence level of 90% a $K^+ - \pi^+$ difference, i.e. $2\langle \sin(\phi - \phi_S) \rangle_{UT}^{K^+} - 2\langle \sin(\phi - \phi_S) \rangle_{UT}^{\pi^+}$, is measured in the order of 10^{-2}.

In detailed studies, presented in section 5.4, no influence from experimental effects on the $K^+ - \pi^+$ difference is found. The observed difference might imply that other quark flavours than u contribute to the Sivers amplitudes for positively charged pions ($\pi^+ = |u\bar{d}\rangle$) and kaons ($K^+ = |u\bar{s}\rangle$). But the disagreement in these amplitudes could be also caused by the convolutions in the Sivers amplitudes different in the numerator and denominator (equation 6.4). The $K^+ - \pi^+$ difference might also be affected by higher twist effects. The difference found at lower scale, $Q^2 < \langle Q^2(x) \rangle$, vanishes at the higher scale $Q^2 > \langle Q^2(x) \rangle$ (figure 6.5). This facet of the data, suggesting a possible higher twist effect on the Sivers amplitudes for π^+ and K^+, will stimulate further phenomenological discussion.

In the studies of twist-four (or even higher twist) effects, no evidence for significant $\frac{1}{Q^2}$-suppressed contributions is provided (section 5.3). These studies are hampered by the strong correlation of x and Q^2 and thus higher twist effects cannot be ruled out. But this question can be resolved in a comparison with an experimental result with higher Q^2-resolution. The COMPASS collaboration recorded events from deep-inelastic scattering on a transversely polarised NH$_3$ target with average kinematics of $\langle Q \rangle = 3.29\,\mathrm{GeV}^2$, $\langle x \rangle = 0.045$, $\langle z \rangle = 0.37$ and $\langle \mathbf{P}_{h\perp} \rangle = 0.49\,\mathrm{GeV}$. A comparison with their upcoming results will provide more insight into the possible role of higher twist effects.
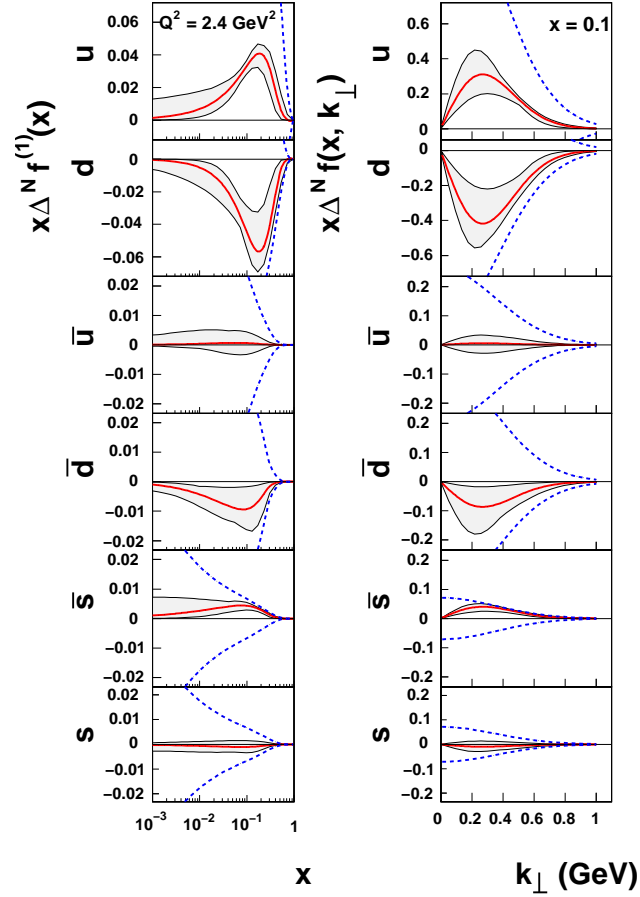
Figure 6.6.: The Sivers function extracted from measurements of single-spin azimuthal asymmetries by HERMES and COMPASS [ABD$^+$09a]: Here, the Sivers function $f_{1T}^{\perp,q}\left(x, \mathbf{p}_T^2\right)$ is not only denoted as $\Delta^N f(x, \mathbf{k}_\perp)$ but also defined with opposite sign. The red solid lines represent the Sivers function at a scale of $Q^2 = 2.4\,\text{GeV}$ for u and d quarks as well as sea quarks. In the left panel the first moment of the Sivers function is shown as a function of x within the positivity limits (blue dashed lines). In the right panel, the $\mathbf{p}_T$-dependence (appearing as $\mathbf{k}_\perp$) is presented for a fixed value of $x = 0.1$. The grey bands represent the uncertainty in the extraction due to the statistical accuracy of the measurements.
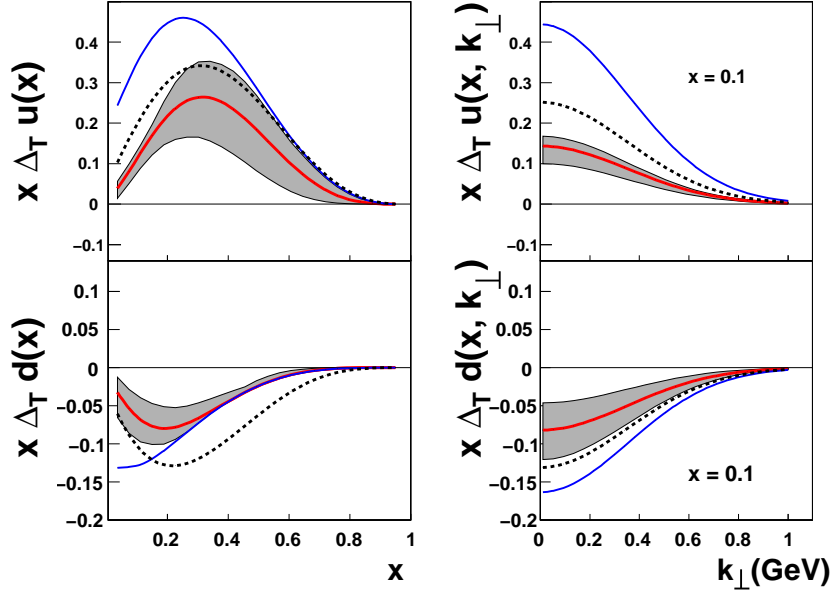
Figure 6.7.: The transversity distribution extracted from measurements of single-spin azimuthal asymmetries by HERMES, COMPASS and Belle [ABD⁺09b]: The transversity distribution, here denoted as $\Delta_T q$ instead of h_1^q, at a scale of $Q^2 = 2.4\,\mathrm{GeV}$ is presented for u and d quarks as a function of x and $\mathbf{p}_T$, here labelled as $k_\perp$. The results for the transversity distribution (red solid line) are compared to those of the helicity distribution (black dashed line) and a positivity bound (blue solid line). The grey band represents the uncertainty in the extraction due to the statistical accuracy of the measurements.

6.2. Signals for the chiral-odd transversity distribution

6.2.1. The Collins amplitude

In the year 2005, the first experimental evidence for the Collins mechanism was provided by the HERMES collaboration based on an analysis of transverse single-spin asymmetries for charged pions [HERMES05c]. The SSA amplitude of the $\sin(\phi + \phi_S)$ modulation in the cross section is sensitive to the convolution of the transversity distribution and the Collins fragmentation function:

$$2\left\langle \sin\left(\phi + \phi_S\right)\right\rangle_{\mathrm{UT}}^h = \frac{\mathscr{C}\left[-\dfrac{\hat{\mathbf{h}} \cdot \mathbf{k}_T}{M_h} h_1^q\left(x, \mathbf{p}_T^2\right) H_1^{\perp,q}\left(z, z^2\mathbf{k}_T^2\right) \right]}{\mathscr{C}\left[f_1^q\left(x, \mathbf{p}_T^2\right) D_1^q\left(z, z^2\mathbf{k}_T^2\right) \right]}. \tag{6.6}$$

Both functions were unmeasured in those days. An analysis of the Collins fragmentation function in electron-positron annihilation, $e^- e^+ \to h_1 h_2 X$, by the Belle collaboration [Belle06, Belle08] allowed for the first quantitative extraction of the transversity distribution [ABD⁺07, ABD⁺09b]. The phenomenological studies are based on Collins amplitudes extracted from transverse single-spin asymmetries by the HERMES [Die05a, Die07a] and COMPASS [COMPASS09] collaborations and the Belle results. In figure 6.7 the results for the transversity distribution are shown for u and d quarks as a function of their longitudinal momentum fraction x and their transverse momenta $\mathbf{p}_T$. Before discussing the more detailed results on the Collins amplitudes, $2\left\langle \sin\left(\phi + \phi_S\right)\right\rangle_{\mathrm{UT}}^h$, an intuitive picture for the Collins mechanism is given.

Chapter 6

6.2.2. The Collins mechanism in a string fragmentation model

The hadronisation process can be well-described by the LUND string model [AGIS83]. In this phenomenological model, a confinement with a linearly rising potential is assumed. The colour dipole field between a $q\bar{q}$ pair is treated as a relativistic string with a constant amount of energy and mass density per unit length, respectively. When the fragmenting quark, q_0, moves apart from the target remnant, $\bar{q}_0$, the energy stored in the colour string increases and a $q_1\bar{q}_1$ pair can tunnel from the vacuum removing some of the energy stored and breaking the string between $\bar{q}_0 q_0$ into two strings between $\bar{q}_0 q_1$ and $\bar{q}_1 q_0$. The (sub)strings fragment until only $q\bar{q}$ pairs confined as mesons remain.

According to the $^3P_0$ model [LYOPR73], the $q_1\bar{q}_1$ pair created during string breaking is assumed to be in a $J^p = 0^+$ state. The positive parity of the $q_1\bar{q}_1$ pair implies that the quark spins are aligned parallel and their total spin, $S = 1$, has to be compensated by their total orbital angular momentum, $L = 1$, which can be generated in the tunnelling mechanism.

The Collins fragmentation function describes the production of unpolarised hadrons from transversely polarised quarks. In order to form a spin-0 meson, the quarks q_0 and $\bar{q}_1$ must have anti-parallel spin orientation, e.g $s_T^{q_0} = +\frac{1}{2}$, $s_T^{q_1} = s_T^{\bar{q}_1} = -\frac{1}{2}$ and $L_T^{q_1\bar{q}_1} = +1$. As a consequence, the transverse orbital momentum of $\bar{q}_1$ is pointing in direction of the transverse spin component of the fragmenting quark. In the hadronisation process, the transverse orbital angular momentum is transferred to the produced meson resulting in a preference to move to the left (for the given example) with respect to the momentum direction of the fragmenting quark [ACY97]. The left-right asymmetry caused by the naive-T-odd Collins mechanism relates the transverse momentum of the produced mesons to the polarisation of the fragmenting quarks. It is revealed in a $\sin(\phi - \phi_q)$ modulation of the azimuthal angles ϕ_q of the spin component of the fragmenting quark (also defined around the virtual-photon direction) and ϕ.

The polarisation of the fragmenting quark is correlated to that of the nucleon via the transversity distribution. On average the polarisation direction of the fragmenting quarks and the struck quarks are not identical as the quark spin component along the virtual-photon polarisation flips in the absorption of the virtual photon. Given the linear polarisation of the virtual photon in the lepton-scattering plane, the azimuthal angle ϕ_q of the fragmenting quark is related to the azimuthal angle ϕ_S of the target spin axis, $\phi_q = \pi - \phi_S$, resulting in a $\sin(\phi + \phi_S)$ signature for the Collins mechanism.

6.2.3. The results for the Collins amplitude

The Collins amplitudes for π-mesons and charged K-mesons are shown in figure 6.8. The amplitudes' dependence on x is mainly influenced by the transversity distribution. In contrast to the momentum distribution (figure 2.2), the contribution of valence quarks is dominant for the transversity distribution. This is reflected in the observation of Collins amplitudes consistent with zero in the first x-bin and rising in magnitude with x. The influence of the Collins fragmentation function is revealed in the increase of the amplitudes' magnitude with z. Possible higher twist contributions could not be constrained given the available statistics and the strong correlation in x and Q^2 (section 5.3).

Significantly positive (negative) amplitudes are extracted for π^+ (π^-). The amplitudes for neutral pions are consistent with zero and in agreement with the isospin relation among the Collins amplitudes for π-mesons (section 5.2). In particular at large x, the magnitude of the π^- amplitudes is larger than for π^+. This observation was unexpected as the opposite trend has been found for the helicity distribution in an analysis of longitudinal double-spin asymmetries [HERMES05b]. The naive expectation, the transversity distribution being positive for u quarks and negative and smaller in magnitude for d quarks, is confirmed by QCD Lattice calculations. Thus, a substantial difference in the involved fragmentation functions $D_1^q(z, z^2\mathbf{k}_T^2)$ and $H_1^{\perp,q}(z, z^2\mathbf{k}_T^2)$ was suggested [HERMES05c].
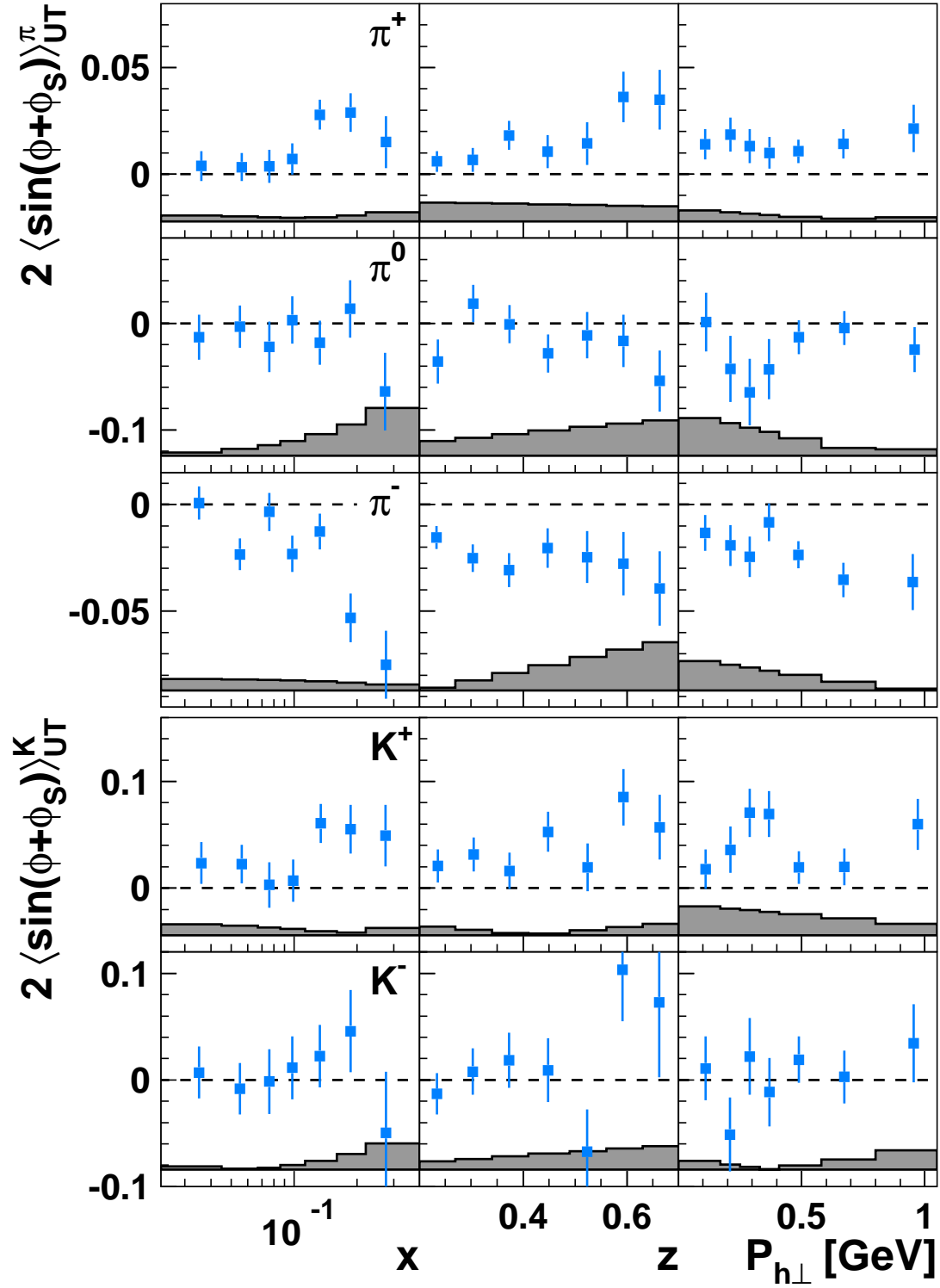
Figure 6.8.: The Collins amplitudes for π-mesons and charged K-mesons are presented as a function of the Bjorken scaling variable x, the fractional meson energy z and the transverse momentum $|\mathbf{P}_{h\perp}|$ of the meson.
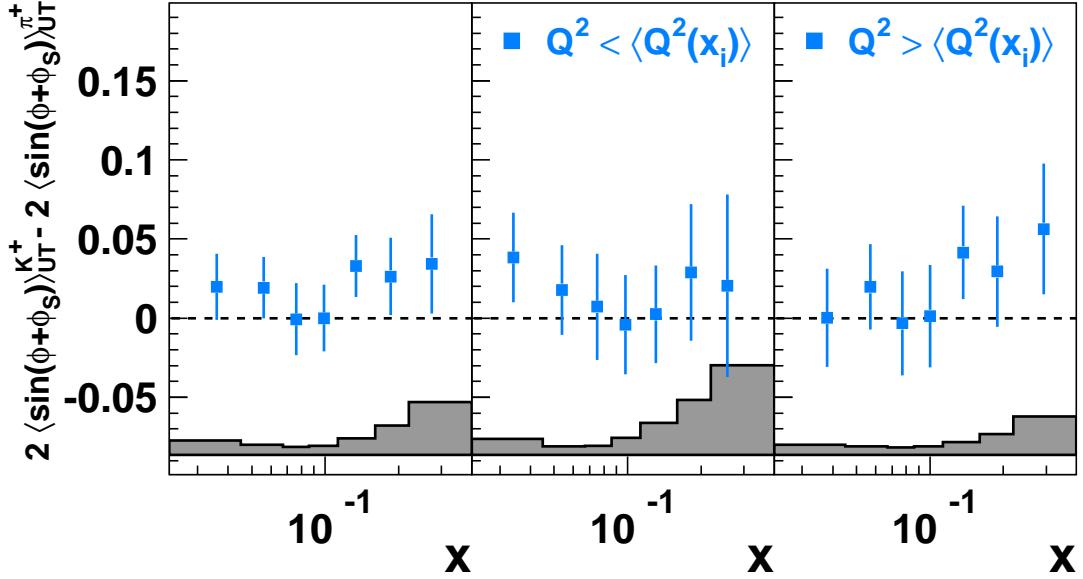
Figure 6.9.: Analogue to figure 6.5, the $K^+ - \pi^+$ difference in the Collins amplitudes is presented.

Due to charge conjugation ($D_1^{u \to \pi^+} = D_1^{\bar{u} \to \pi^-}$) and isospin symmetry ($D_1^{u \to \pi^+} = D_1^{d \to \pi^-}$), three independent fragmentation functions $D_1^q(z)$ are found in the production, $q \to \pi^\pm$, of π^+ ($= |u\bar{d}\rangle$) and π^- ($= |\bar{u}d\rangle$) from a fragmenting quark of flavour u, d or s:

$$D_{1,\mathrm{fav}}(z) \equiv D_1^{u \to \pi^+}(z) = D_1^{\bar{d} \to \pi^+}(z) = D_1^{d \to \pi^-}(z) = D_1^{\bar{u} \to \pi^-}(z), \tag{6.7}$$

$$D_{1,\mathrm{dis}}(z) \equiv D_1^{u \to \pi^-}(z) = D_1^{\bar{d} \to \pi^-}(z) = D_1^{d \to \pi^+}(z) = D_1^{\bar{u} \to \pi^+}(z), \tag{6.8}$$

$$D_{1,\mathrm{s}}(z) \equiv D_1^{s \to \pi^+}(z) = D_1^{\bar{s} \to \pi^+}(z) = D_1^{s \to \pi^-}(z) = D_1^{\bar{s} \to \pi^-}(z). \tag{6.9}$$

The favoured ($D_{1,\mathrm{fav}}$), disfavoured ($D_{1,\mathrm{dis}}$) and strange ($D_{1,\mathrm{s}}$) spin-independent fragmentation functions obey the hierarchy: $D_{1,\mathrm{fav}} \gg D_{1,\mathrm{dis}} \gg D_{1,\mathrm{s}}$. To explain the Collins amplitudes for charged pions, disfavoured and favoured Collins fragmentation function of similar magnitude and with opposite signs have been suggested [HERMES05c]. This explanation is not in contradiction to the results on the Collins function obtained by the Belle collaboration [Belle06, Belle08] and supported by a phenomenological study [ABD+09b]. The opposite sign of the disfavoured and favoured Collins functions can be understood in the string fragmentation model [BMN10]: "If a favourite pion forms as the string end created by the first break, a disfavoured pion from the next break will inherit transverse momentum from the first break in the opposite direction from that acquired by the first pion." As a consequence of the anti-correlation, any correlation between $\mathbf{P}_{h\perp}$ and another kinematic or spin variable has opposite signs for favoured or disfavoured pions.

The Collins amplitudes for K^+ are significantly positive and those for K^- are consistent with zero. At a confidence level of 90%, a difference in the Collins amplitudes for K^+ and π^+ is found in the order of 10^{-2} (left panel of figure 6.9). Similar to the discussion of the Sivers amplitudes for K^+ and π^+ (section 6.1.3), this observed difference might reflect the role of sea quarks in the Collins mechanism and in particular might indicate possible large fragmentation functions of sea quarks. The $K^+ - \pi^+$ difference might also be influenced by the $\mathbf{k}_T$-dependence of the fragmentation functions different for π^+ and K^+, which can affect the convolutions present in the Collins amplitudes (equation 6.6). In addition to these factors, the vanishing Collins amplitudes for K^- might be related to the suppressed transversity distribution for sea quarks.

6.3. The vanishing signals for the pretzelosity function

An analysis of the so far unmeasured pretzelosity function $h_{1T}^{\perp,q}\left(x,\mathbf{p}_T^2\right)$ will provide insights into the non-spherical shape of the nucleon caused by significant contributions from orbital angular momentum (section 2.2.2). The $2\left\langle\sin\left(3\phi-\phi_S\right)\right\rangle_{\mathrm{UT}}^{h}$ amplitude provides a leading-twist signal for the chiral-odd pretzelosity function in conjunction with the chiral-odd Collins fragmentation function:

$$2\left\langle\sin\left(3\phi-\phi_S\right)\right\rangle_{\mathrm{UT}}^{h} = \frac{\mathscr{C}\left[\frac{2\left(\hat{\mathbf{h}}\cdot\mathbf{p}_T\right)\left(\mathbf{p}_T\cdot\mathbf{k}_T\right)+\mathbf{p}_T^2\left(\hat{\mathbf{h}}\cdot\mathbf{k}_T\right)-4\left(\hat{\mathbf{h}}\cdot\mathbf{p}_T\right)^2\left(\hat{\mathbf{h}}\cdot\mathbf{k}_T\right)}{2M^2 M_h} h_{1T}^{\perp,q}\left(x,\mathbf{p}_T^2\right)H_1^{\perp,q}\left(z,z^2\mathbf{k}_T^2\right)\right]}{\mathscr{C}\left[f_1^q\left(x,\mathbf{p}_T^2\right)D_1^q\left(z,z^2\mathbf{k}_T^2\right)\right]}. \quad (6.10)$$

The convolution involves a weight that is expected to scale according to $\left|\mathbf{P}_{h\perp}\right|^3 = \left|z(\mathbf{p}_T-\mathbf{k}_T)\right|^3$. As relatively low transverse meson momenta are observed, i.e. $\left\langle\left|\mathbf{P}_{h\perp}\right|\right\rangle < 1\,\mathrm{GeV}$, the $2\left\langle\sin\left(3\phi-\phi_S\right)\right\rangle_{\mathrm{UT}}^{h}$ amplitudes are suppressed with respect to the Collins amplitudes, which scale according to $\left|\mathbf{P}_{h\perp}\right|$ given the weight of $-(\hat{\mathbf{h}}\cdot\mathbf{k}_T)/M_h$ in the convolution. In the analysis, the $2\left\langle\sin\left(3\phi-\phi_S\right)\right\rangle_{\mathrm{UT}}^{h}$ amplitudes are found to be consistent with zero within the statistical accuracy (as shown in figure 6.10).

6.4. The subleading-twist SSA amplitudes

The $2\left\langle\sin\left(2\phi-\phi_S\right)\right\rangle_{\mathrm{UT}}^{h}$ amplitude is related to a subleading-twist cross-section contribution:

$$F_{\mathrm{UT}}^{\sin(2\phi-\phi_S)} = \frac{2M}{Q}\mathscr{C}\left\{\frac{2(\hat{\mathbf{h}}\cdot\mathbf{p}_T)^2-\mathbf{p}_T^2}{2M^2}\left(xf_T^{\perp,q}\left(x,\mathbf{p}_T^2\right)D_1^q\left(z,z^2\mathbf{k}_T^2\right)-\frac{M_h}{M}h_{1T}^{\perp,q}\left(x,\mathbf{p}_T^2\right)\frac{\tilde{H}^q\left(z,z^2\mathbf{k}_T^2\right)}{z}\right)\right.$$
$$-\frac{2(\hat{\mathbf{h}}\cdot\mathbf{k}_T)(\hat{\mathbf{h}}\cdot\mathbf{p}_T)-\mathbf{p}_T\cdot\mathbf{k}_T}{2MM_h}\left[\vphantom{\frac{M_h}{M}}\right.$$
$$\left(xh_T^q\left(x,\mathbf{p}_T^2\right)H_1^{\perp,q}\left(z,z^2\mathbf{k}_T^2\right)+\frac{M_h}{M}g_{1T}^{\perp,q}\left(x,\mathbf{p}_T^2\right)\frac{\tilde{G}^{\perp,q}\left(z,z^2\mathbf{k}_T^2\right)}{z}\right)+$$
$$\left.\left.\left(xh_T^{\perp,q}\left(x,\mathbf{p}_T^2\right)H_1^{\perp,q}\left(z,z^2\mathbf{k}_T^2\right)-\frac{M_h}{M}f_{1T}^{\perp,q}\left(x,\mathbf{p}_T^2\right)\frac{\tilde{D}^{\perp,q}\left(z,z^2\mathbf{k}_T^2\right)}{z}\right)\right]\right\}.$$
$$(6.11)$$

As a consequence of quark-gluon correlations, the extended structure function $F_{\mathrm{UT}}^{\sin(2\phi-\phi_S)}$ involves a mixture of either twist-two distribution and twist-three (interaction-dependent) fragmentation functions or twist-three distribution and twist-two fragmentation functions. The interaction-dependent fragmentation functions $\tilde{H}^q$, $\tilde{G}^{\perp,q}$ and $\tilde{D}^{\perp,q}$ are indicated by a tilde. Due to the mixture and the presence of interaction-dependent (fragmentation) functions, the interpretation of the $2\left\langle\sin\left(2\phi-\phi_S\right)\right\rangle_{\mathrm{UT}}^{h}$ amplitude is hampered. There is also no probabilistic interpretation for higher twist functions.

Due to the weighting factors in the convolution, a similar argument as for the $2\left\langle\sin\left(3\phi-\phi_S\right)\right\rangle_{\mathrm{UT}}^{h}$ amplitude can be drawn. The subleading-twist $2\left\langle\sin\left(2\phi-\phi_S\right)\right\rangle_{\mathrm{UT}}^{h}$ amplitudes are expected to scale according to $\left|\mathbf{P}_{h\perp}\right|^2$ and thus are suppressed with respect to the leading-twist Collins amplitudes by one order in $\left|\mathbf{P}_{h\perp}\right|$ and in addition by $2M/Q$.

The $2\left\langle\sin\left(2\phi-\phi_S\right)\right\rangle_{\mathrm{UT}}^{h}$ amplitudes are consistent with zero (as shown in figure 6.11). When integrating over the full kinematic range of the measurement, non-vanishing amplitudes can only be reported for π^+, π^0 and K^+ at a statistical significance of less than 2σ: $2\left\langle\sin\left(2\phi-\phi_S\right)\right\rangle_{\mathrm{UT}}^{\pi^+} = 0.0056\pm 0.0027$, $2\left\langle\sin\left(2\phi-\phi_S\right)\right\rangle_{\mathrm{UT}}^{\pi^0} = 0.0116\pm 0.0079$ and $2\left\langle\sin\left(2\phi-\phi_S\right)\right\rangle_{\mathrm{UT}}^{K^+} = -0.0118\pm 0.0071$.

Chapter 6

6. The interpretation of the measured SSA

Also the $2 \langle \sin (\phi_S) \rangle_{\mathrm{UT}}^h$ amplitude is related to a subleading-twist cross-section contribution:

$$
\begin{aligned}
F_{\mathrm{UT}}^{\sin(\phi_S)} = \frac{2M}{Q} \mathscr{C} \Bigg\{ & \left(x f_T^q \left(x, \mathbf{p}_T^2\right) D_1^q \left(z, z^2 \mathbf{k}_T^2\right) - \frac{M_h}{M} h_1^q \left(x, \mathbf{p}_T^2\right) \frac{\tilde{H}^q \left(z, z^2 \mathbf{k}_T^2\right)}{z} \right) \\
& - \frac{\mathbf{p}_T \cdot \mathbf{k}_T}{2MM_h} \Bigg[\\
& \left(x h_T^q \left(x, \mathbf{p}_T^2\right) H_1^{\perp,q} \left(z, z^2 \mathbf{k}_T^2\right) + \frac{M_h}{M} g_{1\mathrm{T}}^{\perp,q} \left(x, \mathbf{p}_T^2\right) \frac{\tilde{G}^{\perp,q} \left(z, z^2 \mathbf{k}_T^2\right)}{z} \right) - \\
& \left(x h_T^{\perp,q} \left(x, \mathbf{p}_T^2\right) H_1^{\perp,q} \left(z, z^2 \mathbf{k}_T^2\right) - \frac{M_h}{M} f_{1\mathrm{T}}^{\perp,q} \left(x, \mathbf{p}_T^2\right) \frac{\tilde{D}^{\perp,q} \left(z, z^2 \mathbf{k}_T^2\right)}{z} \right) \Bigg] \Bigg\} .
\end{aligned} \tag{6.12}
$$

The extended structure function $F_{\mathrm{UT}}^{\sin(\phi_S)}$ is of particular interest as it is the only contribution to the cross section σ_{UT}^h that survives integration over transverse hadron momentum:

$$
F_{\mathrm{UT}}^{\sin(\phi_S)} \left(x, Q^2, z\right) = \int d^2 \mathbf{P}_{h\perp} F_{\mathrm{UT}}^{\sin(\phi_S)} \left(x, Q^2, z, \mathbf{P}_{h\perp}\right) = -x \frac{2M_h}{Q} \sum_q e_q^2 h_1^q (x) \frac{\tilde{H}^q (z)}{z}, \tag{6.13}
$$

and thus provides sensitivity to the transversity distribution without involving a convolution over intrinsic transverse momenta. A major drawback of this measurement is the lack of knowledge about the interaction-dependent fragmentation function $\tilde{H}^q (z)$. Another drawback could be the systematic effect arising from the possible incomplete integration over $\mathbf{P}_{h\perp}$ due to limitations in the geometric acceptance or kinematic requirements.

In the analysis, a statistical correlation between the non-zero Collins, Sivers and $2 \langle \sin (\phi_S) \rangle_{\mathrm{UT}}^h$ amplitudes is found (section 4.2.2.3). To avoid a possible cross-contamination, the amplitudes are extracted simultaneously. However, a similarity in size but also in shape is observed for the Collins and $2 \langle \sin (\phi_S) \rangle_{\mathrm{UT}}^h$ amplitudes (figure 6.12). The intriguing similarity, in particular for π^-, might be influenced by remaining correlation effects but can be also explained within the Wandzura-Wilczek approximation [WW77]. In this approximation all interaction-dependent terms are expected to vanish and the extended structure function $F_{\mathrm{UT}}^{\sin(\phi_S)}$ has dominant contributions due to the Sivers and Collins mechanism only:

$$
\begin{aligned}
F_{\mathrm{UT}}^{\sin(\phi_S)} = \frac{2M}{Q} \mathscr{C} \Bigg\{ & \left(\frac{\mathbf{p}_T^2}{2M^2} f_{1\mathrm{T}}^{\perp,q} \left(x, \mathbf{p}_T^2\right) D_1^q \left(z, z^2 \mathbf{k}_T^2\right) \right) \\
& + \frac{\mathbf{p}_T \cdot \mathbf{k}_T}{2MM_h} \Bigg[\\
& \left(-2 h_1^q \left(x, \mathbf{p}_T^2\right) + \frac{m}{M} g_{1\mathrm{T}}^{\perp,q} \left(x, \mathbf{p}_T^2\right) \right) H_1^{\perp,q} \left(z, z^2 \mathbf{k}_T^2\right) \Bigg] \Bigg\} .
\end{aligned} \tag{6.14}
$$

The contribution of the convolution of the worm-gear distribution $g_{1\mathrm{T}}^{\perp,q} \left(x, \mathbf{p}_T^2\right)$ and the Collins fragmentation function is suppressed by the quark mass m. As the $1/Q$ suppression of the subleading twist $2 \langle \sin (\phi_S) \rangle_{\mathrm{UT}}^h$ amplitudes can be compensated by the $|\mathbf{P}_{h\perp}|$-suppression of the Collins amplitudes in the range, $\langle |\mathbf{P}_{h\perp}| \rangle < 1\,\mathrm{GeV}$, the similar size of both amplitudes can be understood. For a final answer, more detailed studies of the $2 \langle \sin (\phi_S) \rangle_{\mathrm{UT}}^h$ amplitudes and its interpretation will be required.
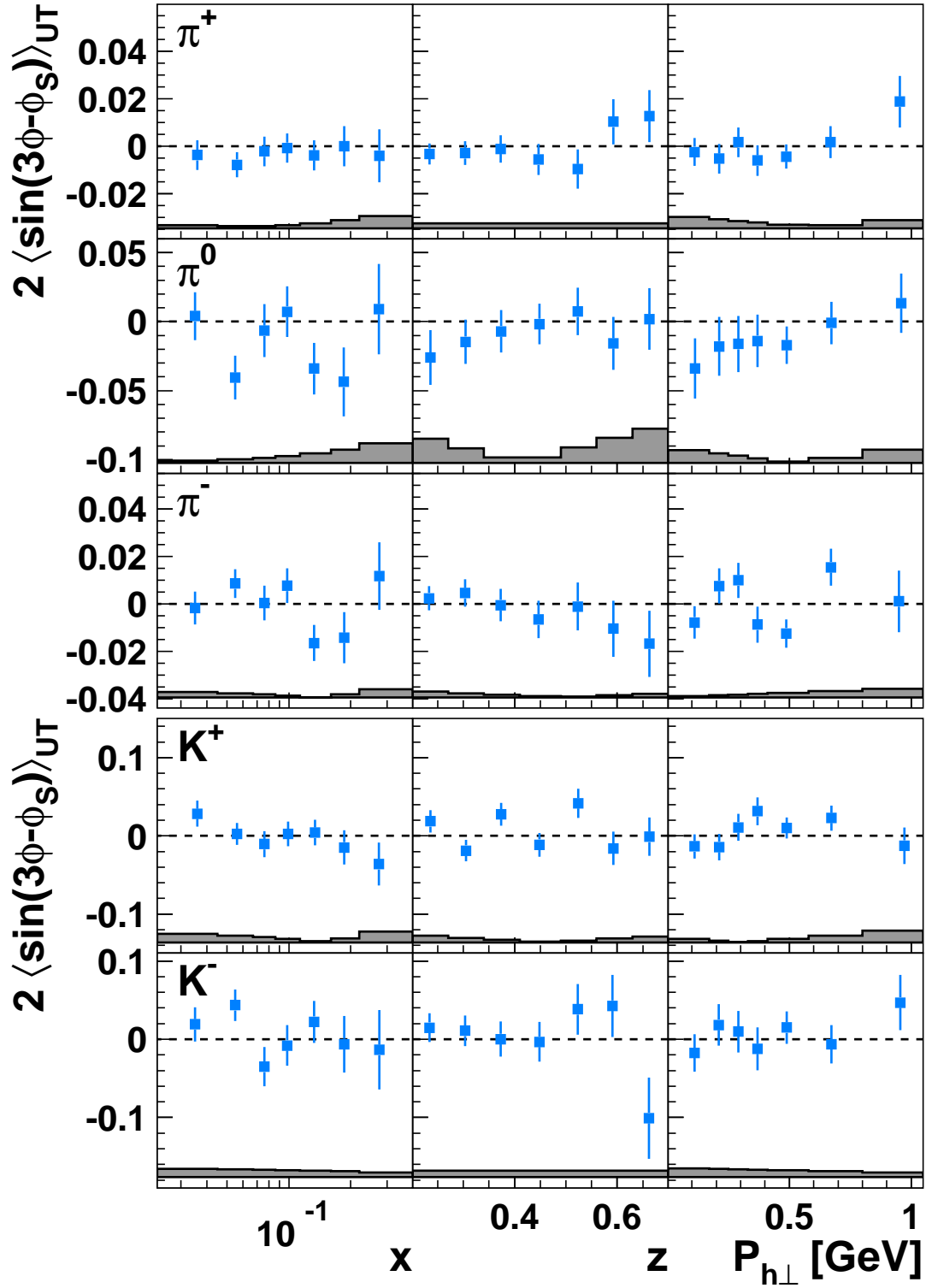
Figure 6.10.: The $2 \langle \sin(3\phi - \phi_S) \rangle_{UT}^h$ amplitudes for π-mesons and charged K-mesons are presented as a function of the Bjorken scaling variable x, the fractional meson energy z and the transverse momentum $|\mathbf{P}_{h\perp}|$ of the meson.

Figure 6.11.: The $2\langle\sin(2\phi-\phi_S)\rangle^h_{\mathrm{UT}}$ amplitudes for π-mesons and charged K-mesons are presented as a function of the Bjorken scaling variable x, the fractional meson energy z and the transverse momentum $|\mathbf{P}_{h\perp}|$ of the meson.
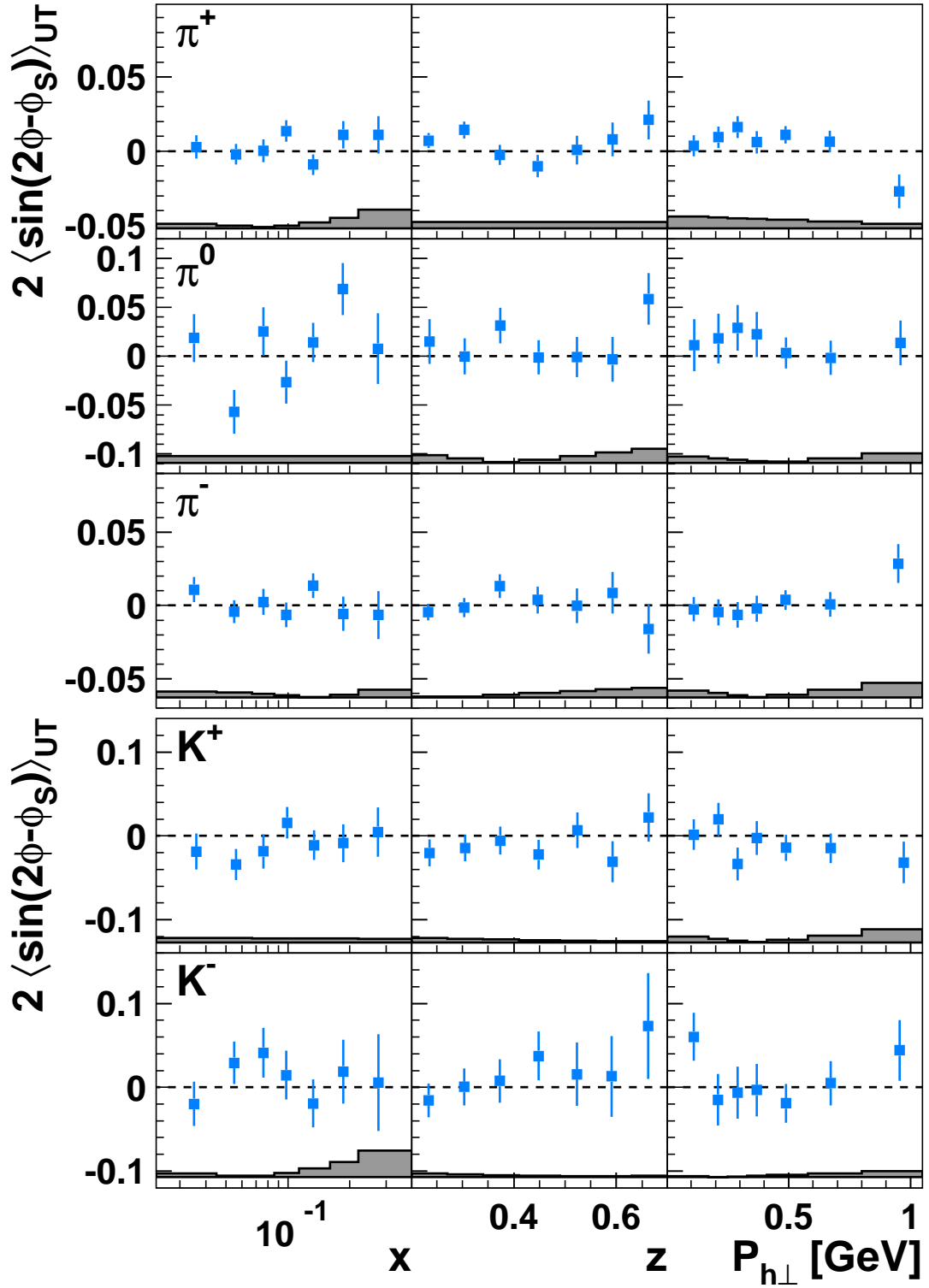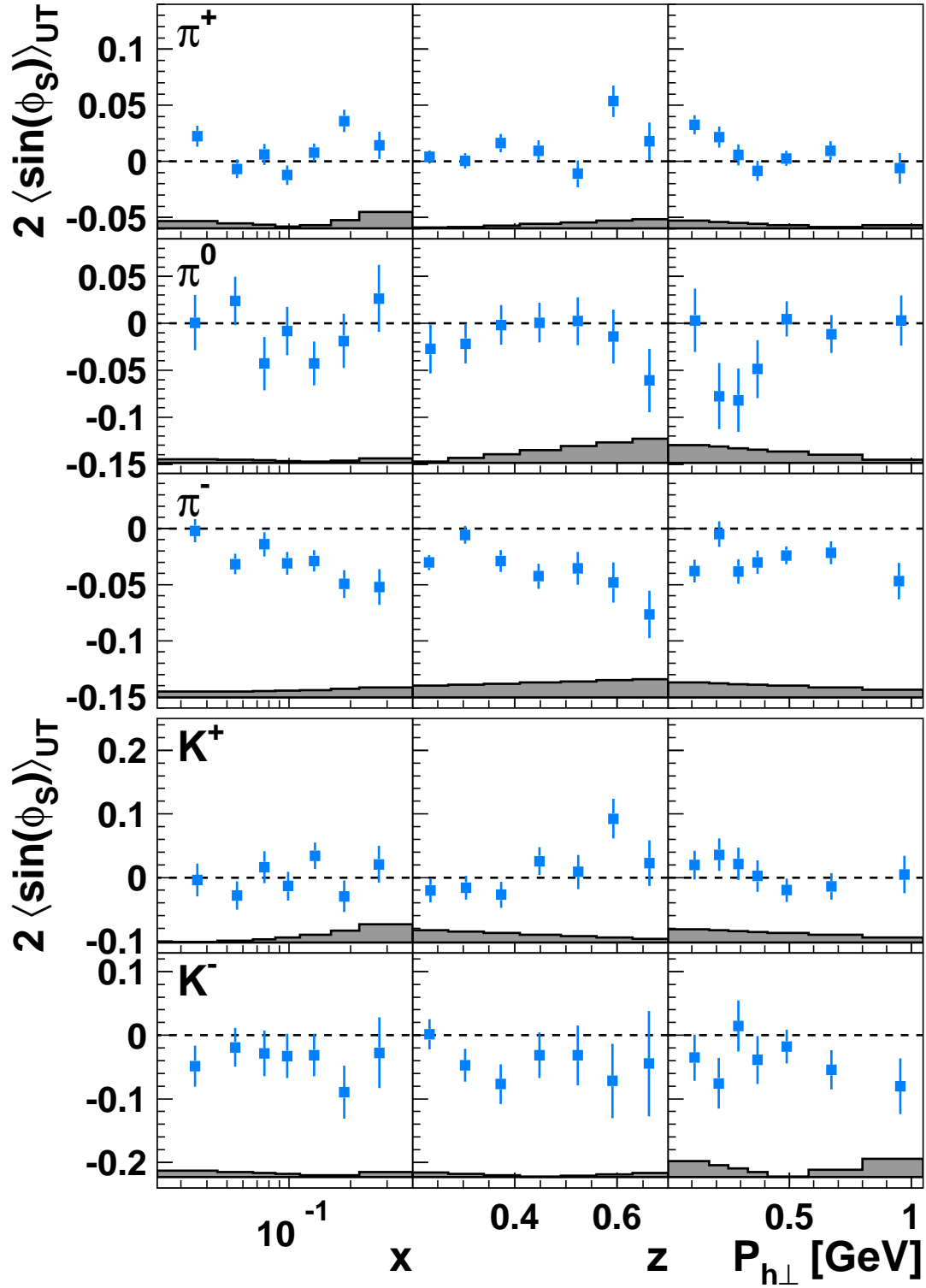
Figure 6.12.: The $2\left\langle\sin\left(\phi_S\right)\right\rangle_{\mathrm{UT}}^{h}$ amplitudes for π-mesons and charged K-mesons are presented as a function of the Bjorken scaling variable x, the fractional meson energy z and the transverse momentum $\left|\mathbf{P}_{h\perp}\right|$ of the meson.

6.5. Signals for the worm-gear distributions

The worm-gear distributions $h_{1L}^{\perp;q}\left(x,\mathbf{p}_T^2\right)$ and $g_{1T}^{\perp;q}\left(x,\mathbf{p}_T^2\right)$ arise from relativistic boosts (section 2.2.3). Approximate relations are known correlating these TMD with the transverse-momentum dependent transversity $h_1^q\left(x,\mathbf{p}_T^2\right)$ and helicity $g_1^q\left(x,\mathbf{p}_T^2\right)$ distributions.

The worm-gear distribution $h_{1L}^{\perp;q}\left(x,\mathbf{p}_T^2\right)$ describes the distribution of transversely polarised quarks in a longitudinally polarised nucleon. When detecting unpolarised hadrons in the final state, the chiral-odd TMD can only be accessed via the chiral-odd Collins fragmentation function. The effect of the worm-gear distribution in conjunction with the final-state interaction of the naive-T-odd Collins function is revealed in a $\sin\left(2\phi\right)$ modulation in the cross section. The amplitudes of the associated longitudinal single-spin asymmetries A_{UL}^h are given by:

$$
2\left\langle\sin\left(2\phi\right)\right\rangle_{\mathrm{UL}}^h = \frac{\mathscr{C}\left[-\dfrac{2\left(\hat{\mathbf{h}}\cdot\mathbf{k}_T\right)\left(\hat{\mathbf{h}}\cdot\mathbf{k}_T\right)-\mathbf{k}_T\cdot\mathbf{p}_T}{MM_h}h_{1L}^{\perp;q}\left(x,\mathbf{p}_T^2\right)H_1^{\perp;q}\left(z,z^2\mathbf{k}_T^2\right)\right]}{\mathscr{C}\left[f_1^q\left(x,\mathbf{p}_T^2\right)D_1^q\left(z,z^2\mathbf{k}_T^2\right)\right]}.
\tag{6.15}
$$

The $2\left\langle\sin\left(2\phi+\phi_S\right)\right\rangle_{\mathrm{U}\perp}^h$ amplitudes in the Fourier decomposition of the transverse single-spin asymmetries A_{UT}^h are not sensitive to an extended structure function of the transverse target spin-dependent cross-section contribution σ_{UT}^h. They are related to the $2\left\langle\sin\left(2\phi\right)\right\rangle_{\mathrm{UL}}^h$ amplitudes:

$$
2\left\langle\sin\left(2\phi+\phi_S\right)\right\rangle_{\mathrm{U}\perp}^h \propto \frac{1}{2}\sin\left(\theta_{l\gamma^*}\right)2\left\langle\sin\left(2\phi\right)\right\rangle_{\mathrm{UL}}^h,
\tag{6.16}
$$

as a consequence of the small longitudinal target-spin component with respect to the virtual photon direction (section 5.1.5.3). The opening angle $\theta_{l\gamma^*}$ between the momentum direction of the incoming lepton beam and that of the virtual photon is determined by the lepton beam kinematics. Its sine is in the order of 10^{-1}.

Vanishing $2\left\langle\sin\left(2\phi\right)\right\rangle_{\mathrm{UL}}^h$ amplitudes for π-mesons have been reported by the HERMES collaboration [HERMES00, HERMES01] in an analysis of longitudinal single-spin asymmetries. The $2\left\langle\sin\left(2\phi+\phi_S\right)\right\rangle_{\mathrm{U}\perp}^h$ amplitudes for π-mesons and charged K-mesons extracted in the presented analysis are shown in figure 6.13. The amplitudes for π-mesons are consistent with zero and thus in agreement with the A_{UL}^h measurement. Also the amplitudes for negatively charged kaons are consistent with zero. But for positively charged kaons non-vanishing amplitudes are extracted. The K^+ amplitude, integrated over the full kinematic range of the measurement is $2\left\langle\sin\left(2\phi+\phi_S\right)\right\rangle_{\mathrm{U}\perp}^{K^+} = 0.0195\pm0.0070$. When taken the systematic uncertainties (not) into account, the amplitudes as a function of x, z, and $|\mathbf{P}_{h\perp}|$ are positive at a confidence level of at least 90% (95%), providing thus evidence for the worm-gear distribution $h_{1L}^{\perp;q}\left(x,\mathbf{p}_T^2\right)$ in deep-inelastic scattering.

The other worm-gear distribution, $g_{1T}^{\perp;q}\left(x,\mathbf{p}_T^2\right)$, is unique in the sense that it is the only TMD that vanishes when integrating over $\mathbf{p}_T$ but neither entails nor is affected by final-state interactions. At leading twist, this TMD cannot contribute to naive-T-odd effects that cause single-spin asymmetries. Its spin-orbit correlation, $\lambda S_T^i p_T^i$, involves a common product of the helicity of the struck quark and the transverse spin direction of the nucleon. In combination with the selection of quarks with certain helicity by a longitudinally polarised lepton beam, the worm-gear distribution $g_{1T}^{\perp;q}\left(x,\mathbf{p}_T^2\right)$ can be related to a $\cos\left(\phi-\phi_S\right)$ modulation manifested in a double-spin asymmetry. The Fourier decomposition of double-spin asymmetries A_{LT}^h is beyond the intended scope of this thesis. However, the amplitudes of the double-spin asymmetry $A_{\mathrm{L}\perp}^h$ are already presented within the scope of a systematic study (section 4.2.2.3). For a complete analysis only the systematic uncertainties would have to be estimated and thus a brief discussion of these amplitudes is not withheld.

Figure 6.13.: The $2\left\langle\sin\left(2\phi+\phi_S\right)\right\rangle_{U\perp}^h$ amplitudes for π-mesons and charged K-mesons are presented as a function of the Bjorken scaling variable x, the fractional meson energy z and the transverse momentum $|\mathbf{P}_{h\perp}|$ of the meson.
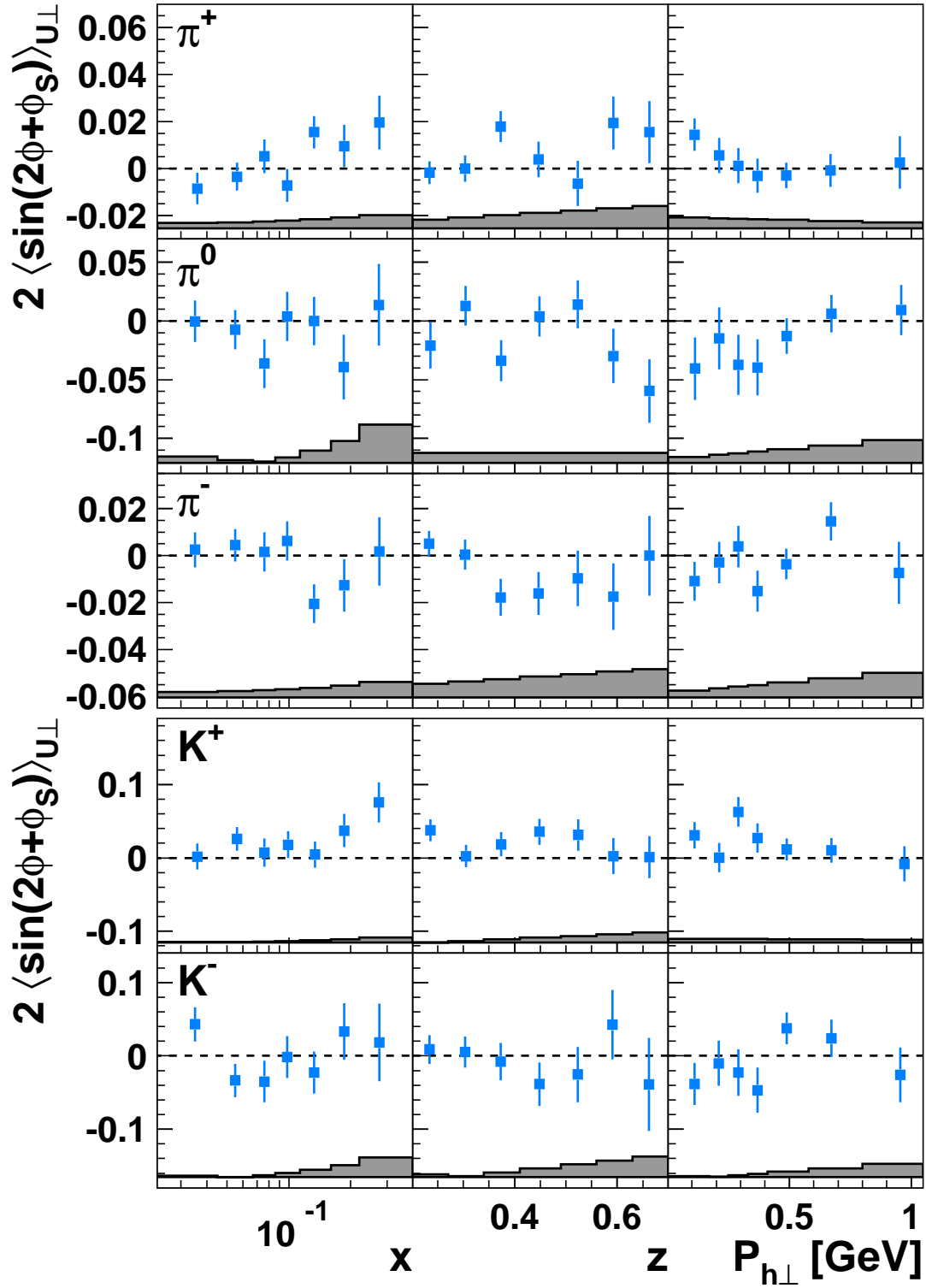
6. The interpretation of the measured SSA

The $2\langle\cos(\phi-\phi_S)\rangle^h_{LT}$ amplitudes amplitude provide a leading-twist signal for the naive-T-even and chiral-even worm-gear distribution $g^{\perp,q}_{1T}(x,\mathbf{p}^2_T)$ in conjunction with the spin-independent fragmentation function $D^q_1(z,z^2\mathbf{k}^2_T)$:

$$2\langle\cos(\phi-\phi_S)\rangle^h_{LT} = \frac{\mathscr{C}\left[-\dfrac{\hat{\mathbf{h}}\cdot\mathbf{p}_T}{M}g^{\perp,q}_{1T}(x,\mathbf{p}^2_T)D^q_1(z,z^2\mathbf{k}^2_T)\right]}{\mathscr{C}\left[f^q_1(x,\mathbf{p}^2_T)D^q_1(z,z^2\mathbf{k}^2_T)\right]}. \tag{6.17}$$

In figure 6.14, amplitudes extracted from $A^h_{L\perp}$ are presented for π-mesons and charged K-mesons. As a consequence of the relatively small degree of polarisation of the HERA lepton beam in the years 2002–2005, the statistical uncertainties are larger than the amplitudes extracted in the Fourier analysis of transverse single-spin asymmetries. Only for negatively charged pions and positively charged kaons non-vanishing $2\langle\cos(\phi-\phi_S)\rangle^h_{L\perp}$ amplitudes are extracted. The significance of these amplitudes, integrated over the full kinematic range of the measurement:

$$2\langle\cos(\phi-\phi_S)\rangle^{\pi^-}_{L\perp}=0.0291\pm0.0086,\quad 2\langle\cos(\phi-\phi_S)\rangle^{K^+}_{L\perp}=0.0466\pm0.0204,$$

provides indication that these signals are not caused by statistical correlations and thus, in particular for π^-, provide evidence for the worm-gear distribution $g^{\perp,q}_{1T}(x,\mathbf{p}^2_T)$ in a semi-inclusive measurement of deep-inelastic scattering.

The $\cos(\phi_S)$ and $\cos(2\phi-\phi_S)$ modulations in the cross section are related to subleading-twist contributions to σ^h_{LT}. Both the $2\langle\cos(\phi_S)\rangle^h_{L\perp}$ (figure 6.15) and $2\langle\cos(2\phi-\phi_S)\rangle^h_{L\perp}$ amplitudes are consistent with zero for π-mesons and charged K-mesons (figure 6.16). As both amplitudes involve a mixture of either twist-two distribution and twist-three fragmentation functions or twist-three distribution and twist-two fragmentation functions [BDG$^+$07], they are hard to interpret.
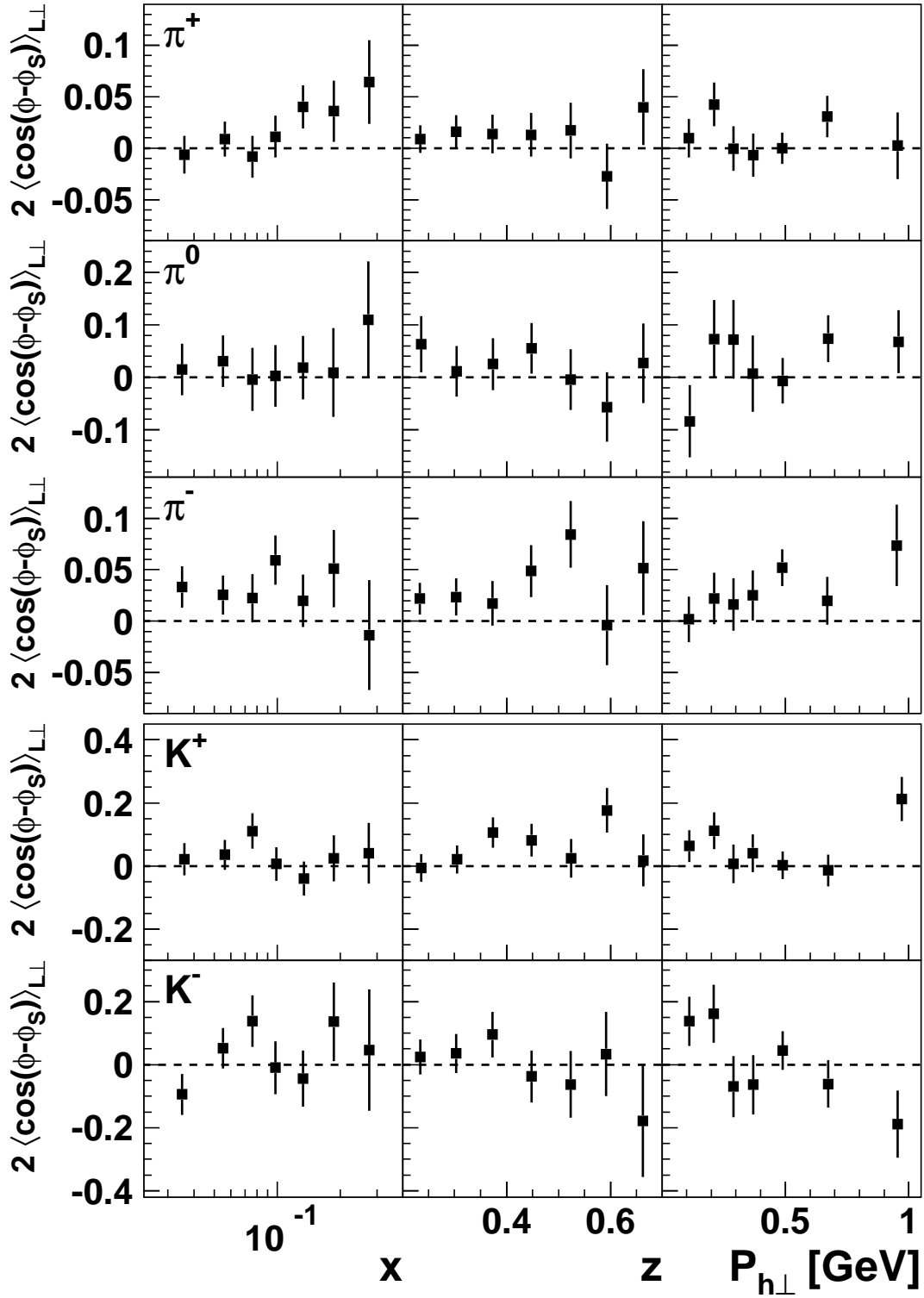
110

Figure 6.14.: The $2\left\langle\cos\left(\phi-\phi_S\right)\right\rangle^h_{\mathrm{L}\perp}$ amplitudes for π-mesons and charged K-mesons are presented as a function of the Bjorken scaling variable x, the fractional meson energy z and the transverse momentum $|\mathbf{P}_{h\perp}|$ of the meson.

Figure 6.15.: The $2\langle\cos(\phi_S)\rangle^h_{L\perp}$ amplitudes for π-mesons and charged K-mesons are presented as a function of the Bjorken scaling variable x, the fractional meson energy z and the transverse momentum $|\mathbf{P}_{h\perp}|$ of the meson.

Figure 6.16.: The $2 \langle \cos(2\phi - \phi_S) \rangle^h_{L\perp}$ amplitudes for π-mesons and charged K-mesons are presented as a function of the Bjorken scaling variable x, the fractional meson energy z and the transverse momentum $|\mathbf{P}_{h\perp}|$ of the meson.

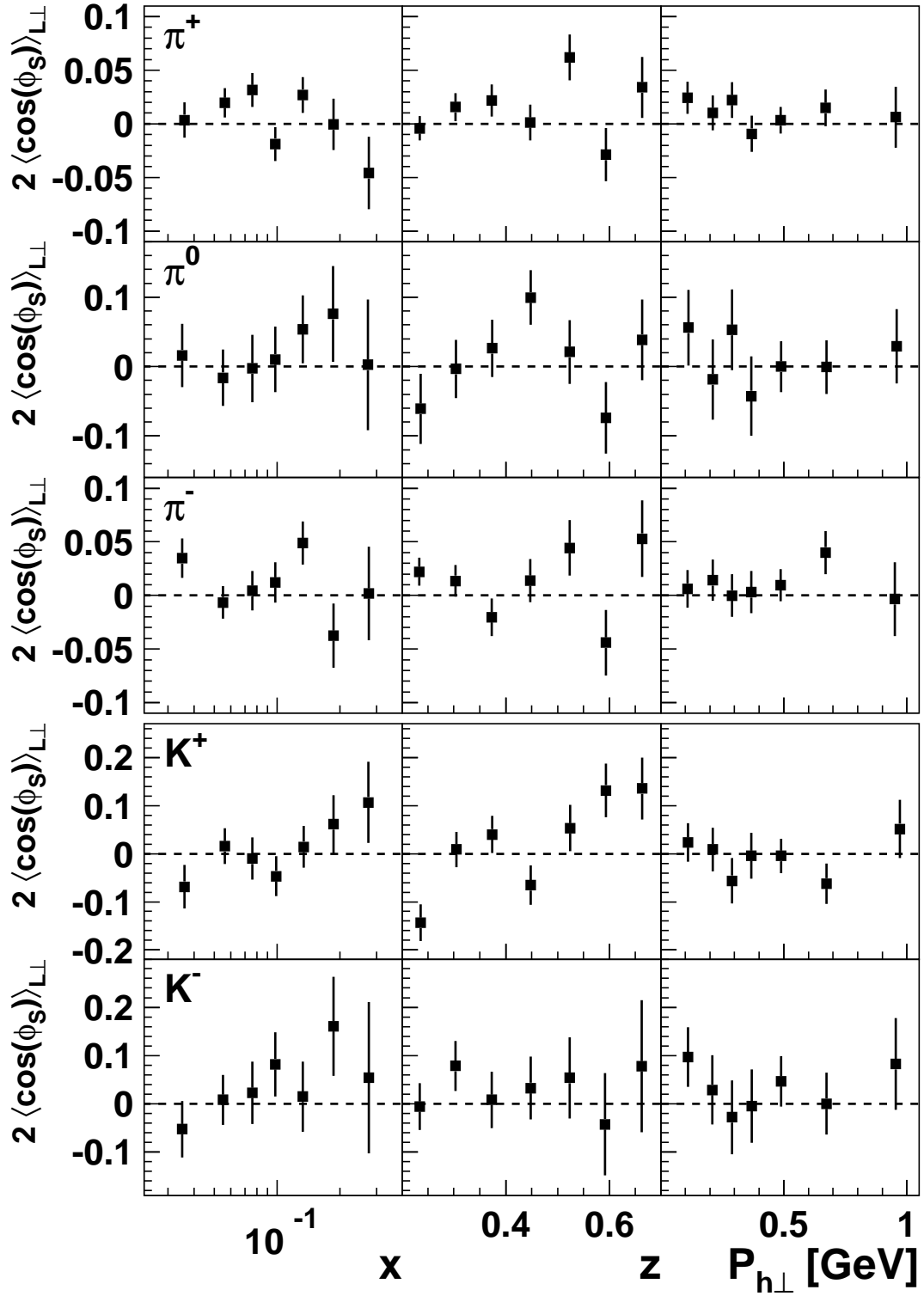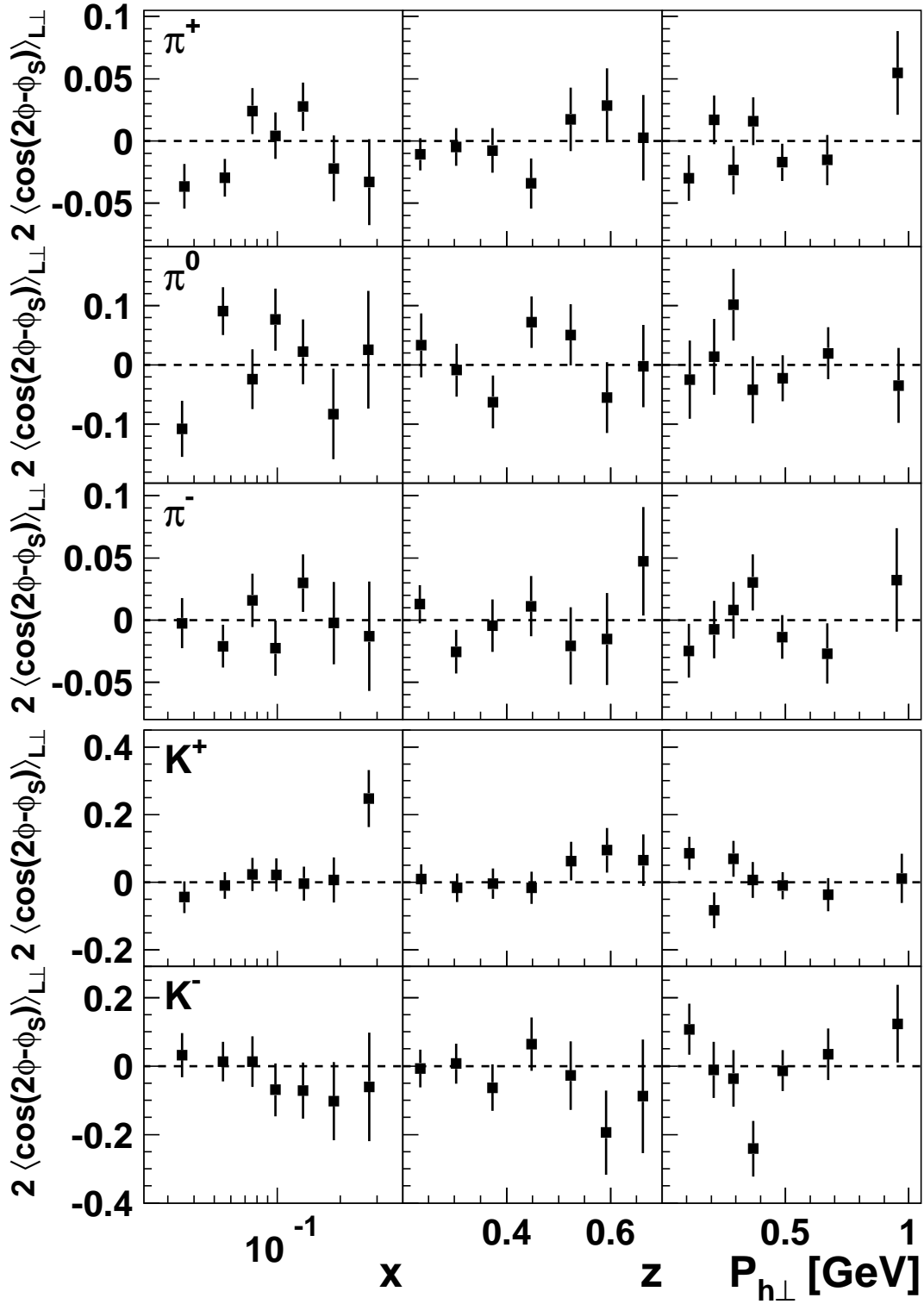*6. The interpretation of the measured SSA*

7. Conclusion

In this work a Fourier analysis of single-spin azimuthal asymmetries A_{UT}^h was presented for π-mesons and charged K-mesons. The azimuthal asymmetries were reconstructed from a semi-inclusive measurement of deep-inelastic scattering off a transversely polarised proton target at the HERMES experiment. The extracted single-spin asymmetry amplitudes can be interpreted as convolutions in transverse momentum space of transverse momentum-dependent distribution and fragmentation functions and provide sensitivity to the transversity, Sivers and pretzelosity quark distributions as well as for one worm-gear quark distribution. Signals for the other worm-gear distribution were extracted in an extended Fourier analysis including also double-spin asymmetries A_{LT}^h. A study of the only remaining transverse momentum-dependent quark distribution, the Boer–Mulders function, cannot easily be performed in the approach applied in this work but requires the analysis of the polarisation-independent contribution of the cross section, e.g. by a multi-dimensional unfolding algorithm [GL09] in order to separate the signal from detector effects, which are almost eliminated in the presented work by the rapid reversal of the target-spin orientation.

Non-zero Collins amplitudes were extracted for π^+, π^- and K^+. These amplitudes provide the most precise signals (in the valence quark region) for the transversity distribution, measuring the helicity flip in the nucleon, and also sensitivity to the Collins fragmentation function, which parameterises the hadronisation of a transversely polarised quark into an unpolarised hadron. The larger magnitude in the amplitudes for π^- than those for π^+ suggests favoured and disfavoured Collins fragmentation functions of similar magnitude but opposite sign.

Non-zero Sivers amplitudes were observed for π^+, π^0, K^+ and K^- as well as for the pion-difference asymmetry. These amplitudes provide evidence for the Sivers function, describing the probability to find an unpolarised quark in transversely polarised nucleon, and thus constraints on scattering amplitudes that are associated with quark orbital angular momentum. As a consequence of the Wilson-line formalism, the Sivers mechanism in the deep-inelastic scattering and Drell–Yan processes have opposite signs. This QCD prediction can be tested in upcoming Drell–Yan measurements given the constraints on the sign from the presented results. The positive values of the pion-difference asymmetry suggest a negative sign for the Sivers function of u quarks, which is in qualitative agreement with the approach of chromodynamical lensing.

Previous versions of this work have significantly contributed to the experimental results on the Collins and Sivers mechanism used for the first quantitative extraction of the transversity and Sivers function. The presented results will improve these extractions due to more detailed kinematic information available, the higher statistical accuracy for the charged kaon amplitudes and the role of sea quarks underlined in the difference of the Collins and Sivers amplitudes for π^+ and K^+. Comparison with measurements of the Collins and Sivers mechanisms by other experiments, preferable at a higher scale in Q^2, are required to test present approaches of the Q^2-evolution of transverse-momentum-dependent parton distribution functions.

The pretzelosity amplitudes are suppressed by two orders in $\mathbf{P}_{h\perp}$ with respect to the Collins amplitudes. As a consequence of the relatively low transverse hadron momenta observed, a better statistical accuracy will be needed to isolate a non-zero signal for the pretzelosity distribution directly related to the shape of the nucleon.

The non-vanishing amplitudes of the $\sin(\phi_S)$ modulation might allow for an alternative measure-

ment of the transversity distribution without requiring sensitivity to transverse hadron momenta. The intriguing similarity between the leading-twist Collins and subleading-twist $2 \langle \sin(\phi_S) \rangle_{\mathrm{UT}}^h$ amplitude, found at least for π^-, has to be further studied and might provide an opportunity to test of the Wandzura-Wilczek approximation.

The worm-gear distribution $h_{1\mathrm{L}}^{\perp;q}\left(x, \mathbf{p}_T^2\right)$, which describes the distribution of transversely polarised quarks in a longitudinally polarised nucleon, could be studied in the Fourier analysis of transverse single-spin asymmetries due to the small component of the longitudinal target spin with respect to the virtual-photon direction. Only for K^+ non-zero signals for $h_{1\mathrm{L}}^{\perp;q}\left(x, \mathbf{p}_T^2\right)$ were observed. Sensitivity to the other worm-gear distribution, $g_{1\mathrm{T}}^{\perp;q}\left(x, \mathbf{p}_T^2\right)$, which characterises the distribution of longitudinally polarised quarks in a transversely polarised nucleon, was provided in the analysis of double-spin asymmetries A_{LT}^h. It was demonstrated that this analysis is feasible given the longitudinal beam polarisation of the HERA lepton beam though hampered by the low degree of polarisation in a large fraction of the recorded deep-inelastic scattering events. For π^- and K^+ non-vanishing signals for the $g_{1\mathrm{T}}^{\perp;q}\left(x, \mathbf{p}_T^2\right)$ quark distribution were extracted.

The Fourier analysis of single-spin azimuthal asymmetries in the semi-inclusive measurement of deep-inelastic scattering at the HERMES experiment presented is this work provides important new information about transverse-momentum-dependent parton distribution functions for quarks, which will significantly contribute to the understanding of various high-energy scattering measurements and fundamental concepts of QCD. Phenomenological studies of these results will help to constrain quark orbital angular momentum and thus provide new insights in the spin structure of the nucleon.

Zusammenfassung Intention der vorliegenden Dissertation war die Untersuchung von transversalimpulsabhängigen Quarkverteilungsfunktionen. Im Fokus stand die innerhalb des HERMES Experiments durchgeführte Fourieranalyse azimutaler Einzel-Spin-Asymmetrien von Pionen und geladenen Kaonen. Diese Asymmetrien wurden aus tiefinelastischen Streuereignissen an einem transversal polarisierten Protonen-Target rekonstruiert und in Fourierkomponenten zerlegt. Im Rahmen der Quantenchromodynamik können derartige Komponenten als Faltung von Quarkverteilungs- und Fragmentationsfunktionen interpretiert werden. Durch die Analyse der vom Transversalimpuls abängigen Quarkverteilungsfunktionen wurde die Untersuchung von Spin-Bahn-Korrelationen im Inneren des Nukleons ermöglicht. Somit können Rückschlüsse auf den Bahndrehimpuls der Quarks gezogen werden. Die extrahierten Fourierkomponenten erweitern die bisher verfügbaren Informationen über vom Transversalimpuls abhängige Quarkverteilungsfunktionen beachtlich. Die vorgestellte Fourieranalyse ermöglichte nicht nur einen Nachweis der Collins- und Siverseffekte, sondern darüber hinaus die Extraktion von Signalen der Pretzelosity- und Wormgear-Verteilungen. Die so erlangten Ergebnisse werden maßgeblich zum Verständnis zukünftiger Messungen auf diesem Gebiet beitragen und weiterführend eine Überprüfung fundamentaler Vorhersagen der Quantenchromodynamik ermöglichen.

A. Acknowledgment

"Der Reiz der Erkenntniss wäre gering, wenn nicht auf dem Wege zu ihr so viel Scham zu überwinden wäre", schreibt Friedrich N. nieder. Jenseits der Scham ist dieser Weg aber auch mit Inspiration und Motivation verbunden. Hält man in einem Moment der Erkenntnis inne, erfüllt einen daher nicht nur ein Gefühl von Erleichterung sondern auch ein Gefühl tiefster Dankbarkeit:

A. Acknowledgment

A. Acknowledgment

VIII

B. Bibliography

[A$^+$02]   N. Akopov et al., *The HERMES dual-radiator ring imaging Cherenkov detector*, Nucl. Instrum. Meth. **A479**, 511–530 (2002).

[ABD$^+$05] M. Anselmino, M. Boglione, U. D'Alesio, A. Kotzinian, F. Murgia et al., *Role of Cahn and Sivers effects in deep inelastic scattering*, Phys.Rev. **D71**, 074006 (2005).

[ABD$^+$07] M. Anselmino, M. Boglione, U. D'Alesio, A. Kotzinian, F. Murgia, A. Prokudin and C. Türk, *Transversity and Collins functions from* SIDIS *and* e^+e^- *data*, Phys.Rev. **D75**, 054032 (2007).

[ABD$^+$09a] M. Anselmino, M. Boglione, U. D'Alesio, A. Kotzinian, S. Melis, F. Murgia, A. Prokudin and C. Türk, *Sivers effect for pion and kaon production in semi- inclusive deep inelastic scattering*, Eur. Phys. J. **A39**, 89–100 (2009).

[ABD$^+$09b] M. Anselmino, M. Boglione, U. D'Alesio, A. Kotzinian, F. Murgia, A. Prokudin and C. Türk, *Update on transversity and Collins functions from* SIDIS *and* e^+e^- *data*, Nucl.Phys.Proc.Suppl. **191**, 98–107 (2009).

[ABR98]   I. Akushevich, H. Böttcher and D. Ryckbosch, RADGEN *1.0: Monte Carlo Generator for Radiative Events in* DIS *on Polarized and Unpolarized Targets*, (1998), arXiv:hep-ph/9906408.

[ACY97]   X. Artru, J. Czyzewski and H. Yabuki, *Single spin asymmetry in inclusive pion production, Collins effect and the string model*, Z.Phys. **C73**, 527–534 (1997).

[AEG$^+$08] H. Avakian, A. V. Efremov, K. Goeke, A. Metz, P. Schweitzer and T. Teckentrup, *Are there approximate relations among transverse momentum dependent distribution functions?*, Phys. Rev. **D77**, 014023 (2008).

[AESY08] H. Avakian, A. V. Efremov, P. Schweitzer and F. Yuan, *Transverse momentum dependent distribution function* $h_{1T}^\perp$ *and the single spin asymmetry* $A_{UT}^{\sin(3\phi-\phi_S)}$, Phys. Rev. **D78**, 114024 (2008).

[AGIS83] B. Andersson, G. Gustafson, G. Ingelman and T. Sjöstrand, *Parton fragmentation and string dynamics*, Phys.Rept. **97**, 31–145 (1983).

[AM90]   X. Artru and M. Mekhfi, *Transversely polarized parton densities, their evolution and their measurement*, Z. Phys. **C45**, 669–679 (1990).

[AMS$^+$07] W. Augustyniak, A. Miller, G. Schnell, S. Yen and P. Zupranski, TMC— *Vertex Reconstruction in the Presence of the* HERMES *Transverse Target Magnet*, HERMES Internal Report (June 2007).

[B$^+$93]   D. P. Barber et al., *The* HERA *Polarimeter and the First Observation of Electron Spin Polarization at* HERA, Nucl. Instrum. Meth. **A329**, 79–111 (1993).

Bibliography

[B⁺94]   D. P. Barber et al., *High spin polarization at the* HERA *Electron Storage Ring*, Nucl. Instrum. Meth. **A338**, 166–184 (1994).

[B⁺95]   D. P. Barber et al., *The First Achievement of Longitudinal Spin Polarization in a High Energy Electron Storage Ring*, Phys. Lett. **B343**, 436–443 (1995).

[Bar04]   R. Barlow, *A note on* $\Delta \ln L = -\frac{1}{2}$ *Errors*, (2004), arXiv:physics/0403046.

[BDE⁺06] A. Bacchetta, M. Diefenthaler, U. Elschenbroich, L. Pappalardo and G. Schnell, *Collins and Sivers moments for charged kaons* K^+ *and* K^- , HERMES Release Report (April 2006).

[BDG⁺07] A. Bacchetta, M. Diehl, K. Goeke, A. Metz, P. J. Mulders and M. Schlegel, *Semi-inclusive deep inelastic scattering at small transverse momentum*, JHEP **0702**, 093 (2007).

[Bec00]   M. Beckmann, *Extraction of polarised quark distributions of the nucleon from deep inelastic scattering at the* HERMES *experiment*, PhD thesis, Albert-Ludwigs-Universität Freiburg, 2000.

[Belle06] R. Seidl et al. (Belle Collaboration), *Measurement of Azimuthal Asymmetries in Inclusive Production of Hadron Pairs in* e^+e^- *Annihilation at Belle*, Phys. Rev. Lett. **96**, 232002 (2006).

[Belle08] R. Seidl et al. (Belle Collaboration), *Measurement of azimuthal asymmetries in inclusive production of hadron pairs in* e^+e^- *annihilation at* $s = 10.58 GeV$, Phys. Rev. D **78**, 032011 (2008).

[BEM⁺04] A. Bacchetta, U. Elschenbroich, Y. Miyachi, G. Schnell, R.-C. Seidl, T.-A. Shibata, Y. Takubo and H. Tanaka, *On the way to a decomposition of the flavor dependent Sivers functions: Transverse asymmetries, the decomposition and the transverse* MC *generator* GMC_TRANS , HERMES Internal Report (November 2004).

[Ber87]   E. L. Berger, Semi-inclusive inelastic electron scattering from nuclei, in *Proceedings of NPAS Workshop on Electronuclear Physics with Internal Targets*, January 1987.

[BESS03] A. Bacchetta, U. Elschenbroich, G. Schnell and R.-C. Seidl, *Single-Spin Azimuthal Asymmetries in* SIDIS *off a Transversely Polarized Proton Target — The Release*, HERMES Release Report (May 2003).

[BHS02]   S. J. Brodsky, D. S. Hwang and I. Schmidt, *Final-state interactions and single-spin asymmetries in semi-inclusive deep inelastic scattering*, Phys. Lett. **B530**, 99–107 (2002).

[BJM00]   D. Boer, R. Jakob and P. J. Mulders, *Angular dependences in electroweak semi-inclusive leptoproduction*, Nucl. Phys. **B564**, 471–485 (2000).

[BJY03]   A. V. Belitsky, X. Ji and F. Yuan, *Final state interactions and gauge invariant parton distributions*, Nucl. Phys. **B656**, 165–198 (2003).

[BJY04]   A. V. Belitsky, X.-d. Ji and F. Yuan, *Quark imaging in the proton via quantum phase-space distributions*, Phys. Rev. **D69**, 074014 (2004).

[BM98]   D. Boer and P. J. Mulders, *Time-reversal odd distribution functions in leptoproduction*, Phys. Rev. **D57**, 5780–5786 (1998).

[BMN10]   M. Burkardt, A. Miller and W.-D. Nowak,   *Spin-polarized high-energy scattering of charged leptons on nucleons*, Rep. Progr. Phys. **73**, 016201 (2010).

[BP69]   J. D. Bjorken and E. A. Paschos,   *Inelastic Electron-Proton and γ-Proton Scattering and the Structure of the Nucleon*, Phys. Rev. **185**, 1975–1982 (1969).

[Bur00]   M. Burkardt,   *Impact parameter dependent parton distributions and off-forward parton distributions for $\zeta \to 0$*, Phys. Rev. **D62**, 071503 (2000).

[Bur02]   M. Burkardt,   *Impact parameter dependent parton distributions and transverse single spin asymmetries*, Phys.Rev. **D66**, 114005 (2002).

[Bur04a]   M. Burkardt,   *Chromodynamic lensing and transverse single spin asymmetries*, Nucl.Phys. **A735**, 185–199 (2004).

[Bur04b]   M. Burkardt,   *Quark correlations and single spin asymmetries*, Phys. Rev. **D69**, 057501 (2004).

[Bur07]   M. Burkardt,   *Spin-orbit correlations and single-spin asymmetries*,   (2007), arXiv:0709.2966.

[CDP$^+$09]   M. Contralbrigo, M. Diefenthaler, L. Pappalardo, A. Rostomyan and G. Schnell,   *The other (than Sivers and Collins) amplitudes in the Fourier decomposition of the transverse single-spin asymmetries on transversely polarized protons*,   HERMES Release Report (September 2009).

[CDPS07a]   M. Contralbrigo, M. Diefenthaler, L. Pappalardo and G. Schnell,   *Collins and Sivers amplitudes for π-mesons and charged K-mesons*, HERMES Release Report (April 2007).

[CDPS07b]   M. Contralbrigo, M. Diefenthaler, L. Pappalardo and G. Schnell,   *Data compatibility studies*, HERMES Release Report (April 2007).

[CDPS08]   M. Contralbrigo, M. Diefenthaler, L. Pappalardo and G. Schnell,   *Selected candies from transverse single-spin asymmetry measurements*, HERMES Release Report (September 2008).

[CEG$^+$06]   J. Collins, A. Efremov, K. Goeke, M. Grosse Perdekamp, S. Menzel, A. Metz and P. Schweitzer,   *Sivers effect in semiinclusive deeply inelastic scattering*, Phys.Rev. **D73**, 014021 (2006).

[CG69]   J. C. G. Callan and D. J. Gross,   *High-energy electroproduction and the constitution of the electric current*, Phys. Rev. Lett. **22**, 156–159 (1969).

[Cis97]   E. Cisbani,   *Working note on the direct ray-tracing particle identification method for the* RICH *detector at* HERMES , HERMES Internal Report (July 1997).

[Col93]   J. C. Collins,   *Fragmentation of transversely polarized quarks probed in transverse momentum distributions*, Nucl. Phys. **B396**, 161–182 (1993).

[Col02]   J. C. Collins,   *Leading-twist single-transverse-spin asymmetries: Drell–Yan and deep-inelastic scattering*, Phys. Lett. **B536**, 43–48 (2002).

[CS81]   J. C. Collins and D. E. Soper,   *Back-To-Back Jets in* QCD , Nucl. Phys. **B193**, 381–443 (1981).

Bibliography

[DE05]   M. Diefenthaler and U. Elschenbroich, *Single-spin azimuthal asymmetries in semi-inclusive deep-inelastic scattering on a tansversely polarized hydrogen target*, HERMES Release Report (April 2005).

[dFSS07]   D. de Florian, R. Sassot and M. Stratmann, *Global analysis of fragmentation functions for protons and charged hadrons*, Phys. Rev. **D76**, 074033 (2007).

[dFSSV09] D. de Florian, R. Sassot, M. Stratmann and W. Vogelsang, *Extraction of spin-dependent parton densities and their uncertainties*, Phys. Rev. **D80**, 034030 (2009).

[DH05]   M. Diehl and P. Hagler, *Spin densities in the transverse plane and generalized transversity distributions*, Eur. Phys. J. **C44**, 87–101 (2005).

[Die02]   M. Diehl, *Generalized parton distributions in impact parameter space*, Eur. Phys. J. **C25**, 223–232 (2002).

[Die05a]   M. Diefenthaler, *Transversity measurements at HERMES* , AIP Conf. Proc. **792**, 933–936 (2005).

[Die05b]   M. Diehl, Semi-exclusive isospin symmetry, discussion during HERMES drafting, January 2005.

[Die07a]   M. Diefenthaler, HERMES *measurements of Collins and Sivers asymmetries from a transversely polarised hydrogen target*, (2007), arXiv:0706.2242.

[Die07b]   M. Diefenthaler, Reevaluation of acceptance effects, presentation at HERMES collaboration meeting, October 2007.

[Die08]   M. Diefenthaler, Cut on $\theta_{\gamma^* h}$, presentation at HERMES meeting, January 2008.

[Die09]   M. Diefenthaler, The Sivers amplitudes for π^+ and K^+ and various estimates for the systematic uncertainty, presentation at HERMES meeting, April 2009.

[DM04]   U. D'Alesio and F. Murgia, *Parton intrinsic motion in inclusive particle production: unpolarized cross sections, single spin asymmetries, and the Sivers effect*, Phys.Rev. **D70**, 074009 (2004).

[DM08]   U. D'Alesio and F. Murgia, *Azimuthal and single spin asymmetries in hard scattering processes*, Prog. Part. Nucl. Phys. **61**, 394–454 (2008).

[DS05]   M. Diehl and S. Sapeta, *On the analysis of lepton scattering on longitudinally or transversely polarized protons*, Eur. Phys. J. **C41**, 515–533 (2005).

[ESS03a]   U. Elschenbroich, G. Schnell and R.-C. Seidl, *Single-Spin Azimuthal Asymmetries in SIDIS off a Transversely Polarized Proton Target*, HERMES Release Report (September 2003).

[ESS03b]   U. Elschenbroich, G. Schnell and R.-C. Seidl, *Single-Spin Azimuthal Asymmetries in SIDIS off a Transversely Polarized Proton Target — MC Studies*, (March 2003).

[Fey72]   R. P. Feynman, *Photon-hadron interactions*, W. A. Benjamin, Inc., Advanced Book Program, 1972.

[GL09]   F. Giordano and R. Lamb, *Measurement of azimuthal asymmetries of the unpolarized cross section at HERMES* , AIP Conf. Proc. **1149**, 423–426 (2009).

[HERMES 90] K. Coulter et al. (HERMES Collaboration),   *A proposal to measure the spin-dependent structure functions of the neutron and proton at HERA*, (1990).

[HMNS09] P. Hägler, B. Musch, J. Negele and A. Schäfer, *Intrinsic quark transverse momentum in the nucleon from lattice* QCD , Europhys.Lett. **88**, 61001 (2009).

[HZ09]   F. Aaron et al. (H1 and ZEUS Collaborations), *Combined Measurement and* QCD *Analysis of the Inclusive $e^{\pm}p$ Scattering Cross Sections at HERA*, (2009).

[Jaf97]   R. L. Jaffe, Spin, Twist and Hadron Structure in Deep Inelastic Processes, in *Lectures on* QCD*: Applications*, edited by F. Lenz, volume 496, pages 178–249, Springer, Berlin, New York, 1997.

[Jam94]   F. James,   MINUIT— *Function Minimization and Error Analysis*, 94.1 edition, March 1994.

[Ji03]   X.-d. Ji, *Viewing the proton through "color"-filters*, Phys. Rev. Lett. **91**, 062001 (2003).

[JJ91]   R. L. Jaffe and X.-D. Ji, *Chiral-odd parton distributions and polarized Drell–Yan process*, Phys. Rev. Lett. **67**, 552–555 (1991).

[JMY04]   X.-d. Ji, J.-P. Ma and F. Yuan, QCD *factorization for spin-dependent cross sections in* DIS *and Drell–Yan processes at low transverse momentum*, Phys. Lett. **B597**, 299–308 (2004).

[JMY05]   X.-d. Ji, J.-P. Ma and F. Yuan, *QCD factorization for semi-inclusive deep-inelastic scattering at low transverse momentum*, Phys. Rev. **D71**, 034005 (2005).

[JY02]   X.-d. Ji and F. Yuan, *Parton distributions in light-cone gauge: where are the final-state interactions?*, Phys. Lett. **B543**, 66–72 (2002).

[KPR78]   G. L. Kane, J. Pumplin and W. Repko, *Transverse Quark Polarization in Large-p_T Reactions, e^+e^- Jets and Leptoproduction: A Test of Quantum Chromodynamics*, Phys. Rev. Lett. **41**, 1689–1692 (1978).

[LH08]   R. Lamb and A. Hillenbrand, *Event Level* RICH *algorithm: An explanation and user guide*, HERMES Internal Report (July 2008).

[LYOPR73] A. Le Yaouanc, L. Oliver, O. Pene and J. Raynal, *"Naive" Quark-Pair-Creation Model of Strong-Interaction Vertices*, Phys.Rev. **D8**, 2223–2234 (1973).

[Mak03]   N. C. Makins, *"Back-of-the-Envelope" Interpretation of our First Transversity Data*, (May 2003).

[Mil06]   A. Miller, Extracting azimuthal Fourier moments from sparse data, presentation at HERMES Transversity Week, June 2006.

[Mil07]   G. A. Miller, *Densities, parton distributions, and measuring the non-spherical shape of the nucleon*, Phys. Rev. **C76**, 065209 (2007).

Appendix B

[MT96] P. J. Mulders and R. D. Tangerman, *The complete tree-level result up to order* $1/Q$ *for polarized deep-inelastic leptoproduction*, Nucl. Phys. **B461**, 197–237 (1996).

[Mus07] A. Mussgiller, HERMES measurement of DVCS from p and d targets, and status and prospects of the recoil detector, in *Proceedings for 15th International Workshop on Deep-Inelastic Scattering and Related Subjects (*DIS2007*)*, edited by G. Grindhammer and K. Sachs, April 2007.

[Pap08] L. L. Pappalardo, *Transverse spin effects in polarized semi inclusive deep inelastic scattering*, PhD thesis, University of Ferrara, 2008.

[Pap09] L. Pappalardo, z-vertex position studies, presentation at HERMES Transversity Week, May 2009.

[PTVF92] W. H. Press, S. A. Teukolsky, W. T. Vetterling and B. P. Flannery, *Numerical Recipes in C: The Art of Scientific Computing*, Cambridge University Press, Cambridge, New York, Port Chester, Melbourne, Sydney, second edition, 1992.

[Raj05] R. Raja, *A general theory of goodness of fit in likelihood fits*, (2005), arXiv:physics/0509008.

[RP02] J. P. Ralston and B. Pire, *Femtophotography of protons to nuclei with deeply virtual Compton scattering*, Phys. Rev. **D66**, 111501 (2002).

[RS79] J. P. Ralston and D. E. Soper, *Production of dimuons from high-energy polarized proton-proton collisions*, Nucl. Phys. **B152**, 109–124 (1979).

[S$^+$01] T. Sjostrand et al., *High-energy physics event generation with* PYTHIA 6.1, Comput. Phys. Commun. **135**, 238–259 (2001).

[Siv90] D. W. Sivers, *Single-spin production asymmetries from the hard scattering of pointlike constituents*, Phys. Rev. **D41**, 83–90 (1990).

[Sol64] F. T. Solmitz, *Analysis of experiments in particle physics*, Ann. Rev. Nucl. Part. Sci. **14**, 375–402 (1964).

[ST64] A. A. Sokolov and I. M. Ternov, *On Polarization and spin effects in the theory of synchrotron radiation*, Phys. Dokl. **8**, 1203–1205 (1964).

[STM10] P. Schweitzer, T. Teckentrup and A. Metz, *Intrinsic transverse parton momenta in deeply inelastic reactions*, (2010), arXiv:1003.2190.

[BRAHMS08] I. Arsene et al. (BRAHMS Collaboration), *Single-Transverse-Spin Asymmetries of Identified Charged Hadrons in Polarized pp Collisions at* $\sqrt{s} = 62.4$ *GeV*, Phys. Rev. Lett. **101**, 042001 (2008).

[COMPASS07] V. Y. Alexakhin et al. (COMPASS Collaboration), *The Deuteron Spin-dependent Structure Function* g_1^d *and its First Moment*, Phys. Lett. **B647**, 8–17 (2007).

[COMPASS09] M. Alekseev et al. (COMPASS Collaboration), *Collins and Sivers asymmetries for pions and kaons in muon-deuteron deep-inelastic scattering* , Phys.Lett. **B673**, 127–135 (2009).

[E581 91] D. L. Adams et al. (E581 Collaboration), *Comparison of Spin Asymmetries and Cross Sections in π^0 Production by 200-GeV Polarized Antiprotons and Protons*, Phys. Lett. **B261**, 201–206 (1991).

[E704 91] D. L. Adams et al. (E704 Collaboration), *Analyzing power in inclusive π^+ and π^- production at high x_F with a 200 GeV polarized proton beam*, Phys. Lett. **B264**, 462–466 (1991).

[HERMES98] K. Ackerstaff et al. (HERMES Collaboration), *The HERMES spectrometer*, Nucl. Instrum. Meth. **A417**, 230–265 (1998).

[HERMES00] A. Airapetian et al. (HERMES Collaboration), *Evidence for a Single-Spin Azimuthal Asymmetry in Semi-inclusive Pion Electroproduction*, Phys. Rev. Lett. **84**, 4047–4051 (2000).

[HERMES01] A. Airapetian et al. (HERMES Collaboration), *Single-spin azimuthal asymmetries in electroproduction of neutral pions in semi-inclusive deep-inelastic scattering*, Phys. Rev. **D64**, 097101 (2001).

[HERMES02] A. Borisenko et al. (HERMES Collaboration), *The HERMES Recoil Detector — Technical Design Report*, HERMES Internal Report (2002).

[HERMES05a] A. Airapetian et al. (HERMES Collaboration), *The HERMES polarized hydrogen and deuterium gas target in the HERA electron storage ring*, Nucl. Instrum. Meth. **A540**, 68–101 (2005).

[HERMES05b] A. Airapetian et al. (HERMES Collaboration), *Quark helicity distributions in the nucleon for up, down, and strange quarks from semi-inclusive deep-inelastic scattering*, Phys. Rev. **D71**, 012003 (2005).

[HERMES05c] A. Airapetian et al. (HERMES Collaboration), *Single-spin asymmetries in semi-inclusive deep-inelastic scattering on a transversely polarized hydrogen target*, Physical Review Letters **94**, 012002 (2005).

[HERMES05d] A. Airapetian et al. (HERMES Collaboration), *Subleading-twist effects in single-spin asymmetries in semi-inclusive deep-inelastic scattering on a longitudinally polarized hydrogen target*, Phys. Lett. **B622**, 14–22 (2005).

[HERMES07] A. Airapetian et al. (HERMES Collaboration), *Precise determination of the spin structure function g_1 of the proton, deuteron and neutron*, Phys. Rev. **D75**, 012007 (2007).

[PDG08] C. Amsler et al. (PDG Collaboration), *Review of particle physics*, Phys. Lett. **B667** (2008).

[STAR04] J. Adams et al. (STAR Collaboration), *Cross Sections and Transverse Single-Spin Asymmetries in Forward Neutral-Pon Production from Proton Collisions at $\sqrt{s} = 200$ GeV*, Phys. Rev. Lett. **92**, 171801 (2004).

[VY05] W. Vogelsang and F. Yuan, *Single-transverse spin asymmetries: From deep-inelastic scattering to hadronic collisions*, Phys.Rev. **D72**, 054028 (2005).

Bibliography

[Wan96]   W. Wander, *Reconstruction of high-energy scattering events in the* HERMES *experiment,* PhD thesis, Friedrich-Alexander University Erlangen-Nürnberg, 1996.

[Wen03]   J. Wendland, *Polarized Parton Distributions Measured at the* HERMES *Experiment,* PhD thesis, Simon Fraser University, 2003.

[Wii81]   B. Wiik, *The* HERA *Proposal,* DESY HERA Report 81-10 , 292 (1981).

[WW77]   S. Wandzura and F. Wilczek, *Sum rules for spin-dependent electroproduction — test of relativistic constituent quarks,* Phys.Lett. **B72**, 195–198 (1977).